Phys. Status Solidi B, 1–81 (2013) / **DOI** 10.1002/pssb.201248392

physica status solidi b
www.pss-b.com
basic solid state physics

Review Article

Controlled manipulation of single atoms and small molecules using the scanning tunnelling microscope**

Karina Morgenstern*,[1], Nicolas Lorente[2,3], and Karl-Heinz Rieder[4,5]

[1] Ruhr-Universität Bochum, Lehrstuhl für Physikalische Chemie I, Universitätsstr. 150, 44801 Bochum, Germany
[2] ICN2 – Institut Català de Nanociència i Nanotecnologia, Campus UAB, 08193 Bellaterra (Barcelona), Spain
[3] CSIC – Consejo Superior de Investigaciones Científicas, ICN2 Building, Campus UAB, 08193 Bellaterra (Barcelona), Spain
[4] EMPA, Swiss Federal Laboratories for Materials Testing and Research, Überlandstrasse 129, 8600 Dübendorf, Switzerland
[5] Fachbereich Physik der Freien Universität Berlin, Arnimallee 14, 14195 Berlin, Germany

Received 21 August 2012, revised 19 April 2013, accepted 3 May 2013
Published online 24 July 2013

Keywords inelastic tunnelling, manipulation, scanning tunnelling microscopy, scanning tunnelling spectroscopy

* Corresponding author: e-mail karina.morgenstern@rub.de, Phone: +49 234 32 25529, Fax: +49 234 32 14182
** This article will be published in edited form in Vol. 5–6 "Solid–Gas Interfaces" of the book series "Surface and Interface Science," edited by K. Wandelt (Wiley-VCH, Weinheim, 2013ff.), ISBN 978-3-527-41157-3.

This article reviews manipulation of single molecules by scanning tunnelling microscopes, in particular vertical manipulation, lateral manipulation, and inelastic electron tunnelling (IET) manipulation. For a better understanding of these processes, we shortly review imaging by scanning tunnelling microscopy – as a prerequisite to detect the manipulated species and to verify the result of the manipulation – as well as scanning tunnelling spectroscopy and IET spectroscopy which are used to chemically identify the molecules before and after the manipulation that employs the tunnelling current.

1 Introduction

In Primo Levi's novel "The monkey's wrench" [1] a chemist tells a construction engineer how chemists sometimes fantasize about building molecules: "We don't have those tweezers we often dream of … that would allow us to pick up a segment, hold it firm and straight, and paste it in the right direction on the segment that has already been assembled. If we had those tweezers – and it's possible that one day we will – we would have managed to create some lovely things that so far only the Almighty has made." With the invention of scanning tunnelling microscopy (STM) [2] such "tweezers" have been realized and the "segments" became as small as single molecules or even atoms.

STM is used in modern surface science to explore conducting surfaces, adsorption processes on them, and excitations on the atomic and molecular scale. Elastic electron tunnelling provides the basic mechanism for imaging, whereas inelastic electron tunnelling (IET) provides the basic mechanism for chemical characterization via vibrational spectroscopy. One important application provided by the small size of the tip is the manipulation of individual adsorbates including single molecule chemistry. Only STM is able to successively detect single atoms or molecules, spectroscopically characterize, modify, and reanalyze them using the same instrument. By combining imaging, manipulation, and vibrational spectroscopy, significant understanding of surface chemistry can thus be gained. These capabilities opened up new aspects of science on the smallest scale currently accessible in surface science.

The main focus of this review article is the manipulation with the STM. Nonetheless, we will shortly review STM imaging as a prerequisite to detect the manipulated species and verify the result of the manipulation and STM inelastic electron tunnelling spectroscopy (IETS), which is used to chemically identify the molecules before and after manipulation. Understanding IETS is also a prerequisite for the manipulation that employs the tunnelling current.

Note that based on the didactic approach of this tutorial examples in the introductory Sections 3 and 4 are drawn from the work of the authors. This is not meant to imply that these are the first or even only examples. In the following

Contents

Karina Morgenstern studied Physics and Computer Science in Bonn and Knoxville, Tennessee. Her Ph.D. thesis in the field of surface science in 1996 was supervised by George Comsa, FZ Jülich, and Flemming Besenbacher, Universitet Aarhus. After a postdoctoral stay at the University of Lausanne, she finished her habilitation in the group of Karl-Heinz Rieder at the Free University in Berlin in 2002. In 2005 she became Professor of Solid State Physics (W3) at the University of Hannover. Since 2012 she is holding the chair of Physical Chemistry (W3) of the Ruhr-Universität Bochum.

Sections 5–9 original works (mostly in chronological order) are referenced in the subsections entitled "Further reading" (5.2.11, 7.4, and 9.3.3).

1.1 Historical remarks The scanning tunnelling microscope (STM), invented in 1981 [2] was in its initial conception intended to work as an imaging instrument. It became, however, clear soon to its inventors Gerd Binnig, Heinrich Rohrer, Christoph Gerber, and Edmund Weibel that the scope of its possibilities exceeded pure imaging by far and they early started to pursue the spectroscopic possibilities of the instrument [2]. Indeed, their experimental experience already then went further, as the following episode proves, which one of the present authors (KHR) remembers very vividly: on October 12th 1986, the day, when the Nobel Prize in Physics for 1986 was announced to Binnig and Rohrer, the new laureates were asked by some journalists present at the IBM Rüschlikon Research Laboratory: "Now that you have developed this wonderful instrument, with which atoms can be made visible, can you say what will be the future of it?" Gerd Binnig answered decidedly: "We will play soccer with the atoms!" (Fig. 1) He expressed in this way their occasional observations that the tip would influence individual particles at the surface during scanning in such a way that they were moved to other places on the substrate. For faithful imaging any uncontrolled modification of the surface was, of course, regarded a serious disadvantage, but Binnig foresaw even at such an early stage that the disadvantage could be turned eventually into an advantage by using the tip for influencing and modifying surfaces in a desired way. ("We will play soccer with the atoms!" was chosen as motto by the German Physical Society for the Year of Physics 2000, although Gerd Binnig himself does not remember his own citation.) The idea to manipulate atoms and molecules in a precise way remained

Figure 1 The IBM soccer team on the evening of October 12th, 1986, the day when the Nobel prize was announced to Gerd Binnig and Heinrich Rohrer (right and left with the flower bouquets, respectively) for the invention of the STM. Their collaborator Christoph Gerber playing goalie holds the ball. (Courtesy of C. Gerber.)

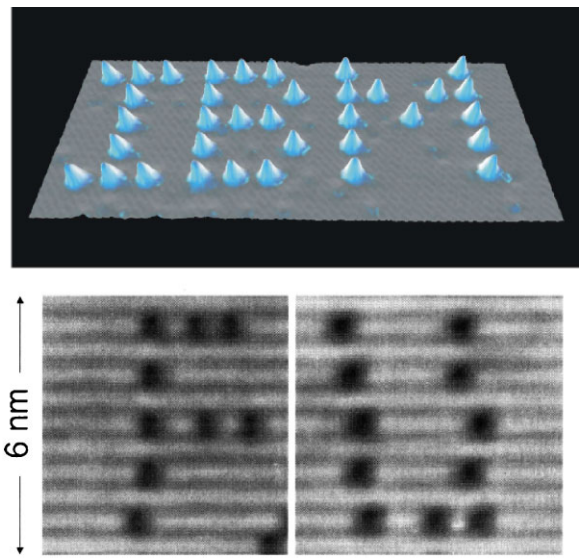

Figure 2 The first artificially assembled structures by the first two groups being able to perform atom-by-atom work. Upper part: "IBM" by Schweitzer and Eigler and Schweizer [3] built with Xe atoms on Ni(110) at 4 K and FU by Meyer et al. [5] built with CO molecules on Cu(211) at 25 K.

at IBM, where Donald Eigler and colleagues at the IBM Almaden Research Center built a very stable low temperature STM, with which they proved precise manipulation via the build-up of several artificial structures at the beginning of the 1990s (Fig. 2, upper part) [3, 4]. The second – much simpler and less expensive – apparatus able for manipulation on the atomic scale was designed and built by Gerhard Meyer at the Free University in Berlin and this group started systematic investigations on the manipulation mechanisms in 1995 [5] (Fig. 2, lower part). These investigations proved that, for reliable positioning of single atoms and molecules, mainly the forces between tip and adsorbate were responsible [6]. At the same time, however, several different possibilities for surface modifications on atomic or nanometer scale using also field and force effects were reported [7, 8].

This article is organized in nine main sections. In Sections 2 and 3, we review STM, STS, and IETS. Readers well familiar with these methods might directly start reading at Section 4 that gives an overview over the different manipulation methods. Each method is then explained in detail in Sections 5–7, which review lateral manipulation, vertical manipulation, and manipulation via the tunnelling current, respectively. Sections 8 and 9 explain some particularly beautifully examples that used manipulation, in particular physics in artificially created structures in Section 8 and manipulation on insulating films in Section 9. The review closes with an outlook in Section 10.

2 Scanning tunnelling microscopy STM is a real space method that can be used on conducting samples. The first scanning tunnelling microscope (STM) came into operation in 1981 built by G. Binnig and H. Rohrer [9].

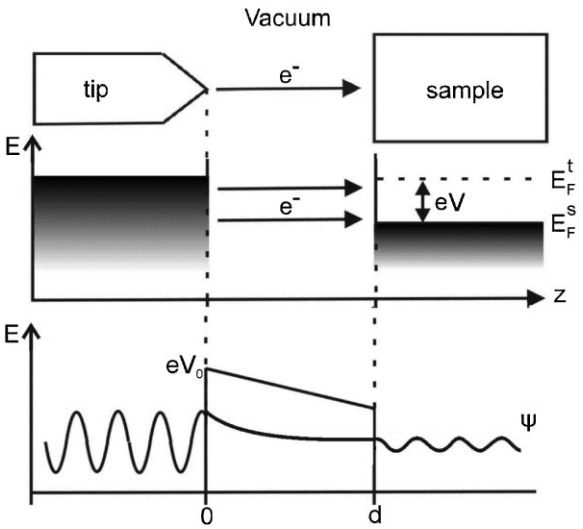

Figure 3 Top: schematics of tunnelling process between metallic tip and conducting sample. Middle: electrons of energies up to eV above the Fermi energy of the sample E_F^S may tunnel from occupied states (shaded) in the tip to unoccupied states in the sample (or vice versa, not shown). V is the applied bias that displaces the two Fermi levels of sample and tip against each other and eV is the energy difference between the Fermi levels. Bottom: the electron wave function Ψ decays exponentially in the vacuum region between the two electrodes; d is the distance between the two electrodes.

A year later the first atomic resolution images were recorded [10]. Today, STMs obtain routinely a resolution of 100 pm in lateral and of 1 pm in vertical resolution.

The systems studied by STM include metallic surfaces, semiconductor surfaces, oxide surfaces with a narrow band gap, superconductor surfaces, and quasi-crystalline surfaces. The only requirement is a conducting substrate material in order to establish a tunnelling current. On top of this substrate, molecules or thin insulating films were imaged to a thickness of a few layers.

The main applications of STM are to clarify the surface topography and to study electronic and vibrational properties. STM provides atomic resolution offering the possibility to study solitary surface defects and single adsorbates. It is able to resolve electronic and vibrational properties locally. Chemical bonding and adsorption, cluster formation, film growth, magnetic properties, and other surface relevant phenomena were studied by STM.

Often STM images are interpreted in terms of the topological structure of the surface. However, the interpretation of a topographic image is rarely straightforward: different adsorbates have been imaged either as protrusions or as depressions, and sometimes they were even found to be transparent to the microscope. This problem in interpretation occurs since the STM image is a superposition of the topographic and the electronic structure of the adsorbate-substrate system, which we will sketch in the following.

Basically, STM is based on the quantum mechanical phenomenon of tunnelling, in which an electron travels through a barrier that it cannot surmount in classical physics, because its energy is smaller than the barrier's height (Fig. 3). As tunnelling is based on the wave nature of electrons, the tunnelling probability depends not only on the width of the barrier but also on the electron's wave function.

In STM, the electrons tunnel through the vacuum between two conducting electrodes. One of them has ideally only a few atoms at its end. This tip is approached with the aid of piezoelectric elements (called piezos) to the other electrode to a distance of only about a tenth of a nanometer or less. At such a distance, the wave functions of tip and sample start to overlap. Such an overlap is equivalent to a finite tunnelling probability of the electrons between the two electrodes. Application of a bias voltage between tip and sample directs the tunnelling into one direction, from the occupied electronic states at one of the electrodes to the unoccupied states at the other one (Fig. 3). An applied bias voltage of typically a few mV to a few V leads to a tunnelling current of typically pA to nA. This tunnelling current depends exponentially on the distance between tip and sample because wave functions decay exponentially into the vacuum. The current is thus a sensitive measure of the distance between the electrodes.

2.1 Experimental aspects Mostly, STMs are operated in constant current mode, where the height of the tip above the sample is varied by a feed-back loop such that the tunnelling current stays constant (Fig. 4). The tip is scanned line-by-line in a chosen area, typically 128–512 points per line and an equal number of lines, and the feedback is adjusted on each pixel. In this mode, the tip follows a surface, where the local density of states integrated from the Fermi energy to eV is constant (see Fig. 4).

The feed-back loop controls the distance between tip and sample via the voltage applied to the piezo. The tip height is translated into gray values at each pixel giving the STM image. Because of the superposition of the topography with electronic effects in the image, one usually quotes "apparent" heights.

The major advantage of STM as compared to methods operating in reciprocal space is its ability to investigate local deviations from average behavior, see, e.g., the example in

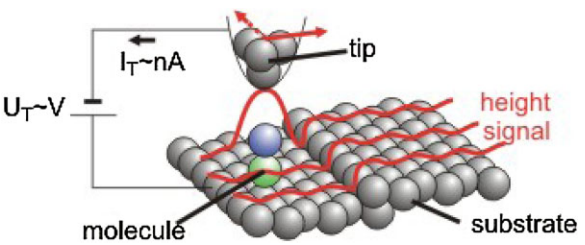

Figure 4 Schematics of constant current mode: the feedback loop changes the tip height above the surface so that the tunnelling current stays constant. The display of the z position of the tip's height signal versus the scanning motion delivers the STM image.

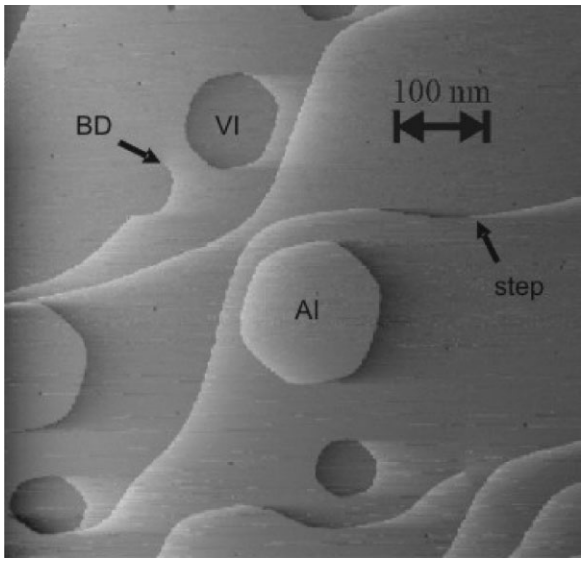

Figure 5 STM image showing a Ag(111) surface with many local defects as steps, vacancy islands (VI) of monatomic depth, monatomic high adatom islands (AI), and emerging bulk dislocations (BD) [11]. A slow integrating part of the feedback loop results in an image, where it seems, as if the surface was illuminated from its left-hand side. This form of display is used to make several terraces visible in the same display.

Fig. 5. The nominally flat surface shows deviations from a perfect single crystal surface. Some intrinsic surface steps result from the unavoidable slight miscut angle of the crystal. Each crystal has also an equilibrium number of intrinsic bulk dislocations that emerge to the sample surface. If such a dislocation has a component of the Burgers vector in perpendicular to that surface, a surface step ends at it (BD). The surface in Fig. 5 shows in addition some holes in the surface layer (VI) and some additional agglomeration of atoms on it (AI). These result from sputtering the surface at elevated temperature [11]. In methods operating in reciprocal space, all of these features would only contribute to the diffuse background signal and could thus neither be identified nor further investigated.

Furthermore, STM allows to image surfaces in atomic resolution. In Fig. 6 each of the protrusions represents one atom of Ag(111), a surface with hexagonal symmetry.

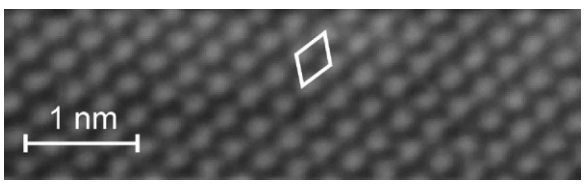

Figure 6 STM image of Ag(111) in atomic resolution; 0.2 nA, 11 mV. The apparent height above the atoms is higher and thus each protrusion represents one atom. A unit cell connecting four atoms with a distance of $a = 0.289$ nm is indicated.

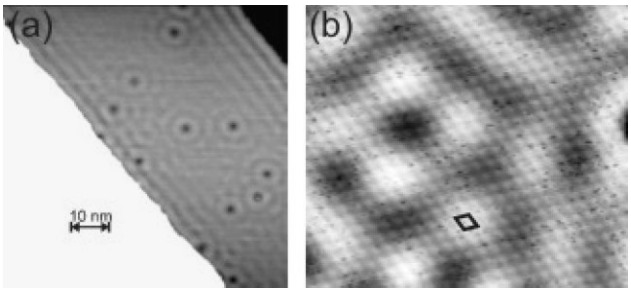

Figure 7 Standing waves from electrons in occupied surface state: (a) on Ag (111) close to defects, here CO molecules (black dots) and surface steps, 0.34 nA, 32 mV; (b) on Cu(111): atomic resolution (small dots) superimposed with standing wave pattern of surface state electrons. Scattering is at CO molecules outside of the region shown. A unit cell ($a = 0.255$ nm) is indicated, 1.8 nA, 26 mV.

A topographic interpretation of STM images as exemplified for Figs. 5 and 6 assumes that the density of states of the sample is constant above equivalent surface sites. In reality the interpretation of STM images is not always straightforward topological because of the superposition with electronic effects. See, e.g., Fig. 7a that shows standing wave patterns on a topological flat terrace. These are circular waves around black dots and planar waves coming from the straight step edges and a superposition of those in between the defects. In Fig. 7b such a standing wave pattern is imaged simultaneously with the atomic resolution of Cu(111). In both images, the standing waves originate from electrons in the surface state of Ag(111) and Cu(111), respectively, scattered off defects (see Section 2.1.1 for a short explanation of the surface state). These standing waves alter the electron density locally. As a consequence the atoms in Fig. 7b, which all have the same geometric height within the surface plane, are imaged, as if they had different heights.

This superposition of geometric and electronic effects is even more important when imaging adsorbates. As exemplified in Fig. 8 oxygen atoms adsorbed on Ag(100) are imaged either as depressions or as protrusions depending on the applied bias voltage [12].

The interpretation of STM images of molecules is further complicated, because the features resolved do not

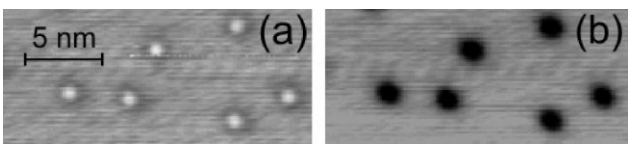

Figure 8 STM images of oxygen atoms on Ag(100) [12] at opposite polarity: (a) at negative bias voltage (−1.44 V) each atom is imaged as a protrusion, (b) at positive bias voltage (+1.44 V) as a depression.

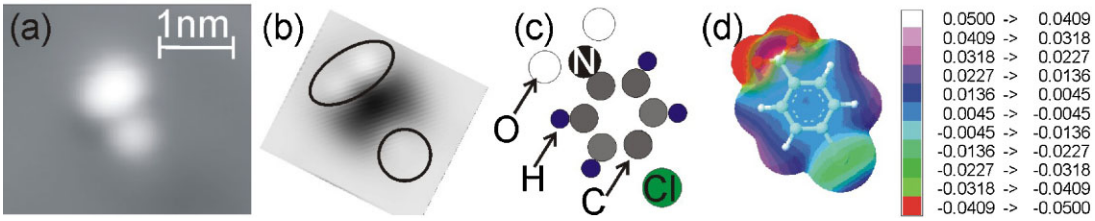

Figure 9 Para-chloronitrobenzene: (a) STM image shows two protrusions of different apparent height and shape. (b) Calculation in tight-binding approach shows that the nitro group leads to an ellipsoidal protrusion and the chlorine atom to a circular protrusion of smaller height as indicated by ellipse and circle, respectively. (c) Comparison of experiment in (a) to theory in (b) allows identifying the orientation of the molecule on the surface as shown. (d) ESP map as optimized semi-empirically in gas phase using the Parametric Method 3 parameterization of MNDO for the Hamiltonian with ArgusLab 4.0.1, Mark A. Thompson, Planaria Software LLC, Seattle, WA, http://www.arguslab.com (at large distance from the molecule of 0.0003 electrons/Bohr^3 with 1B = 0.0529 nm); potential is given in Hartrees (1H = 27.2 eV).

simply reflect the atomic positions within the molecule but electronic states that contribute to the tunnelling. Figure 9a shows a STM image of a chloronitrobenzene molecule. This molecule consisting of 14 atoms leads to two protrusions of different heights and shapes only. Interpretation of this image demands a theoretical description (Fig. 9b), here based on Green's functions in tight-binding approach (see Section 2.2.3), which allows to determine the orientation of the molecule (Fig. 9c).

A less involved method to identify physisorbed adsorbates is the electrostatic potential mapped on the electron density contour of gas phase molecules (ESP map), which can be easily calculated with semi-empirical methods for the quantum calculation of the molecular electronic structure in computational chemistry. It was rationalized [13] that the inverted of this potential, representing the potential energy felt by a negative test charge, is a good concept to interpret changes in the dielectric constant through the influence of physisorbed molecules and to understand their submolecular resolution images. The resemblance between ESP and STM image can be explained by a molecule-induced change in dielectricity as compared to the dielectricity of the vacuum. A large dielectric constant increases the tunnelling probability as compared to the vacuum. The higher the dielectricity in the gap between tip and sample the more the tip is retracted to draw the same current at the same voltage. Thus, a larger dielectric constant leads to a larger apparent height.

Indeed, for the example shown in Fig. 9d, only those regions of the molecule with negative ESP values show protrusions in the STM image and the higher of the two protrusions corresponds to the larger ESP value above the nitro group.

A further difficulty presents the dependence of the STM image on the usually unknown electronic structure of the tip. Figure 10 demonstrates that such a simple molecule as CO adsorbed on Cu(111) is imaged in many different forms with slightly different tips. Experimentalist should modify their tip till known surface structures, e.g., surface steps, show the "usual" shape in order to avoid misinterpretations.

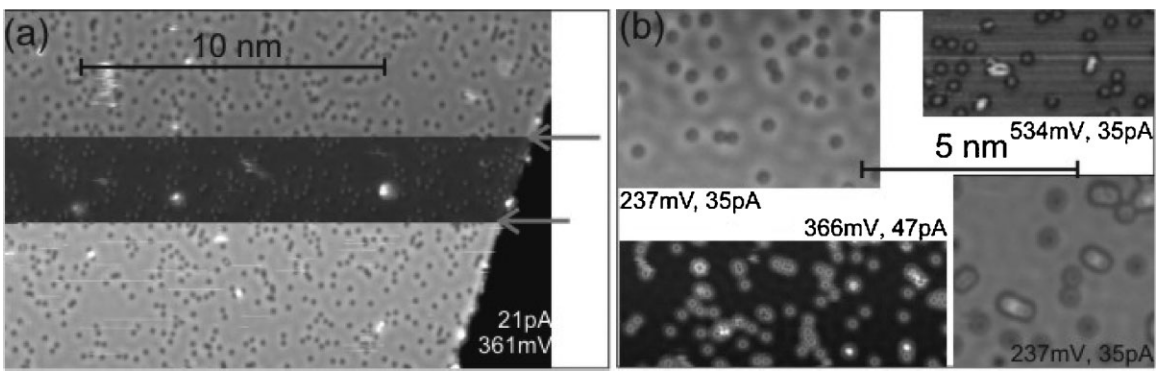

Figure 10 Different images of CO on Cu(111) at the tunnelling parameters indicated. In (a) the tip picks up a molecule at the first arrow (scanning is from top to bottom). The surface is then imaged darker, i.e., at a lower height, and the molecule changes appearance from depressions to protrusions. The molecule is deposited back to the surface at the second arrow and the original contrast is restored. (b) CO molecules imaged with "different" tips that lead to several different types of sombrero shapes. Note that molecules in close proximity are imaged higher than isolated molecules with some tips.

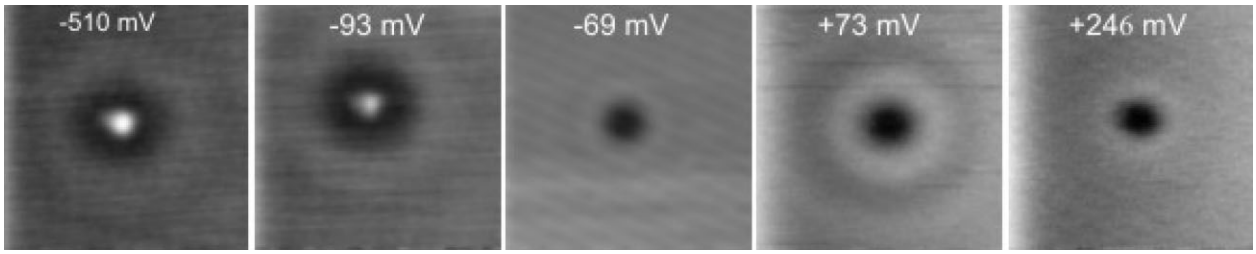

Figure 11 STM images of a H_2O cluster on Ag(111) at different voltages, 0.64 nA. The change in apparent height is explained by a field induced rotation of the dipolar H_2O molecules [14], 15 nm × 15 nm.

Finally, the electric field in the tunnelling region might transiently influence the adsorption orientation of molecules, in particular those with large dipole moments. Figure 11 shows an example, where the same water cluster is imaged as a protrusion at −93 mV and below, but as a depression at −69 mV and above. This change of the appearance of the water clusters was shown to be a result of the reorientation of some of the molecules in the electric field [14]. This problem will even more influence imaging adsorbates on semiconductors, because images on semiconductors demand a larger bias voltage.

2.1.1 Excursus: Surface state As the intrinsic surface state existing on nominally clean surfaces will be encountered more often in this review article, we shortly review its main features. The accurate characterization and fundamental understanding of surface states is a subject of significant interest because of the variety of surface processes, which they govern, including diffusion, epitaxial growth, reconstructions, sticking of atoms and molecules, surface chemistry, molecular ordering, and screening of defects at surfaces.

The fcc(111) surfaces of noble metals exhibit a large sp-band gap in the projected bulk band structure along the *Γ*–*L* line [15, 16] (Fig. 12). These gaps reach down below the Fermi energy at the center of the surface Brillouin zone and support an occupied free-electron surface state [17]. These surface states are confined to the vicinity of the top layer by the vacuum barrier on one side and the band gap in the bulk states on the other side. Electrons occupying surface states cannot scatter into bulk states without changing either energy or momentum. They thus form a two-dimensional high-density nearly free electron gas parallel to the surface [18, 19].

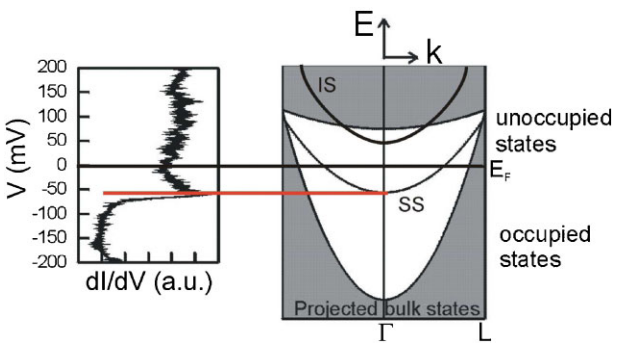

Figure 12 Schematics of surface state (SS) in projected bulk state pseudo gap (right hand side) and spectrum as taken by STM on a Ag (111) surface, where the surface state onset is situated at −69 mV. Note, that usually STS spectra are displayed as d*I*/d*V* versus *V* in contrast to the spectrum shown here. For the usual display see Fig. 17; IS depicts an image state.

The surface states dominate in the zone between the tip and the surface and can be detected by scanning tunnelling spectroscopy (STS), which allows measuring the electronic density of states at the center of the Brillouin zone (Γ point; see Section 3.1) [20]. Such a spectrum (Fig. 12) shows a strong increase in d*I*/d*V* signal, i.e., in conductivity, at the bottom of the surface state band, which is called the onset of the surface state.

Interactions of electrons in surface states with adsorbates [21, 22], steps [21, 23–27] and other structures [28] lead to standing wave patterns (see Fig. 7). These spatial oscillations are quantum mechanical interference patterns caused by scattering of the two-dimensional electron gas at defects. Dependence of the wavelength of these spatial oscillations on temperature and on energy facilitates measuring the electron's life time and the surface state dispersion, respectively [29, 30].

2.2 Theoretical background The STM current results from electrons tunnelling elastically from occupied states of one electrode through the vacuum barrier into unoccupied states of the other electrode (Fig. 3). It depends on the electronic structure of the sample, on the distance between tip and sample, on the applied bias voltage, and on the geometric and electronic properties of the tip. Even though the theoretical background behind STM is quite well-understood, a general agreement on the details of the formation of the tunnelling current has not been achieved yet. Several competing methods sharing the same basic principles were developed. The most common way to model the tunnelling current and thus STM images is as follows. First, density functional theory (DFT) is used to calculate the density-of-states (DOS) of the electrodes and then the tunnelling current is calculated from this DOS using the Tersoff–Hamann theory (see

Section 2.2.2) based on the transfer Hamiltonian method (see Section 2.2.1). Despite some severe limitations, the Tersoff–Hamann approach is conveniently used, because of its simplicity. It is useful to check quickly, whether the model derived from a STM image is reasonable. However, this theory fails in describing, e.g., atomic resolution of metal surfaces, because it neglects the interactions between tip and sample. In particular on close-packed surfaces, the tip has to approach closely to the sample and distort it (lift up the atoms) in order to achieve atomic resolution [31]. Thus, for an exact reproduction of STM images, image charge effects, van-der-Waals forces, and chemical forces between tip and sample have to be included.

The interpretation of STM images of molecules imaged in the highest occupied molecular orbital–lowest occupied molecular orbital gap (HOMO–LUMO) [13] adsorbed on metals can also not be explained by this approach. Instead, understanding STM images of molecules demands to treat the surface–adsorbate–tip system as an entity (see Section 2.2.3).

2.2.1 The transfer Hamiltonian method The transfer Hamiltonian formalism is a perturbation theory. It was used originally by Bardeen [32] to explain the first tunnelling spectra obtained in metal oxide junctions [33]. Tersoff and Hamann [34] and Baratoff [35] are the ones who first applied this formalism to STM.

In this formalism, the electron waves in the two metal electrodes are considered to be independent and the coupling of the electron waves in the gap is treated as a perturbation. This Ansatz leads to a total Hamiltonian

$$H = H_{\mathrm{L}} + H_{\mathrm{R}} + H_{\mathrm{T}}. \tag{1}$$

H_{L} and H_{R} are the unperturbed Hamiltonians of the two electrodes and H_{T} the one between them. For the wave functions the WKB (Wentzel–Kramers–Brillouin) approximation is used. The WKB approximation is a semi-classical calculation in quantum mechanics, in which the wave function is recast as an exponential function, semi classically expanded, and then either the amplitude or the phase is taken to be slowly changing. The initial wave functions inside and outside the barrier in WKB approximation are

$$\begin{aligned} \Psi_\mu &= \frac{1}{\sqrt{k_z}} \mathrm{e}^{i(k_x x + k_y y)} \sin(k_z + \gamma), \\ \Psi_\nu &= \frac{1}{\sqrt{|k_z|}} \mathrm{e}^{i(k_x x + k_y y)} \mathrm{e}^{-\int_0^d |k_z| \mathrm{d}z}, \end{aligned} \tag{2}$$

with wave vector $\vec{k} = (k_x, k_y, k_z)$, z being the junction direction, $k_z = \sqrt{2m(V(z) - E)}/\hbar$, d the width of the barrier, $V(z)$ the potential in the barrier, and γ a constant phase shift.

The elastic tunnelling current is a linear combination of an initial state and of a sum of final states, which is inserted into the time-dependent Schrödinger equation and solved to first order in the coefficients leading to a transition rate per unit time of:

$$\omega_{\mu\nu} = \frac{2\pi}{\hbar} \left|M_{\mu\upsilon}\right|^2 \delta(E_\nu - E_\mu). \tag{3}$$

The tunnelling matrix element $M_{\mu\nu}$ is determined by the overlap of the wave functions Ψ_μ and Ψ_υ to the right and to the left of the potential barrier at a virtual dividing plane S, whose normal vector $\vec{n}$ points from one electrode to the other:

$$M_{\mu\nu} = -\frac{\hbar^2}{2m_e} \int_S \mathrm{d}\vec{S} \, (\Psi_\mu{}^* \, \Psi_\nu - \Psi_\nu \, \Psi_\mu{}^*). \tag{4}$$

The total tunnelling current is calculated by first multiplying the transition rate (3) with the mean occupancy f of the state in one of the electrodes and the non-occupancy $(1 - f)$ of the states in the other electrode. Then the sum over all initial and final states on both sides of the barrier is formed:

$$\begin{aligned} I = \frac{2\pi e}{\hbar} \sum_{\mu\nu} &[f(E_\mu)(1 - f(E_\nu + eV))] \left|M_{\mu\nu}\right|^2 \\ &\times \delta(E_\mu - (E_\nu + eV)) \end{aligned} \tag{5}$$

with $f(E)$ the Fermi distribution and V the applied bias voltage.

Two assumptions simplify Eq. (5):

(i) At low temperature the Fermi distribution is a step like function.
(ii) For low bias voltage only states close to the Fermi energy are relevant.

These assumptions lead to:

$$I = \frac{2\pi eV}{\hbar} \sum_{\mu\nu} \left|M_{\mu\nu}\right|^2 \delta(E_\mu - E_{\mathrm{F}}) \delta(E_\nu - E_{\mathrm{F}}). \tag{6}$$

2.2.2 Tersoff–Hamann theory for calculating the tunnelling current Tersoff and Hamann [20, 34] developed the first three-dimensional theory for tunnelling based on the transfer Hamiltonian method, which implies that this theory can be employed as long as tip and sample are only weakly coupled. It takes into account the detailed electronic states of two electrodes.

The Tersoff–Hamann theory explicitly includes the wave function form of the electrons in tip and sample. The wave functions of the surface electrons are considered to

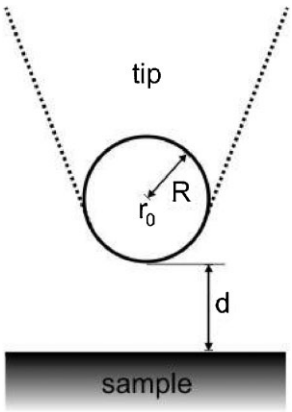

Figure 13 Schematics of tip-sample geometry for Tersoff–Hamann theory: the tip is replaced by a sphere with radius R at a distance d from the sample [20, 34]. The sample wave function is calculated at r_0.

move freely in the surface plane, but to decay exponentially in perpendicular to the surface:

$$\Psi_\nu = \Omega_s{}^{-1/2} \sum_G a_G \exp\left(-z\sqrt{\kappa_s^2 + \left|\vec{k}_{||} + \vec{G}\right|^2}\right) \times \exp(i(\vec{k}_{||} + \vec{G})\vec{r}_{||}) \quad (7)$$

with $\kappa_s = \sqrt{2m\Phi_s}/\hbar$ the minimum inverse decay length for the wave function in vacuum, which depends on the work function Φ_s of the sample. Ω_s is the sample volume and $\vec{G}$ a surface lattice vector in reciprocal space. Here Cartesian coordinates are used.

Because the exact tip shape is unknown, Tersoff and Hamann considered the geometry depicted in Fig. 13, a sphere of radius R. For this spherical tip only wave functions symmetric around the tip apex are considered. With $\vec{r}_0$ the center of the sphere it follows (in polar coordinates):

$$\Psi_\mu = \Omega_t^{-1/2} c_t \kappa_t R e^{\kappa_t R} \frac{e^{-\kappa_t(|\vec{r}-\vec{r}_0|)}}{\kappa_t|\vec{r}-\vec{r}_0|}, \quad (8)$$

where $\kappa_t = \sqrt{2m\Phi_t}/\hbar$, Φ_t is the work function of the tip, and Ω_t is the volume of the tip. The normalization coefficient c_t is determined by the geometry and the detailed electronic structure of the tip and by the tip-vacuum boundary conditions; usually $c_t \approx 1$.

Despite the spherical approximation, the tip structure does not enter the theory explicitly. The assumption that the electronic structure of the tip is totally symmetric around the tip apex means that the electronic wave functions are spherical, but it does not imply that the electrons of the tip atoms are s-electrons. The wave function of the atoms within a tip made out of s-electrons might have other spherical harmonics in their composition, because the spherical harmonics in the Tersoff–Hamann approach are centered about the tip apex and not about each atom's centers.

The tip wave function is expanded in terms of the sample wave functions under the assumption that the work function of tip and sample are equal $\Phi = \Phi_s = \Phi_t$ and large compared to the bias voltage. The expanded wave functions are used to evaluate the transfer matrix element. Substituting the matrix element (see Eq. 4) in the equation for the tunnelling current (Eq. 6) yields:

$$I = \frac{32\pi^3 e^2}{\hbar} \frac{V\Phi^2 \rho_t(E_F) R^2}{\kappa^4} e^{2kR} \sum_\nu |\psi_\nu(\vec{r}_0)|^2 \delta(E_\nu - E_F)$$
$$\rightarrow I = \frac{32\pi^3 e^2}{\hbar} \frac{V\Phi^2 \rho_t(E_F) R^2}{\kappa^4} e^{2kR} \rho_s(\vec{r}_0, E_F) \quad (9)$$

with $\rho_t(E_F)$ the density of states of the tip per volume and the sum defined as ρ_s, the local density-of-states (LDOS) per unit volume of the sample at the Fermi energy and at the center of curvature r_0 of the tip. The LDOS is thus the sum over all the one-electron eigenstates, given by the label ν of the square of the wave function of each eigenstate, ψ_ν, times a Dirac delta function. The delta function selects the number of states per unit energy at the Fermi level. Thus, the contribution of each eigenenergy to the DOS is weighted by the spatial distribution of the corresponding eigenstate.

Note that the bias voltage does not enter explicitly into the theory that is consequently valid only in the low voltage regime, where the current is linear with voltage.

If the transition probabilities for the different states within each energy interval can be added up to an average transition probability $M(E,V) = \langle |M_{\mu\nu}|^2 \rangle$ per state and if the Fermi energy is a step-like function, then the sum in Eq. (6) can be replaced by an integral, which leads to the usually cited result of the Tersoff–Hamann theory:

$$I(r_0, V) = \frac{2\pi}{\hbar} \int_{E_F}^{E_F+eV} dE \rho_t(r_0, E - eV) T(r_0, E, eV) \rho_s(r_0, E) \quad (10)$$

with ρ_i the density of states of tip (t) and sample (s) and T the transmission coefficient that depends on the energy of the electrons and the applied voltage.

2.2.3 Green's functions method Quantitative prediction of STM images, in particular for adsorbates, asks for a more involved theoretical treatment, where the system is no longer separated into two independent subsystems, but the total wave functions of the tip–adsorbate–substrate system are calculated. The tip–adsorbate–substrate system is considered to be a defect, at which the electrons are scattered [36, 37]. From the scattering matrix the transmission coefficients, from these coefficients the conductivity,

and finally, the three-dimensional contours of constant current surfaces are calculated for a specific voltage.

The scattering matrix can be calculated with the formalism of Green's function [38], which is used to describe the electronic structure of substrate, tip, and adsorbate. This approach based on the Todorov–Pendry model [39, 40] with an approximation developed by Sautet [41, 42] results in a more exact determination of the tunnelling current. A very didactical description of these procedures can be found in Ref. [43]. This method allows calculating the effect of different possible tip geometries.

For an exact comparison of the so calculated STM images to the experimental ones, it is necessary to calculate the electronic structure of tip and sample. For this calculation there is a wide variety of theoretical approaches, from accurate *ab initio* to more approximate semi-empirical tight-binding calculations. The latter is a one-electron approximation, where the electrons of a system are assumed to be localized strictly at their original atoms. The orbitals are constructed as linear combinations of atomic orbitals. The tight-binding approach provides a convenient way to model electronic properties and it gives the contribution of different atomic orbitals to eigenstates of the system, the contribution of orbitals to bonding, and the role of orbitals in forming tunnelling channels. Including only the valence orbitals of the molecule in tight-binding approach already allows a qualitative understanding, why molecules can be imaged at voltages within their HOMO–LUMO gap, though they do not have any density of states there.

The idea behind the calculation is qualitatively depicted in Fig. 14. The scattering matrix is interpreted in terms of different tunnelling paths of the electrons. The overall current und thus the contrast in the tunnelling image results from an interference of these different tunnelling channels. Phase shifts lead to destructive interference and can explain molecules that are imaged as depressions, despite having a larger geometrical height than the surface (cf. Fig. 8) [12]. The different tunnelling channels are named through space (TS, a and c) and through adsorbate (TA, b). For TS there is one path independent of the presence of the adsorbate and one, where the electrons are scattered at the adsorbate. For TA different channels through different molecular orbitals are possible with different phase shifts. In dependence of the molecular adsorption angle different orbitals of the molecule contribute to the tunnelling current. This means that TA depends on the orientation of the molecule and the position of the energetic position of the orbital. The multitude of possible channels makes a prediction of the molecule's appearance without a detailed calculation difficult.

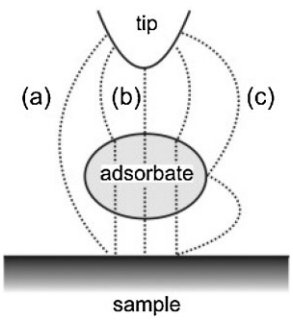

Figure 14 Schematics of possible tunnelling paths of the electrons: (a) through space current, (b) through adsorbate current, (c) through space current scattered at adsorbate.

The method was successfully used to explain, e.g., the change in contrast at different bias voltages of several adsorbed species (Fig. 8) [12] and because of reorientation of molecules in the electric field (Fig. 11) [14]. It was also used to calculate the STM image of chloronitrobenzene shown in Fig. 9. The latter example also demonstrates the limit of the tight-binding approach: it is not quantitative, i.e., absolute apparent heights are only poorly reproduced.

3 Spectroscopy with the STM Two types of spectroscopy are possible in STM. By measuring the first derivative of the tunnelling current versus voltage electronic features of the sample are measured. This spectroscopy is called STS (scanning tunnelling spectroscopy). The measurement of the second derivative reveals vibrational excitations of the substrate and adsorbed molecules. This spectroscopy is called inelastic electron tunneling spectroscopy (IETS).

STM is often not capable of identifying adsorbates via STS because of significant level broadening and shifting of electronic levels that occur upon chemisorption. It was first predicted by theory that IETS should be used to probe the vibrational properties of individual adsorbates in their local bonding environment [44, 45] and later proven in a multitude of experiments to be possible in particular by the pioneer of IETS, Wilson Ho [46].

STS and IETS can be performed either by taking the numerical derivative from a I/V spectrum or by a lock-in technique. Though in the early days the $\mathrm{d}I/\mathrm{d}V$ curve was mathematically derived from the measured I/V characteristics, it is nowadays routine to use the lock-in technique, at least for STS. The advantage is a higher signal-to-noise ratio and the prevention of artifacts that result from smoothing. Direct measurements of $\mathrm{d}^2I/\mathrm{d}V^2$ curves are technically more demanding, so that the numerical derivate of the $\mathrm{d}I/\mathrm{d}V$ curve is still sometimes opted for. The $\mathrm{d}I/\mathrm{d}V$ curves are then recorded in lock-in technique.

For both spectroscopy modes, the tip is placed above the point of interest; the bias voltage is swept over the energy range of interest with a sinusoidal modulation voltage V_{mod} of typically a few mV superimposed over the bias voltage. This modulation leads to a modulation of the tunnelling current with the same frequency. Fourier decomposed in the base of the applied modulation frequency ω the current I is:

$$I(V,t) = I_0(V) + V_{\mathrm{mod}}\frac{\mathrm{d}I}{\mathrm{d}V}\cos(\omega t) + \frac{1}{2}V_{\mathrm{mod}}^2\frac{\mathrm{d}^2I}{\mathrm{d}V^2}\cos^2(2\omega t) + \cdots \qquad (11)$$

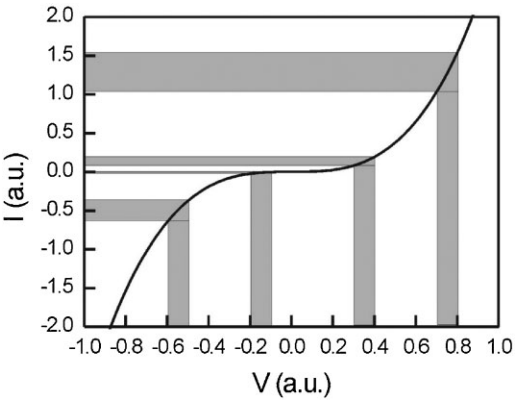

Figure 15 Schematics for determination of local dI/dV through modulation voltage (here 0.1). The signals measured by the lock-in are shaded horizontally and reflect the slope of the I/V curve.

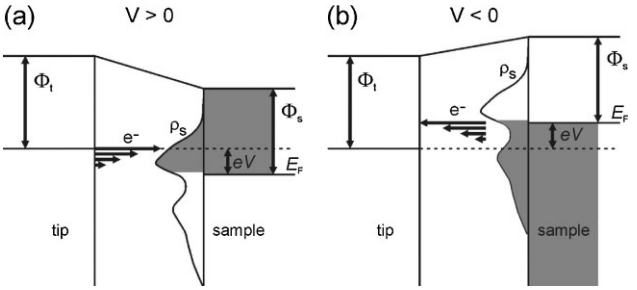

Figure 16 Schematics of the tunnelling process for opposite polarities. The LDOS ρ_S of the tip is assumed to be structure less. By sweeping the bias voltage different states are thus probed. Φ_s and Φ_t are the work function of sample and tip, respectively. Shaded are those states that can be measured at the respective polarity. In the spectroscopy mode, the lock-in technique ensures that additional states are measured. (a) For positive sample bias voltage V electrons from the Fermi level E_F of the tip tunnel into the unoccupied states of the sample. (b) For negative sample bias voltage electrons from occupied states of the sample tunnel to the unoccupied states of the tip.

with time t. This equation shows that the amplitude of the response oscillating with frequency ω and 2ω yields a value proportional to dI/dV and d^2I/dV^2, respectively. This amplitude is then recorded with the aid of a lock-in amplifier tuned to ω or 2ω, respectively.

The principle of the lock-in technique that detects the modulation in tunnelling current at the same frequency as the modulation voltage is visualized in Fig. 15. The constant modulation in V (here 0.1) leads to different modulation amplitudes in I. For small modulation voltages this amplitude is in first approximation proportional to the slope in I/V and consequently to the first derivative of the current, dI/dV.

3.1 STS In the scanning tunnelling spectroscopy (STS) mode the STM probes the local density of states around the Fermi level (see Fig. 16). Such measurements were first presented in 1986 [47] and are 25 years later standard in many laboratories.

3.1.1 Theoretical background Based on the tunnelling current formula (10) the first derivative dI/dV can be derived as:

$$\frac{\mathrm{d}I}{\mathrm{d}V} = \frac{2\pi e^2}{\hbar}\rho_s(E_\mathrm{F}+eV)\rho_\mathrm{t}(E_\mathrm{F})T(r_0,E_\mathrm{F}+eV_0,V_0) + \frac{2\pi e^2}{\hbar}\int_{E_\mathrm{F}}^{E_\mathrm{F}+eV}\mathrm{d}E'\rho_\mathrm{s}(E')\frac{\mathrm{d}\rho_T}{\mathrm{d}E}\bigg|_{E=E'-eV_0}T(r_0,E',eV) + \frac{2\pi e^2}{\hbar}\int_{E_\mathrm{F}}^{E_\mathrm{F}+eV}\mathrm{d}E'\rho_s(E')\rho_t(E'-eV)\frac{\mathrm{d}T}{\mathrm{d}V}\bigg|_{V=V_0}. \quad (12)$$

If one assumes that the tip's density of states is constant in the voltage interval of interest, then (12) simplifies to:

$$\frac{\mathrm{d}I}{\mathrm{d}V} = \frac{2\pi e^2}{\hbar}\rho_\mathrm{t}(E_\mathrm{F})\left[\rho_\mathrm{s}(E_\mathrm{F}+eV)T(r_0,E_\mathrm{F}+eV_0,V_0) + \int_{E_\mathrm{F}}^{E_\mathrm{F}+eV}\mathrm{d}E'\rho_\mathrm{s}(E')\frac{\mathrm{d}T}{\mathrm{d}V}\bigg|_{V=V_0}\right]. \quad (13)$$

In the experiment the tip states are usually changed till the DOS of the tip is constant. Changes to the tip (called tip forming) are achieved experimentally by either controlled contact of the tip with the sample (only for sample materials that are softer than the tip material) or by applying high currents and/or high voltage pulses. A constant tip DOS is important for probing the unoccupied states of the sample, because changes in the tip's DOS are superimposed to the changes in the sample's DOS. It is absolutely necessary for probing the occupied states of the sample, because at negative bias voltage, the contribution from changes in the tip's DOS is stronger than the contribution from changes in the sample's DOS.

The first term in Eq. (13) is proportional to the LDOS of the sample at the energy eV, i.e., dI/dV is proportional to this quantity, if the second term is approximately constant, which is the case under two assumptions: first, the applied bias should be smaller than the work function of tip and sample. This limits the range, over which spectra can be taken, to a few volts. However, most features of interest lie in this voltage range and tip instabilities are often the more severe limit to the voltage range. Second, the transmission

probability T should only vary very slowly with energy. This condition is usually valid over small voltage ranges only. For larger voltage ranges, the tunnelling transmission depends rather exponentially on bias voltage. Thus, dI/dV curves are a rather poor measure of the LDOS, in particular for states far away from the Fermi level, and the de-convolution of the sample's LDOS is a non-trivial task, even if the tip's LDOS is known. For further improvement, experimentalists introduced normalizing STS curves to their static conductivity, i.e., calculated d ln I/d ln V = (dI/dV)/(I/V). This normalization makes spectra taken at different tip-sample distances more comparable and the background that is frequently not very smooth, in particular on semiconductors, can be taken into account. The peak positions in d ln I/d ln V correspond reasonably well to those in the LDOS shifting by some ± 100 meV for large voltages depending on peak width and position [48]. Since the normalized conductivity tends to develop singularities, if there is a gap in the LDOS around the Fermi level, the normalization procedure was further refined by introducing filter functions [49].

More recently a formula based on the one-dimensional WKB approximation (see Eq. 10) was derived to recover the LDOS ρ from dI/dV spectra [50]:

$$\rho = \frac{1}{T(E,V)}\left(\frac{\partial I}{\partial V} + \frac{d}{2\alpha\sqrt{\Phi}}\left(1 + \frac{(2\sqrt{\Phi}d + 3)V^2}{96\Phi^2}\right)I(V)\right) \tag{14}$$

with the transmission coefficient $T(E,V) = \exp(-\sqrt{\Phi + V/2 - E}d)$ for a trapezoidal approximation; d is the tip sample distance and Φ the effective tunnelling barrier height; The coefficient α is close to 2, but can be determined exactly from bias dependent measurements [50]. Further suggested improvements neglect the intrinsic experimental uncertainty.

3.1.2 Experimental aspects In order to record STS spectra, the tip is placed above the spot of interest, the feedback loop is switched off, and the bias voltage is swept over the desired voltage range. For positive voltages the unoccupied states, for negative voltages the occupied states of the sample are probed.

As the recording of the spectra takes typically several minutes, a high stability of the microscope is required. Such a high stability is usually best achieved at cryogenic temperatures, where temperatures are most easily stabilized. Another advantage of low temperatures is a reduced thermal broadening.

Figure 17 displays as an example spectrum the surface state onset on Ag(111) (for a short description of the surface state see Section 2.1.1). The onset of the surface state at -69 meV opens an additional tunnelling channel leading to a steep rise in conductivity.

Though surface states were measured previously with the better energy resolution of photoemission, only STS

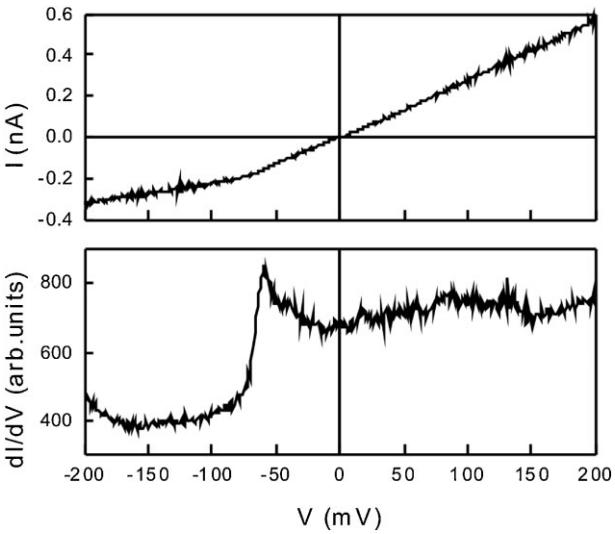

Figure 17 I/V (top panel) and dI/dV (bottom panel) of Ag(111). The cusp in the upper panel and the steep increase in the lower panel indicate the bottom of the surface state band that resides at -69 meV on this surface. Log-in parameters: modulation of 1 mV at 223.4 Hz, current set point: 0.28 nA.

can measure local shifts. Figure 18 shows that the surface state onset differs on the scale of several nanometers because of intrinsic surface steps [26]. This shift results from confinement of the electrons in between the step edges.

By recording such spectra at different locations above a molecule, spectral information with submolecular spatial resolution is recorded. An example is shown in Fig. 19, where the spectrum above the nitro group of a nitrobenzene molecule hardly differs from the surface spectrum, but the one taken above the phenyl shows a distinct step like increase in the unoccupied region [52].

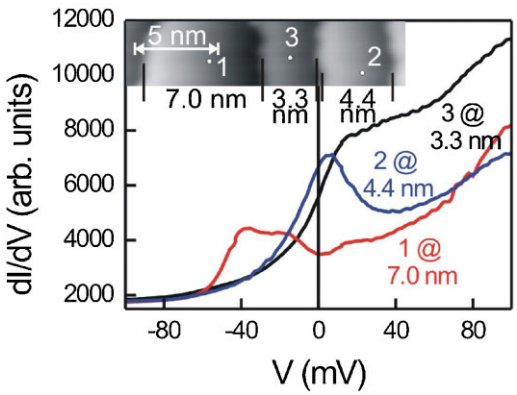

Figure 18 Dependence of surface state onset on terrace width: the onset of the surface state shifts with decreasing terrace width into the unoccupied region, i.e., above the Fermi energy situated at 0 V. The positions, where the spectra were recorded, are indicated on the STM image, which displays an array of terraces [26].

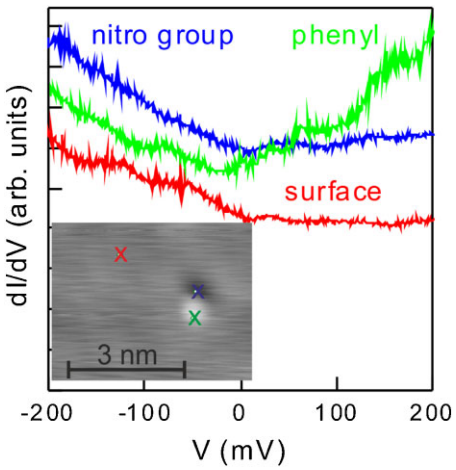

Figure 19 Dependence of STS spectra on tip position above the molecule: the STM image shows a nitrobenzene molecule that is imaged as a combination of a protrusion above the nitro group with a depression above the phenyl [51]. The d*I*/d*V* spectra are recorded where indicated by the crosses in the STM image [52].

STS was furthermore used to determine the band gap of semiconductors as well as the HOMO–LUMO gap for adsorbed molecules. It has been extended to d*I*/d*V* mapping, where a map of the d*I*/d*V* signal at a specific energy allows spatially resolving electronic states.

Mostly, molecules adsorbed in parallel to the surface were investigated by STS. An exception is pyridine-2,5-dicarboxylic acid chemisorbed in perpendicular to the Cu (110) surface [53]. For this molecule, it was shown that by changing the tip-sample distance, different states that are situated in different levels of the molecules can be mapped [53].

3.2 Vibrational spectroscopy IETS probes the vibrational properties of single molecules by measuring those electrons that excite molecular vibrations by tunnelling inelastically. Figure 20 sketches the general idea behind IETS. For STM imaging as well as d*I*/d*V* spectroscopy, we considered only those electrons that retain their energy in the tunnelling process, i.e., electrons that tunnel elastically through the tip-sample gap (upper path in Fig. 20). Most tunnelling electrons follow indeed this path. However, a small part of the electrons (of the order of 10^{-4} or less) loose energy during the tunnelling current flow by exciting vibrations of adsorbates or surface phonons, or by creating electron–hole pairs within a region of atomic dimensions.

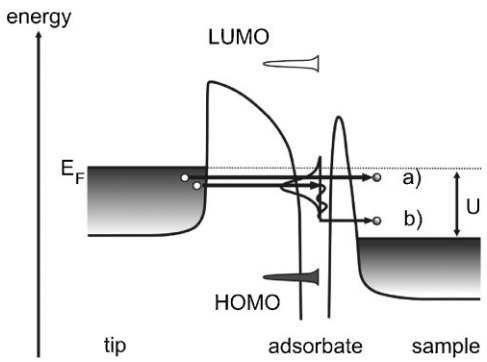

Figure 20 Schematics for illustrating inelastic tunnelling processes (lower path) as opposed to elastic tunnelling (upper path).

For adsorbed molecules, the so called inelastic channel (lower path in Fig. 20) opens when the electron energy matches $\hbar\omega$ of a molecular vibration. Above $\hbar\omega$ the inelastic tunnelling electron can continue into a different state with a proportionate smaller energy. IETS uses the abrupt changes in conductance at $\hbar\omega/e$ to measure the vibrational threshold energy. In first approximation, opening of the inelastic channel increases the conductivity, since the sum over all final states is larger. However, theory (see Section 3.2.3) showed that the elastic channel is reduced at the same energy because of the many-body character of the inelastic contribution to the conductance and thus the total conductivity might even decrease.

A unified theoretical effort showed that a dip is expected in STM-IETS, only if there is an electronic resonance present. Otherwise, a peak is expected [54].

Molecular vibrations by tunnelling electrons were first observed in metal/metal oxide/organic impurity/metal tunnelling junctions [55]. In these junctions an conductance increase by approximately 2% was found at the vibrational frequencies of molecules confined in the organic impurity. The possibility to observe molecular vibrations by STM was discussed already in 1985 [56], the first vibrational spectra were recorded in 1998 [57].

The first derivative of the tunnelling current shows these vibrations as steps and could be used to extract the inelastic signal. However, usually the second derivative is recorded in order to discriminate the steps due to inelastic processes from those due to electronic states. Derivation of the first derivative increases the weight of the inelastic processes, because the electronic structure changes more slowly with voltage than the vibrational one.

In contrast to the higher voltages necessary for STS of molecules, which easily lead to bond breaking, IETS gives chemical sensitivity often without disturbing the molecule. In combination with topographic STM images, IETS can identify individual adsorbed molecules and explore how the vibrational properties are influenced by the local structure of the substrate or nearby coadsorbed species. By placing the tip above different parts of the molecule, submolecular resolution of these properties is achieved.

For larger molecules, chemical analysis is possible by IETS through fingerprints.

3.2.1 Experimental aspects Figure 21a–c sketches expected changes in the spectra for the case that the inelastic

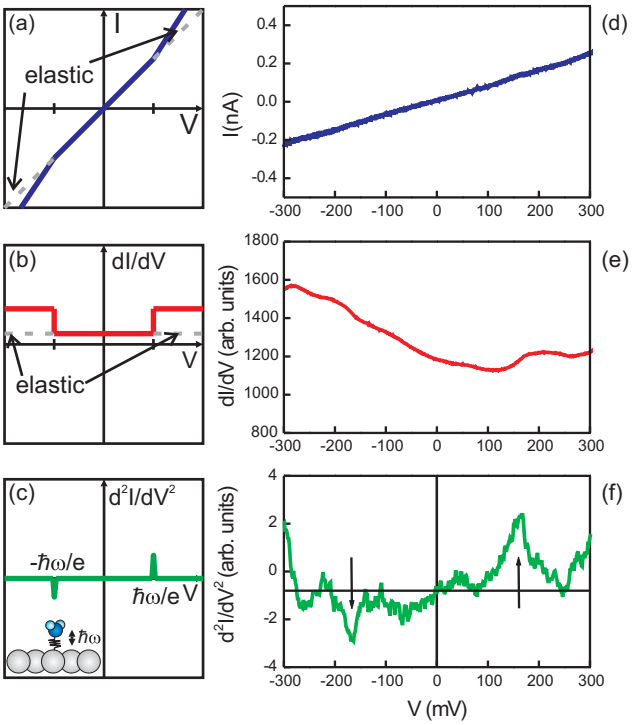

Figure 21 Schematic illustration of the effect of inelastically tunnelling electrons on spectra (a to c) and single spectra on closed layers of H_2O/Cu(111) [58] (d to f): (a,d) I/V characteristic. (b,e) dI/dV: experimental spectrum is recorded in lock-in technique, $V_{mod} = 10$ mV; for a structure less I–V characteristic as in this particular case, dI/dV does not differ from the normalized dI/dV. (c,f) d^2I/dV^2: experimental spectrum is numerically derived from dI/dV; a point symmetric peak (with respect to 0 V) is indicated by arrows.

channel dominates, so that the conductivity of the sample rises at $\hbar\omega/e$. In this case, more electrons tunnel from tip to sample leading to a steeper slope in the I/V curve beyond $\hbar\omega/e$ (Fig. 21a). Changes are both in the occupied and unoccupied region of the sample, because electrons can both first tunnel and then excite the vibration and vice versa. This increase in slope leads to a step-like increase of the dI/dV signal at the voltages $+\hbar\omega/e$ and $-\hbar\omega/e$ (Fig. 21b). In the second derivative a delta function would be expected at $\pm\hbar\omega/e$. The peak is, however, broadened by the lifetime of the excited state, by the instrumentation, by the modulation voltage V_{mod} (peak-to-peak), and by the measurement temperature T. These contributions have different line shapes and thus the correct calculation of the total width is demanding. In experiment, the intrinsic line width is usually approximated from the total measured width W by using the following formula [59–61]:

$$W_I \approx \sqrt{W^2 - \left(\frac{\pi}{2}V_{mod}\right)^2 - \left(\frac{6kT}{e}\right)^2}. \quad (15)$$

For a small instrumental broadening the natural line width dominates the intrinsic width W_I. For the often employed 5 K, a resolution in the vibrational spectra of some meV is achieved, which is sufficient for small molecules with well separated vibrations. Some groups have achieved temperatures in the 100 mK range and modulation voltage in the 100 μV range and thus sub-meV resolution [62, 63].

To record an IETS spectrum, the tip of the STM is placed above the molecule and the sample bias is scanned along the energy window of interest (typically tens to hundreds of milli Volts), searching for sharp variation in the d^2I/dV^2 spectrum. The experimental spectra in Fig. 21 demonstrate why the second derivative is used for the identification of molecular vibrations. The inelastic fraction of the current is typically only a very small fraction of the total current. This change in conductivity is too small to identify the change in slope in the I/V spectrum. In the dI/dV spectrum steps are observed, but this spectrum is dominated by electronic effects, here the contribution from the surface state of Cu(111), whose onset lies outside the recorded region at −450 meV (cf. Fig. 17 for the surface state on Ag(111)). Only in the d^2I/dV^2 spectrum point symmetric peaks can be identified; the one indicated by arrows at ±165 meV lies close to the region of the scissoring mode of H_2O.

A characteristic of the spectra is that peaks/dips at certain values in the positive voltage range are reproduced as similar dips/peaks at opposite polarity. This point symmetric position of the vibrational peaks with respect to zero voltage is a general feature and is used as a test of the vibrational origin of the measured peaks. The symmetry implies that the inelastic channel is open for electrons tunnelling in both directions and that the magnitude of the Stark effect in the energy position of the vibrations is negligible. Peaks that are observed only in one side of the spectrum are (and have to be) disregarded.

The intensity of peaks at opposite polarity is expected to vary because the tunnelling probability is not symmetric (cf. Fig. 16). The asymmetry thus increases for higher energy modes. A qualitative explanation is that electrons have a higher probability of tunnelling before losing a vibrational quantum of energy at positive bias than after having lost it at negative bias. Strong asymmetries of the sample's DOS might lead to a further variation in peak intensity. A relatively smooth LDOS is therefore desirable for discriminating vibrational peaks from electronic contributions to the spectra. Metals usually provide such properties better than semiconductors.

Integrating the peak areas in d^2I/dV^2 versus V and normalizing them by the conductance dI/dV gives an estimation of the normalized change of conductance. This change corresponds to a lower limit for the inelastic fraction of the specific inelastic channel for the tunnelling-active modes. Employing large current densities of the order of 1 nA per molecule, IETS is able to detect changes of the conductance smaller than 1%.

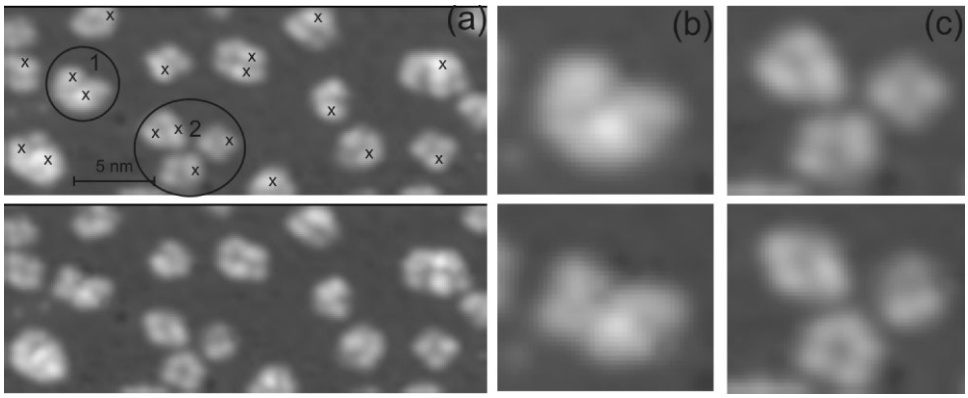

Figure 22 Manipulation of water clusters on Cu(111). Upper row before and lower row after ramping the voltage from 100 to 500 mV within 0.4 s at the 19 crosses: (a) complete image, 81 mV, 100 pA; (b) cluster "1" encircled in (a); (c) group of clusters "2" encircled in (a).

IETS demands a large z-stability of the tip of the order of 0.5 pm [59].

A major concern should be tip features that might be superimposed over the intrinsic spectrum of the molecule. The interpretation of the spectra is much facilitated, if the tip is structure less. For this aim, tip forming is continued till the bare surface does not show any features in the dI/dV spectra apart from the intrinsic surface electronic structure and the d^2I/dV^2 spectrum is featureless in the region of interest. Also a slowly varying background might shift the peaks and should be subtracted. To do so the background spectrum is fitted by a polynomial, which then is subtracted from the spectrum taken above the molecule. The ideal background spectrum is not taken above the bare surface, but above an isotope [64] because isotopes have the same electronic structure and make the same changes to the electronic structure of the surface.

Usually the features in the tunneling spectrum from the states of the tip are a nuisance. However, IETS spectra may contain modes characteristic for the tip's apex structure [65]. The influence of molecules adsorbed onto the tip onto IETS spectra was addressed theoretically [66]. Different tips not only show different intensities of the signal, but also a slight shift in energy.

A further influence of the tip is a distance-dependence shift of vibrational modes by the close proximity upon approach of the tip even before formation of a contact as demonstrated for a CO molecule adsorbed on Cu(111) [67].

Furthermore, electron induced manipulation might interfere with the recording of the spectra. Figure 22 exemplifies this difficulty often encountered when performing spectroscopy at weakly adsorbed molecules or molecular clusters. While ramping the voltage in the voltage range of vibrational modes even at a current and a ramping time that are both at the lower limit for reliable spectra, many of the water clusters change appearance, because hydrogen bonds reorder after excitation of molecular vibrations [58]. Excitation of molecular modes can also lead to dissociation, desorption, or other reactions (see Section 7).

These reactions limit the applicability of IETS. A way to circumvent at least diffusion is to offer special binding sites to molecules as exemplified in Fig. 23. After adsorption

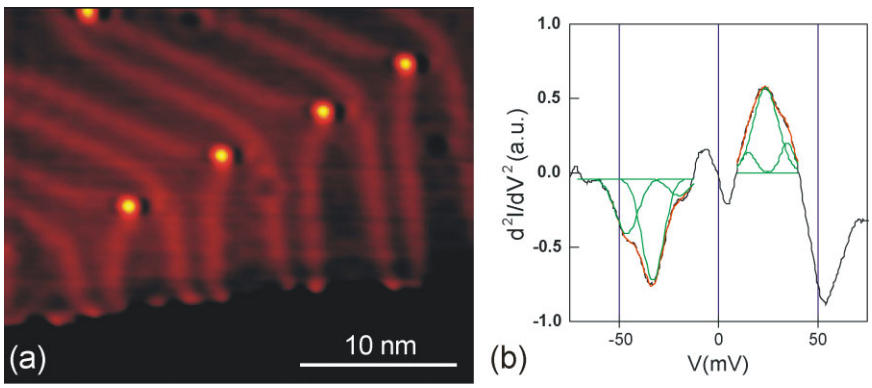

Figure 23 (a) STM image of D_2O monomers (yellow protrusions) adsorbed in the elbows of the Au(111) reconstruction, 115 mV, 32 pA. (b) Average of several d^2I/dV^2 spectra taken above the monomers; a triple Gaussian profile is fit to the peaks on both sides of the Fermi energy ($V = 0$ V) [68]. The number of peaks is more easily identifiable in the negative part of the spectrum, but it is clearly observed on both sides.

of D_2O on Au(111) the molecules preferentially decorate the elbow sites of the $(22\sqrt{3})$ reconstruction, where the dislocation lines change direction and a gold atom has either five or seven neighbors in the surface plane instead of six. At this specific binding site the molecule is bound sufficiently to take vibrational spectra in the range up to 75 mV (Fig. 23b) [68]. The IET spectrum reveals a multiple peak in the region between 10 and 50 meV, which is best fitted by a triple Gaussian. Averaging over several spectra is used here to increase the signal-to-noise ratio.

Vibrational modes can either be assigned through comparison to calculated modes or to modes experimentally determined in infrared spectroscopy or in electron energy loss spectroscopy (EELS). For D_2O on Au(111) (Fig. 23) the three vibrational modes in the region up to ± 50 mV are identified through comparison with EELS spectra as the frustrated rotation vibrations (librations) [68], a procedure described in detail in Ref. [69].

A univocal assignment of modes is possible by comparing their isotope shift; for the example shown comparing D_2O to H_2O. However, we found that in this particular case the extrinsic peaks are too broad to observe the shift.

Spectra taken above different parts of a molecule might differ in peak intensity therefore demonstrating the spatial extent of vibrations and their excitation probability. IETS has consequently been extended to d^2I/dV^2 mapping, where a map of the d^2I/dV^2 signal at a certain vibrational energy allows spatially resolving the vibration within a molecule [64]. Not only molecular vibrations, but also surface phonons can be detected [70]. Also the signature of paramagnetism was detected in IETS spectra for O_2 on Ag(110) [71].

Mostly, molecules adsorbed in parallel to the surface were investigated by IETS. An exception is a self-assembled monolayer, on which the IETS spectra showed a multitude of modes with intensity variation with tip-sample distance [72]. These modes were assigned to different C–C and C–H modes. This example underlined the problem of identifying IETS maxima on a noisy background. In a follow up study, improved spectra were compared to theoretical calculations and methyl and methylene groups were differentiated [73].

3.2.2 Theoretical background Most treatments of IETS use perturbation theory [69]. This is justified by assuming that in IETS only one quantum of vibration is excited at the first vibrational threshold in the positive voltage range, the one that is a peak in the second derivative of the tunnelling current with respect to the bias voltage. Hence, the final state of the molecule is not extraordinarily excited, and the vibrational excitation is assumed to be a weak perturbation to the molecular ground state. Let us try to substantiate this claim with some order-of-magnitude analysis [74].

3.2.2.1 Order-of-magnitude analysis The passing electron should spend enough time in the molecular environment in order to be able to excite it. The lifetime of an electron in a molecule is the inverse of its resonance width, $\tau_{\mathrm{mol}} = \hbar/\Gamma$. For a chemisorbed molecule on a metal surface the electronic width, Γ, is of the order of 1–3 eV, this means lifetimes of some 0.1 fs. Next, in order to estimate the change in conductance in an IETS experiment, we need to know the time to excite the molecular vibration. This time is the inverse of the vibrational excitation rate, $1/\tau_{\mathrm{vib}}$.

By using Fermi's Golden Rule one can have a quantitative estimate of the rate of an electronic process:

$$\frac{1}{\tau} = \frac{2\pi}{\hbar}\sum |\langle i|\delta\hat{H}|f\rangle|^2 \delta(E_f - E_i), \tag{16}$$

where i and f are the initial and final states in the excitation process and $\delta\hat{H}$ is the perturbation on the electronic Hamiltonian due to the vibrational excitation. Assuming again that only one quantum of vibration is exchanged, we expect a small displacement $\delta\hat{Q}$ of the nuclear coordinates. We used the explicit operator format for the displacement because our i and f states are both states of electronic and nuclear coordinates. Hence $\delta\hat{Q}$ acts on these states, such that by virtue of Taylor's expansion we can approximate the first perturbation to the Hamiltonian by

$$\delta\hat{H} \approx \frac{\partial\hat{H}}{\partial Q}\delta\hat{Q}, \tag{17}$$

where we have factored the perturbation in a first factor acting on electronic coordinates and the second one on nuclear ones. If we use the electronic eigenstates, $|\lambda\rangle$, and the harmonic eigenstates $|n\rangle$ (we assume a perfect harmonic oscillator for the vibrations) then:

$$\begin{aligned} |i\rangle &= |\lambda\rangle \otimes |n=0\rangle, \\ |f\rangle &= |\mu\rangle \otimes |n=1\rangle, \end{aligned} \tag{18}$$

with energies:

$$\begin{aligned} E_i &= E_\lambda + \frac{\hbar\Omega}{2}, \\ E_f &= E_\mu + \frac{3\hbar\Omega}{2}. \end{aligned} \tag{19}$$

Even with these assumptions, it starts to be difficult to evaluate the vibrational excitation rate. Let us assume that the electron–vibration coupling is somehow averaged over the different states and we can take it out of the summation. The summation is then over a delta of energies. This is just a density of states. Since we are dealing with the molecular states in contact with a surface, we will assume that they are simply following a Breit–Wigner density of states: that of a single electronic level in front of a featureless continuum of electronic states. This density of states is then

$$\mathrm{DOS}(\omega) = \frac{1}{\pi}\frac{\Gamma/2}{(\omega - \varepsilon_a)^2 + (\Gamma/2)^2}. \tag{20}$$

Since the delta function assures energy conservation, we will assume that we are in resonance and hence we replace the summation over the delta function by $\mathrm{DOS}(0) = 2/\pi\Gamma$. Then, the vibrational excitation rate becomes:

$$\frac{1}{\tau_{\mathrm{vib}}} = \frac{4|\langle \delta H \rangle|^2}{\hbar\Gamma}. \tag{21}$$

We can now compute the vibrational excitation rate, if we know how the potential energy surface (PES) changes with the coordinate, so that we can have a realistic estimate of $|\langle \delta H \rangle|^2$. Let us for the time being remain as simple as possible for the sake of gaining as much physical insight as possible. Hence we pursue the harmonic potential model and take for the negative ion the following PES: $E_- = 1/2K(Q - Q_-)^2$, we assume that the frequency for the negative ion is the same one as for the neutral molecule, which is a rather crude assumption, such that $K = m\Omega^2$, with m the generalized reduced mass of this mode. Here, Q_-, is the new configuration of the molecule in its negatively charged state. In the case of an adsorbate, the negative adsorbate is generally at a different distance from the surface.

The emerging picture is that during the electron flow through the molecule, the molecule is temporarily in a negative state. Hence, the PES changes suddenly from the neutral one, $E_0 = 1/2KQ^2$, to the negatively charged one, $E_- = 1/2K(Q - Q_-)^2$. Hence, the nuclei experience a force given by$F = -\partial E_-/\partial Q|_{Q=0}$which translates into a classical speed of the order of $v \approx (\hbar/m)(\partial E_-/\partial Q)|_{Q=0} \times \tau_{\mathrm{mol}}$, where τ_{mol} is the lifetime of the electron in the molecule, that we estimated above from the value of the electronic current. Using that the lifetime and the broadening, Γ, of the molecular levels are inversely proportional, let us then take $\tau_{\mathrm{mol}} \approx \hbar/\Gamma$. Hence, $v \approx KQ_-/m\Gamma$. Now the maximum speed of the nuclei in a semi-classical analogy is at the center of the neutral PES, which is $v_{\max} = \sqrt{2\hbar\Omega/m}$ just from equating the energy gain in the excitation process to the classical kinetic energy of the nuclei. From this, we find an upper limit for Γ, in order to excite the molecule: $\Gamma \leq \langle \delta H \rangle$.

This simple estimation shows that for strong electron–vibration coupling, vibrational excitation is unavoidable, where strong means larger than the molecule–electrode coupling, Γ.

Weak coupling is then the regime when $\Gamma \gg \langle \delta H \rangle$. We can use the above Fermi's Golden Rule to estimate the vibrational excitation rate. Assuming that the fraction of inelastic electrons is just the ratio of lifetimes between the time it takes to create an excitation and the time the electron stays in the molecule, a 1% of inelastic electrons means: $\tau_{\mathrm{mol}}/\tau_{\mathrm{vib}} \approx 0.01$ This leads to $|\langle \delta H \rangle|^2/\Gamma^2 \leq 1/400$.

Hence, for chemisorbed molecules, the electron–vibration coupling needs to be in the range of 0.01 eV, in order to have more than 1% of inelastic electrons due to vibrational excitation. In this first approximation, we can relate the change in conductance with the inelastic fraction. In practice as we explain below, other more complex effects prevent us from making a direct connection between inelastic fraction and change in conductance. This electron–vibration coupling is easily found in a large class of molecules, and therefore IETS is a feasible spectroscopy.

3.2.3 Theoretical basis of inelastic tunnelling spectroscopy A current is created when two electron reservoirs are connected. In equilibrium no electron flow takes place: the chemical potential (i.e., the Fermi energy at $T = 0$) is well-defined. When a bias voltage is applied between the electrodes, the chemical potential is no longer defined. If the electrodes are large enough we can consider them to be in equilibrium and the voltage drop will take place in a small region connecting both electrodes. In the case of tunnelling junctions the voltage drop happens in the insulator layer: the vacuum in STM. Electrons can now flow because the final states will be empty: the chemical potential of both electrodes differ by the applied bias voltage times the charge of the electron.

When the bias voltage corresponds to chemical potential shifts smaller than the quantum of vibration the electron cannot yield its energy to the vibration. Let us assume that the temperature is very low (<10 K) such that the probability of finding the vibrator in an excited state is negligible. In this case the electron will not gain energy from the vibrator but will cede its energy. In order to yield its energy the final state of the electron has to be empty, in other words, the final channel must be open. The only way of opening the channel is that the bias voltage energy is larger than the quantum of vibration. In this case the electron can excite the vibration and continue its propagation in an electronic state above the Fermi level of the second electrode: the vibration opens a new channel.

3.2.3.1 The inelastic channel When a vibration is excited by an electronic current, new channels contribute to the electron flow. The conduction process is described as a scattering process: electrons enter the interaction region through well-defined channels. A channel is defined by the solution of Schrödinger's equation in the region well before the interaction so that the solution is exactly known. Each of the possible solutions before and after the interaction defines the initial and final channels. Newly open channels lead to an increase of the electron current. The infinite electron reservoirs act as a pressurized container: whenever an electron can leak from the reservoir, it will do it. Hence the increase of final electron channels leads to an increase of the electron current.

The picture just given is not accurate. It actually depends on what type of coupling exists between the vibrator and the flowing electrons. Caroli et al. [75] give a formal but complete account of the different scenarios leading to a rich variety of behaviors of the current with the excitation of localized vibrations. In their analysis of metal-insulator-metal junctions they consider different types of coupling that differ by where the vibrator (molecular impurity) lies within the junction. If the impurity lies inside the insulator layer,

then the above picture turns out to be correct: the vibrational excitation is an opening of a new channel and the current increases. If the impurity is in contact with one of the electrodes the case is much more complex, and particular details on the impurity–metal interaction need to be taken into account. The reason behind this classification is that the electron–vibration scattering in the insulator layer is a one-electron process equivalent to the electron-molecule scattering problem. In contact with the metal, many-body features appear. The states are multi-electronic and the vibration mixes them efficiently. The simple channel-opening picture is no longer valid. As a matter of fact, Caroli et al. [75] show that the current can actually decrease.

Prior to the work by Caroli et al. [75], Davis [76] did some model calculations where the defining parameter of the type of electron–vibration coupling was the distance of the vibrator to the metal contacts. He reached some conclusions in the line of the more systematic and profound description by Caroli et al. [75]. Namely, he showed that the main many-body effect is the anti-symmetry of the many-body wave function. In order to take this anti-symmetry into account, he considered Slater determinants of the one-electron wave functions, and then performed perturbation theory on the electron–vibration interaction. The effect of the electron–vibration coupling is to mix up the electronic states: the states of the full Hamiltonian contain the electron and vibration coordinates. One way of putting this mixing is to claim that "virtual" phonons are emitted and reabsorbed. This is a description that comes from perturbation theory, in which electrons and vibrations are treated separately and they are mixed gradually through perturbation theory. Indeed, what it means is that the actual ground state contains vibration contributions that one cannot neglect. These contributions are very efficient in mixing two-electron coordinates with the vibration coordinates in the full-system wave function. Our initial picture of one-electron channels needs to be reconsidered in certain cases.

When tackling the task of developing a theory for the description of IETS with the STM, a many-body approach is thus unavoidable. The work by Davis [76] shows that one can actually get away with a simple many-body theory, in which only the anti-symmetry of electron states is needed. The mandatory question is what a theory should account for. In order to answer this we need to re-consider what the IETS-STM technique is.

By measuring the change in conductance, IETS-STM gives information on the localized vibrations of the STM junction. Hence there are two processes: the electron propagation and the vibration excitation. IETS-STM is performed at low temperatures (typically below 10 K) and at low currents (in the nano Ampère range). These are conditions that allow an identification of vibration excitation by single electrons: the vibrator is probably in its ground state and the time between electrons is much longer than the lifetime of the vibrations.

A theory should just consider electron propagation with a weak probability of exciting a vibration. Perturbation theory seems to be justified due to the smallness of the electron–vibration coupling and the dynamics of the process (excitation and de-excitation) is considerably simplified by the above experimental conditions.

Basically, there are two approaches to describe the vibration excitations: approaches that compute the probability of vibration excitation by an electron current and approaches that compute the change in conductance by vibration excitation. In the first case the accent is put on the description of the excitation, making the change in conductance a secondary process. In the second case, the conductance description is emphasized.

3.2.3.2 Approaches based on scattering theory The process of vibrational excitation is described with great detail in these approaches. The underlying idea is to calculate transition times (or excitation rates) and from here to obtain the contribution to the current coming from the inelastic process. A current can be seen as a transition time between electrodes times the charge of the electron. In this way, these theories expect that the inelastic contribution to the current is the rate of vibration excitation times the charge of the electron. This simplistic picture is wrong and theories taking into account inelastic effects in electron transport are complicated (see e.g., [77, 78]). Nevertheless, in the tunneling regime these theories turn out to be good approximations. In the tunnelling regime, one can basically picture the electron transport as single-electron conduction events, where the static electronic structure is not strongly modified by transport itself.

Persson and Baratoff [45] have been the first to estimate the inelastic contribution to the current by using a scattering-like approach. They show that fundamental aspects of the transport problem can be taken into account, only if the propagation of the electron is treated on the same level as the vibration excitation. Similar approaches are those by Gata and Antoniewicz [79] and Spataru and Budau [80]. All of these approaches start by writing a Newns–Anderson type Hamiltonian:

$$H = \varepsilon_a c^+ c + \sum_{k_{\mathrm{L,R}}} \varepsilon_{k_{\mathrm{L,R}}} c^+ c_{k_{\mathrm{L,R}}} + \sum_{k_{\mathrm{L,R}}} [V_{a k_{\mathrm{L,R}}} c^+ c_{k_{\mathrm{L,R}}} + \mathrm{H.c.}] + \hbar\Omega \left(b^+ b + \frac{1}{2} \right) + \sum_{\mu,\nu} V_{\mu,\nu} c_\mu^+ c_\nu (b^+ + b). \tag{22}$$

The first term of Hamiltonian (22) refers to the molecular orbital a, it is just the energy of the corresponding level when the state is populated (this is the meaning of the creation and annihilation couple $c^+ c$). The second term refers to the extended electron states in the left (k_{L}) and right (k_{R}) electrodes. The third term is the coupling between the molecular and electrode states, given by the matrix element $V_{a k_{\mathrm{L,R}}}$. H.c. stands for hermitian conjugate. Hence, this term sets the width of the molecular resonance in contact with the electrode continua. The

fourth term is the corresponding vibrational Hamiltonian for the local vibration of single frequency Ω. The creation and annihilation operators of one quantum of vibration are denoted by b^+ and b, respectively. The last term is the electron–vibration coupling, where μ and ν are in principle any electronic states of the full system. This term permits an electronic transition induced by a vibrational one and vice versa.

These theories assume that there is an electronic state of the molecular impurity that will be populated and will induce the vibration excitation. This description is usually called resonance scattering because the active electronic state (a in Hamiltonian (22)) becomes a resonance in presence of the electrode's continuum of states. In the gas-phase formulation [81, 82] a negative ion resonance is formed. This negative ion has in general a different conformation from the neutral molecule, hence when the ion resonance decays into the neutral molecule, the molecule is left in a vibrationally excited state. This process is very efficient in producing the coherent multiple excitations of molecular modes [83]. However, it is quite different from what the above theories using Eq. (22) try to model. In Eq. (22), resonance scattering means that there is basically a single molecular orbital that determines much of the relevant electronic structure. In the gas phase, the above exciting mechanism is dealt with the impact-scattering approach, also called sudden approximation. One can understand the excitation as caused by the brief appearance of an extra electron in the system which leads to the mixing of the different states of the quantum oscillator (the molecular modes). Indeed, the residence time of an electron in a chemisorbed molecular resonance is orders of magnitude smaller than the typical times involved in any vibrational quantity. This is different from the negative-ion resonance excitation in the gas-phase where the resonance lifetime is of the order of the vibrational period.

The impact scattering or sudden mechanism has been used to explain the vibrational excitation of chemisorbed molecules in electron energy loss spectra (EELS). See in particular the reference by Tong et al. [84].

The above approaches estimate the excitation rate by using either second-order perturbation theory [45] or a re-summation to all orders in perturbation theory [79, 80]. In order to be able to sum the infinite series of perturbation theory, Refs. [79, 80] use an orthogonal basis-set of the model Hamiltonian (22) (the creation and destruction operators need to be canonical in order to use Green's function perturbation theory). This approximation leads to the neglect of the mixing of electronic states in the electrode due to the molecular vibration. Despite the more approximate treatment of Ref. [45] this coupling is not neglected. The outcome is that Refs. [79, 80] neglect many-body effects that explain the decrease of conductance in certain systems as Persson and Baratoff predicted in the case of IETS-STM [45]. In the case of metal-insulator-metal junctions the decrease in conductance had been predicted two decades earlier by Davis [76].

The weakest point of these approaches is the difficulty to find parameters for the initial Hamiltonian that are reliable and realistic enough for predictions and analyses.

3.2.3.3 Approaches based on conductance calculations

More direct, these approaches focus on the measured quantity: the conductance. There are two main groups of theories. One is based on a tight-binding description of the transport processes where the electron current $j_{i,j}$ between two adjacent sites i and j, is evaluated by using [85–88]:

$$j_{i,j} = \frac{2e}{\hbar}\mathrm{Im}(\psi_j^* t_{j,i}\psi_i), \tag{23}$$

where ψ_i is the electronic wave function for the site i and $t_{j,i}$ is the Hamiltonian matrix element between adjacent sites or hopping matrix element.

This approach allows for a complete calculation of transport in the presence of vibrations and interacting with them. In this way, the effect of temperature (through phonon population, i.e., the degree of excitation of the vibrations) and of multiple excitations is taken into account. The inclusion of multiple electronic channels permits them to go beyond the above resonance models: the molecule can have several orbitals contributing to the conductance and to the coupling with its vibrations [87].

Emberly and Kirczenow [88] have included explicitly the effect of exchange in the evaluation of inelastic transport in the above approach. As we saw above, the effect of exchange is fundamental to understand the decrease in conductance when a vibration is excited (i.e., a phonon is emitted). However Mingo and Makoshi [86] claim that the formalism of Bonča and Trugman [85] includes this exchange effect, if the formalism is used with Green's functions instead of wave functions. They claim that the expressions of Ref. [45] are recovered, if they developed perturbatively their own expressions.

The other type of theory uses non-equilibrium Green's functions. Green's functions are more tractable in a localized basis set, such as the one corresponding to a tight-binding description [75]. Nevertheless an extended basis description is also possible [89]. The use of tight-binding implies the simplification of the problem to Hamiltonian (22), hence having the same problems of pertinence and accuracy as we mentioned above.

The real space or extended basis description has the advantage of building upon accurate results from plane-wave calculations of the electronic structure [89]. Nevertheless, electronic structure calculations based on localized basis sets can become as accurate and predictive as plane-wave based results [90]. Plane-wave based calculations have the difficulty of how to transpose the calculated electronic structure into a form useful for transport calculations. Transport calculations are better suited for description in localized basis sets, hence transport based on *ab initio* localized basis codes are turning to be the best tool [91].

When a tunnelling calculation is undertaken, many simplifications render the task easier than a complete transport calculation such as the one of Ref. [91]. Let us take the formulation by Caroli et al. [75] using the change induced by the vibration in the spectral function of the lead. In this description, the current and thus the conductance are proportional to the density of states (spectral function) of the leads (here tip and substrate). This is tantamount to using some perturbational scheme on the electron transmission amplitude between tip and substrate. This is what Bardeen's transfer Hamiltonian achieves. The main advantage of this approximation is that one can use the electronic structure calculated by some standard way, for example plane-wave codes, and use perturbation theory to account for the inelastic effect. In Ref. [92], a careful description of the Bardeen approximation in the context of inelastic tunnelling is given, and how the equivalent of Tersoff and Hamann theory [20, 34] of the STM is obtained in the inelastic case.

Tersoff and Hamann theory (Section 2.2.2) says that the tunnelling conductance, σ, is proportional to the local density of states (LDOS) evaluated at the tip's center, $\vec{r}_0$, and at the Fermi energy, ε_F:

$$\sigma \propto \sum_{\nu} |\psi_\nu(\vec{r}_0)|^2 \delta(\varepsilon_\nu - \varepsilon_F). \tag{24}$$

The LDOS is then a sum over all the one-electron eigenstates given by the label ν, of the square of the wave function of each eigenstate, ψ_ν, times a Dirac's delta function that selects those eigenstates at the Fermi energy. This quantity is then a density of states (the Dirac's delta gives the number of states per unit energy at the Fermi level) times an electron density (the contribution of each eigenenergy to the density of states is weighed by the spatial distribution of the corresponding eigenstate).

The corresponding generalization to inelastic tunnelling takes on a very simple form (see Ref. [92] for a complete description beginning in Bardeen's approach). It basically says that the inelastic contribution to the change in conductance will be caused by the change in the LDOS due to the vibration. Now the problem is complicated by the many-body aspects of the theory. There is a first term that can be traced back to a transfer of a quantum of vibration by the impinging electron. This is called the inelastic contribution to the change in conductance [75, 76, 89, 93, 94]:

$$\Delta\sigma_{\text{inel}} \propto \sum_{\nu} |\Delta\psi_\nu(\vec{r}_0)|^2 \delta(\varepsilon_\nu - \varepsilon_F). \tag{25}$$

This equation says that there is an increase of conductance due to the modulation of the wave function by the vibration. The spatial resolution of the wave function carries the information of the exponential decay in vacuum of the tunnelling probability. Hence, during the vibration this tunnelling probability will be modulated in a way given by the change of the wave function. The change of wave function is calculated in perturbation theory:

$$\Delta\psi_\nu(r_0) = \sum_{\mu} \psi_\mu(r_0) \frac{\langle\mu|V|\nu\rangle}{\varepsilon_\nu - \varepsilon_\mu + i0^+}. \tag{26}$$

We approximate the principal part of $\Delta\psi$ by its finite difference:

$$\mathcal{P}\Delta\psi(\vec{r}_0, \vec{Q}_0) \approx \psi\left(\vec{r}_0, \vec{Q}_0 + \frac{\delta\vec{Q}}{2}\right) - \psi\left(\vec{r}_0, \vec{Q}_0 - \frac{\delta\vec{Q}}{2}\right) \tag{27}$$

where $\vec{Q}_0$ is the vector of atomic positions and $\delta\vec{Q}$ is the eigenvector corresponding to the displacement of the molecule's atoms for a given mode. The modulus of this vector is the root mean square displacement of the vibration (in the case of a vibrating single atom of mass m, we have $\delta Q = \hbar/\sqrt{2m\Omega}$ where Ω is the mode's frequency). The electron–vibration matrix elements, $\langle\mu|V|\nu\rangle$, can be obtained from Eq. (25): $\langle\mu|V|\nu\rangle = \langle\psi_\mu|\Delta\psi_\nu\rangle$.

Notice that Eq. (26) is not evaluated directly because the metallic states are a continuum, here taken care of by the infinitesimal element 0^+. The principal part, Eq. (27), corresponds to the real part of the denominator in Eq. (26).

The second contribution to the change in conductance at the same order in the electron–vibration coupling, $\langle\mu|V|\nu\rangle$, has been termed the elastic contribution. The name originates from the fact that the initial and final electron states are at the same energy, they do not differ in a quantum of vibration as in the inelastic term, Eq. (25). The origin of this term is the many-body character of electron transport in the presence of vibrations. In the absence of vibrations one can approximate the many-body wave functions in terms of one-electron wave functions, that are solutions of an effective one-body Hamiltonian. When the electron–vibration coupling, $\langle\mu|V|\nu\rangle$, is included the one-electron wave functions are no longer eigenstates of the Hamiltonian. The vibration mixes them up. The complexity appears because the full wave function needs to be anti-symmetric under electron exchange, i.e., two electrons cannot be in the same quantum state. The elastic contribution reflects the exchange of two electrons mediated by the electron–vibration interaction. This exchange term gives a negative contribution to the change in conductance due to the anti-symmetric character of the wave function.

Exchange is made possible by the excitation of the vibration. Otherwise the Fermi occupation and the one-electron states are an excellent approximation in the transport problem.

The elastic contribution is given by:

$$\Delta\sigma_{\text{elas}} \propto -\pi^2 \sum_{\nu} \left| \sum_{\mu} \psi_\nu(\vec{r}_0) \langle\mu|V|\nu\rangle \delta(\varepsilon_\mu - \varepsilon_\nu) \right|^2 \delta(\varepsilon_\mu - \varepsilon_F). \tag{28}$$

The notation is the same as in Eq. (25). There are two fundamental differences between Eqs. (25) and (28). The first one is the sign. The elastic contribution, Eq. (28), is negative. It is the term responsible for the decrease in conductance as we announced. The second difference is the range of evaluation of the inner summation over ν. In Eq. (28) this summation is restricted to states at the Fermi level, while in Eq. (25) it extends over all energies. Hence the elastic contribution Eq. (28) will become particularly important when the density of states is very high at the Fermi level: namely, in the case of a sharp resonance at the Fermi level.

The total change in the conductance will be determined by the sum of the two contributions Eqs. (25) and (28): $\Delta\sigma = \Delta\sigma_{\text{inel}} + \Delta\sigma_{\text{elas}}$.

Hence the outcome of the vibration excitation on the conductance is complicated to predict. This is particularly true when there is a strong mixing of molecular states with metallic states. In this case, the interplay between the elastic contribution (exchange effects) and the purely inelastic one (increase of tunnelling probability) is difficult to assess except after complete electronic structure calculations.

The conditions of applicability of this simple extension of Tersoff and Hamann theory into the inelastic regime are usually in good agreement with the experimental conditions. Namely the conditions are:

(1) Linear regime: small tip-surface bias voltage as compared to the electronic structure of the surface. This is usually the case since vibrational quanta are one order of magnitude smaller than the energy spacing between electronic resonances.
(2) Highly symmetric tips, ideally with s-wave symmetry for its electronic structure at the Fermi level.
(3) Low current regime: the time between tunnelling electrons should be much larger than the vibrational lifetime. The theory only assumes one excitation at a time.
(4) For reason 3, the temperatures should be low: the excitation probability depends on the phonon population; hence the theory assumes that the molecule is in its vibrational ground state.

Advantages are the accuracy of the electronic structure and of the vibration calculation, yielding quantitative results, plus the simplicity of the theory that allows an understanding of the basics behind an IETS-STM spectrum.

3.2.4 What can we learn from theory? As in many areas of science, a good theoretical understanding is needed for the full exploitation of the technique. Not only from the point of view of enhancing and optimizing the amounts of information obtained, but also from the point of view of obtaining some useful information at all.

As we show in the experimental technique the STM vibrational spectroscopy has good energy and spatial resolutions. The change in conductance can be mapped spatially. The geometrical pattern of the variation of conductance has relevant information that theory can exploit. Ideally, any theoretical approach should then be able to account for the change in conductance at a given location of the STM tip and at a given surface-tip bias voltage. In this way, the mode at the origin of the change in conductance can be identified. In the following paragraphs, we analyse how to do so. The first issue is when and why there is a measurable change in conductance. This leads us to analyze the possible cancellations in the inelastic current. Secondly, once that a change in conductance is obtained we address the problem of how the mode's signature shows in the experimental data.

3.2.4.1 Elastic–inelastic cancellations IETS is a technique that combines the exciting with the detecting probes. Theory shows that the probability of exciting the vibration by the electron current is not directly connected with the change in conductance at the bias voltage threshold of the vibration. Indeed, the excitation probability can be high but the change in conductance remains negligible.

The situation becomes thus quite complicated, because the absence of inelastic signals may come from the absence of excitation or from the absence of change in conductance.

In the case of sharp resonances at the Fermi level (a situation encountered in the case of magnetic impurities) the elastic contribution to the change in conductance will likely be the largest one, leading thus to a decrease of conductance above the vibration threshold.

When the change of conductance is large (in the range of 10%) the elastic contribution will be negligible in front of the inelastic one. Only in this case the change of conductance can be directly linked to the probability of exciting the vibration: the relative change of conductance can be assigned to the fraction of electrons leading to an excitation; it is the inelastic fraction.

3.2.4.2 Mode assignment and symmetry selection rules Equation (28) contain the matrix element $\langle\mu|V|\nu\rangle$. When this matrix element is zero, the conductance at the vibration threshold will be zero. Hence, the symmetry of the electronic states μ and ν, and of the vibration can determine when this matrix element will be zero.

The electron–vibration coupling V has the symmetry of the vibration. This is because the Hamiltonian is totally symmetric under transformations of the point group of the ensemble molecule plus substrate. In order to preserve the invariance of the Hamiltonian under transformation of the nuclear coordinates, the electronic coordinates must transform in the same way [95]. Hence, if a symmetric mode is excited, the electron–vibration coupling will be also symmetric in the electronic-coordinate transformations. Thus only electronic states of the same symmetry will give non-zero matrix elements for a symmetric vibration. This

kind of reasoning can be used over the different vibrations of the molecule.

Reference [94] shows unequivocally that the change in tunnelling conductance in the spectra of one deuterated acetylene molecule chemisorbed on Cu(100) originates in the anti-symmetric mode of the C–D stretch. The experimental vibrational spectra were recorded on a deuterated acetylene molecule (C_2D_2) because its rotation rate under the STM tip was lower, and hence it was easier to obtain meaningful spatial maps of the inelastic signal. Chemisorbed acetylene can have two almost-degenerate modes for the C–D stretch: an anti-symmetric mode, in which the D-atoms move out of phase, one approaching its corresponding C-atom while the other one elongates from its C-atom (calculated frequency 275 meV) and a symmetric mode in which the D-atoms elongate or contract the C–D bond in phase (calculated frequency 281 meV). The calculation shows that the maximum change of conductance was 9.6% for the anti-symmetric mode, but the maximum change of conductance was only 1.4% for the symmetric one. Experimentally, the energy resolution was better than 6 meV (the calculated mode frequency mismatch) and the maximum of the signal was $(8 \pm 1)\%$. The conclusion is that the anti-symmetric C–D stretch mode is being detected.

Equations (25) and (28) give information on the mode symmetry without performing a complex electronic structure calculation. Equation (25) gives us the spatial distribution of the change in conductance. It basically tells us that the tip will plot the state $\psi_\mu(r_0)$ of Eq. (26). We see that the matrix element is between the states, $\psi_\mu(r)$ and $\psi_\nu(r)$. This last state, $\psi_\nu(r)$, is just the state at the Fermi energy of the molecule plus surface electronic system, following Eq. (25). Hence we can have some indirect information about the symmetry of all relevant states through: (i) the constant current image (related to states at the Fermi energy, here $\psi_\nu(r)$, Eq. (24)) (ii) the spatial distribution of the change in conductance (related to the states $\psi_\mu(r)$, Eqs. (25) and (26)). This information is indirect because it refers to the modulus square of the wave function rather than the wave function itself.

Due to the reduced symmetry of the molecule on the surface, there are only a few symmetry elements that survive after chemisorption. Generally, these elements are mirror planes and molecular axes both perpendicular to the surface. We are dealing with symmetry in two dimensions.

In the case of deuterated acetylene, the constant current image presents a depression in the plane perpendicular both to the surface and to the C–C axis. The origin of this depression lies largely in the anti-symmetry of the $\psi_\nu(r)$ states at the Fermi level. As is shown in Ref. [94], the plane of the depression is indeed a nodal plane of $\psi_\nu(r)$. The calculated spatial mapping of the change in conductance presents no depression and is symmetric with respect to the different elements of symmetry of the local point group. This means that contrary to $\psi_\nu(r)$, the states $\psi_\mu(r)$ are symmetric. The electron–vibration coupling V has to be anti-symmetric, so that the product anti-symmetric times anti-symmetric times symmetric is symmetric. Put in group theory terms, the product of the representations of the terms in the matrix element must contain the identity [95].

This same kind of reasoning can be applied to more complex systems. In the case of the measured change of conductance in spectroscopy of C_{60} [96], the mode giving the largest change in conductance at a bias voltage of 54 meV (432 cm^{-1}) was assigned to the breathing mode $H_g(\omega_2)$. In order to reach this conclusion we can use symmetry arguments plus the energy resolution of the measured spectra. From the constant current STM images we know that the states at the Fermi level have a strong molecular character. This character coincides with the LUMO of the C_{60} molecule [96]. The inelastic signal mapping has a worse resolution, but one can conclude that it probably has LUMO character, since the HOMO would have a much more symmetrical aspect than the experimental images plotted in Ref. [96]. The irreducible representation of the C_{60} LUMO is Γ_2 (F_1). For the direct product of this representation, we find $\Gamma_2 \otimes \Gamma_2 = \Gamma_1 + \Gamma_2 + \Gamma_5 = A + F_1 + H$ (see for example [97]). Hence, by using the above symmetry selection rule, the vibration can only have one of the A, F_1, or H representations. Due to the small adsorption interaction, the free-molecule frequencies are probably not terribly shifted upon adsorption of C_{60} on a metal surface. If we take the free-molecule frequencies, we have only one mode within ± 5 meV of the 54 meV peak: the $H_g(\omega_2)$.

3.2.4.3 Decreases in conductance during the excitation of a vibrational mode: The case of O_2 on Ag(110) In the previous sections, we have described the change in conductance as due to the effects of the vibration on the elastic and inelastic channels of transport. Davis [76] and later on Persson and Baratoff [45] showed that in certain conditions the change in conductance due to the perturbation of the elastic channel can outpace the effects in the inelastic channel. Above we give some estimations of the different contributions to the conductance due to the excitation of the vibration by the flowing electrons. Equation (28) gives the overall change of conductance. We see that it is a negative contribution leading to a decrease of conductance over the vibrational threshold. This is in stark contrast to the inelastic contribution that is always positive as we have already discussed in Section 3.2.4.1. An extra feature of Eq. (28) is the delta function of the inner summation: this function selects electronic states near the Fermi energy in such a way that the change in conductance in the elastic channel is maximized, if there is a large density of states at the Fermi energy. Hence, a decrease in conductance can be expected, if there is a molecular orbital that is easily coupled to some molecular vibration, and the maximum of the density of states with molecular character is close to the Fermi energy.

Experimentally, Hahn et al. [98] showed that the IETS of O_2 molecules adsorbed on Ag(110) could present decreases

of conductance instead of increases. Their IETS maps show decreases for the only two modes that give a signal when the tip is located roughly at the oxygen atoms. However, the change in conductance is positive in between the atoms. In particular, for the antisymmetric stretch mode of the adsorbed molecule, there is a large positive contribution in a sharply confined region in between the oxygen atoms, and it evolves rapidly to a negative contribution above the atoms. This competition between the inelastic and elastic contributions is perfectly captured by the theory of Lorente and Persson [89] as calculations by Alducin et al. [71] show. However, initials calculations by Olsson, Lorente, and Persson failed even to obtain some qualitative resemblance with the experimental results of Ref. [98]. The final solution to the problem, by Alducin et al. [71], came through a careful analysis of the electronic structure of the adsorbed molecule. As these authors realized, contrary to density functional theory (DFT) results, the oxygen molecule was still an open shell system and hence, in the mean-field approach of DFT (that forces broken-symmetry solutions) it should keep a spin. The DFT results with local and semilocal approximations yield a non-spin polarized solution. The above authors realized that DFT tends to underestimate the internal Coulomb repulsion of molecules, hence by using a DFT + U approach (LDA + U) they managed to increase the Coulomb charging energy (U) of the molecule and hence avoid extra charge capture from the substrate. Now, the effects of a U term in the mean-field Hamiltonian are far from straightforward: the extra U does not really prevent charge capture by the oxygen molecule but rather it forces the spin polarization by increasing the occupation of one of the spins with respect to the other one. As a consequence, one of the molecular orbitals of the oxygen molecule empties and becomes resonant with the Fermi energy [71]. This is the exact condition for a sizeable elastic contribution to the change in conductance.

The consequences of this work are very interesting: IETS becomes a probe of the electronic states of the adsorbed molecule. Indeed, the above description of an occupied spin-polarized orbital and a spin-polarized orbital resonant with the Fermi energy corresponds to the definition of an adsorbed mixed-valent molecule. Mixed valency entails fast charge fluctuations between the molecule and the substrate. This is due to two competing mechanisms: on the one hand, the hybridization of the orbitals with the substrate that permits the capture of electrons, on the other hand, the intramolecular Coulomb repulsion (U) that pushes charge away from the molecule. Hence, the molecule on the surface is fluctuating between two valency states. These states are elusive and difficult to prove. Due to their spin-polarization characteristics they are the limit of strong hybridization of the Kondo effect, and as such they are interesting states with extraordinary physics. The results of Ref. [71] show that the elusive mixed-valency state can be revealed via IETS measurments, being the decrease of conductance its hallmark.

4 STM-parameters for manipulation and basic manipulation modes Although the STM was initially intended to produce images of surfaces and has widely proven its unique abilities down to atomic resolution, it was soon experienced that the STM tip, due to its close proximity to the surface atoms, influences and sometimes modifies the surface because of tip-induced migration of surface adsorbates. Being disadvantageous for faithful imaging it was, however, readily recognized that the tip–substrate interactions could be considered in a positive way and could be used to deliberately induce modifications of the surface. It was proven that the tip surface forces indeed offer the possibility to move single atoms and molecules in a very precise way on the atomic scale (see Fig. 2) [3–8, 99, 100]. It was also recognized that both the electron current and the electric field between tip and surface could be used to modify surfaces. Thus, the longstanding dreams of building up man-designed functional nanostructures and to create new material combinations or even new materials in an atom-by-atom or molecule-by-molecule manner and to characterize them *in situ* by STM and STS are now reality.

The STM provides three different parameters for modifications of surfaces (Fig. 24) [3–8, 99, 100]:

(i) forces between tip and surface,
(ii) electrical field between tip and substrate,
(iii) electron tunnelling current.

On working with single atoms and molecules, *lateral* and *vertical manipulation* modes are distinguished. In the

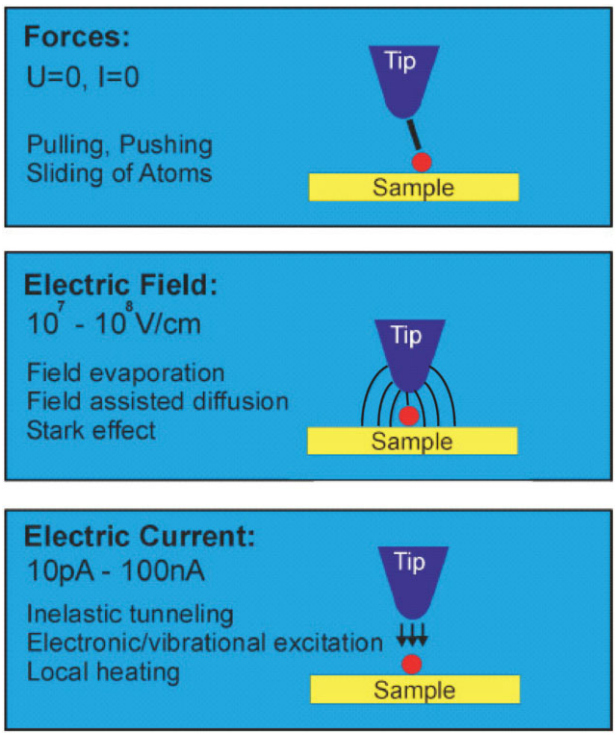

Figure 24 Experimental parameters available in STM for modifications of surfaces.

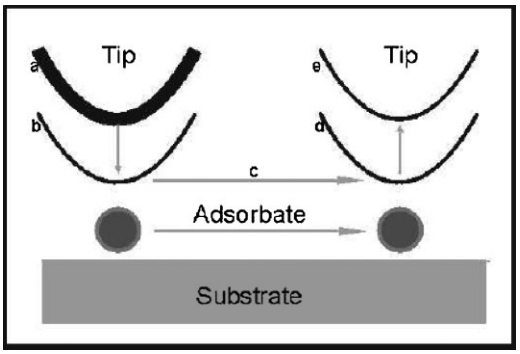

Figure 25 Principle of soft lateral manipulation using the tip of a STM.

lateral manipulation mode, a particle on the surface is moved along the surface to the desired place without losing contact to the substrate (Figs. 25 and 26), while upon vertical manipulation a particle is deliberately picked up to the tip (Figs. 27 and 28).The bond between tip and particle usually changes the tip's physical and chemical properties with sometimes favorable consequences for imaging and spectroscopy. The picked-up particle can finally be released back to the surface (Fig. 28).

Reliable atomic scale precision for the build-up of man-designed structures by manipulation in an atom-by-atom or molecule-by-molecule manner was achieved mainly by *soft lateral manipulation*, where *only the tip–substrate forces* are employed. These forces can be tuned by changing the distance between the tip and the manipulated particle (Fig. 25). The mechanisms of soft manipulation as well as the build-up and characterization of artificial structures in an atom-by-atom or molecule-by-molecule way are discussed in detail in Sections 5 and 8. As an example, Fig. 26 shows the gradual build-up of an artificial regular triangular structure consisting of 52 Ag atoms assembled atom-by-atom on a Ag(111)-substrate Using the electron current desorption of atoms and molecules can be induced whereby different physical mechanisms come into play, and also orientational and even conformational changes of molecules as well as molecular restructuring and dissociation and even

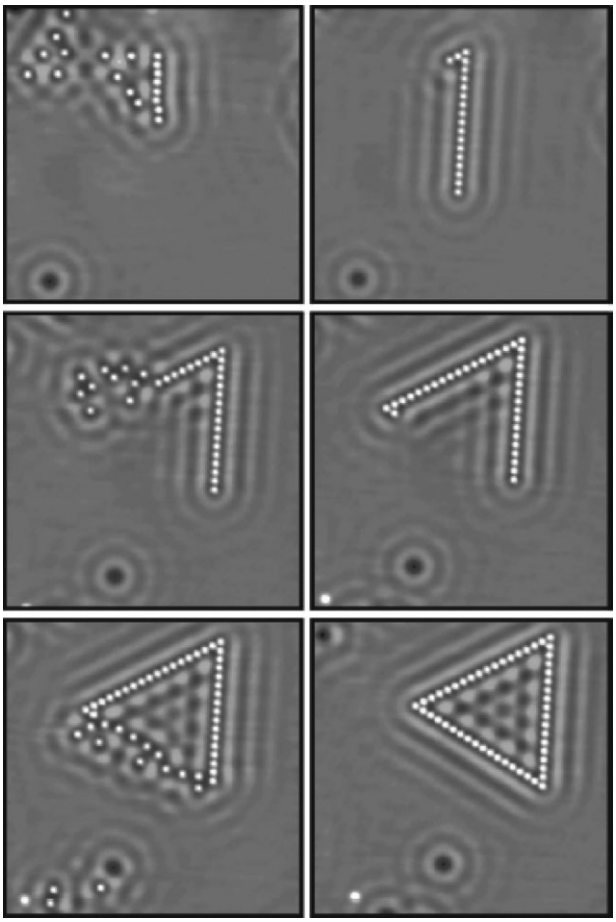

Figure 26 Example of the atom-by-atom build-up of a triangular corral consisting of 52 Ag-atoms on a Ag(111)-surface at $T = 5$ K (after Ref. [101]).

molecular association were proven [46]. These topics will be covered extensively in Section 7.

With both tip-particle forces and electron current individual atoms and molecules can be addressed in a very precise way so that working with individual surface particles is possible. Although field effects can also be used for surface modifications, this parameter yields mainly

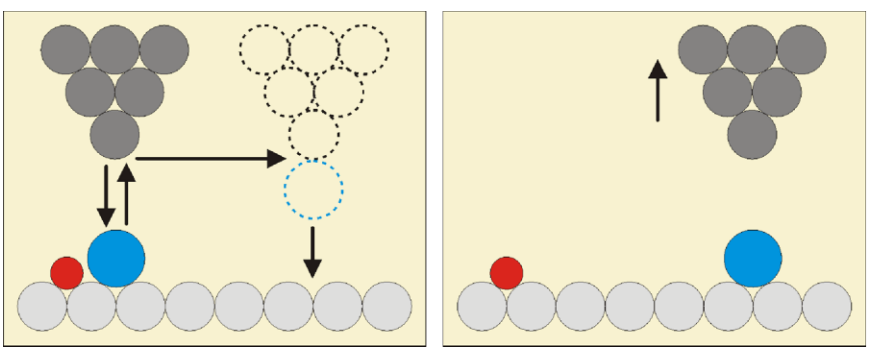

Figure 27 Principle of vertical manipulation (schematic, arrows indicate direction of tip motion). The blue particle is picked up by the tip and transferred back to another place at the surface. The red particle serves as a marker. Arrows indicate the direction of the tip (courtesy of L. Grill).

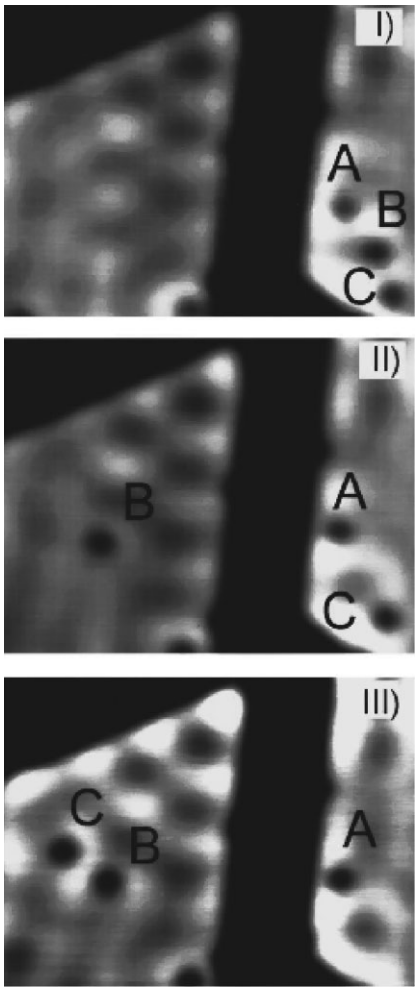

Figure 28 Example of vertical manipulation of CO molecules: STM images show a Cu(111) terrace interrupted by a lower terrace. Three adsorbed CO molecules A, B, C imaged as depressions are indicated to be distinguished from the surface standing wave features. A serves as a marker. Molecules B and C are picked up individually from the right part of the upper terrace, transported over the crevasse to the left part and put down there (after Ref. [102]).

changes like attraction or repulsion of particles carrying a charge or a dipole moment; the spatial extension of the electric field has, however, the consequence that particles in an extended region under the tip are affected at random. As example, Fig. 29 shows the attraction of positively charged Cs atoms towards a negatively charged tip; by applying positive tip biases the Cs atoms are repelled and the area below the tip becomes depleted [103]. Another effect is the conformational change of azobenzene molecules whose switching from the *cis*- to the trans-configuration (and vice versa) is shown in Fig. 30 [104]. An interesting transition from force to field effects was found as a function of tip surface distance for the movement of a single leg of a TBBP molecule and is discussed in Section 5.2.8 [105].

Combinations of effects due to the interplay of two or all three parameters are also possible and useful. As an

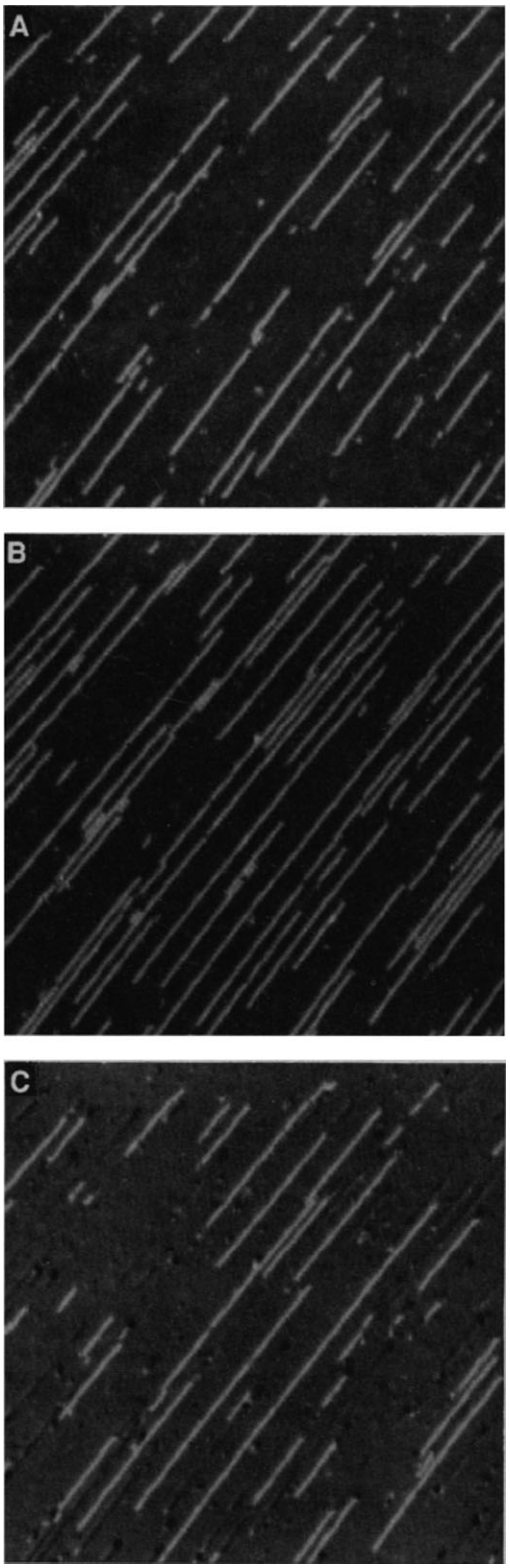

Figure 29 Example of a field induced surface modification: collecting or repelling charged Cs particles on a surface under the STM tip. STM images: (a) after Cs-deposition, (b) after application of a negative pulse there are more Cs chains in the same area, (c) after application of a positive pulse the density of Cs chains has decreased (courtesy of J. Stroscio [103]).

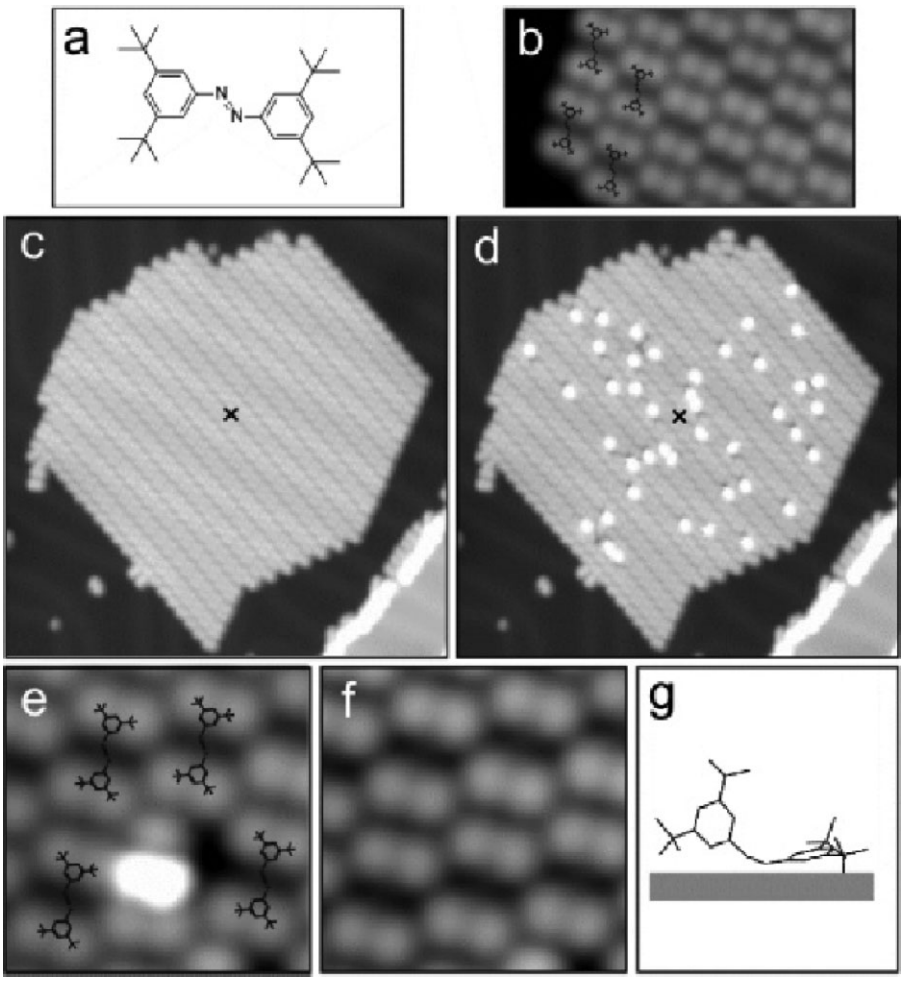

Figure 30 Switching individual azobenzene molecules with a field applied between tip and surface. (a) *trans*-tetra-*tert*-butylazobenzene (*trans*-TBA). (b) Corner of a molecular island (70 × 40 Å^2) on Au(111). The molecular adsorption geometry is indicated by structure models. (c and d) Switching experiment. (c) Island of *trans*-TBA with about 400 molecules (370 × 370 Å^2). Subsequent voltage pulses (20 s, $V_m = 2$V, tip height = 6 Å) are applied at the position indicated by the cross. (d) STM image (370 × 370 Å^2) after nine pulses: 43 molecules have been switched to the *cis*-form. (e) Zoomed STM image of a molecular island (35 × 35 Å^2). One TBA molecule has been switched to the *cis*-configuration (bright lobe), while the other TBA molecules are in the *trans*-configuration. (f) After applying a voltage pulse ($V_m = 1.5$ V, $t = 5$ s, tip height = 5 Å), the molecule is switched back to the *trans*-configuration (35 × 35 Å^2). (g) Schematic model of an adsorbed *cis*-TBA molecule (side view). In all images, the STM parameters are $I = 0.1$ nA, $V = 1$ V, $T = 5$ K (after Ref. [104]).

example in Fig. 31 the removal of single sulfur atoms from the surface of the layered material MoS_2 is shown, which is thought to arise from an interplay of all three parameters provided by STM ("tip-assisted desorption" [7]). These experiments were performed at room temperature in UHV [106–108]. It should also be noted that with the related material WSe_2 even in air nanosized hill structures have been produced and erased again [109]. These results emphasize the importance of materials aspects for the build-up of stable artificial structures at ambient conditions and are certainly worthwhile to be pursued further. Single atoms have also been extracted from semiconductor surfaces with related techniques: the tip is brought close to the surface to induce a strong chemical bond and a voltage pulse of several Volts induces field evaporation of the substrate atom ("chemically assisted field evaporation" [110] or "transfer on contact"). Using this technique, Becker et al. [111] were the first to report in 1987 the creation of an atomic-scale "bit" by removing single Germanium atoms from Ge (111)-2 × 8. The mechanism was investigated by Lyo and Avouris [110] upon experimenting with Si(111)-7 × 7. Using the same surface Uchida et al. [112] found that center atoms in the 7 × 7 reconstruction are more frequently removed than atoms near corner holes and concluded that the latter are stronger bound by 0.1 eV. Similar conclusions for Ge(111)-2 × 8 were reported by Dujardin and coworkers [113]. Furthermore, the removal of Si atoms

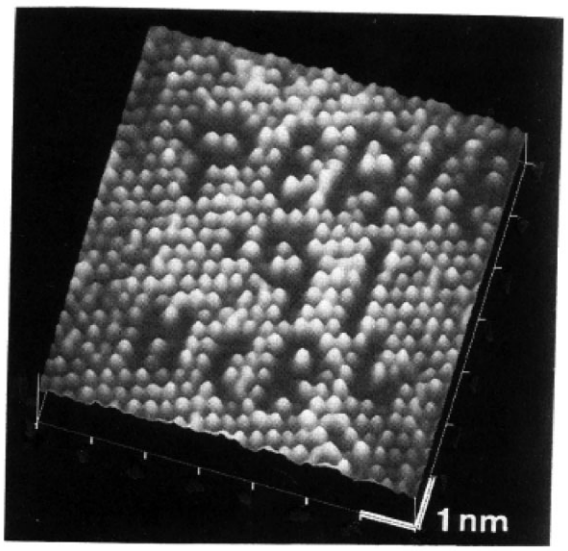

Figure 31 Removing single sulfur anions from the surface of the layered compound MoS_2. The manipulation mechanism is thought to be due to a combination of force, field, and current effects. The letters "PEACE '91 HCRL" (for Hitachi Company Research Laboratory) are clearly visible. The experiments have been performed under UHV at room temperature (after Refs. [106, 107]).

from a Si (111)-5 × 2-Au surface at RT as a memory application has been proposed [114].

5 "Soft" lateral manipulation using tip particle forces

5.1 Pulling, pushing, and sliding of atoms and small molecules The ability to create artificial structures with the STM by lateral manipulation is proven in Figs. 2 and 32. Figure 2 shows the first structures built by the first two groups who have succeeded to use manipulation reliably on the atomic scale. In the upper part the three letters I B M constituting the abbreviation of their company are shown as constructed by D. Eigler and E. Schweitzer with a 4K-STM using 35 Xenon atoms on a Ni(110) surface [3]. In the lower part, the two letters F and U formed at 25 K with a total of 20 carbon monoxide molecules on Cu(211) designate the short form of the Free University of the Berlin group of G. Meyer and K.H. Rieder [5]. Notice that at this slightly elevated temperature the CO molecules were still rather mobile, so that it was impossible to keep them in the desired places due to thermally induced irregular molecular jumps and the experimenters had to fight continuously against entropy. At temperatures lower than 15 K, however, structures can be built with CO with atomic precision, as proven in Fig. 32, where the millennium number "2000" and the Brandenburg Gate of Berlin built on the nanometer scale are shown. These structures were built on Cu(211) by manipulating laterally 47 and 53 CO molecules, respectively. A sphere model of the stepped (211)-substrate is shown in Fig. 33. Below 15 K, the molecules become frozen to a sufficient degree, so

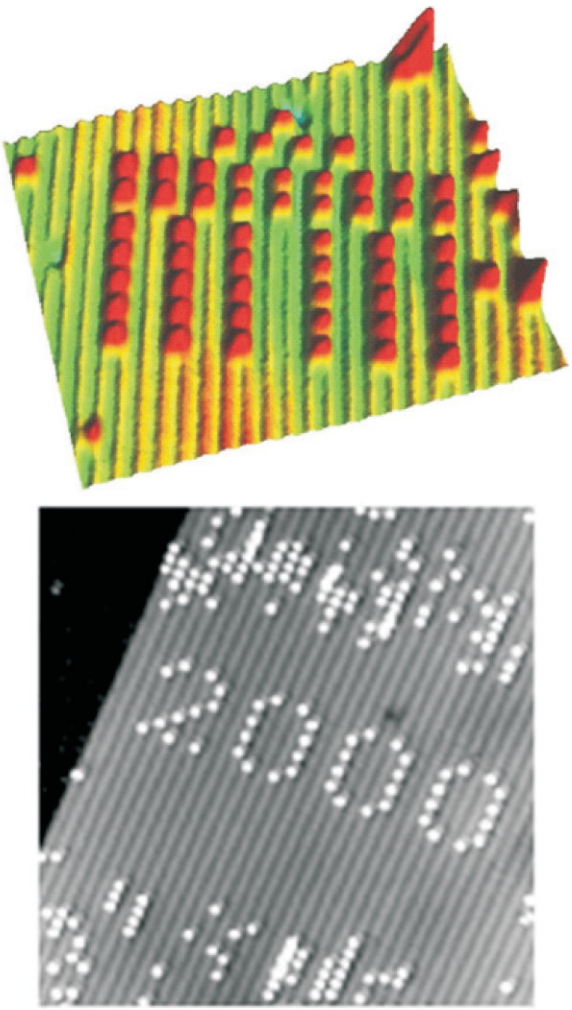

Figure 32 Brandenburg gate and millennium number 2000 fabricated in a one by one fashion with CO molecules on Cu (211) (courtesy of G. Meyer).

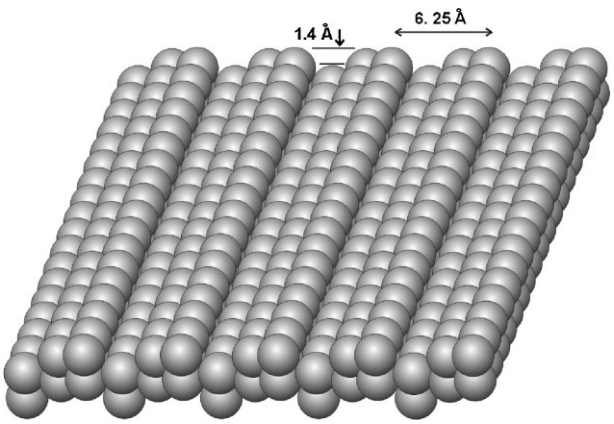

Figure 33 Sphere model of the Cu(211) surface consisting of (111) terraces and (100) steps.

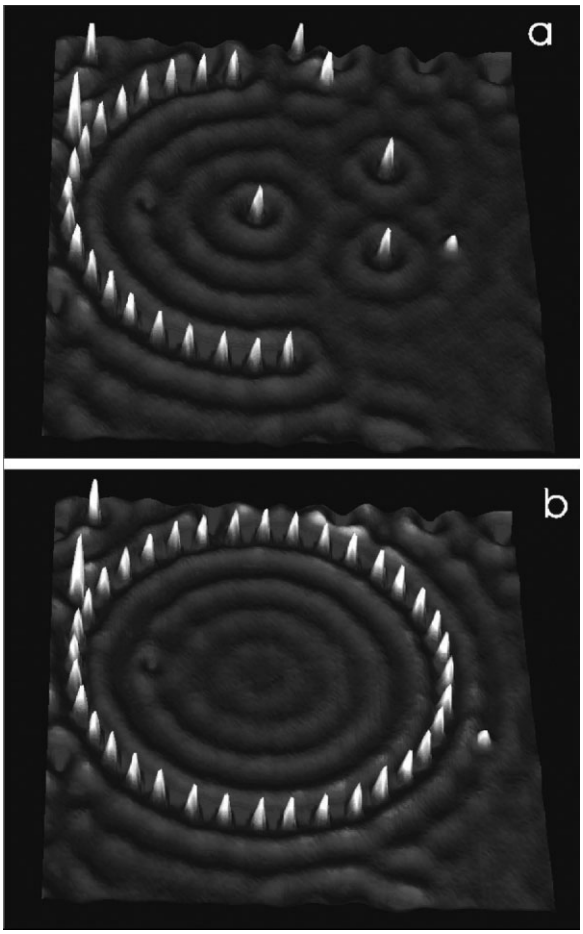

Figure 34 Different stages during the build-up of a circular artificial structure (corral): (a) half circle, (b) full circle. Notice the standing wave pattern due to the surface state on Ag(111) inside and outside the circle (after Hla et al. [115]).

that precise working is possible with a rather large number of particles and the artificial structures remain stable for a long time.

An example of the different stages during the build-up work of a circular artificial structure (corral) on a close-packed fcc(111) substrate is given in Fig. 34.

Technically, for performing soft manipulation the tip is brought closer to the particle to be moved from the imaging distance (0.8–1.0 nm) to a distance (0.3–0.5 nm), in which the tip-particle force is strong enough, so that upon moving the tip parallel to the surface to the desired position the diffusion barriers can be surmounted. At the end point the tip is then withdrawn to the imaging distance and a control image can be taken. The sequence of steps is indicated in Fig. 25. It is clear that the tip-particle forces necessary for secure manipulation should scale with the height of the diffusion barriers for different ad-particle–surface combinations. Since the tip-particle forces cannot be measured directly with STM, as a good measure the tunnelling threshold resistance can be taken, which is roughly inverse to the manipulation force. Table 1 shows the data for manipulation resistances and diffusion barrier heights available up to now and proves roughly the inverse correlation of the two quantities. The lateral and vertical force necessary to move a Co atom on a Pt(111)-surface were directly measured by AFM [117].

Table 1 Anti-correlation between threshold resistivity and surface diffusion barriers for noble gas on metal, molecular chemisorption on metal, and metal on metal systems: the larger E_{act} the lower is R_t.

threshold resistances for manipulation R_t (kΩ)			activation barriers for diffusion E_{act} (eV) [116]	
Xe/Ni(110)	5000	[4]	Xe/W(110)	0.052
CO/Cu(211)	600	[6]	CO/Ni(100)	0.207
CO/Pt(111)	200	[4]		
Cu/Cu(211)	400	[6]	Ni/Ni(100)	1.65
Ag/Ag(111)	210	[115]		
Pb/Cu(211)	120	[6]		
Pt/Pt(111)	20	[4]		

As discussed above, the first successful manipulation experiments at low substrate temperatures were performed with Xe atoms [3, 4] and small molecules like CO and C_2H_4 [118–120]. Manipulations of metal atoms like Cu, Ag, Fe, and Pb followed [22, 115, 121]. In Ref. [6] it was observed that increasing forces have to be applied in the respective order Pb, Cu, Ag when using the same tip. With still increasing forces, it was shown on Cu(211) that it is also possible to release native substrate atoms from six-fold coordinated kink sites (Fig. 35a–c) and even from sevenfold coordinated regular step-edge sites (Fig. 35d–f) [119]. This important result in principle opens the way for structuring the surface itself. One promising prospect is that also deeper lying substrate layers may be included in the build-up of artificial prototype structures, although this has not been pursued up to now. It could also be shown that vacancies at step edges of regularly stepped surfaces like Cu(211) can be "healed out" by manipulating single atoms into them; interestingly, a larger force is required for this purpose than for manipulation along defect free step edges indicating that a local barrier due to atom relaxations around the vacancy has to be surmounted [122]. The manipulation of "native" substrate atoms on Cu(211) to positions close to foreign ad-species could be used to determine adsorption sites of the latter due to the known ad-sites of the metal atoms [118]. Manipulation of Ag atoms perpendicular to the step edges on Ag(110) can also lead to particle exchange at the steps [123]. Figure 34 shows the formation of an artificial metallic structure: by lateral manipulation 36 Ag atoms have been positioned in a circle with diameter of 31.2 nm on a Ag(111) surface [115]. The electrons of the surface state are scattered at the adatoms resulting in an energy dependent interference pattern as well visible in Fig. 34. The closed scattering geometry results in an (imperfect) confinement of the electrons inside of the quantum corral as has been

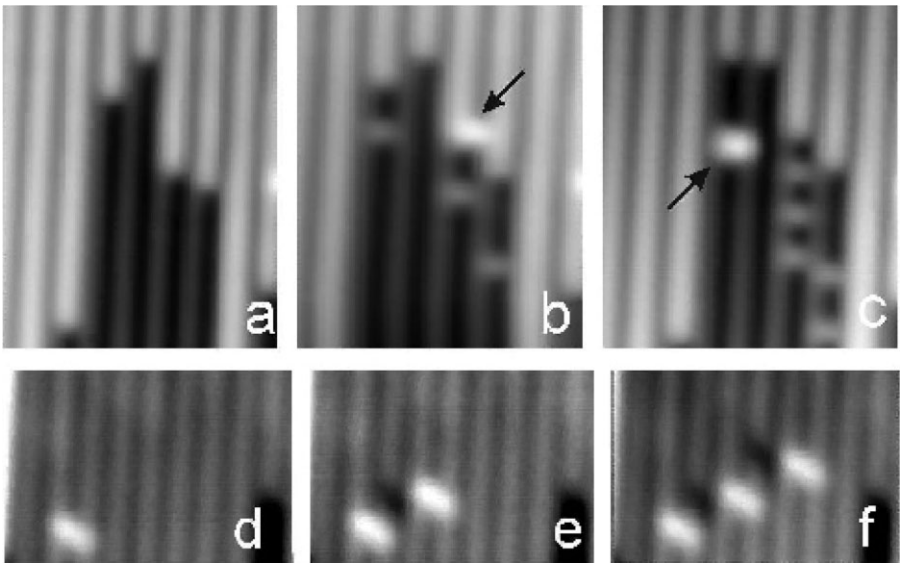

Figure 35 Manipulation of substrate atoms: (a–c) removal of sixfold coordinated kink sites from defect step edges on Cu(211). (d–f) Removal of sevenfold coordinated sites from regular step edges on Cu(211) (after [118]).

demonstrated first by Crommie et al. [22]. Various experiments with quantum corrals are discussed in detail in Section 8.1.

The construction of atomically perfect structures with many atoms or small molecules is to date still bound to low temperatures, although at room temperature tip induced migration of the radical C_5H_5 on Cu(111) with the STM was demonstrated [124]. Noticeably, manipulation of Sn atoms by exchange with Ge atoms in a surface alloy formed by Sn on Ge(111) was convincingly demonstrated by using an atomic force microscope (AFM) [125].

Systematic manipulation experiments with Cu atoms, Pb atoms, and CO molecules on Cu(211) revealed that three different manipulation modes, depending on the applied tip-particle force (qualitatively measured by the tunnelling resistance) could be distinguished [6, 115]. In these experiments, which were performed in the constant current mode, the tip height was recorded during manipulation. The three basic manipulation modes are *pulling*, *pushing*, and *sliding*. An experimental proof that these lateral manipulation modes are dominated by the force interactions between the tip and the object to be manipulated is discussed below.

Schematic tip height curves characteristic for the three different basic manipulation modes are shown in Fig. 36. In the *pulling mode* the tip first goes over the maximum corrugation of the particle and comes closer to the surface again so that a lateral attractive force is exerted on the particle, which causes the particle to jump below the tip; this causes the tip to retract immediately from the surface; afterwards the tip scans down on the particle corrugation again and the procedure repeats (Fig. 36, top). In the *sliding mode* a larger force is exerted on the particle by coming closer with the tip until the tip–particle interaction is increased so strongly that the tip together with the ad-particle scans the corrugation of the substrate, while the particle substrate interaction is still strong enough to keep the particle on the substrate. Thus a corrugation picture of the substrate is obtained (Fig. 36, bottom). In the *pushing mode* the particle hops away from the tip before the tip reaches the maximum ad-particle corrugation causing the tip to come closer to the surface immediately; then the tip goes up the particle corrugation again and the process repeats (Fig. 36, middle).

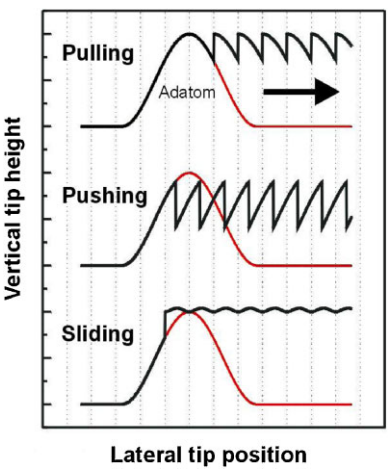

Figure 36 Schematic pulling/pushing/sliding tip height curves. In the case of sliding and sometimes also in the case of pulling, the particle is drawn towards the tip already when the tip approaches.

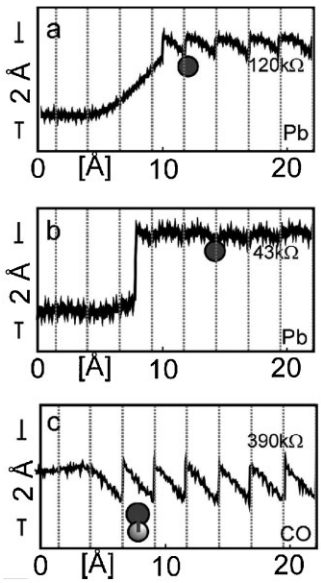

Figure 37 Experimental pulling (a), sliding (b), and pushing (c) tip height curves. Notice that the experimental pushing curve for CO is inverted against the schematic curve as the CO molecule appears as a depression when imaged with a metal tip (after Ref. [6]).

Corresponding experimental curves are shown in Fig. 37. The topmost tip-height scan demonstrates that Pb- (and also Cu- and other metal) atoms are manipulated via *attractive tip–adatom interactions* whereby the ad-particle follows the tip discontinuously by hopping from one chemisorption site to the next (pulling mode, Fig. 37a, compare Fig. 36 (top)). Note that in the case shown the ad-particle first jumps towards the approaching tip proving again that the tip ad-particle interaction is attractive. Upon application of larger forces than for pulling as signalled by the lower tunnelling resistance, Pb atoms can also be manipulated attractively in a continuous way (sliding mode, Fig. 37b and Fig. 36 (bottom)); in this mode the tip–particle interaction is increased so strongly that the tip–ad-particle system scans the corrugation of the substrate, while the particle substrate interaction is still strong enough to keep the particle on the substrate. Finally, single CO molecules as well as rows of several CO molecules could reliably be manipulated via *repulsive interaction* (pushing mode, Fig. 37c and Fig. 36 (middle)); note that in this case the intrinsic step edges of the Cu(211) surface, on top of which the CO-molecules are bound, act as railway trails [6]. Notice that the experimental pulling curve is inverted against the schematic curve, because individual CO molecules are imaged as minima.

A particularly transparent example to prove repulsive tip ad-particle interaction is shown in Fig. 38. A single CO molecule is pushed against a row of CO molecules, whereby all molecules start to move together, when the first molecule comes in nearest neighbor distance to the row. When the tip is withdrawn, the entire row remains intact [126]. In an analogous way, a repulsive interaction and consequent

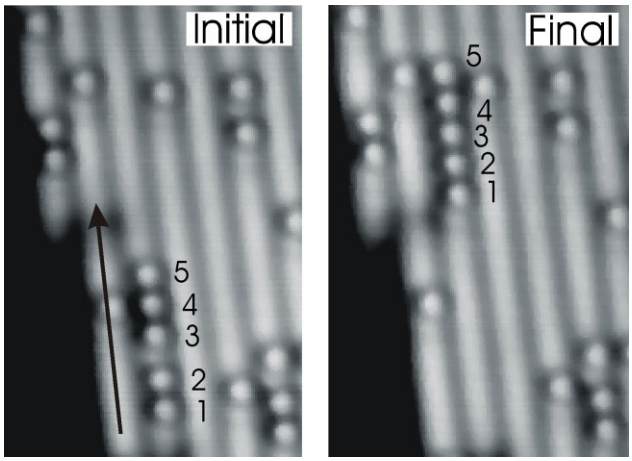

Figure 38 Pushing of a row of CO-molecules along an intrinsic step edge of a Cu(211)-surface (after Ref. [126]).

pushing of C_{60} molecules was proven as manipulation mode, although there are hints for an occasional rolling motion of these spherically symmetric particles [127].

In a remarkable manipulation experiment with CO, G. Meyer recognized that – using the same tip (!) – a larger tunnelling resistance (smaller force) was sufficient to push a CO molecule on a single Cu atom located at the step edge of a Cu(211) single crystal surface than to push it back to the step edge again (Fig. 39). This may point to a larger binding

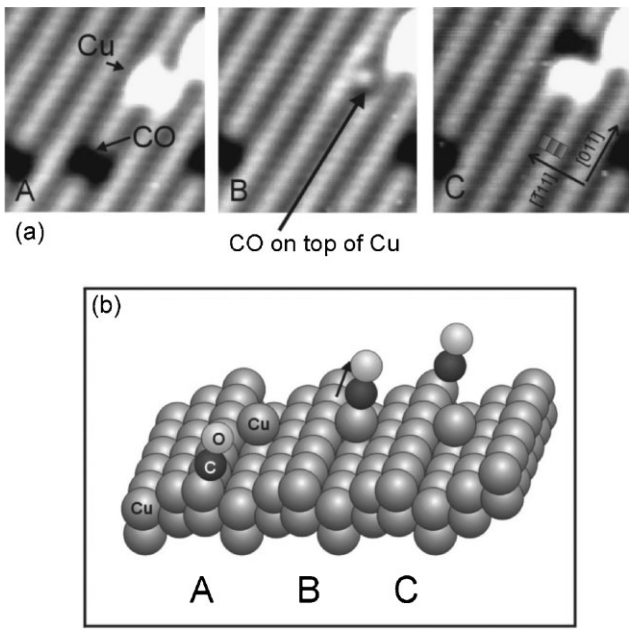

Figure 39 A larger force with $R_{down} = 270$ kΩ is needed to push a CO molecule from a single Cu atom located at the step back to the step of a Cu(211) surface (B, C) than with $R_{up} = 400$ kΩ to push it along the step edge (A) pointing to a larger binding energy in the isolated adsorption site: (a) STM images, (b) schematics (after Ref. [128]).

energy at the single Cu adatom than on a Cu atom located at a row of Cu atoms forming the step edge (provided the shapes of the potentials are not too different). This conjecture was confirmed by calculations of Gajdoš et al. [128], which gave a larger binding energy of ∼0.1 eV at the single Cu atom than on the step. This result shows that even very subtle differences in binding properties can be recognized in careful manipulation experiments.

The pulling and sliding manipulation modes can be performed with great precision and have consequently been used to build most of the man-designed artificial structures discussed in Section 7. It should be mentioned that on close-packed surfaces with several symmetry equivalent directions pushing becomes unreliable as the particle can move to the side of the tip and escape from the vicinity of the tip. However, it has been shown that also the pulling mode can be induced to precisely move CO-molecules on hexagonally close-packed surfaces [129].

This transition from pulling to sliding can be reproduced by simple model calculations assuming an analytical surface potential mimicking the substrate corrugation and a Morse potential for the interaction between tip and particle. The ad-particle positions during manipulation are calculated by searching for the respective closest energy minima [130]. The same procedure was also used to reproduce manipulation experiments, which were done in different directions on a close-packed Ag(111) surface (Fig. 40). Whereas in the close-packed [1–10] direction a clear pulling behavior is observed, at an angle of 20° from this direction the pulling curve indicates that at regular distances the tip has to come very close to the surface so that the force between tip and particle is big enough that the particle can follow the tip by jumping over to the next close-packed row. In these situations the manipulation process becomes unstable and insecure. For this reason

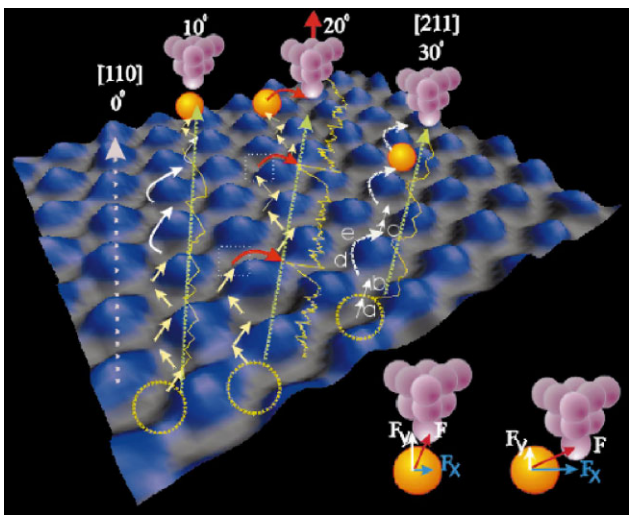

Figure 40 Pulling in different directions of atoms on a close-packed surface. Various pulling curves are indicated. The curve at 20° is discussed in the text (after Ref. [115]).

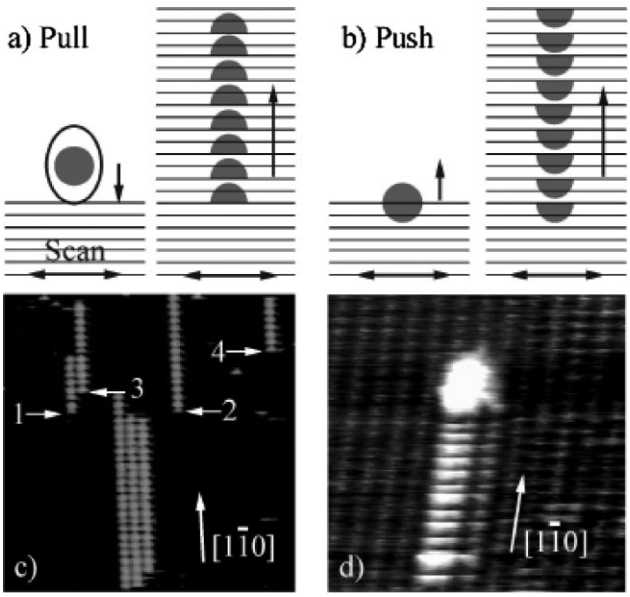

Figure 41 Tip-induced migration of Ag atoms on Ag(110) in pulling (a,c) and pushing mode (b,d) (after Refs. [132, 133]; courtesy of R. Berndt).

Stroscio et al. [131] in their automated version of the manipulation pulling process have chosen paths along the close-packed directions, even if the particles have to go long distances.

An interesting example of tip induced migration of Ag atoms on an Ag(110) surface is reproduced in Fig. 41. Depending on the applied voltage the atoms were moved in a pushing or pulling mode along the close-packed rows or across the rows, respectively [132, 133]. It is important to notice that here the tip is moved in the direction roughly normal to the particle movement; however, by constructing tip height lines along the maxima of the half-moon structures of Fig. 41c and d, one gets respective pulling and pushing curves as in Figs. 36 and 37.

The threshold tunnelling resistance necessary to move an Ag atom on a Ag(111) surface was precisely determined by systematically varying the manipulation parameters over a wide range. An extensive set of several thousand computer-automated manipulations has been taken for this purpose. The atom manipulations were performed by using tunnelling current values ranging from 8 to 950 nA and tunnelling voltages ranging from ±10 to ±55 mV. Figure 42a shows a plot for the probability of a successful atom manipulation versus tunnelling current at −45 mV bias. At this bias, the probability of a successful atom manipulation changes from zero below 147 nA to one above 250 nA and an average threshold current is determined as 200 nA. The entire measurement procedure is repeated for a wide range of bias voltages. Evaluation of these measurements yields the minimum current necessary to move the atom as a function of the tunnelling voltage averaged over all surface directions. Figure 42b depicts the results, which clearly display a

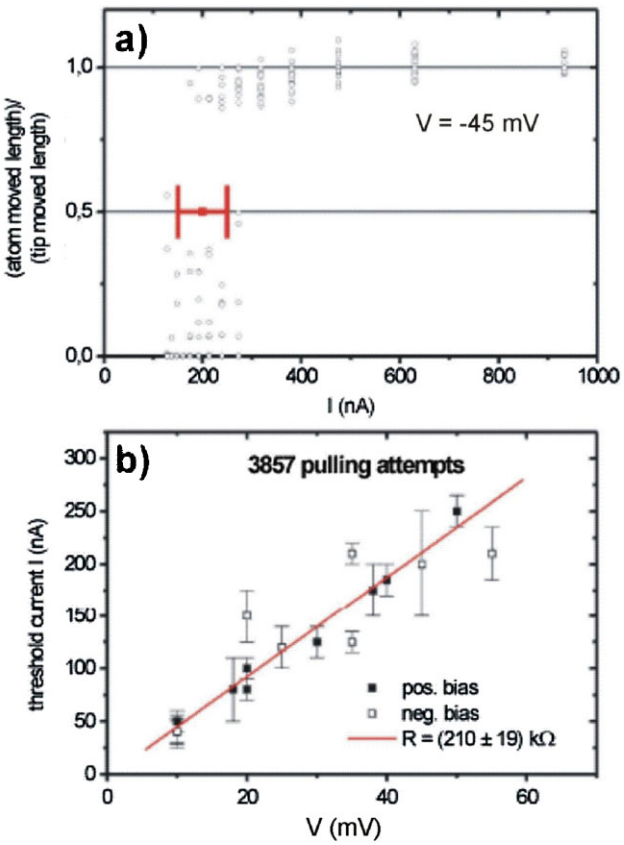

Figure 42 Motion of Ag on Ag(111): (a) Probability of successful atom manipulation. (b) Demonstration of linear behavior for the threshold current I versus tunneling voltage V for secure lateral manipulation. The I–V linearity proves the dominant influence of the tip-particle forces for the manipulation process (after Hla et al. [115]).

linear dependence between the tunnelling voltage and the threshold current, independent of the bias polarity. In this low bias regime, the influence of electric field effects in the manipulation process is negligible. From the slope of the curve in Fig. 42b, a tunnelling resistance of (210 ± 19) kΩ has been measured. This linear relationship unambiguously reveals that the tunnelling resistance is the ultimate parameter to move an atom within the bias range used in this experiment. This tunnelling resistance value corresponds to a tip-atom distance of (0.13 ± 0.02) nm before the formation of an Ohmic point contact, as can determined from I–z spectra. The lateral center-to-center distance between the apex atom and the adatom was measured to be typically 0.35–0.42 nm, depending on the exact path of the atom as discussed in detail in Ref. [115]. Since this is a distance where the tip and manipulated atom wave functions are overlapping to form bonds, the chemical nature of tip–atom interaction is proven to be the main responsible force in the lateral manipulation process. Theoretical calculations have been made for the pulling of a Cu atom adsorbed at a Cu step edge only. The calculated threshold distances are in fair agreement with the experimental findings for the pulling of Ag atoms on an Ag(111) surface. Also the calculated tip distances necessary to deform the diffusion potentials is with 0.3 in the estimated experimental range [134]. Deviations from linearity were observed at higher voltages and point to the beginning of influences of current and field effects [135].

Sometimes extreme conditions have to be applied in STM-imaging so that systematic (unwanted!) tip induced migration is a consequence. An example is given in the following: upon imaging of hydrogen ad-atoms (which are weak electron scatterers) on Rh(100) such low tunneling resistances had to be chosen that the tip executed a sufficiently strong force to drag the H adatoms from their high coordination fourfold hollow equilibrium chemisorption sites to bridge sites where they were imaged as protrusions [136]. The equilibrium fourfold sites were determined by different other experimental techniques including low energy electron diffraction (LEED) as well as by density functional calculations. The DFT calculations also could elucidate the dragging effect of the tip at the necessary extreme imaging conditions.

5.2 Manipulation of large molecules

5.2.1 Lateral manipulation in constant height mode The technique of single particle manipulations by means of the STM can also be applied to the controlled displacement of large molecules at low and even at room temperature. To understand and control the manipulation process in detail, it is useful to experimentally measure the intramolecular movement during the manipulation by recording the feedback signal in real time. To assure a low noise level and high stability such experiments have to be performed at low temperature. Due to the low surface mobility of large (and heavy) molecules, attractive tip-particle forces can only rarely be used, but repulsive forces constitute a secure way of manipulation in the pushing mode. Experimental experience showed that it is of advantage to perform the manipulation in the constant height mode [137] rather than in the constant current mode and to measure the changes in tunnelling current during manipulation as shown schematically in Fig. 43. The basic characteristics of the manipulation signal for the pushing mode are the same in both constant current and constant height modes, although fine structure within every hopping step [138] may reveal details of molecular conformation changes during movement (see Section 5.2.2). The low surface mobility of large molecules has also an advantage: molecules can be manipulated at room temperature (although intramolecular movement details tend to disappear due to noise) and indeed the first experiments were performed at RT with Cu-TBPP (tetra-*di*-*t*-butylphenyl-porphyrin) molecules [139].

5.2.2 Intramolecular mechanics during manipulation For larger organic molecules intramolecular manipulation is feasible. In LT-STM, Cu-TBPP on Cu (100) shows four bright lobes, while the porphyrin ring

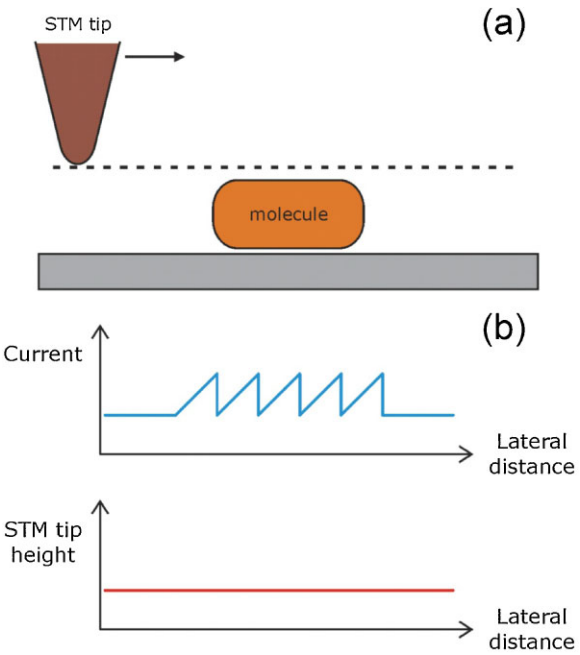

Figure 43 (a) Scheme of pushing a large molecule in the constant height mode. Note that in contrast to the pushing mode shown in Fig. 36 the current variation is measured during the manipulation procedure. The general appearance of the signals in both cases has similar characteristics. (Courtesy of L. Grill.) (b) Current and height signals during manipulation.

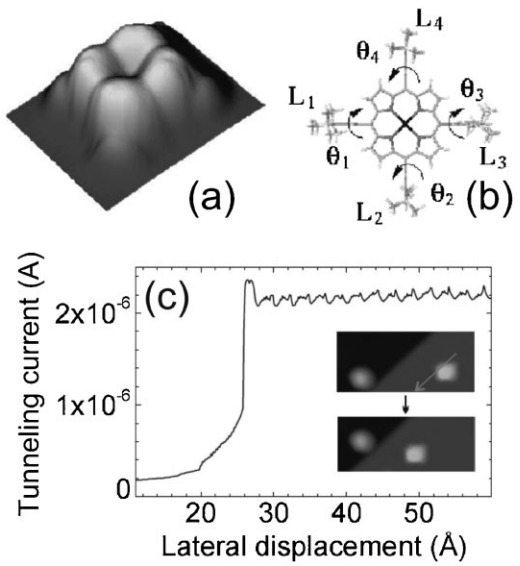

Figure 44 (a) STM image of a TBPP molecule deposited on Cu (100) (tunnelling current 400 pA and bias voltage of 300 mV). (b) Chemical structure of TBPP. (c) Experimental current versus distance curve recorded during the manipulation of a TBPP molecule of a leg. Inset shows the molecule before and after manipulating a leg upward. The arrow on the upper image indicates the exact path followed by the tip. (Reprinted from Ref. [138], with permission from APS.)

is hardly visible (Fig. 44a and b) [138]. Elastic scattering quantum chemistry (ESQC) calculations [37] of the STM image show that each lobe corresponds to a leg oriented nearly perpendicular to the surface, at an angle of about 80°.

TBPP molecules were manipulated at cryogenic temperatures by pushing at one of the legs. The recorded manipulation signal is presented in Fig. 44c. The sequence reflects first of all the Cu(100) lattice periodicity, but details in each period do not resemble the regular saw tooth signals recorded during STM manipulations of atoms and diatomic molecules (compare Fig. 43). Zoomed parts of the signal show a characteristic intra-period signature, peculiar of this specific type of manipulation. To extract from the manipulation signal the details about the intramolecular mechanics occurring during a manipulation sequence, ESQC-calculations and dynamical computer simulations revealed that the main contributor to the signal is the leg, which directly interacts with the tip apex, and that a minor contribution comes from the leg in front of the tip. These movements are very small, the oscillations of the legs amount only to a few half degrees. Such a very fine analysis demonstrates however that detailed "on line" information on the internal mechanics of molecule motion can be extracted from $I(x)$-curves measured over many manipulation steps.

5.2.3 Contacting molecules Synthetic chemists nowadays can design and build molecules with specific functions, which can be exploited on a single molecule basis with STM and STS. One such molecule is the Lander molecule ($C_{90}H_{98}$), which consists of an elongated long poly-aromatic inner board (presumably conductive, thus constituting a model electric wire) and again four di-*tert*-butyl-phenyl-legs, which act as spacers for the inner board (Fig. 45, left). As these molecules can be manipulated in the pushing mode parallel and perpendicular to defect step edges of otherwise flat (111) surfaces, interesting model experiments concerning electrical contacts can be performed [140]: whereas in the orientation parallel to the step edges, where the molecules touch with the legs the wall of the step, no change in the standing wave pattern of the Cu (111) substrate on the upper part of the step is found, in the orientation perpendicular to the step edge, where the inner board touches the step, an interference pattern analogous to that of an optical pattern upon diffraction by a slit is observed (Fig. 45). Calculations to fit the observed pattern with the scattering theory of Heller (which is discussed in Section 8.1.1) show that the lateral dimensions of the "slit" agree very well with the dimensions of the end groups of the aromatic inner part of the molecules (Fig. 46).

5.2.4 Making artificial structures at island edges A novel way to create artificial structures with molecules was found with HB-HPB (Hexa-*tert*-butyl-hexaphenylbenzene $C_{66}H_{78}$) molecules, which consist of an inner benzene ring, to which six phenyl groups are attached, each of these being connected to the outermost

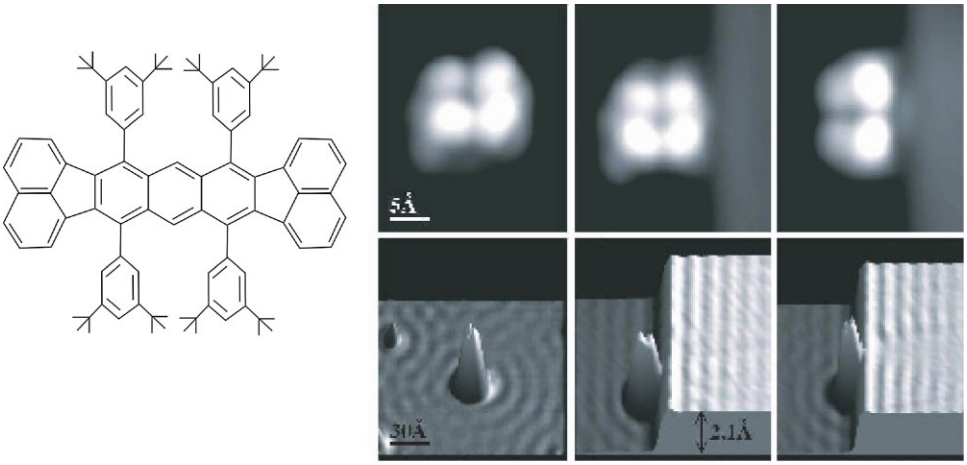

Figure 45 Left: schematic model of Lander molecule. Right: upper series: LT-STM images of Lander on terrace, with the legs parallel to a step edge, and with the legs perpendicular to the step edge, respectively. Lower series: an almost circular standing wave pattern due to the electron surface state on Cu(111) arises from a single Lander molecule. When the legs are oriented parallel to a defect step edge, the wave pattern on the upper part of the terrace is not influenced. When the molecule is oriented perpendicular to the step edge, on the upper part of the terrace a pattern appears due to the electronic contact of the poly-aromatic inner board with the substrate, which is similar to the optical diffraction by a narrow slit [140].

tert-butyl-groups (see Fig. 47, left). These molecules tend to form large islands upon adsorption at elevated temperatures. From the edges of these islands individual molecules can be removed and attached to island edges somewhere else (Fig. 47, middle). As the molecules lock in precisely into the molecular lattice, structures can be artificially formed with atomic precision as shown in Fig. 47, right [141].

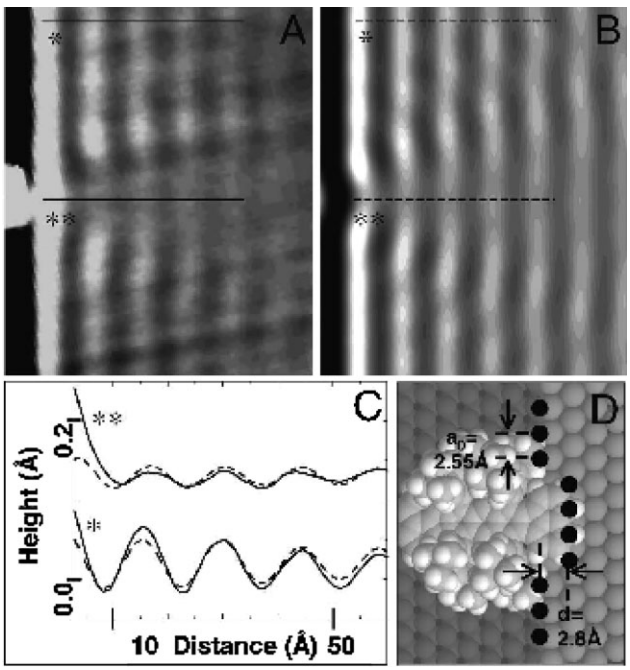

Figure 46 Experimental (a) and calculated (b) scattering patterns of Lander molecule contacting the upper step edge. (c) Respective intensity curves along the lines ** and * of (a) and (b). (d) shows the geometry of the molecule according to ESQC calculations (after Ref. [140]).

5.2.5 "A molecular dumper truck" Individual HB-HPB-molecules can collect single Cu-atoms below their central part as shown in Fig. 48. The inner part of the molecule, which is lowest in the STM-pictures, increases in height linearly with the number of atoms below the molecule. A maximum number of six atoms can be accommodated below the molecule [142]. This allows for a convenient way to assemble atoms and to form nanostructures with clusters of different sizes and might be especially valuable for work on thin films of alkali halides and other insulators, on which atoms are highly mobile and therefore not easy to manipulate in a precise manner.

5.2.6 A molecular rack and pinion system – Rotational motion of molecules in the surface plane HB-HPB-molecules can also be manipulated along the edges of islands, which they form. The question arose whether this movement would be connected with a rotation of the molecules. This is indeed the case as proven with molecules, which contain a pyrimidine group as marker (Fig. 49b). This shows up as a bright spot close to the leg that contains the marker (Fig. 49, bottom). Manipulating the molecule in lateral steps causes the marker to change its direction by 60° in accordance with a rotation of the molecule during a lateral translation step. As the molecule locks into the island edge after every step, this bears an analogy to a "rack and pinion device", Fig. 49a, however on nanometer scale [143].

5.2.7 Rolling motion of molecules out of the surface plane Recently a wheel dimer molecule was

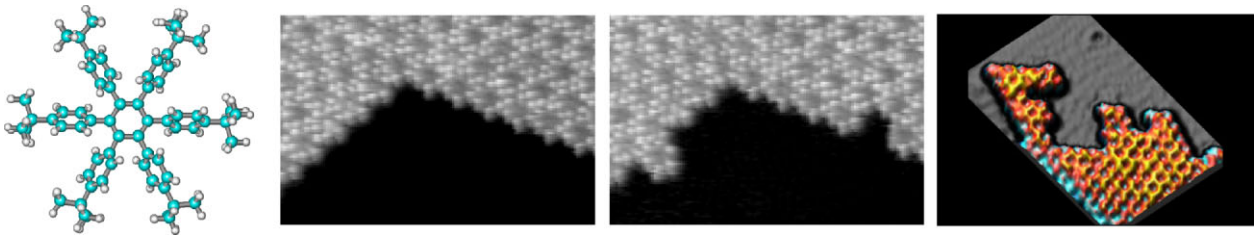

Figure 47 Left: structural model of the six leg HB-HPB molecule. The two STM pictures in the middle demonstrate that a molecule can be manipulated from one side of an extended island to another where it locks in into the molecular lattice. The picture to the right shows an extended artificial structure produced in this way (letters F and U for Free University; after Ref. [141]).

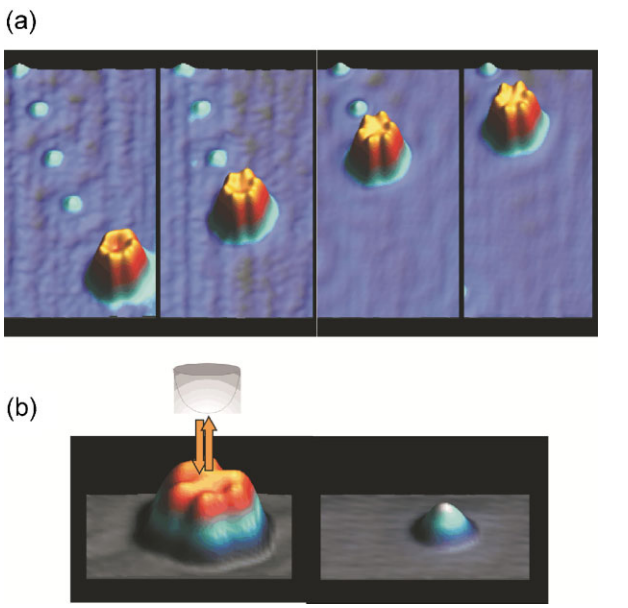

Figure 48 (a) The series of four STM pictures demonstrates the pick-up of several Cu-atoms (maximum number six) underneath the HB-HPB molecule. (b) If the molecule is picked up by the tip via vertical manipulation, the Cu-atom-cluster remains on the surface (after Ref. [142]).

synthesized ($C_{44}H_{24}$) where two trypticen wheels are connected via a di-alkyne axle consisting of four linearly arranged carbon atoms (Fig. 50a). Manipulation experiments on Cu(110) with molecules oriented with the axle along the dense packed Cu rows (Fig. 50b) revealed beside the usual pulling and pushing behavior (Fig. 51), which were found at small tip heights, a new mode was found for larger tip heights, which was interpreted as rolling [144, 145]. The rolling motion and its experimental evidence are explained with the help of Figs. 50–52.

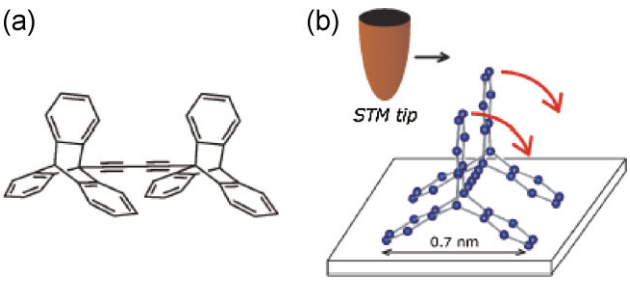

Figure 50 (a) Chemical structure of the wheel-dimer molecule ($C_{44}H_{24}$). (b) Scheme of a manipulation with the STM tip to induce a rolling motion (arrows indicate the tip movement and the rotation of the wheels, respectively). From Ref. [144].

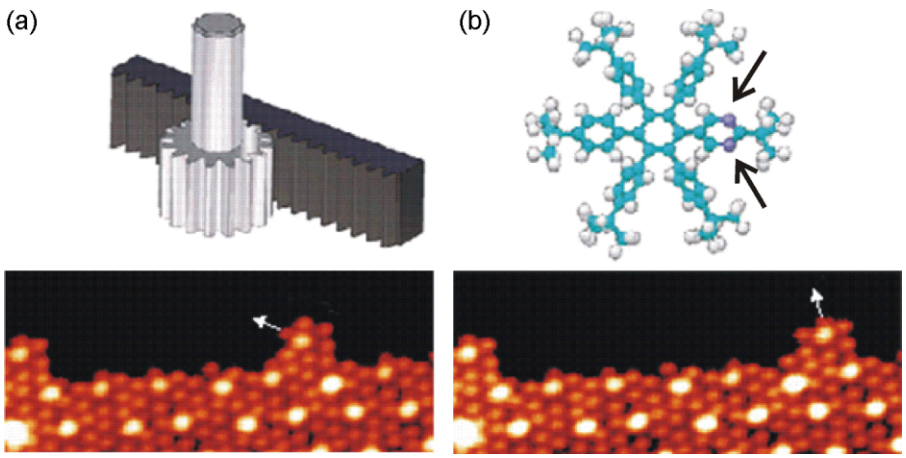

Figure 49 (a) A classical rack and pinion device. (b) Model of an HB-HPB molecule containing a pyrimidine marker in the direction of one leg (arrows point to it), which is visible in the STM pictures as bright spot (bottom images). Notice that upon manipulating the molecule one step to the right, it locks into the island edge with atomic precision and rotates by 60° at the same time [143].

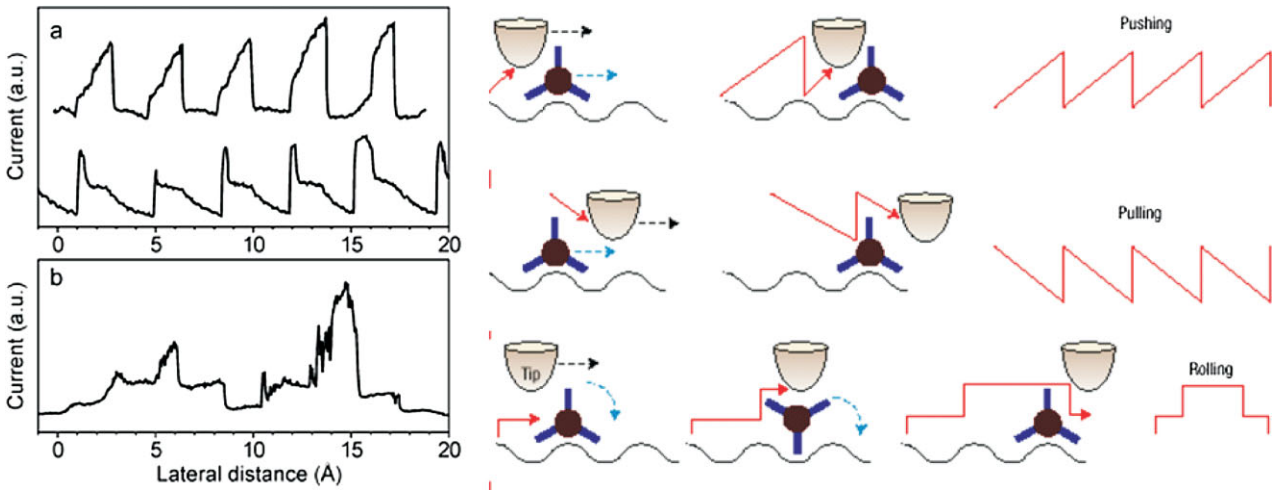

Figure 51 Left part: tunneling current signals during lateral manipulation: hopping (a): top for push and bottom for pull, and rolling motion (b). While the periodicity of the signals in (a) corresponds to the atomic distances of the substrate, the rolling motion (b) exhibits a completely new, hat-shaped signal. Right part: For comparison with the experimental data schematic pictures of the pushing, pulling and rolling behavior are shown. Concerning the rolling mechanism the first step is the tip approach towards the molecule, the second step is a 120° rotation of a wheel around its molecular axle and in the last step the tip reaches the other side of the molecule. It shows that in principle only one rotation of a wheel can be induced (the direction of movement is marked by arrows). From Refs. [144] (left) and [145] (right).

5.2.8 Manipulating parts of a molecule: A mechanically operated electric molecular switch Manipulation using tip-particle forces can also be performed in such a fine manner that only parts of a molecule are affected: TBPP molecules consist of a central porphyrin ring, to which four *tert*-butyl-phenyl-legs are attached, which in the gas phase are perpendicular to the center ring. On Cu (211), however, the legs lie flat (Fig. 53a and c). Using lateral manipulation a single leg can be transformed into an almost perpendicular conformation (Fig. 53b and d). The leg can be pushed back into the flat position with the tip again (Fig. 53e). As the perpendicular and parallel conformations

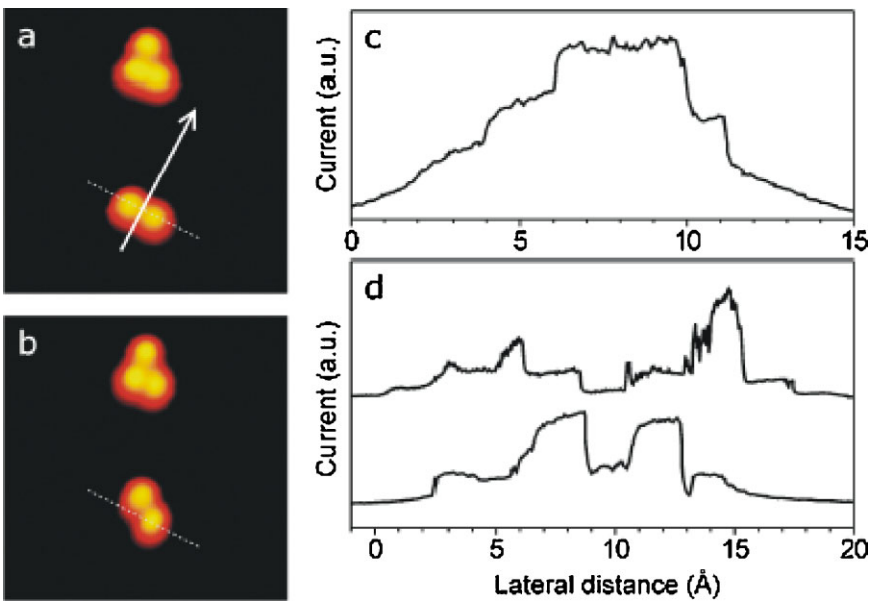

Figure 52 STM images (9 × 9 nm^2) before (a) and after (b) a rolling manipulation. The arrow marks the pathway of the tip apex during the manipulation and dashed lines indicate the initial position of the wheel-dimer molecule. (c and d) Tunnelling current signals during rolling manipulation: (c) rolling of only one wheel, (d) the rolling of one wheel is followed by the rolling of the second at different times. From Ref. [144].

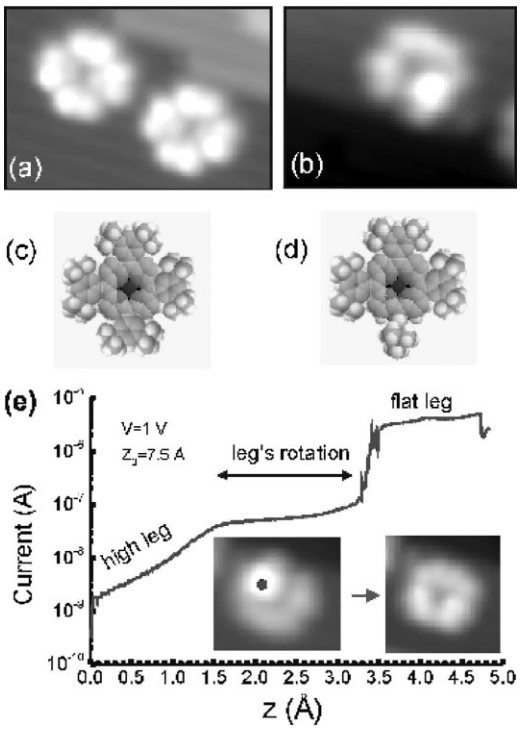

Figure 53 (a) STM image of a Cu-TBPP molecule on Cu(211) lying on the surface and oriented parallel to the intrinsic step edges. (b) STM image of a Cu-TBPP molecule on Cu(211) showing one leg rotated out of the porphyrin plane. (c and d): Sketch of the approximate molecular conformation for (a) and (b). (e) Current through a single leg versus the tip–surface distance during a vertical manipulation process leading to a leg's rotation. STM images of the molecule before and after the manipulation are shown in the inset. The black dot in the left image shows the exact position of the tip during the vertical manipulation (reprinted from Ref. [146], with permission from APS).

exhibit orders of magnitude different conductivities these experiments open a road to a molecular switch, in which a mechanical action causes switching from non-conducting to conducting behavior and vice versa [146].

5.2.9 Molecular shooting In manipulation experiments with atoms and most molecules the particle stays at the site on the surface, above which the tip is withdrawn from the manipulation distance to the (larger) imaging distance. In building artificial structures with single atoms and molecules this is a necessary prerequisite. It was therefore a surprise when Hla et al. [147] upon experimenting with sexi-phenyl ($C_{36}H_{36}$) molecules found that the molecules went beyond the point of tip withdrawal and moved on until they hit a step edge or some other obstacle at the surface. Hla used this property to build an artificial "nanogun" consisting of two parallel rows of Ag-atoms on a Ag(111) substrate. The different steps in the build-up of this artificial structure are shown in Fig. 54 [147].

Two sexi-phenyl molecules were then manipulated towards one end of the gun and two Ag-atoms towards the other end (Fig. 55a). One of the sexi-phenyl molecules was then fetched with the tip and manipulated to about one third of the length of the gun where the tip was withdrawn. The molecule continued to move in the straight standing wave potential until it hit the Cu-target atom at the other end. The Cu atom was enrolled by the molecule to form a metal atom–molecule complex (Fig. 55b). Remarkably, this complex showed the typical signature of pulling in the manipulation tip-height curves, whereas the molecule alone exhibited a more complex behavior, which allowed the conclusion that the shooting motion of the molecule could constitute the experimental verification of a molecular engine proposed theoretically by Porto et al. [148]: this

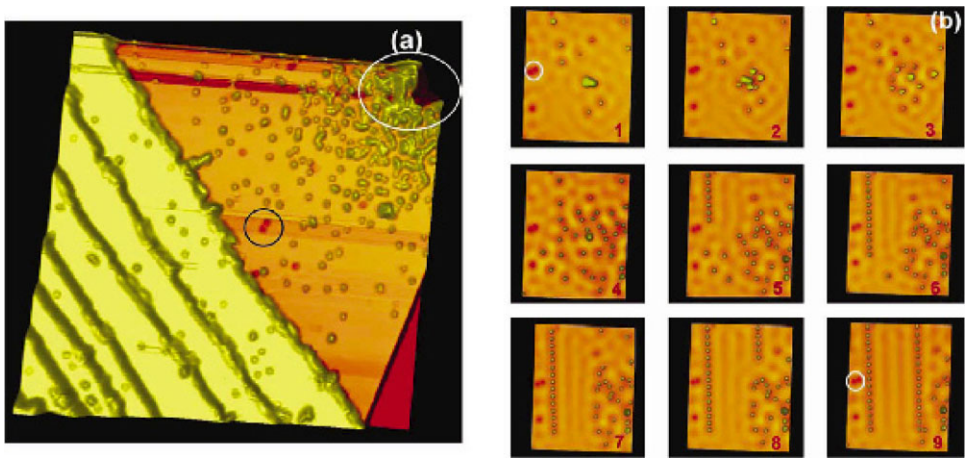

Figure 54 (a) For preparation of a suitable sharp and stable tip, the tip is gently dipped into the substrate leaving a hole (indicated by the ellipse) surrounded by many atoms and clusters. (b) One of the clusters is taken apart in an atom by atom manner and the two parallel rows of atoms are built up atom by atom near the surface defect indicated by the circle [147].

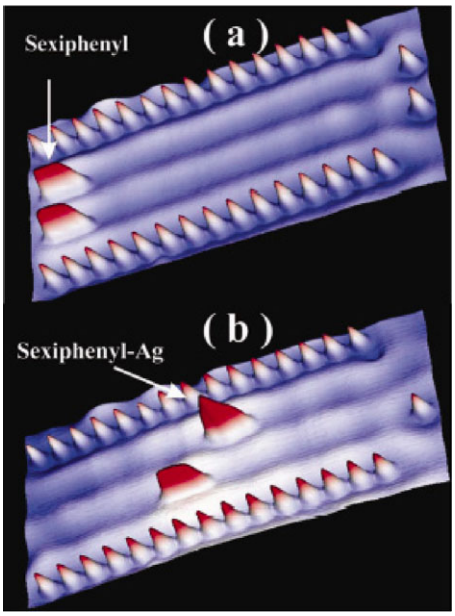

Figure 55 (a) Initial configuration of the "nanogun" with the sexi-phenyl bullets and the Ag-atom targets at the opposite ends of the gun. (b) The Ag-atom-sexi-phenyl complex has been manipulated to the middle of the gun for comparison with the sexi-phenyl molecule. From the different manipulation behavior of molecule and atom-molecule-complex important conclusions could be drawn on the origin of the molecular "shooting" process [147].

engine consists basically of two parts, a supporting carrier and a moving object. Directional motion of the engine is based on the dynamical competition between the two intrinsic lengths of carrier and object. This competition is used to transform potential energy initially fed into the movable object (in the experimental case by the tip) into the directed motion. Porto et al. demonstrated this process on a linear chain consisting of three particles whereby the distance between the first and the second is initially changed by an external force, whereas in the sexi-phenyl case probably a twist between neighboring phenyl groups causes the prolonged motion.

5.2.10 Transition from force to field effects upon manipulating the legs of a molecule Pairs of legs of the Lander molecule ($C_{94}H_{98}$) can be "switched" from one stable configuration to another by vertically approaching the STM tip, thus bringing the molecule from the so-called parallel to the crossed legs conformation (as shown in Fig. 56a and b) [105]. This procedure turns out to be highly reproducible as it can be repeated on the same molecule many (>100) times, due to the particular adsorption configuration of the molecule, lifting up the central board [149]. Consequently, the manipulation is highly reliable with a rate of success of more than 99%. All four possible molecular conformations are achieved (Fig. 56a–e, bottom).

This extraordinary precision in molecular manipulation allows studying the underlying forces in detail with one and the same molecule. This is an important prerequisite for such studies, because the potential barriers, and therefore manipulation parameters, usually differ for each single molecule due to the local atomic environment. Analyses of many equivalent manipulation processes revealed that the tip height, at which the manipulation process occurs during the approach, is crucial for the conformational change. On the other hand, the applied bias voltage plays an important role, as typically a certain voltage threshold has to be overcome. Figure 57a shows that the threshold voltage changes with

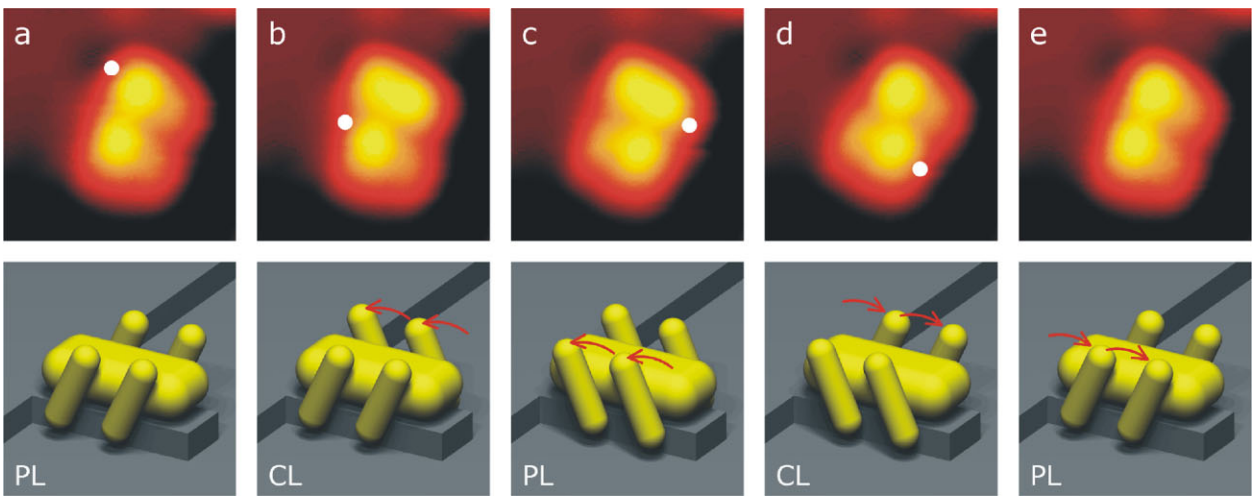

Figure 56 Series of STM images (upper panel), bringing one and the same reactive Lander molecule in all four possible conformations (two with parallel and two with crossed legs) by vertically approaching the tip. The lower panel shows schemes of the corresponding conformations (PL = parallel legs; CL = crossed legs). The lateral tip position of the subsequent manipulation is marked in the STM images by a white dot and the achieved conformational changes are indicated in the schemes by arrows. From Ref. [105].

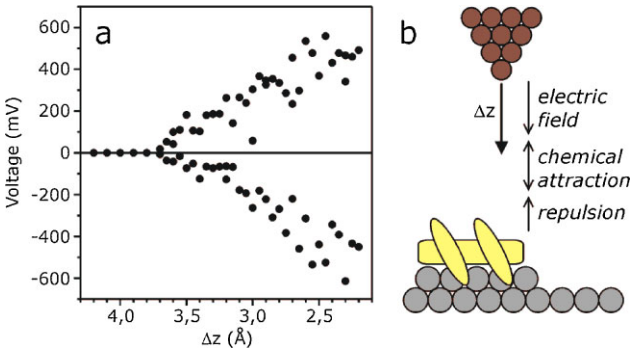

Figure 57 (a) Threshold voltage as a function of the vertical tip approach Δz of the manipulation process (for the conformational change from parallel to crossed legs for one and the same molecule). (b) Scheme of the three observed regimes of interatomic forces (at different tip heights) (after Ref. [105], courtesy of L. Grill).

the tip height: when approaching the tip (i.e., increasing Δz), the necessary threshold voltage decreases approximately linearly, which proves that the process is driven by the electric field in the junction. If the tip is sufficiently close ($\Delta z > 0.37$ nm), no bias voltage is required and the legs rotate due to the attractive chemical forces, while at very small tip heights the regime of repulsive forces is reached [105]. Hence, it is possible to explore different regimes of interactions during molecular manipulation with the STM tip, as shown schematically in Fig. 57b.

5.2.11 Further reading for lateral manipulation

In an early work, lateral manipulation was used for separation of a racemic mixture of two-dimensional molecular clusters [150], which themselves were consisting of prochiral molecules [151].

Some earlier review of lateral manipulation exist [152–154]. A more recent review on intramolecular STM manipulation by directional forces is given in [155]. While lateral displacement of single molecules is a well-established technique, only recently the manipulation of supramolecular rings could be shown where small molecular networks, each consisting of exactly six azobenzene derivatives due to the specific intermolecular linkers, are laterally displaced as a whole on the surface without any damage to the assembly [156]. Within crossed azobenzene dimers the individual molecules can be moved between specific orientations realising a molecular-level machine [157].

With the STM tip it is not only possible to manipulate single atoms or molecules, but also NaCl islands, which can also be bent and broken, thus yielding much information on the elastic properties of such nanometer-"cantilevers" so that they can be predicted now with relatively simple models [158]. Furthermore, it could be shown that the STM tip can not only be used to assemble structures, but also to disrupt supramolecular assemblies of "nano-trains" to obtain information on the kind of intermolecular linking via metal-ligand bonds [159].

6 Vertical manipulation

6.1 Vertical manipulation with particle transfer to the tip

Vertical manipulation is the deliberate pick-up of a particle initially sitting on a surface to the apex of the tip. Imaging can be performed with the so modified (or functionalized) tip and the particle can finally again be put down on the surface. Vertical transfer was first reported by Eigler's group [160], who demonstrated an "atomic switch" by transferring repeatedly a Xe atom from a Ni(110) surface to the tip and vice versa. Figure 58 shows switching behavior in a current versus time curve with the tip residing above the adsite of the Xe atom and STM pictures with the Xe atom initially at the surface, the same site then imaged with the Xe at the tip and finally the Xe atom transferred back to the surface again.

Another way to prove successful transfer of an adsorbate to the tip was shown for Xe [120]: a Xe atom was picked up to the tip apex and the Xe functionalized tip was used for imaging the same area as before with the bare tip (Fig. 59). The improved resolution proved that the single Xe atom "sharpens" the tip. Theoretical attempts to describe the vertical manipulation mechanism of Xe atoms can be found in Refs. [161–163] as well as other atoms [164, 165]. They claim that mainly force effects are responsible for the vertical transfer, but that also current and polarity effects can have an influence.

The vertical transfer of single CO molecules from Cu-surfaces to the tip was investigated in detail by Bartels et al. [102]. This manipulation procedure is interesting, as it is well-known that CO stands upright on metal surfaces

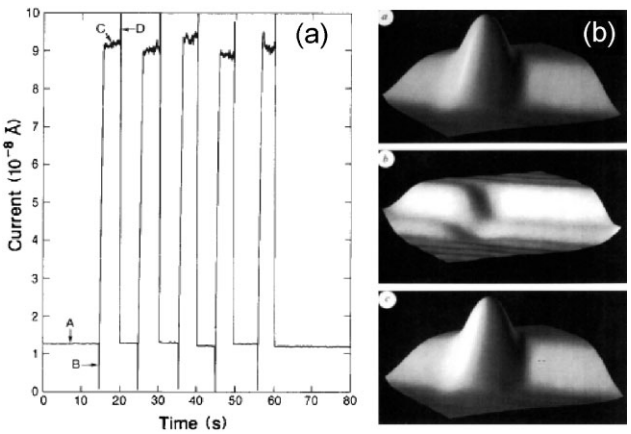

Figure 58 Switching behavior of Xe on Ni(110) surface. (a) Time dependence of the current through the Xe switch operation. A: low conductance state with Xe at surface. B: Current spike due to application of a short positive pulse to the tip causing transfer of the atom to the tip (high conductance state C). D: Current spike due to short negative pulse causing Xe to go back to the surface so that state A is regained. (b) 2.5 × 2.5 nm^2 STM images showing the Xe atom residing at a kink site of the surface (state A, top), the same site with Xe at the tip (state C, center), and the Xe atom back on surface again (bottom) (after Eigler et al. [160]).

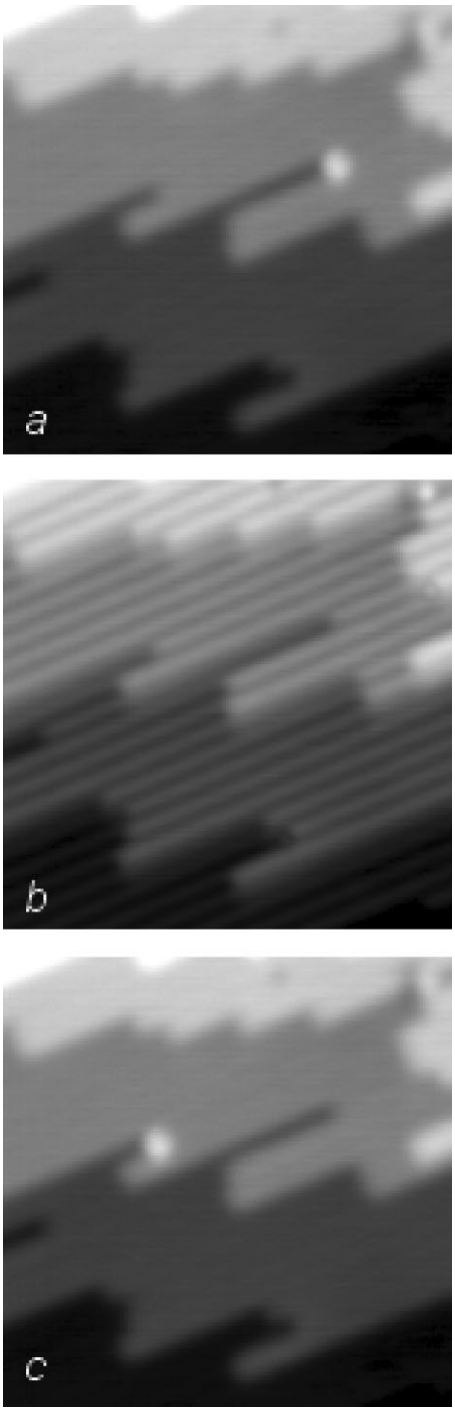

Figure 59 Vertical manipulation of Xe on Cu(211). (a) A single Xe atom is visible as a bright protrusion. (b) The Xe atom has been picked up with the tip and the STM picture is taken with the Xe atom on the tip apex. Notice that the surface is now imaged with an improved resolution. (c) The Xe atom has been released back to another point at the surface and the imaging is back to the initial resolution (after Ref. [120]).

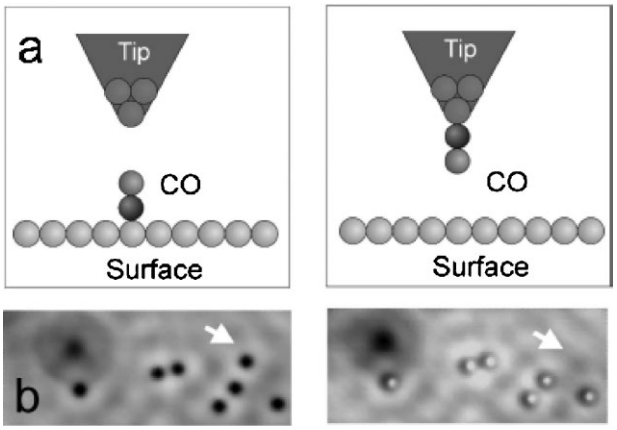

Figure 60 Vertical manipulation of CO on Cu(111). (a) Upon pick up of a CO molecule to the tip the molecule has to turn around to maintain bonding to the metal with the C-end. (b) The CO molecule indicated by the white arrow is transferred to the tip. Imaging the same surface area with the CO functionalised tip changes the CO depressions into protrusions whereas the O-atom also imaged as a hole retains its appearance (after Bartels et al. [102]).

with the carbon atom binding to the substrate [166]. Upon transfer to the tip, the molecule has consequently to turn around (Fig. 60a). A reliable experimental procedure for transferring single CO-molecules to the tip apex and back to a Cu-surface was found to require ramping of the tunnelling voltage and simultaneous decrease of the tip–CO distance [102]. While the vertical transfer of a Xe atom at higher voltages is attributed to a polarizing effect of the electric field, the investigation of the transfer of CO yielded the following picture: by voltage ramping it was found that a minimum tunnelling bias of 2.4 eV is required to populate the CO $2\pi^*$ level. As the CO hopping rate depends linearly on the tunnelling current, a one electron process is responsible for the excitation. Although only 0.5% of the tunnelling current pass through the $2\pi^*$ orbital and the lifetime of the electrons in this anti-bonding level is only of the order of femtoseconds, the continuous supply of tunnelling electrons eventually causes the release of the CO from the surface. The approach of the tip in the pickup procedure just increases the probability that the molecule is "caught" at or near the tip apex upon desorption [167].

An advantageous by-product of the ability to deliberately transfer CO to the tip is demonstrated in Fig. 60b. As one can see, all species imaged with a clean metal tip appear as depressions. When a CO-molecule (denoted in this case by the white arrow) is transferred to the tip apex, all CO molecules change their appearance to protrusions (Fig. 60b, left), whereas the oxygen atom in the upper left part of Figs. 60b, right retains its appearance [102]. In this way, chemical contrast upon imaging with the STM is achieved, a phenomenon, which is considered extremely useful for the analytical abilities of the STM. The dependence of STM

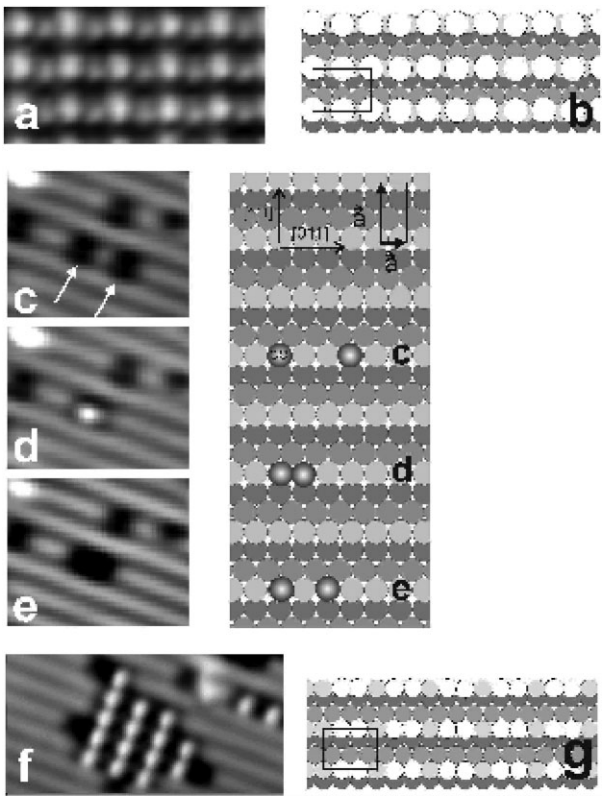

Figure 61 (a) STM image of a regular adlayer of CO on Cu(211) with (3 × 1) periodicity. The coverage is 2/3 of a monolayer. (b) Naive model of the (3 × 1) structure. The CO molecules occupy on-top and bridge sites. (c–e) STM images and corresponding sphere models of the manipulation of two CO molecules to shortest lateral distance and apart again. Notice that a dramatic change in the appearance of the two CO molecules occurs when their mutual distance changes. (f) Local CO (3 × 1) domain formed by lateral manipulation. (g) Correct model of the CO (3 × 1) structure (reprinted from Ref. [168], with permission from NH-Elsevier).

images on parameters like the chemical constitution of the tip or the density of adsorbed species on the surface is, however, still a puzzling problem, as can be realized from Fig. 61 [168]. Figure 61a shows a regular adlayer of CO on Cu(211) with (3 × 1) periodicity. With the knowledge that the coverage is 2/3 of a monolayer, a structural model like the one illustrated in Fig. 61b, where CO molecules occupy on-top and bridge sites thus maximizing their mutual distance, appears plausible. Figure 61c–e show, however, that laterally manipulating together two CO molecules into adjacent on-top sites changes the image from two minima into one maximum located between the two on-top sites. Thus, upon formation of a CO-"dimer," a dramatic change in the appearance of the two CO molecules has occurred (Fig. 61d). By separating the two CO molecules their appearance changes to the initial shape (Fig. 61e). Using the lateral manipulation technique also an extended domain of the (3 × 1) structure was formed (Fig. 61f), which lead to the conclusion that the model depicted in Fig. 61g is the proper one and has to replace that of Fig. 61b. Progress in the theoretical description of these phenomena in STM imaging can be found in Refs. [43, 169].

Figures 59 and 60 have already shown that functionalising the tip by vertical manipulation can improve or even change the contrast in STM images. In their work on NaCl films on metal substrates Repp et al. [170] were able to image the HOMO and LUMO of the pentacene molecule (see the molecular model in the lowest part of Fig. 62, right) lying on such a film. The left part of Fig. 62 shows STS data, from which the energetic location of the frontier orbitals are deduced. With d*I*/d*V* mapping at these energies, respectively, the HOMO and the LUMO can be imaged, whereas at energies within the gap only the coarse elongated form of the pentacene is visible (Fig. 62, right part, top: metal tip). The HOMO and LUMO pictures become even more pronounced and clear, when a pentacene molecule is picked

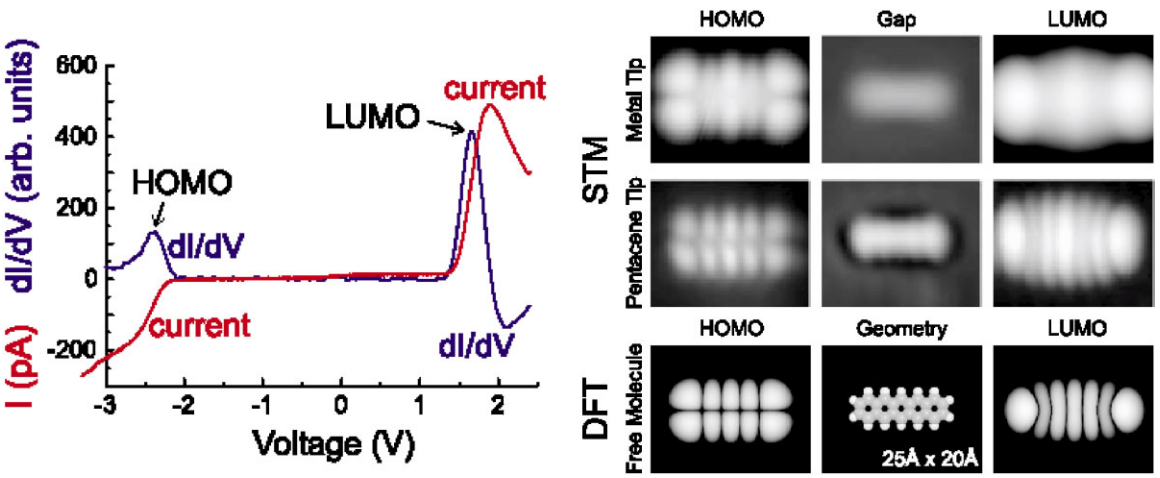

Figure 62 Effect of vertical uptake of a pentacene molecule on the imaging of the HOMO and LUMO of pentacene molecule physisorbed on a 2 ML NaCl film on Cu(100). Notice that the details of the orbitals are much more pronounced than with a pure metal tip (after Repp et al. [170]).

up to the tip and the STS-imaging is done with the so functionalized tip (Fig. 62, right part, middle: pentacene tip). The STM data compare extremely well with the shapes of the orbitals obtained by DFT calculation (Fig. 62, right part, bottom).

6.2 Vertical manipulation forming a wire The conductance of a single molecular wire between STM tip and surface was determined by a very new manipulation procedure, pulling up the molecular wire off the surface. In this way, the conductance was derived for the first time as a continuous function of the wire length, thus allowing to determine the important decay length that is fundamental for charge transport in molecules [171]. Similar experiments, but with very short molecules, were done by the Tautz group [172, 173] while Gaub and co-workers [174, 175] picked up long biologically relevant chains in a more random process. Moreover, single molecular wires could be pulled up by STM manipulation from a metal surface onto NaCl islands on the same surface, thus realizing very interesting configurations where one end of the molecule lies on the metal while the other is adsorbed on the insulating sodium chloride film [176]. Very recent work concerns the determination of the conductance of graphene nanoribbons and the first correlation of the charge transport properties of a single molecular wire with its electronic structure [177]. It could be proven that the conductance strongly improves as soon as the electron energy matches the energetic position of the molecular orbitals, even leading to ballistic transport.

7 Manipulation employing the electron current

The STM has the capability to induce reactions of single adsorbed molecules via vibrational excitation of the molecules above the potential energy barrier by inelastically tunnelling electrons. Inelastic effects were successfully used to induce bond-breaking processes at the single molecule level such as diffusion, rotation, desorption, dissociation, complete reactions, and reversible processes. The underlying physics is distinctly different from the mechanical manipulation employing tip–adsorbate forces discussed in the previous sections.

When a current flows through a system, where vibrations are possible, inelastic effects take place. In STM, when an electron tunnels through an adsorbate, inelastic electron scattering may induce elementary electronic, vibrational, or vibronic (=*vibr*ational and electr*onic*) excitations of the adsorbate (see Fig. 63a). The inelastic electrons, which represent a small fraction of the tunnelling current, transfer energy from the electrons to the adsorbate. The energy stored in the vibrational excitation of the molecule is transferred to the reaction coordinate modes corresponding to the relevant nuclear motions and chemical reactions; eventually triggering chemical transformation on the nanoscale.

Based on the electron energy, the molecular reactions induced by STM electrons can be separated into the field emission and the IET regime. High electron energies (above the work function of the metal) are used in the field emission regime (Fowler–Nordheim tunnelling), where the tip acts as an electron emission gun. These manipulations are not molecule specific and will not be further discussed (see Section 7.4 for some references). Reactions involving the IET process use low STM bias voltages to achieve more control and a much higher spatial resolution.

IET might be based on two different excitations depending on the applied bias voltage. At high voltages an electron may transiently occupy an electronic orbital of the adsorbate; at low voltages vibrational modes may be excited. Most often electronic excitations were found to be operative on semiconductors, while on metals vibrational excitations were found to be operative.

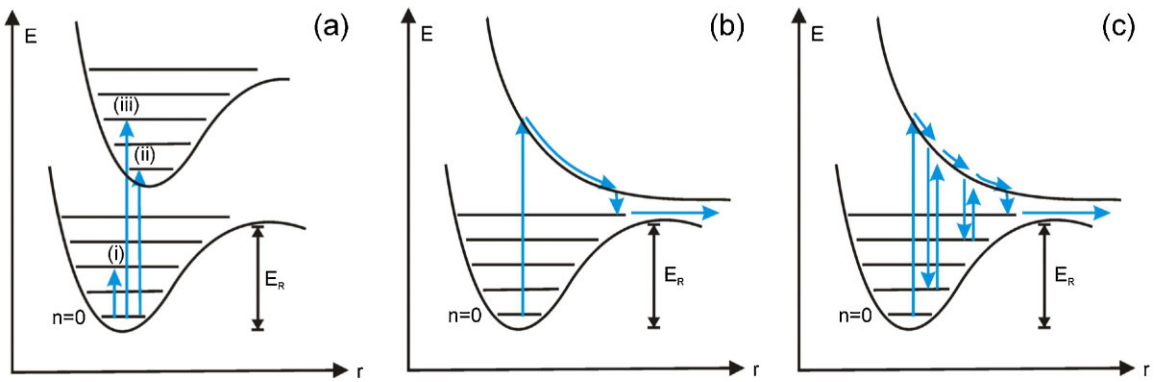

Figure 63 (a) Schematics of elementary excitations: (i) vibrational, (ii) electronic, and (iii) vibronic excitation. (b) Schematics of DIET process: electronic transition onto repulsive state is followed by evolution along the reaction coordinate that lasts long enough so that the back transition leads to a vibrational state above the reaction energy barrier. (c) Schematics of DIMET process: transition back leads to a vibrational excited state below the energy for reaction; a second electronic transition occurs during the lifetime of the vibrationally excited state; this cycle is repeated till a vibrational state above the reaction energy barrier is reached. All transitions are assumed to be Franck–Condon like, i.e., there is no evolution along the reaction coordinate r during the transition as indicated by the arrows that are in parallel to the energy axis.

At voltages below electronic resonances, vibrations can be excited directly, as soon as the energy of the tunnelling electrons exceeds the vibrational energy. The internal energy distribution of the adsorbate can be perturbed far away from the initial equilibrium by successive electron scattering. Such a vibrational heating by tunnelling electrons enhances substantially the probability for the adsorbate to pass the reaction barrier. The successive increase in vibrational energy deposited in adsorbates is similar to excitation in DIMET (dynamics induced by multiple electronic excitations, see Fig. 63c) induced by femtosecond laser excitation.

The ultimate spatial resolution of the STM down to 100 pm enables local excitations to be performed even at specific sites within a molecule. The exciting electrons are localized in space essentially with the same spatial resolution that defines the STMs atomic resolution imaging properties. Sub-molecular chemistry is achieved by confining the initial excitation to a specific chemical bond either by injecting the electrons above that bond or by tuning the energy of the tunnelling electrons to the bond's energy. The spatial resolution of the molecular excitation is limited by the localization of the electronic states inside the molecule. However, the surface-enhanced coupling between vibrational modes of the adsorbate facilitates the quick redistribution of the vibrational energy and limits localization to a specific reaction coordinate.

The unmatched advantage of IET manipulation is access to intrinsic properties of individual molecules and environmental effects that cannot be probed in an ensemble of molecules. For example, the molecular reaction yield is very sensitive to the adsorption site and the number and type of surrounding molecules. The STM enables to determine precisely the position of the molecules with respect to other molecules or defects before manipulation. Correlating the reaction yield to this information leads to an understanding of properties and chemistry of molecules at the ultimate spatial limit. Consequently, IET induced manipulation has opened a new world of chemical control.

7.1 Experimental aspects In STM, electrons with high enough energies can tunnel inelastically through an adsorbed molecule (Fig. 64a) either by excitation of a vibrational level at lower energy or through an electronic level at higher energy (symbolized by $\hbar\omega$ and E_{LUMO} in Fig. 64a). The inelastically tunnelling electrons deposit energy into the molecule.

The STM tip can be considered as an electron source with high local electron current density. A typical tunnelling current of $I = 1$ nA leads to current densities up to 10^{10} A m^{-2}. Such current densities are difficult to realize with conventional electron sources. Despite the large current densities, current induced substrate heating is expected to be small because of the small injection area down to a single molecule. The electron density up to 10^{12} e^{-} s^{-1} through an area of less than one nm^2 can be used to promote multiple vibrational excitations. Using a STM tip as a source of electrons furthermore facilitates to localize the region of impact within a molecule. In contrast to conventional electron sources the electrons can also be injected below the vacuum level and close to the Fermi level.

Experimentally (see Fig. 64b), the IET reaction is realized by positioning the STM tip above the location of the molecular bond at a fixed height. There the feedback loop is switched off and tunnelling current and/or voltage are increased from imaging to manipulation parameters. The electrons can be injected either from the tip or from the substrate depending on bias polarity. The moment of reaction is determined by monitoring the tunnelling current in time. At the beginning of the manipulation the tunnelling current has a value that corresponds to

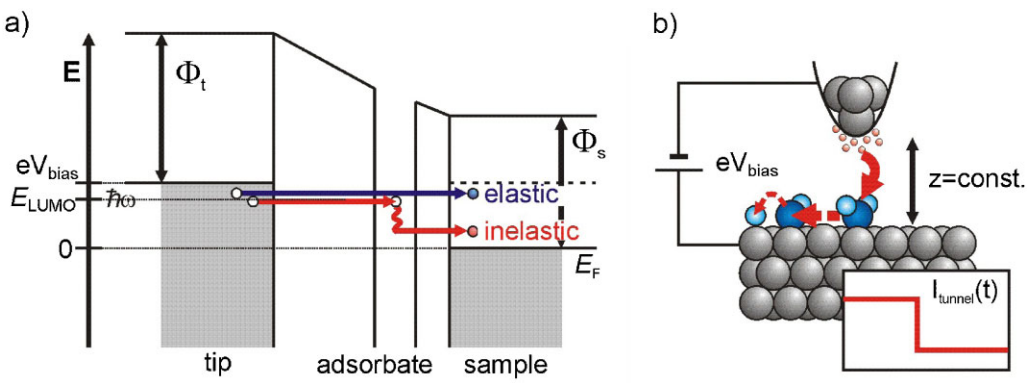

Figure 64 (a) Energetic schematics during tunnelling through a molecule: the vast majority of the electrons will follow the blue path and conserve energy during tunnelling. However, some electrons might loose an energy quantum of $\hbar\omega$ typical for a vibrational excitation within the molecule. (b) Schematics of manipulation procedure: the tip is placed above the molecule with feedback loop switched off. The excited molecule transforms the vibrational energy gained through inelastically tunnelling electrons into motion. The recorded current shows a sudden drop upon motion of the molecule.

the electronic structure (apparent height) of the adsorbed molecule. A sudden change in current is indicative of the success of the manipulation. These sudden changes are caused by changes in the apparent height of the molecule either through nuclear motion or through modification of the electronic structure. They are associated with the moment of reaction with a time resolution of the STM clock (typically several tens of microseconds) and thus allow determining the reaction yield. The success of a manipulation is verified by rescanning the surface with imaging (i.e., non-manipulative) parameters.

The yield of these processes is typically of the order of $10^{-8}/e^{-}$. The reason for the low yield is twofold: first, the number of inelastically tunnelling electrons is small as already seen in vibrational spectroscopy. Second, additional decay channels compete with the transformation of the energy into a reaction coordinate, e.g., decay via phonons, photons, or excitons.

To illustrate the schematics shown in Fig. 64b, we give an example for diffusion of small clusters of heavy water adsorbed on Ag(111) (Fig. 65). This example constitutes one of the many processes induced by IET in water systems including the diffusion of single molecules [178], the reorganization of hydrogen bonds within water clusters [58, 179], the cleavage of hydrogen bonds, and the dissociation of water molecules within clusters [180].

The STM image in Fig. 65a, taken with tunnelling parameters of 71 mV and 12 pA, shows four clusters of heavy water. Such images are used to identify those molecules or clusters that are interesting for manipulation. For the manipulation the STM tip is moved above the cluster in the middle of the image, here indicated by a white cross. After positioning the tip, the bias voltage is increased to 150 mV and the tip height is adjusted to obtain a preset tunnelling current of 30 pA. Then, the feedback loop is switched off. Current and voltage are applied for 800 ms. During this time the tunnelling current is recorded (Fig. 65b). After 530 and 700 ms, sharp drops are seen. After the manipulation the same area of the surface is imaged again (Fig. 65c). This image shows that the cluster moved away from the region under the tip by approximately 0.62 nm. The diffusion of the cluster that is imaged as a protrusion leads to the sudden drop in current at 530 ms (Fig. 65b). For other reactions, where the conductivity of the adsorbate increases, the reaction might also lead to a sharp rise in current. The second drop at 700 ms shows that the cluster moved twice within the 800 ms. As the total distance moved is approximately $2a$ ($a = 0.289$ nm on Ag(111)), it is reasonable to conclude that the cluster moved between equivalent adsorption geometries separated by one lattice spacing. From the time till the first diffusion event and the current between 25 and 30 nA we deduce that $\sim 10^9$ electrons are needed for inducing the first reaction. The second reaction needs only another $\sim 2 \times 10^8$ electrons. This difference demonstrates the statistical nature of the manipulation.

For manipulation experiments it is of utmost importance to ensure that the tip has not changed during the manipulation. In Fig. 65, the other clusters are imaged similarly in the two images and serve for this purpose.

For reactions other than diffusion, IETS (see Section 3.2) is a promising candidate for chemical analysis of the reaction product.

The repetition of an experiment as shown in Fig. 65 (typically hundreds to thousands of times) is used to quantify the reaction probability. The distribution of time intervals for inducing a specific reaction should be exponential, implying that the probability of the reaction per time unit is constant and does not depend on any previous history. For the example shown in Fig. 66a, such a distribution is indeed found. An initial increase is sometimes observed in such histograms and points towards two rate determining steps in the reaction.

The inverse of the time constant τ of the exponential decay of histograms as in Fig. 66a gives the reaction rate $R = 1/\tau$ at the chosen sample bias voltage and current. The reaction yield Y is determined from the time constant τ and the manipulation current I via: $Y = e/I\tau$.

Quantitative understanding of the reaction can be gained by determining the reaction rate for different bias

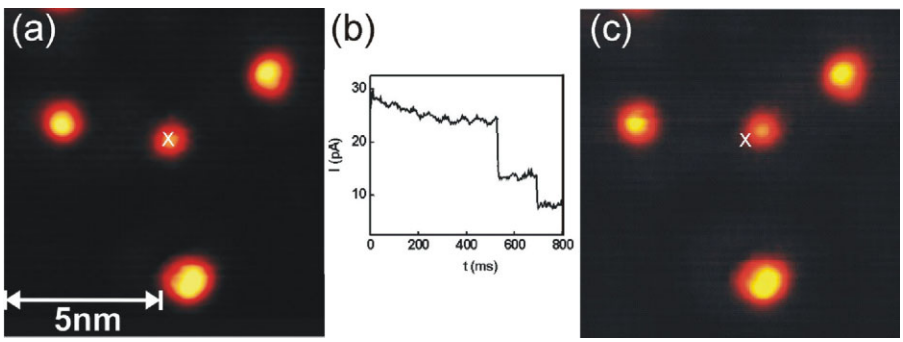

Figure 65 Induced diffusion of D_2O hexamer on Ag(111). Imaging parameters are 71 mV, 12 pA [58]: (a) before manipulation, (b) tunnelling current during manipulation, (c) after manipulation. During manipulation the tip was placed at the site of the cross and the bias was increased to 150 mV, the current to 30 pA, and held there for 800 ms.

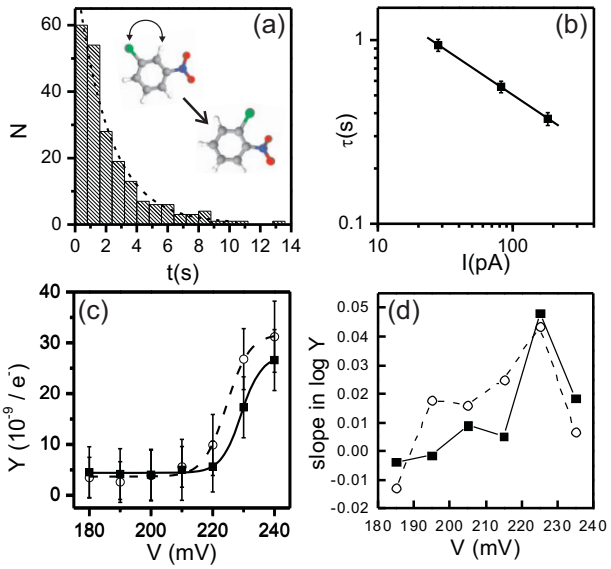

Figure 66 Determination of threshold and electron number for isomerization of chloronitrobenzene molecules [181]: (a) Histogram of times till reaction at fixed voltage and current. Exponential fit gives decay rate τ. Ball-and-stick models depict isomerization from *meta*- to *ortho*-chloronitrobenzene. (b) Doubly logarithmic display of decay rate τ versus current. Slope $n = 1$ corresponds to the number of electrons needed for the reaction. (c) Reaction yield Y versus voltage V. Lines are Boltzmann fits to the experimental data. (d) Slope of (c) for determination of threshold barrier. Lines serve to guide the eye. In (c) and (d) filled (open) symbols and solid (dashed) lines refer to isomerization from *meta* to *ortho* (*ortho* to *meta*) isomerization.

voltages and tunnelling currents. If the field effect is negligible, the dependence of the time constant τ or reaction rate R on current (Fig. 66b) at fixed bias voltage can be used to determine the number of electrons involved in the reaction because of the following reasoning: the temporary occupation of an adsorbate-induced resonance with a tunnelling electron corresponds to an electronically excited state of the molecule with a lifetime of a few femtoseconds. During this occupation, energy is transferred to the vibrational mode of the molecule. The current dependent vibrational excitation rate competes with a current independent vibrational relaxation rate resulting from coupling of the vibrations to substrate phonons and/or electronic excitations. If eV_{bias} is greater than the reaction barrier, the barrier can be overcome in one excitation event. This single step process will dominate over multiple step processes when the relaxation rate of the reaction mode is much larger than the maximum electron tunnelling rate leading to a linear dependence of the reaction rate on current. Note that sometimes the yield is displayed. For a single-electron process the yield is independent of current ($Y \propto R/I$). If eV_{bias} is smaller than the barrier to reaction, one excitation is not sufficient to overcome the reaction barrier. At least a second excitation is needed during the lifetime of the first excitation that promote(s) the molecule to a higher quantum state of the vibrational mode. Because of the usually short lifetimes of vibrational states, the reaction rate is dominated by excitation processes that follow the path with the least number of intermediate states that are needed. The overall reaction rate for an n electron process is proportional to the current to the power of n: $R \propto I^n$.

In the case shown in Fig. 66b, the slope is $n \approx 1$. This linear dependence of the reaction rate on current indicates a reaction mechanism involving the inelastic tunnelling of a single electron.

Measuring the reaction yield as a function of bias voltage at fixed tunnelling current (Fig. 66c) allows determining the energy threshold of the excitation. However, the dependence of reaction yield on bias voltage could also reflect a dependence on the changing electric field, which in turn depends on the separation between the tip and the sample, which decreases at low voltages. In contrast, the field does not vary significantly with tunnelling current because the separation depends only logarithmically on current.

After having ensured that the effect is not field induced, threshold voltages are determined (Fig. 66c). A first idea of the region of the threshold can be found by ramping the voltage above the molecule and recording the current. It should be noted, however, that the reaction happens statistically and the position of sudden change in current depends on the slope of the ramp. Thus, the voltage should be set to a fixed value within the region of the threshold. The reaction yield is then determined for this particular energy and current from sudden drops in the I–t curve and displayed versus V.

Theory (see Section 7.2) showed that the inflection point of the rise in yield in the Y–V dependence corresponds to $\hbar\omega$, the energy of the vibrational mode. More precisely, the threshold voltage should be assigned to the maximum in $\mathrm{d}(\log y)/\mathrm{d}V$. The correct procedure is to display $\log Y$ versus V and to determine the slope between adjacent measurement points. Maxima in this slope displayed versus the (mean) voltage (Fig. 66d) correspond to the threshold of the reaction. As shown in the example, multiple thresholds (here the lower lying at $\sim$200 mV) might remain undiscovered in the simple Y versus V graph. The shorter the lifetime, the sharper is the resonance at the threshold energy. This implies that the width of the maximum should be related to the lifetime of the electrons [182], but is in most experiments so far rather determined by the experimental separation between voltage set points.

Next, thresholds determined in this way for both polarities are compared. An asymmetry of the reaction threshold with respect to polarity is an indication for an electronic mechanism, i.e., an excited electronic state of the molecule surface system is formed, which couples strongly to the nuclear motion of the molecule. A symmetric threshold points to a vibrational excitation. The two usually

differ also in energy, the former lying in the range of *eV*, while the latter is in the range of tens to hundreds of meV. In both cases, the rates of reactions are usually lower (by a certain factor) at negative bias than at positive bias. An intriguing explanation for this phenomenon is that the tunnelling probability decreases for an electron that has lost energy before tunnelling from the substrate to the tip. In the opposite direction, the electron has already tunnelled before it looses energy. Large variation in reaction yields were attributed to tip effects [183].

The influence of the electric field has mostly been neglected in the description of IET manipulation. However, recent results showed that for water clusters, i.e., molecules with a strong dipole moment, the outcome of the reaction is influenced by the presence of the electric field [179]. This influence could be used to force reactions that otherwise might not occur. Examples for IET manipulation are given in Section 7.3.

In principle, a spatial dependence of the reaction rate restricted to the extent of the molecule in a STM image suggests orbital specificity in the coupling of the tunnelling electron to the reaction of the molecule.

The inelastic electron transition rate depends on the position and width of the adsorbate resonance through which electrons tunnel. The yield of most processes investigated so far is in the range of 10^{-6} to 10^{-10} reactions per electron.

Increasing the yield could be achieved by electronic decoupling of the atom or molecule from the substrate, either by using a thin insulating layer, wide gap semiconductors, passivated semiconductor surfaces, or using physisorbed rather than chemisorbed species.

7.2 Theory of inelastic tunnelling electron manipulation At the moment different models that describe IET manipulation with different approaches and at different levels of sophistication coexist. The experimentally observed nonlinear dependence of the reaction yield on current as observed in many manipulation experiments was described within the model of vibrational heating by successive excitation of the substrate–adsorbate bond through multiple electron scattering processes (sequential heating scenario) [83, 184–186]. In order to model IET manipulation the same approximations as in IETS modeling were used (see Sections 3.2.2 and 3.2.3), i.e., the truncation of harmonic potential wells. Though this approach neglects intermode coupling due to anharmonicity and is far from quantitative, it provides some simple rules that differentiate between systems undergoing a single electron excitation or multiple electron excitations [83]. Another approach performs the correct nuclear dynamics while trying to have the best estimates for the actual potential that directs the evolution. On top of the treatment of the nuclear evolution, the electronic event is either assumed to take place instantaneously, and hence the description of the electronic excitation problem is absent, or treated within a single-molecular orbital model. This last model is that of a resonance in contact with the substrate's electronic structure. In this model electron vibration coupling is introduced by means of an effective resonance lifetime only [187–190]. These simulations give information about processes that are absent or cannot be described in the first type of approximation.

The electron–vibration coupling is usually a weak interaction that can be treated perturbatively, which is easily accomplished by using Green's functions. This approach has the advantage of including many-body effects.

The vibrational heating mechanism is in contrast to the usual picture for an electron-stimulated process, where an electron is absorbed resonantly into the adsorbate or excited by a Franck–Condon transition, initiating nuclear motion on the excited potential energy surface within the lifetime of the excited state (see Fig. 63). There, the adsorbate dynamics is triggered by a transient formation of negative ion states of the adsorbates. The electronically excited molecule–metal complex has a different equilibrium configuration than the ground state. Energy of the electron is transferred into energy of the nuclei during the lifetime of the electron within the molecule (1–10 fs). This energy transfer might be sufficient to lead to a reaction or to vibrational excitation of the adsorbate. In contrast, it has been proposed that the vibrational excitation in STM results from resonance coupling in non-resonant conditions (impact scattering) [45]. This is possible, because the resonances are broadened upon adsorption. The reaction mechanism results from the passing electron that leaves the molecule in a mixed excited state caused by the transient appearance of an extra charge in the system.

7.2.1 Different types of excitations Adsorbate reaction occurs when the relevant reaction coordinate mode is excited above the potential barrier. Three different types of excitations (see Fig. 67) have been treated theoretically to explain how an adsorbed molecule overcomes the reaction barrier following the excitation of a vibrational mode by tunnelling electrons, though more combinations exists. Direct excitation (a) and indirect excitation (b) are discriminated. For the former the excitation and the reaction coordinate are the same, while for the latter these two are different and anharmonically coupled.

For direct excitation (Fig. 67a), two different processes are discussed, coherent superposition of multiple-step excitation by a single electron (i) [83], and incoherent multiple-stepwise excitation (ii) also called stepwise vibrational ladder climbing [186].

For indirect excitation, the excitation could in principle be again incoherent or coherent and the reaction coordinate mode could be excited by a single anharmonic coupling directly above the reaction energy barrier or stepwise. However, mostly the former case is discussed, because for indirect excitation the energy for reaction is more efficiently pumped into the molecule via excitation of one single quantum of an internal coordinate rather than exciting directly several quanta of the reaction levels.

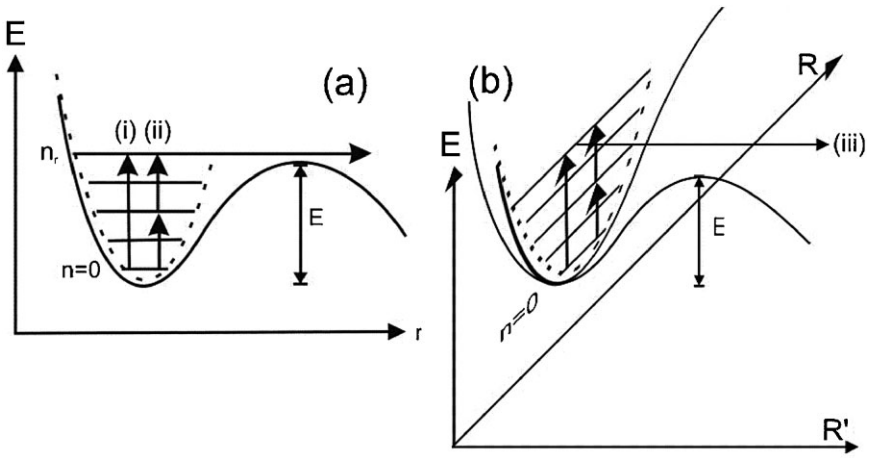

Figure 67 Harmonic potential with energy barrier E and n vibrational levels: (a) direct excitation along the reaction coordinate r; the barrier might be overcome by (i) coherent or (ii) incoherent stepwise excitation. (b) Indirect excitation along one coordinate R, but reaction in a different coordinate R'. The excited mode couples anharmonically to the reaction coordinate R', where the barrier for reaction lies below the vibrational energy. At low temperature the excess energy mainly goes to the electron–hole pair continuum that also efficiently dissipates energy localized in the vibration. The reaction coordinate differs for the different processes and might be, e.g., a distance on the surface for diffusion, the distance between atoms within a molecule for dissociation, or a bond angle for isomerization.

7.2.2 Coherent versus incoherent excitation If the electron energy lies above the potential barrier, the reaction barrier can be overcome in a single excitation event. This process is called coherent excitation and is similar to DIET (dynamics induced by electronic transitions, see Fig. 63b). Coherent excitation dominates at sufficiently low currents and sufficiently high relaxation rates. The vibrational excitation competes with the vibrational relaxation resulting from the energy dissipation to other molecular modes, substrate phonons, or electron–hole pair excitation in the adsorbate–metal system. At low temperature the vibrational relaxation results mainly from the electron–hole pair continuum that efficiently dissipates the energy localized in the vibration.

It is known from DIET processes that the dynamics rarely occurs when the system is in the excited electronic state, but rather it occurs after electronic relaxation when the system has acquired vibrational energy in its electronic ground state. Characteristic for the coherent mechanism is a linear dependence of the reaction rate on current.

If the energy of the tunnelling electrons is below the reaction barrier, several electrons are necessary to induce the reaction. A second electron can excite the molecule to a higher level, if the lifetime of the excited level is longer than the average time between inelastically tunnelling electrons. In the high current limit the tunnelling rate is more rapid than the vibrational relaxation rate. Then, IET results in a quasi-Boltzmann distribution of the vibrational relaxation corresponding to vibrational heating through a sequence of vibrational excitations. Substantial energy can thus be localized in the bond, which is then available for chemical reactions. The reaction is possible, only if the accumulated excitation energy exceeds the energy barrier. This implies that the barrier is overcome by a stepwise vibrational excitation of the bond, which in between the excitations does not return to its vibrational ground state. This is called incoherent multiple excitations (Fig. 63c) [83]. The model is closely related to the DIMET (dynamics induced by multiple electronic transitions) mechanism. In the incoherent mechanism the number of necessary electrons (or vibrational steps) determines the dependence of the reaction rate on current ($R \propto I^n$).

A key factor in distinguishing coherent from incoherent excitation is the vibrational relaxation rate γ with respect to the tunnelling current I. The coherent process dominates the incoherent one at low I, where the average time between successive tunnelling electrons is much longer than the vibrational relaxation time $\hbar/\gamma$. The incoherent process becomes dominant at higher currents. The two regimes are separated by

$$I_{\mathrm{sep}} \approx e\gamma \left(\frac{n!}{n-1} \right)^{1/(n-1)} \tag{29}$$

with n the number of levels in the ground state energy surface to be overcome.

The vibrational relaxation rate depends on the relative position of the resonance energy to the phonon energies of the substrate, which determines their coupling, or the formation of electron–hole pairs. For adsorbates on metals with the resonance state near the Fermi level, the vibrational lifetime is dominated by electron–hole-pair excitation and thus it is of the order of a few picoseconds. Tunnelling currents typically used in IET manipulation

are sub nA to 100 nA. If one assumes the inelastic tunnelling fraction of the order of 10^{-3}, the time between successive electrons is much larger than the relaxation rate. In contrast, for adsorbates on semiconductor surfaces, which have much longer lifetimes of the order of nanoseconds owing to the absence of electronic damping, the relaxation time is often longer than the time between successive electrons. There the condition for the stepwise ladder climbing via multiple incoherent vibrational excitations and vibrational heating by sequential inelastic scattering of tunnelling electrons is very common. For examples see Section 7.4.

7.2.3 Indirect excitation For the adsorbate on the surface the coupling between modes is greatly enhanced as compared to the gas phase because of the possibility to excite electron–hole pairs for energy conservation. Also the higher anharmonicity of the potential walls on the surfaces enhances coupling between different vibrational modes. These properties promote the third excitation type, an indirect excitation of the reaction coordinate mode. In indirect excitation, two vibrational modes are involved. One mode is excited, but does not promote a reaction and the other one, usually lower in energy, is not directly excited, but is the reaction coordinate mode. The tunnelling current excites the high-energy mode that decays by simultaneous excitation of the low-energy reaction coordinate mode and of electron–hole pairs for energy conservation. Anharmonic coupling between the modes is important for energy transfer from one mode to the other one. The reaction rate depends on various key parameters as inelastic tunnelling current fraction, bias voltage, vibrational frequency, vibrational excitation probability, vibrational relaxation rate, anharmonic intermode coupling strength, and potential barrier height (see Section 7.2.4.2).

7.2.4 Theoretical models The models to explain the measured dependencies of the reaction rate on current and voltage in IET manipulation are similar to those used to explain femtosecond laser induced surface chemistry. In order to achieve quantitative modeling of the IET manipulation, an accurate knowledge of the electronic structure of the molecules, condensed matter interaction, electron–vibration coupling, and total energies are needed.

Inelastic molecule manipulation relies on very subtle effects, such as vibrational excitation that in addition are typically quantum mechanical, demanding *ab initio* methods in order to obtain very accurate estimations of total energy, forces, and electron–vibration couplings.

7.2.4.1 Direct excitation When a molecule is adsorbed onto a metal, interaction broadens the adsorbate levels into resonances. A tunnelling electron can induce vibrations in the adsorbate through such an electronic resonance state of the adsorbate. The adsorbate induced resonance is modelled by a single orbital, which is assumed to have a Lorentzian shape with energy E_a (Fig. 68) that interacts with two

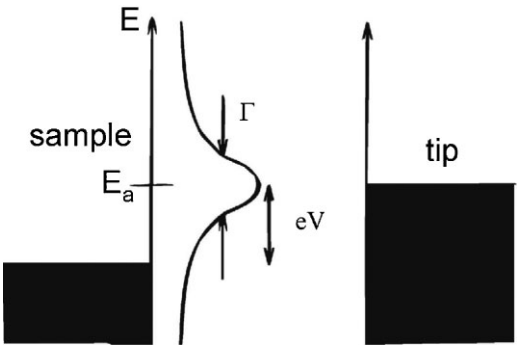

Figure 68 Schematics of energies for IET manipulation theory: adsorbate resonance at E_a above the Fermi energy E_F of width Γ. V is the applied bias voltage between tip and sample.

continuous electron levels of tip and sample. Its width $\Gamma = \Gamma_s + \Gamma_t$ resulting from broadening through the tip (t) and the sample (s) is dominated by the sample broadening (Γ_s). For a negative ion resonance above the Fermi level the occupancy is $n_a \ll 1$, while for a positive ion resonance well below the Fermi level the occupancy is $1 - n_a \ll 1$.

The STM-IET theory of vibrational heating [191] uses a truncated oscillator model, i.e., the ground-state potential energy surface for the adsorbate is modelled through a harmonic potential wall with n vibrational levels (see Fig. 67, dashed line) and the continuum of levels above the barrier is represented by discrete levels. In this theory [192], a relation between inelastic tunnelling current and vibrational heating, i.e., the effective vibrational temperature because of vibrational excitation by tunnelling currents, is calculated using the Keldysh–Green's function method for an adsorbate induced resonance model of IET. Using a standard Keldysh's diagram technique a stationary non-equilibrium vibrational distribution functions is obtained from the Fourier transform of the vibrational number operator. From the distribution function a general formula of the vibrational heating by IET is derived.

7.2.4.1.1 Incoherent excitation First, the incoherent single step-by-step ladder climbing process for a vibration with energy $\hbar\Omega$ is described. A Pauli master equation for P_m, the probability of finding the reaction coordinate mode in its mth excited state at time t, is given by [193]

$$\frac{dP_m}{dt} = (m+1)\Gamma_{\downarrow}P_{m+1} + m\Gamma_{\uparrow}P_{m-1} - \left[m\Gamma_{\downarrow} + (m+1)\Gamma_{\uparrow}\right]P_m \quad . \tag{30}$$

The Γs describe the excitation (deexcitation) rate between the vibrational states in the presence of IET current I_{inel} and are given by:

$$\Gamma_{\downarrow} = [1 + n(\hbar\Omega, T)]\gamma + \frac{I_{inel}}{e}$$
$$\Gamma_{\uparrow} = n(\hbar\Omega, T)\gamma + \frac{I_{inel}}{e} \tag{31}$$

where $n(\hbar\Omega, T)$ is a Bose–Einstein distribution function with a sample temperature T, and $\gamma = \gamma_{eh} + \gamma_{ph}$ denotes the vibrational relaxation rate from electron–hole pair excitations γ_{eh} and from the energy transfer to the substrate phonons γ_{ph}. The second term I_{inel}/e in Eq. (31) can be related to the IET current-induced transition rate Γ_{in} between the vibrational ground state and the first excited state. Using the adsorbate-induced resonance model for STM-IETS [45], Gao et al. [186] obtained for $|eV| \gg \hbar\Omega \gg kT$

$$\Gamma_{in} = \frac{|eV|}{\hbar\Omega}\frac{\Delta_t}{\Delta_s}\gamma \tag{32}$$

where Δ_i is the partial width of the density of states of the adsorbate state from the interaction with the substrate (s) or the tip (t). In terms of the elastic tunnelling current I_{elas} Gao obtained [194]:

$$I_{elas} = \frac{e^2V}{\pi\hbar}\frac{\Delta_t\Delta_s}{(E_a - E_F)^2 + \Delta^2}, \quad \Delta = \Delta_t + \Delta_s \tag{33}$$

through the adsorbate-induced resonance located at E_a above the Fermi level E_F of the substrate. Combining Eqs. (32) and (33), one obtains:

$$\begin{aligned}\Gamma_{in} &= \frac{\pi\gamma}{\Omega}\frac{(E_a - E_F)^2 + \Delta^2}{\Delta_s^2}\frac{|I_{elas}|}{e} \\ &\approx \frac{\pi\gamma}{\Omega}\frac{(E_a - E_F)^2 + \Delta_s^2}{\Delta_s^2}\frac{|I_{elas}|}{e} \approx \frac{\pi\gamma}{\Omega}\frac{|I_{elas}|}{e} \\ &=: f_{in}\frac{|I_{elas}|}{e} = \frac{|I_{inel}|}{e}.\end{aligned} \tag{34}$$

Equation (34) is valid, because the broadening of the adsorbate resonance is in the STM geometry dominated by coupling to the substrate, i.e., $\Delta_s \gg \Delta_t$. At the usually employed low temperature, γ is determined by $\gamma_{eh} = 2\pi\Omega[\lambda\rho_a(E_F)]^2$ with λ the electron–vibration coupling. This relation means that in the limit of $|eV| \gg \hbar\Omega$ the vibrational transition rate is the same as the inelastic tunnelling current.

In the absence of IET for $|eV| < \hbar\Omega$, $\Gamma_\uparrow$ and $\Gamma_\downarrow$ are related by detailed balance $\Gamma_\downarrow = e^{-\hbar\Omega/kT}\Gamma_\uparrow$. Upon opening the inelastic tunnel channel, a non-equilibrium situation emerges. A theory of stochastic processes gives the steady state solution to the master equation as $P_m \sim (\Gamma_\uparrow/\Gamma_\downarrow)^m$ for the probability that the reaction coordinate is in its mth excited state.

The rate of reaction, R, is then determined by the quasi-static ionic population of the level $(n-1)$ times the excitation rate $\Gamma_\uparrow$ to the level n. Here, it is implicitly assumed that upon reaching the highest level n the molecular motion is induced, and the coupling to the surroundings does not quench the excited state before the molecule passes the top of the potential barrier. Using the Boltzmann distribution for the population of the $n-1$ level, the Arrhenius type law with the effective temperature is assumed for R via the stepwise vibrational ladder climbing in the potential well

$$R \cong n\Gamma_\uparrow \exp\left(-\frac{(n-1)\hbar\Omega}{kT_{eff}}\right), \tag{35}$$

where $(n-1)\hbar\Omega$ is supposed to be very close to the barrier height E (see Fig. 67) and T_{eff} is an effective vibrational temperature produced by the IET process based on the vibrational heating and higher than the sample temperature T. In the presence of an IET current, T_{eff} is given by Gao et al. [186]:

$$kT_{eff} = \frac{\hbar\Omega}{\ln\left(\frac{\Gamma_\downarrow}{\Gamma_\uparrow}\right)} \cong \frac{\hbar\Omega}{\ln\left(\frac{I_{inel}/e+\gamma}{I_{inel}/e+\gamma\exp(-\hbar\Omega/kT)}\right)}. \tag{36}$$

Equation (36) is used to introduce an effective Bose–Einstein distribution $n_{ph,T}(\omega)$ that gives the vibrational population in thermal equilibrium at the sample temperature T. The vibrational excitation by tunnelling electrons disturbs the thermal equilibrium and leads to a vibrational temperature that exceeds the substrate temperature. The modified distribution $n_{ph}(\omega)$ is:

$$n_{ph}(\omega) = n_{ph,T}(\omega) + \frac{\Gamma_{in}(\omega)}{\gamma(\omega)} \tag{37}$$

with $\Gamma_{in}(\omega) = I_{inel}/e$ the rate of vibrational excitation and $\gamma(\omega)$ the vibrational damping rate.

Depending on the magnitude of $\Gamma_{in}(\omega)/\gamma(\omega)$ relative to $n_{ph}(\omega)$ the reaction is thermally activated $\Gamma_{in}/\gamma \ll n_{ph}$, current activated $\Gamma_{in}/\gamma \gg n_{ph}$, or in the intermediate regime $\Gamma_{in}/\gamma \approx n_{ph}$. Thus, IET manipulation demands $\Gamma_{in}/\gamma \gg n_{ph}$. As IET manipulation experiments are usually performed at low temperature $n_{ph,T}(\omega) \ll 1$ is used.

This derivation clearly indicates that $I_{inel}/e\gamma$ is a key parameter for determining the heating of the vibrational system above the sample temperature, i.e., a larger vibrational population upon opening the IET process at $|eV| \geq \hbar\Omega$. For I_{inel}/e smaller than the vibrational damping rate of the order of 10^{12} s^{-1} on metal surfaces, the second term is much smaller than the first term and no significant vibrational heating can be expected. However, when I_{inel}/e is larger than the vibrational damping rate, the vibrational mode can be excited by the IET current and the vibrational population is not small even at low temperature. The population may deviate noticeably from a Bose–Einstein distribution. Such a high effective vibrational temperature and vibrational population play an important role not only in the vibrational ladder climbing but also in coherent multi-phonon excitations and de-excitations, even when the vibrational damping rate is faster than the inelastic tunnelling rate.

From Eqs. (36) and (37) the power law dependence of the rate at low temperature $\hbar\Omega \gg kT$ and for $\gamma \gg I_{inel}/e$ is

$$R = n\Gamma_{\uparrow}\left(\frac{\Gamma_{\uparrow}}{\Gamma_{\downarrow}}\right)^{n-1} = n\frac{(I_{\mathrm{inel}}/e + \gamma e^{-\hbar\Omega/kT})^n}{(I_{\mathrm{inel}}/e + \gamma)^{n-1}} \propto \frac{I_{\mathrm{inel}}^n}{\gamma^{n-1}}, \tag{38}$$

$\Gamma_{\uparrow}$ and $\Gamma_{\downarrow}$ are the excitation and deexcitation rate between vibrational levels, n is the number of vibrational levels that enables the reaction.

In the case of an anharmonic potential, n is replaced by $E_{\mathrm{B}}/\hbar\Omega$ [195]. The rate of a motion via incoherent multiple-stepwise ladder climbing is then characterized by the power law dependence of the inelastic tunnelling current, I_{inel} with n the number of the vibrational levels in the potential well. Note that the power law of the reaction rate results simply from the assumption of the Arrhenius-like law (see above). With $I_{\mathrm{inel}} = f_{\mathrm{in}}I_{\mathrm{t}}$, where f_{in} is the inelastic tunnelling fraction and $I_{\mathrm{t}} = I_{\mathrm{elas}} + I_{\mathrm{inel}}$ ($I_{\mathrm{elas}} \gg I_{\mathrm{inel}}$; I_{elas} is the elastic tunnel current) results

$$R \propto I_{\mathrm{t}}^n. \tag{39}$$

A noticeable deviation from this simple power law is expected for large I_{inel}/e, comparable to γ or for large tunnelling voltages V where I_{inel} is no longer linear in V. One should also keep in mind that the linear dependence of Γ_{in} on $|eV_{\mathrm{t}}|$ and consequently the simple power law dependence is not valid when V_{t} is too large for the assumption of the slowly varying density $\rho_{\mathrm{a}}(\varepsilon)$ over V to hold.

In conclusion, the power law dependence of the reaction rate on I for incoherent stepwise vibrational ladder climbing (multiple single-step excitations) is a direct consequence of the establishment of quasi-equilibrium distribution characterized by the effective temperature, T_{eff}, and the Boltzmann expression for the population in the vibrational level. The power n represents the number of vibrational levels in the potential well.

7.2.4.1.2 Coherent multiple vibrational excitations The possibility of overcoming a potential reaction barrier via coherent multiple vibrational excitations by a single tunnelling electron has been investigated by Salam et al. [83]. The coherent single multiple-step process takes the path with the smallest number of intermediate states including the virtual excitation. It does not necessarily go through a single step-by-step population of the intermediate levels, nor does it require a longer lifetime of the vibrational excited state compared to the average time of successive tunnelling electrons. Based on the model for desorption induced by electronic transition (DIET) and using the adsorbate-induced resonance model for electron tunnelling via adsorbates, the tunnelling current causing the excitation to the mth vibrational level is calculated. The simplest case is a single electron process, for which the electron energy eV is larger than the barrier for reaction E_{B}, which leads to $n = 1$. For $E_{\mathrm{B}} > eV > \hbar\Omega$ multiple excitation is required to climb above the potential barrier up the vibrational ladder with the single vibrational energy $\hbar\Omega$. The current that induces the excitation to the mth level is written as

$$I_m = \frac{4e\Delta_{\mathrm{s}}\Delta_{\mathrm{t}}}{\hbar\Delta}\int_{\varepsilon_F}^{\varepsilon_F+eV_{\mathrm{t}}} P_m(\varepsilon)\mathrm{d}\varepsilon. \tag{40}$$

$\Delta_{\mathrm{s,t}}(\varepsilon) = \pi\sum_{p,k}\left|V_{p(v)a}\right|^2\delta(\varepsilon - \varepsilon_{k,p})$ are the partial widths of the DOS of the adsorbate state because of interaction with the substrate s and tip t and $\Delta = \Delta_{\mathrm{s}} + \Delta_{\mathrm{t}}$, $P_m(\varepsilon)$ is the probability of the adsorbate to be in the mth excited vibration. If the potential well has n vibrational levels and if an electron can only induce the transition from the ground state to the mth level ($m < n$), then several electron processes are necessary to overcome the barrier. It is assumed that eV is larger than the multiple vibrational excitation of $m\hbar\Omega$ and that the energy of the resonance ε_a (E_{a} in Fig. 68) shifts linearly with the vibrational coordinate Q, i.e., $\varepsilon_a(Q) = \varepsilon_a + \varepsilon'_a Q$, $\varepsilon'_a = \partial\varepsilon_a(Q)/\partial Q$, and a truncated oscillator model for the ground state potential energy surface, $V_0(Q) = (1/2)m^*\Omega Q^2$ is used. In the case of a negative ion resonance created by a temporal occupation of tunnelling electrons, the excited state potential energy $V^*(Q)$ is given by a displaced version of $V_0(Q)$: $V^*(q) = V_0(Q) + \varepsilon'_a(q)$.

The probability, $P_m(\varepsilon)$, of finding a molecule in the mth vibrational state excited from the ground state by an electron scattering through the adsorbate-induced resonance with incident energy ε is given by

$$P_m(\varepsilon) = \frac{\Delta}{\pi}\left|\sum_{j=0}^{\infty}\frac{\langle m|j\rangle\langle j|0\rangle}{(\bar{\varepsilon}_a - \varepsilon) + j\hbar\Omega - i\Delta/2}\right|^2, \tag{41}$$

where $|j\rangle$ are vibrational states on $V^*(Q)$ and $\bar{\varepsilon}_a = \varepsilon_a - \varepsilon_a'^2/(2m^*\Omega^2)$ is the energy of the center of the resonance state including the relaxation shift on the excited potential. When $m\hbar\Omega$ and $\chi\hbar\omega \ll \Delta$, where $\chi = \varepsilon'_a/(2m\hbar\Omega^3)^{1/2}$ is a dimensionless coupling constant, the former equation leads to

$$P_m(\varepsilon) \cong \frac{m!}{\pi}\frac{(\chi\hbar\Omega)^{2m}}{\Delta^m}\rho_a^{m+1}(\varepsilon). \tag{42}$$

For eV_{t} used in the inelastic tunnelling experiment, the variation of $\rho_a(\varepsilon)$ is negligible around the Fermi level ε_{F} over the energy scales eV_{t}, so that Eq. (40) can be approximated to

$$I_m \cong \frac{4e^2\Delta_{\mathrm{s}}\Delta_{\mathrm{t}}}{\hbar\Delta}P_m(\varepsilon_{\mathrm{F}}). \tag{43}$$

For a truncated harmonic oscillator to model the potential well with n vibrational levels, Salam et al. gave a rate of motion by coherent multiple vibrational excitation

of the adsorbate-substrate bond caused by inelastic tunnelling electrons $R_{\rm coh} \sim |I_{\rm n}/e|$. Provided that a single electron emits a single vibrational quantum $R_{\rm coh}$ is expressed in terms of $I_{\rm inel}$:

$$R_{\rm coh} \cong \frac{2e\Delta_{\rm s}\Delta_{\rm t} n!}{\pi\hbar}\frac{(\chi\hbar\omega)^{2n}}{\Delta^{n+1}}\rho_a(\varepsilon_{\rm F})^{n+1}V_t = \frac{n!}{e}\frac{I_{\rm inel}^n}{I_{\rm elas}^{n-1}}, \quad (44)$$

where $I_{\rm elas} = (4e^2\Delta_{\rm s}\Delta_{\rm t}/\hbar\Delta)\rho_a(\varepsilon_{\rm F})V_{\rm t}$ is the elastic tunnelling current. While Eq. (44) exhibits again a power law dependence on the inelastic tunnelling current, $I_{\rm inel}$, the vibrational relaxation rate is absent in the equation, in contrast to the case of the incoherent multiple stepwise excitation discussed in Section 7.2.4.1.1.

As far as the power law dependence is concerned, it does not matter whether one defines the power n as the number of vibrational levels or as the number of tunnelling electrons when a single electron excites one vibrational quantum. However, a single electron can emit multiple vibrational quanta, and the inelastic tunnelling current exciting the adsorbate to the mth vibrational state from the ground state by a single electron is given by Eq. (43). Once multiple excitations are incorporated into the transition matrix elements of the vibrational mode in the reaction coordinate, the molecule is allowed to jump multiple ladders in one scattering event with a single tunnelling electron. Coherent superposition of these jumps by the multi-electron process allows the adsorbate to overcome the potential barrier. In general the rate of motion can be expressed as

$$R_{\rm coh} \cong \prod_{k=1,2,\ldots}\frac{I_{m_k}}{e}, \qquad \sum_k m_k < n. \quad (45)$$

Since $I_m = I_{\rm elas}P_m/\rho_a(\varepsilon_{\rm F})$, and $I_{\rm t} = I_{\rm elas} + I_m$ ($\cong I_{\rm elas} \gg I_m$), one obtains:

$$R_{\rm coh} \cong \prod_{k=1,2,\ldots} P_m\left(\frac{I_{\rm elas}}{e}\right)^N \propto I_t^N, \quad (46)$$

where N is the number of multi-step jumps of the vibrational ladders, i.e., the number of electrons required to overcome the potential barrier via multiple jumps.

For fixed $I_{\rm t}$, coherent and incoherent processes have different behavior with respect to V below the energy barrier for reaction E. For the incoherent excitation process the reaction rate is rather insensitive, while for the coherent single multi-step excitation process the reaction rate changes dramatically at certain V, corresponding to the change in the number of electrons required energetically to induce reactions.

7.2.4.2 Indirect excitation For processes, where a high-energy mode is excited and coupled to the low-energy reaction coordinate mode, mode coupling between the two modes and electron–hole pair excitation are important.

The reaction rate $R_{\rm RC}$ within the reaction coordinate (RC) can be written as the product of the excitation rate $\Gamma_{{\rm RC}(m\to n)}$ times the probability $N_{{\rm HF}(\nu),{\rm RC}(m)} := N_{\nu,m}$ that the high-energy mode is in the state ν ($\nu = 0, 1, 2, \ldots$) and the reaction coordinate mode is in the state m ($m = 0, 1, 2 \ldots$) [196]:

$$R_{\rm RC} = \sum_{m,n}\Gamma_{{\rm RC}(m\to n)}N_{\nu,m}, \quad (47)$$

n represents the vibrational continuum of the reaction coordinate mode above the barrier E. When the vibrational energy $\hbar\Omega$ of the high-energy mode is larger than E, a reaction can occur in a single electron process, where the high-energy mode decays by transferring energy to the reaction coordinate mode via anharmonic interaction, resulting in the excitation of the reaction coordinate mode from the ground state to a state above the barrier. In this case, $\Gamma_{{\rm RC}(m\to n)}$ is the rate of energy transfer from the high-energy mode to the reaction coordinate mode for $\nu = 1$ and $m = 0$.

If $2\hbar\Omega > E > \hbar\Omega$, the reaction coordinate mode can be excited above $E_{\rm B}$ either by two times the decay of the $\nu = 1$ or by energy transfer from the $\nu = 2$ state of the high-energy mode. These indirect excitation processes correspond to $N_{1,m}$ and $N_{2,0}$, respectively. Furthermore, if $\hbar\Omega + m\hbar\omega > E_{\rm B}$ (where m denotes the intermediate excited states of the reaction coordinate mode), a cooperative process leading to a reaction is possible where both the high-energy and the reaction coordinate modes are excited by tunnelling electrons.

Anharmonic coupling between two modes involves in general depositing some energy ε in the continuum of electron–hole pair excitations (for metals) or bulk phonon excitations, i.e., $\hbar\Omega = \hbar\omega + \varepsilon$. The reaction rate $R_{\rm RC}$ induced by a single-electron process is [196]

$$R_{\rm RC} = \sum_{n>n_{\rm th}}\frac{1}{\tau_{\nu(1\to 0){\rm RC}(0\to 1)}}N_{1,0}, \quad (48)$$

where $1/\tau_{\nu(1\to 0){\rm RC}(0\to 1)}$ is the transition rate of deexciting the ν mode from its first excited state to the ground state while exciting the reaction coordinate mode from its ground state to the higher-lying states n. The sum is over all the levels n above the top of the barrier $E_{\rm B}$ that satisfy energy conservation $\hbar\Omega = \hbar\omega + \varepsilon$. The calculation of the transition rate requires a detailed knowledge of the potential energy surface of the system.

The change of $N_{1,0}$ can be expressed as [45]:

$$\frac{{\rm d}N_{1,0}}{{\rm d}t} = p_\nu N_{0,0} - \frac{1}{\tau_\nu}N_{1,0} - \sum_n\frac{1}{\tau_{\nu(1\to 0){\rm RC}(0\to n)}}N_{1,0}, \quad (49)$$

where $p_\nu = \eta_\nu I$ is the transition rate to excite the $\nu = 1$ state by inelastic tunnelling with the inelastic-tunnelling fraction η_ν and the current I, which corresponds to the number of tunnelling electrons. The vibrational damping τ_ν results from low-energy excitations. This equation is valid as long as $p_\nu \tau_\nu \ll 1$ as it neglects the population of higher vibrational states.

Assuming a stationary state, i.e., $dN_{1,0}/dt = 0$ gives the reaction rate: $N_{1,0} = \tilde{\tau}_\nu p_\nu N_{0,0}$ where the total relaxation rate of the first excited state of the ν mode is given by:

$$\frac{1}{\tilde{\tau}_\nu} = \frac{1}{\tau_\nu} + \sum_n \frac{1}{\tau_{\nu(1\to0)\mathrm{RC}(0\to n)}}. \tag{50}$$

With $N_{0,0} = 1$ the equations lead to the following reaction rate

$$R_{\mathrm{RC}} = \frac{\tilde{\tau}_\nu}{\tau^{>}_{\nu,\mathrm{RC}}} \eta_\nu I \quad \text{with} \quad \frac{1}{\tau^{>}_{\nu,\mathrm{RC}}} = \sum_{n>n_{\mathrm{th}}} \frac{1}{\tau_{\nu(1\to0)\mathrm{RC}(0\to n)}}. \tag{51}$$

When the vibrational rate $1/\tau_\nu$ is much larger than the one from intermode coupling $1/\tau_{\nu,\mathrm{RC}}$ Eq. (51) reduces to:

$$R_{\mathrm{RC}} = \frac{\tau_\nu}{\tau^{>}_{\nu,\mathrm{RC}}} \eta_\nu I. \tag{52}$$

Thus, the rate depends on the ratios of the rate of excitations of the reaction coordinate mode above the potential barrier and the decay rate of the ν mode into low-energy excitations in the substrate.

7.3 Molecule chemistry with the STM Molecular reactions induced by IET have been performed on many adsorbate/substrate systems. Here we give one example each for the elementary processes diffusion, desorption, rotation, bond breaking, a chemical reaction, and a reversible process. For a more complete list we refer the reader to Section 7.4.

7.3.1 Diffusion and desorption One example for diffusion has been shown above for D_2O on Ag(111) (see Fig. 65). Here we give an example where two processes compete, diffusion and desorption.

Different processes might be induced at the same energy because the excited vibrational mode can interact with several reaction modes. Furthermore, there are always also tunnelling electrons of lower energies so that different vibrations might be excited at the same voltage. It is challenging to increase the probability of the desired process and decrease it for all other processes. An instructive example is IET manipulation of ammonia (NH_3) on Cu(100) (Fig. 69) [197]. Both desorption and diffusion are excited at the same energy (Fig. 69a–b) and the reaction probability leaned towards one of the processes by an appropriate choice of manipulation current and voltage.

Figure 69c shows that mainly diffusion was induced by a single excitation of the N–H stretch mode at 400 meV at low current, though about 20% of the molecules diffused. At lower excitation energy, where the umbrella (i.e., inversion) mode is excited with electrons of energies of 270 meV mostly desorption was induced below 1 nA. The preference of excitation by two electrons has been explored theoretically [196].

7.3.2 Rotation Rotation as investigated for acetylene (C_2H_2) on Cu(100) is shown in Fig. 70. On this surface two possible orientations exist (Fig. 70a). If the tip is placed slightly off center from the molecule, the two orientations correspond to two different current values such that the system resembles a two-state fluctuator (Fig. 70b). The isotope shift of the threshold energy (Fig. 70c) showed that

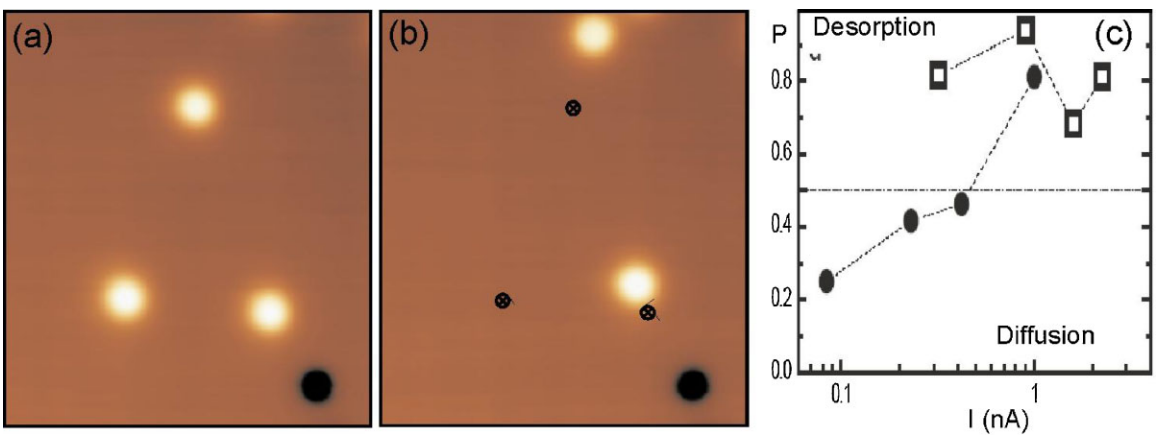

Figure 69 IET manipulation of ammonia on Cu(100) (with courtesy of Pascual et al. [197]): (a) Before manipulation with 420 mV and 0.5 nA; 100 mV, 1 nA, 7×7 nm^2. (b) After manipulation, where is indicated by crosses. (c) Probability of desorption P in dependence of tunnelling current I for manipulation with 420 mV (filled circles) and 320 mV (open squares). Horizontal line separates region of predominant processes as indicated.

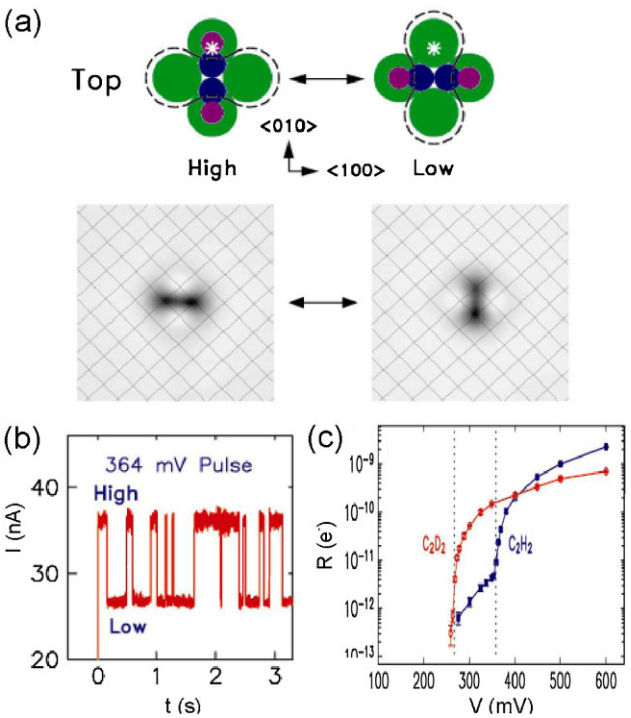

Figure 70 Rotation of acetylene on Cu(100) (with courtesy of Ho and coworkers [198]): (a) STM images of two orientations as depicted in models, 100 mV, 10 nA. (b) Current I during manipulation with 264 mV with the tip positioned 0.15 nm from the center of the molecule. High (low) value correspond to image on the left-hand (right-hand) side in (a). (c) Rotations per electron R for C_2H_2 and C_2D_2 in dependence of bias voltage V at 40 nA. Dashed lines indicate energy of C–H (C–D) stretch mode.

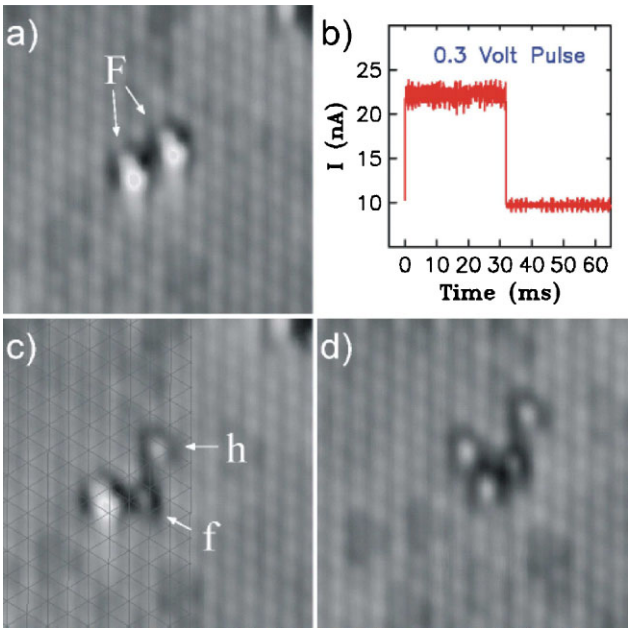

Figure 71 Dissociation of O_2 on Pt(111) (with courtesy of Ho and coworkers [200]): (a) STM image before manipulation; F denotes molecule in fcc site. (b) Current during manipulation with 0.3 V. (c) STM image after manipulation; "f" and "h" denote atoms in fcc and hcp site, respectively. (d) STM image after second manipulation.

the electrons first excite molecular vibrations, in this case the C–H (C–D) stretch mode [198]. This mode is much higher in energy than the hindered rotational mode that is more closely related to rotation. This implies that anharmonic coupling between the two modes is necessary for inducing rotation.

On Pd(111) the rotation of acetylene was used to determine the binding site of the molecule [199].

7.3.3 Bond breaking Single O_2 molecules on Pt (111) were dissociated at 50 K [200]. As shown in Fig. 71a two molecules were imaged on an atomically resolved background. Application of 22 nA and 0.3 V leads to a sudden drop in current after 30 ms indicative of a reaction (Fig. 71b). The image taken after the manipulation shows that the molecule is dissociated into two atoms that are adsorbed on two different types of hollow sites (Fig. 71c). A subsequent manipulation dissociates also the second molecule into two atoms (Fig. 71d). Different current dependencies were observed in dependence of the applied bias voltage that corresponded to a one, two, or three electron process. Dissociation was explained by vibrational ladder climbing via tunnelling through an adsorbate induced resonance leading to direct excitation of the O–O stretch mode. Also the rotation of O_2 was explained by the same mechanism [201].

7.3.4 Chemical reaction Figure 72 shows the successful synthesis of biphenyl from two iodobenzene molecules on a Cu(111) step [202]. The reaction starts with the abstraction of the iodine from the iodobenzene by IET manipulation (Fig. 72a–b). Then the dissociated iodine is removed and the remaining two phenyls are brought together by lateral manipulation (Fig. 72d–e). Finally, the associated phenyls are converted to the final product of biphenyl (Fig. 72e–f). Lateral manipulation proved that the two phenyls are covalently bound (Fig. 72f–g).

7.3.5 Reversible process Reversible processes are attractive as two-state fluctuators and several have been realized by now [203–205]. Figure 73 shows a reversible process based on hydrogen bond rearrangement between two azobenzene derivates [157, 206]. Because of the directional nature of the hydrogen bonding two well-defined states exists, between which the dimer can be switched repeatedly.

7.4 Further reading for single molecule chemistry with the STM In the following we give examples for electron induced manipulation ordered

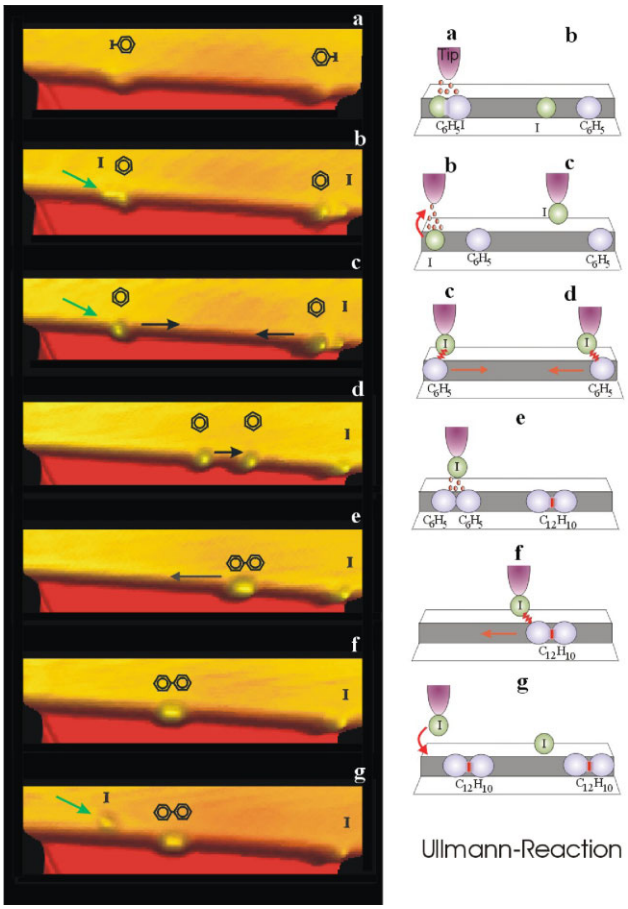

Figure 72 Reaction of a biphenyl molecule from two iodobenzene molecules (C_6H_5I) on Cu(111); reaction steps are depicted on right-hand side [202]: (a) Two molecules adsorbed at Cu(111) step. (b) Molecules dissociated by IET into phenyls and iodine. (c) Iodine molecule is picked up by the tip by vertical manipulation. (d) Molecules are approached by lateral manipulation with functionalized tip. (e) Molecules are associated by IET. (f) Association is proven by sliding the biphenyl molecule along the step edge. (g) Iodine is redeposited onto surface.

according to the induced process and within each subsection in chronological order with the first experiment of the particular system in the literature. Earlier reviews on lateral manipulation include some initial single molecule chemistry [152–154]. Several excellent reviews appeared lately, two experimental ones [46, 207, 208] and several theoretical ones [69, 190, 191, 209]. We direct the reader to these reviews or the original articles for details.

7.4.1 Diffusion Diffusion was first demonstrated for a single Si atom diffusing between two sites on Si(111)-(7 × 7) at 2.25 and 3 V [210].

Diffusion of the different isotopes of ethylene (C_2H_4) on Ni(110) showed markedly different rates at 1 V even those with the same mass [211].

Migration of covalently bond Br atoms on Si(100)-(2 × 1) was induced with a bias voltage above 0.8 V corresponding to electron capture in the Si-Br anti-bonding σ* orbital above the Fermi level, but only at high Br concentration indicating that repulsion between Br molecules assists the diffusion [212].

Diffusion of chlorine atoms chemisorbed on Si(100)-(2 × 1) was induced at +1.25 and −0.75 V through injection of electrons into the Si–Cl anti-bonding state and the surface state, respectively [213].

Diffusion of chlorine chemisorbed on Si(111)-(7 × 7) was induced beyond −2 and +4 V by injection of electrons into the S_3 surface state and the Si–Cl anti-bonding state, respectively [214, 215].

Lateral motion of CO on Pd(110) via excitation of the CO stretch mode showed in comparison with a lack of motion on Cu(110) how important the anharmonic coupling between different modes, the vibrational and the reaction mode, are for IET manipulation [216].

Diffusion of H_2O clusters was induced either by excitation of the OH-stretching or of the scissoring mode [58]. Diffusion of single water (D_2O) monomers from the elbows of the Au(111) reconstruction was possible through the excitation of the combined OD-stretching and

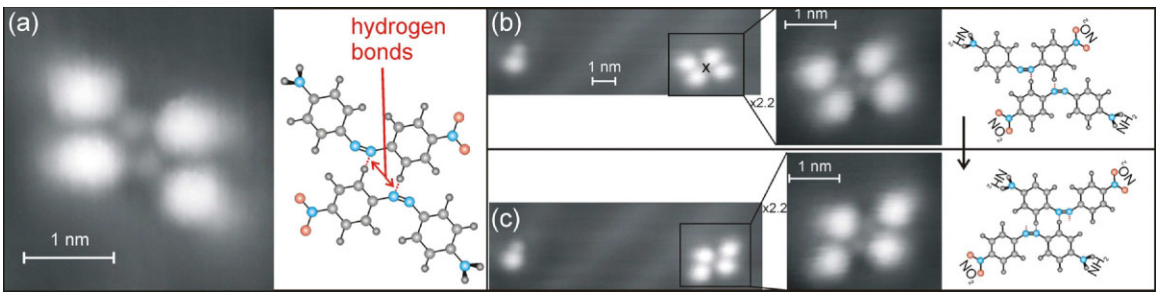

Figure 73 Intermolecular switch from dimers of amino-nitro-azobenzene on Au(111) [206]: (a) high-resolution image of a dimer, and corresponding ball-and-stick model to scale that shows that the dimer is stabilized by two N–H hydrogen bonds. In the STM image each side group, NH_2 and NO_2, corresponds to a bright protrusion and each N_2 group to a smaller and less bright protrusion. (b) Before and (c) after IET induced hydrogen bond rearrangement with high-resolution images (8.5 pA, 6 mV) and corresponding ball-and-stick models demonstrating the change in relative position of the groups; 8.5 pA, 331 mV; voltage has been increased from 450 mV to 1.8 V within 380 ms with the tip position as indicated by the cross.

metal–molecule bending mode [68]. The same study showed a shift of the reconstruction of Au(111) at 440 mV.

Diffusion of Co on Cu(111) from hcp to fcc within a tip modified potential needed 11–12 electrons [131] and could be explained by surmounting the non-adiabatic diffusion barrier of 65 meV via 12 times excitation of the frustrated translation of only (8 ± 1) meV [217]. Theoretically, this experiment was explained by vibrationally assisted tunnelling, a process, in which the energy of the vibrational excitation is slightly lower than the barrier for reaction [218].

The induced diffusion of acetylene on Cu(110) via excitation of the C–H stretch proceeded in two steps via a long-bridge site [219], though this study showed some deficits in data handling.

Diffusion of a chemisorbed molecule, CH_3S, was induced on Cu(111) [220].

Diffusion of normal and heavy water dimers on Pt(111) was induced at up to five stretching and scissoring frequencies [221]. From these measurements the adsorption structure of the dimer was deduced.

Vibrational energy, reaction order, and transition rate are extracted from detailed yield-voltage dependencies via fitting an analytic formula as demonstrated for CO diffusion and configurational change of *cis*-2-butene on Pd(110) [222].

For a hydroxyl monomer on Cu(110) a change in adsorption site via induced hydrogen tunnelling was enhanced by excitation of the OH bending mode, which is the mode along the reaction coordinate [223].

7.4.2 Rotation For the above discussed rotation of acetylene on Cu(100) [198] the rotation rate decreases when the STM tip is laterally displaced away from the center of the molecule. A double exponential distribution for the time intervals at high current for a C_2HD molecule excited off center showed that the rotational motion allows distinction between the two ends of the molecule at a voltage where the C–D stretch is excited but the C–H stretch not.

Though rotation of O_2 on Pt(111) was found as a concurrence reaction to dissociation [201], the only molecule investigated in depth so far with respect to rotation is acetylene (C_2H_2) [198, 199].

Moreover, the rotation of a single molecule [224] or a molecular wheel in a planar adsorption geometry [225] or in a double-decker geometry [226] on the surface were realized.

7.4.3 Desorption A major part of desorption studies concerned hydrogen desorption from hydrogen passivated silicon surfaces.

Desorption of hydrogen was induced at room temperature from Si(111):H-(1 × 1) in the energy range of 2–10 eV through promotion of an electron from the Si–H bonding orbital to the unoccupied anti-bonding orbital [227]. However, this early experiment from 1990 was in the field desorption regime and not yet molecule specific. Desorption of hydrogen from Si(100)-H(2 × 1) was achieved and was explained below 6.5 eV by vibrational heating of hydrogen by tunnelling electrons scattering inelastically with the Si–H 6σ* electron resonance [228] and with a maximum at −7 V by vibrational heating of hydrogen because of inelastic scattering of tunnelling holes with the Si–H 5σ hole resonance in the onset of the field emission regime [229]. This study also confirmed the explanation for the low voltages in the range between 2 and 4 V. The reason for the long lifetime of the hydrogen stretch frequency, which facilitates the multi-electron processes, is its energy in between the Si phonon spectrum and the electron–hole excitation energy, thus inhibiting coupling to these two decay channels.

Desorption experiments on the same system (Si(100)-H (2 × 1)) at cryogenic temperatures [230] (11 K) showed no significant temperature dependence of the threshold and of the yield above a threshold of 6 V, but a strong dependence of the yield (but not the threshold) for the D isotope. This dependence was explained by higher quenching rates for the slower moving heavier isotope. Furthermore below the threshold the yield depended strongly on temperature which was explained by a lifetime effect. Desorption of hydrogen was extended to locally change the (2 × 1) superstructure to a (3 × 1) superstructure at both polarities [231].

All these measurements on the Si(100)-(2 × 1) system were performed in the scanning mode. While the earlier experiments reported a current dependence with a large power law of 10^{-15}, a later experiment showed a dependence of the order of 1 only at a sample voltage of 2.5 V [183]. This discrepancy was explained by the tip dependence of the process and the vibrational heating to a high vibrational level was questioned. Instead it was proposed that the σ* resonance was excited and sufficient to break the H–Si bond. The comparison of desorption in scanning and in stationary mode showed an up to a factor of four higher dependence for the scanning mode and draws into question this latter mode for quantitative measurements. It should be pointed out that reliable power laws can only be extracted for current variations of considerably more than one order of magnitude, which was not the case in any of the measurements.

Desorption of CO [167] and of ammonia [232] was induced from Cu(111). Ammonia desorption needed three electrons at 200 mV, but only two electrons at 400 mV.

Desorption (and some diffusion) of the dimer bound benzene on Si(100)-2 × 1 showed a threshold between −1.6 and −2.7 V [233], which was explained by transient ionization of a π state of benzene by scanning. Other molecules with π bonds were also subject to tunnelling induced changes, while those without π bonds could not be modified.

Desorption of chlorobenzene molecules from Si(111)-(7 × 7) was driven by electron attachment [234].

Mainly desorption of ammonia on Cu(100) was induced by double excitation of the umbrella (i.e., inversion) mode with electrons of energies of 270 meV; about a quarter of the molecules diffuses [197].

H_2 was desorbed from Co islands adsorbed on Cu(111) by ramping the bias voltage from −1V to +1V [235].

7.4.4 Bond breaking Bond breaking was first achieved in 1992 with the dissociation of decaboran ($B_{10}H_{14}$) adsorbed on Si(111)-(7 × 7) [236]. The dissociation during scanning with elevated current was explained by field emitted electrons. On the same surface H_2S and D_2S were dissociated above 2 V [237].

Dissociation of bonds on the surface might be facilitated in a concerted process, where the formation of a new bond assisted the rupture of an old bond [238]. Such concerted reaction reducing its energy is common in the gas-phase. At a surface it requires that the new bond is formed adjacent to the old one, i.e., the reaction is localized. This process was shown to be operative for electron-induced dissociation of chlorobenzene on Si(111)-(7 × 7) at 4 V [239]. The radial and angular distribution of the chlorine atoms depended on the tunnelling current [240]. It was shown that tip states determine the branching ratio of this process as compared to desorption of the molecule from the surface [241]. Desorption of chlorine from the same surface during scanning was shown to proceed via two holes [242].

Dissociation of O_2 on Si(111) was induced via dissociative electron attachment initiated by resonant capture of tip-emitted electrons into the empty $3\sigma_{u^*}$ level of the molecule that is considerably shifted towards the Fermi energy because of adsorption during scanning at increased voltage [243].

On metallic surfaces, the first example was the dissociation of a single O_2 molecule on Pt(111) in 1997 [200].

The dissociation of Cu-tetra-3,5-di-tert-butyl-phenyl porphyrin on Cu(100) resulted in a single reaction product. However, its complexity did not allow identifying it [244].

Dehydrogenation of different isotopes of ethylene to acetylene on Ni(110) between 1.1 and 1.5 V and further to carbon [211] and of acetylene on Cu(100) to dicarbon [245] was achieved and proven by IETS. Dehydrogenation of ethylene showed a strong isotope effect and a lower threshold for the second dehydrogenation than for the first one. Dehydrogenation thresholds lie in between 2 and 3 eV for these processes as well as for benzene and pyridine [246]. One or two hydrogen atoms were dissociated from pyridine (C_5H_5N) and benzene, respectively, adsorbed on Cu(100) above 3 V and the reaction products identified by IETS [246]. The ring of the remaining fragments was broken above 3.75 V. The same reaction on Cu(110) showed a strong isotope effect in the yield that was explained by the slower acceleration of deuterium on the potential energy surface because of its larger mass [247]. Dehydrogenation of benzene is initiated by the temporal negative ion formation, which is formed by trapping of electrons in the resonant levels of the molecule. It changes its adsorption geometry from flat to upright.

Transformation from *trans*-butene to 1,3-butadiene on Pd(110) [248] was explained by vibrational ladder climbing resulting from direct excitation of the C–H stretch mode. Two isomers of *trans*-2-butene were dehydrogenated to 1,3-butadiene at a threshold voltage of −365 meV that corresponds to the C–H(D) stretching mode [248]. One, two, and three electrons were needed for a bias above 1 V, between 600 and 800 mV, and below 400 meV for the deuterated molecule, respectively.

The dissociation of water was found to be only possible within a cluster above 3.1 eV [180, 249].

Iodobenzene adsorbed on a Cu(111) step was dissociated above 1.4 eV [250]. The phenyl was further dissociated above 3.1 eV.

Via excitation of a π^* resonance O_2 on Ag(110) was dissociated either below −390 meV or above +470 meV. The separation of the produced molecules depended on polarity and on both the distance and the direction with respect to the molecular axis of the original molecule [251]. The fact that the threshold at positive bias lies above the threshold for rotation, while it does not for the opposite polarity showed that in the former case rotation of the molecules preceded dissociation.

On Ag(100) the dissociation of O_2 molecules leads to atom pairs that indicate a far range motion of the oxygen atoms after the dissociation [252].

Water within crystalline structures on Cu(111) was dissociated by electron injection into the conduction band of the ice [249]. The dissociation is not limited to the immediate region below the tip.

The sulfur–sulfur bond of $(CH_3S)_2$ on Cu(111) was dissociated and the single molecules were induced to diffuse [220].

More recent work extended this work to state-selective control of water molecules adsorbed on an insulating layer, MgO [253].

7.4.5 Chemical reactions Chemically more demanding than the previous examples is a complete chemical reaction, for which all steps are performed with the STM, which was successful for the synthesis of biphenyl from two iodobenzene molecules on a Cu(111) step [202]. The first step of this reaction, the dissociation of iodobenzene, was later investigated in more detail [250].

CO_2 on Ag(110) was produced by first dissociating O_2 with tunnelling electrons of +470 mV, then positioning CO close to O by repeatedly applying +240 mV pulses to CO, and finally giving a not further specified pulse to form CO_2 that was found to desorb at 13 K [46]. In a second experiment the CO was transferred to the tip and the CO_2 produced by placing this modified tip above an oxygen atom and then applying a voltage pulse of 0.47 V.

Both polymerization and depolymerization of fullerenes was achieved by injecting either holes or electrons into the molecule [254].

Collective reactivity due to electron attachment was shown within self-assembled chains of dimethyldisulfide adsorbed on Au(111) [255]. Thereby, sulfur–sulfur bonds were broken along the chain pointing to a propagating chemical reaction.

A larger compound including the substrate atoms is O–Ag–CO_2–Ag–O that can be formed and broken reversibly [256].

Most recently, bond-selective control was demonstrated for thiol-based π-conjugated molecules co-adsorbed with Au atoms on NiAl(110) [257]. The sequence of reactions steps included cleavage of acetyl groups and Au–S bond formation.

7.4.6 Reversible processes (switches) Triggered by the idea to use single molecules as or within functionalized nanomachines IET was used to demonstrate molecular switches, i.e., to trigger reversible bistable reactions.

Diffusion of a hydrogen atom on a hydrogen passivated Si(100)-2 × 1 surface was induced by scanning at room temperature at negative bias only with a peak near the surface resonance at −2.4 V and as diffusion was limited between two neighboring sites on one dimer named a bistable switch [258, 259]. The atom's diffusion direction was influenced by the tip's relative position to the hydrogen atom.

The back formation of an electrostatically induced conformational change of a more complex molecule (Zn(II)Etioporphyrin) on NiAl(110)) involved electrons that inelastically interacted with a molecular resonance at 1.25 V [260]. Unfortunately, the complexity of the molecule inhibited the identification of the exact chemical change by STM and thus the underlying process has not yet been understood.

Also for two adsorption sites of a biphenyl molecule on Si(100) the bistability included the substrate in form of the adsorption geometries of a molecule [261].

Motion between two fcc and hcp lattice sites of a Co atom in a CoCu linear structure on Cu(111) was deduced from tunnelling noise spectroscopy and had a threshold of 15 mV only [262]. The switching diminishes with longer chain length.

A covalent bond between a metal (Au) and a molecule (pentacene) was reversibly formed on an insulating layer of NaCl [263]. On insulating films the longer lifetime of excited states facilitates such reactions.

A further step forward is a reversible unimolecular bistable reaction as represented by isomerization reactions [203–205]. Both a stereoisomerization [206] and a constitutional isomerization [181, 264] were demonstrated. Mostly, isomerization was induced via vibrational excitation, but for molecules in supramolecular clusters [265] or bound to single metal atoms [266] isomerization was induced by electron attachment. The isomerization was not always reversible, though the reason is still unknown [267]. These reactions are possible within supramolecular layers [265] and for physisorbed molecules both on metals [268] and on NaCl layers [269, 270].

Selective isomerization occurs within close-packed islands, due to the commensurability of the surface lattice with the molecular lattice [271]. This unexpected dependence on the supporting surface causes strong differences in the switching yield for different adsorption sites as the surface acts as a template for the switching process [271].

Another bistable switch is represented by a chirality change of molecules as demonstrated for chloronitrobenzene on Au(111) [272]. The chirality of propene on Cu(211) was likewise induced with a reaction order of two in contrast to diffusion that is induced with a reaction order of one [273] and more recently for an azobenzene derivative [274].

Also the dissociation of hydrogen bonds within water clusters is a reversible process [179]. In this case, the hydrogen bond rearrangement is influenced by the electric field in the tunnelling junction. For water dimers on Cu(110) the intrinsic donor–acceptor exchange rate at 6 K was enhanced by excitation of the donor-substrate stretch mode [275]. This study was extended to a H-atom relay reaction in chains of water and hydroxyl species [276]. The potential energy surface of the reaction was modelled theoretically.

Likewise, hydroxyl dimers were induced to flip by the O–H (O–D) stretch mode [223]. The position dependent reaction rates as well as a Fano-like line shape of IETS spectra for hydroxyl dimers on Cu(110) was successfully reproduced by a DFT calculation [277].

Other switches of small lateral dimensions are charge switching on a single donor [278], a change of a Pt dimer between four configurations on Ge(001) [279], the bending of a bond within a chloro-nitro-benzene molecule [280], a change of adsorption sites of Ag atoms on Ag(111) [281], or the change of adsorption site of a CO_2 molecule bound to an oxygen atom on Ag(100) [256]. The latter process was assumed to be helped by a lowering of the diffusion barrier in presence of the tip, a process that contributes to lateral manipulation [134].

Recently, there is an effort to use such switches within specifically designed molecules that perform selective motions upon electron excitation as a "four-wheeled" molecule that diffuses anisotropically on an isotropic surface [282].

7.4.7 Scanning noise spectroscopy The STM has permitted to study the different types of molecular manipulations and reactions by studying single molecules. The process to understand the manipulations and the underlying mechanism involves the gathering of as many manipulation events as possible in order to have enough data to perform the analysis of Section 7.1. This is generally a painstaking process of localizing a molecule with the STM tip, ramping up the bias on the molecule, look for abrupt changes in current and eventually scan again the surface to find the products of the induced manipulation. Easily, days of work go by to gather a few hundres of events that may render the statistical ananlysis meaningful.

The situation has changed with the advent of scanning noise spectroscopy (SNS) [283]. This technique makes

use of the telegraphic noise induced by switching processes, in which the molecule changes among conformations in a cycled manner. Assume that there are two (or more) local minima in the adsorption of a molecule on a surface. By injecting electrons, one can make the molecule hop between these local minima. As a consequence, there will be rapid changes in the current of the STM junction when the molecule is flipping between minima. During a scan with the STM over the surface, the flipping motion of the molecule translates into a blurred STM image. Statistical analysis of the blurring can be exploited to gain understanding about the type of motion induced by the inelastic electrons. SNS can be performed with an STM modified to include fast electronics that can store the traces of signals coming from the STM tip. By analogical measurements, the statistics of signals can be evaluated on the fly, and in the time of a scan over the surface, hundreds of molecular events can be easily collected. In a few hours work, a complete statistical analysis of the switching behavior of a molecule can be performed. This is in sharp contrast to the slow customary way of performing statistics of molecular motions with a STM.

In Ref. [283] Schaffert et al. study the blurred constant current images of Cu phthalocyanine molecules adsorbed on Cu (111). The SNS permits the authors to learn about the nature of motion, measure the switching rates, study the behavior of the rates with applied bias and currents, and from here learn about the electronic structure of the molecular adsorbates. Indeed, the study of the switching rate with bias gives maxima that can be directly correlated to the energetics of molecular electronic states on the surface. Hence, the systematic study of noise allows for a complete characterization of the adsorbate. For this reason, the technique has been named scanning noise spectrocopy.

7.4.8 Theory A simple model for inelastic tunnelling between a metal tip and a surface with an adsorbed molecule was presented by Persson and Demuth [44] even before the advent of IETS. The inelastic tunnelling was based on dipole scattering using Bardeen's formula for the electric current. The dipole scattering theory was followed by a theory which studied the effect of vibrational damping from electron–hole pair excitations in the adsorbate–metal system on the IET via the vibrational excitation [45, 284]. The model of Persson and Baratoff [45] provided a main conceptual tool that led to further work. A quantum treatment was given [83]. Also *ab initio* calculations were included in an electron–vibration coupling term [285]. Beyond the model of Persson and Baratoff goes a many-orbital approach that included two excitable molecular modes [86]. The latter approach also facilitated to calculate distance dependent rates. It furthermore showed that the likelihood to excite two different modes simultaneously is not negligible. According to this theory the resonant tunnelling via adsorbate states is the dominant channel for the inelastic current. The inelastic fraction of the current is related to the vibrational damping rate because of electron–hole pair excitation. A density functional study of vibrational inelastic tunnelling in STM was also made for acetylene on copper by Lorente and Persson [89]. Under the assumption that the vibrational damping rate is large compared to the rate of tunnelling electrons, they related the tunnelling conductance to the local density of states of electrons interacting with molecular vibrations. From the calculation of elastic and inelastic contributions to the tunnelling conductance they found an importance of the impact scattering mechanism involving a vibration-induced change in the tunnelling amplitude.

Resonant scattering can induce rotational excitation, if the incident electron is captured into a molecular orbital of a symmetry associated with an angular momentum or with contributions from a limited number of angular moments, which has been treated theoretically [286]. The experimental data could not be explained by an excitation energy landscape that has a different geometry than the ground state energy landscape and thus leads to a torque on the molecule, but the electrons are emitted in the directions according to the angular shape of the resonance orbital.

For the desorption of benzene from Si(100) [287] the energy potential surfaces for both the ground and the excited state were calculated through a first principal electronic structure calculation and a quantum mechanical wave packet study of the nuclear motion [189]. It showed the large change in adsorbate structure in the excited state that eventually leads to bond breaking and explains the high efficiency by the long lifetime of the excited state.

The first calculation of a spatially resolved inelastic current was performed by Mingo and Makoshi [86, 87] using a Green's function linear combination of the atomic orbitals method for a C_2H_2 molecule adsorbed on Cu (100) [64, 198]. This theory includes a relation between inelastic tunnelling current and vibrational deexcitation. Spatially resolved inelastic currents were also calculated by Lorente and Persson [89]. A theoretical description of IETS on the basis of the Anderson Hamiltonian supplemented with a phonon system using a non-equilibrium diagram technique showed that the deviation of the distribution function of a vibrational state from its equilibrium might be important [288]. The Keldysh–Green's function method [288] allows obtaining general formulas for the elastic and IET current and the stationary non-equilibrium vibrational distribution function. The power law dependence is not valid close to the threshold $|eV| = \hbar\Omega \pm \hbar/\gamma$ for a vibrational mode with energy $\hbar\Omega$ with V the applied bias voltage and γ the vibrational damping rate from the broadened vibrational density of states. In this region a gradual increase in reaction rate is expected.

Overheating by the inelastic current of the phonon system and the bias voltage were shown to play an important role in understanding current-induced dynamical reactions of adsorbates [192].

The theory by Lorente and Persson for IETS has been extended to include de-excitation of molecular modes and intermode coupling [92, 289]. The damping of molecular vibrational modes by decaying into surface phonons is important when the molecular frequencies overlap with the surface phonon band and can thus be neglected at low lying excitations. The dominant contribution to the higher energy mode damping is electron–hole excitation. The rate of vibration decay into electron–hole pairs can be calculated using Fermi's golden rule. The decay of a given molecular vibration into a group of other molecular vibrations is greatly enhanced in the presence of electron–hole pairs. The excitation of electron–hole pairs guaranties energy conservation in the full process and reduces the number of lower energy quanta needed to match the energy of the decaying high-energy mode. The calculation of the damping rate into different low-energy vibrations assisted by electron–hole pairs can be carried on in a way similar to the calculation of mode damping into electron–hole pairs.

8 Physical investigations with artificial structures

8.1 Quantum corrals It is interesting to observe that the first groups able to fabricate artificial structures constructed and spectroscopically investigated rather complicated shapes like closed circular, elliptic, and triangular structures (called quantum corrals), whereas the intensive investigation of simpler structures like linear chains followed almost a decade later. We therefore start with a discussion of the corral structures. The first artificial structures studied thoroughly with respect to their physical properties were built by the group of D.M. Eigler on close-packed noble metal surfaces, which bear localized electronic surface states. The structures were circles and elliptic motifs, which contained several dozens of atoms. The very first example consisted of 48 Fe atoms arranged in an atom-by-atom way on a Cu(111) surface to mark the circle's circumference [22] and became worldwide known. In its interior the structure showed a nice interference pattern reminiscent of the wave pattern, which a stone falling into the center of a circular pond would create. In Fig. 34 an STM picture of the standing surface waves in the circular corral is shown. The wave pattern in an even simpler structure, called an open resonator, i.e., an arrangement of two parallel atomic lines, is displayed in Fig. 75 (see Section 8.1.3) [147]. As in these nanoscale structures the surface electron waves feel the confinement according to the arrangement of the adatoms, such artificial objects were called "quantum corrals." Whereas the circular and linear structures could be quantitatively analyzed with the simple picture of a particle in a box, for which the analytic solutions can be found in any quantum mechanics textbook, more complicated structures, like the so called "quantum stadium" had to be analyzed in a more advanced way, which was developed by E.J. Heller [294] and is based on quantum mechanical scattering theory. As this theory is of general validity for 2D-nanostructures on the one side and transparent and elegant on the other, it is so often used that it deserves to be outlined in the following. For a discussion of the origin and properties of surface localized electron states see Section 2.1.1.

8.1.1 Scattering theory of Heller Starting point is the circular wave, which the STM-tip emits and whose amplitude at a distance r from the tip is given by [294]

$$a_{\mathrm{tip}}(r) = \sqrt{\frac{2}{\pi k r}}\mathrm{e}^{ikr - i\pi/4}. \tag{53}$$

The length of the wave vector k of the electron waves emitted is given by

$$k = \sqrt{\frac{2m^*(E_{\mathrm{B}} + V_{\mathrm{T}})}{\hbar}}, \tag{54}$$

where E_{B} denotes the energy of the band edge of the localized electronic surface states below the Fermi energy E_{F}, m^* the effective mass of the surface state electrons and V_{T} the tunnelling voltage.

The incoming wave causes a wave scattered from an adatom located at r_{j} with the amplitude

$$a_{\mathrm{tip}}(r_j)a(r) = a_{\mathrm{tip}}(r_j)\sqrt{\frac{2}{\pi k}}\mathrm{e}^{i\pi/4}(\mathrm{e}^{2i\eta_0} - 1)\frac{\mathrm{e}^{ikr}}{2i\sqrt{r}} \tag{55}$$

with η_0 denoting the phase shift caused by the scattering adatom.

Part of the incoming electron wave can be absorbed due to inelastic scattering or elastic scattering into bulk states (absorptive channel). The usual procedure to describe absorption is to allow for η_0 to be complex:

$$\eta_0 = \delta_0 + i\eta_0^{\mathrm{im}}, \tag{56}$$

so that

$$\mathrm{e}^{2i\eta_0} = \mathrm{e}^{2i(\delta_0 + i\eta_0^{im})} = \mathrm{e}^{-2\eta_0^{im}}\mathrm{e}^{2i\delta_0} = a_0\mathrm{e}^{2i\delta_0}. \tag{57}$$

Note that for maximal absorption cause by "black dots" characterized by infinite η_0^{im} or $\alpha_0 = 0$, the scattered wave is given by

$$\begin{aligned} a(r) &= \sqrt{\frac{2}{\pi k}}\mathrm{e}^{i\pi/4}(\mathrm{e}^{2i\delta_0} - 1)\frac{\mathrm{e}^{ikr}}{2i\sqrt{r}} \\ &= \sqrt{\frac{2}{\pi k}}\mathrm{e}^{i\pi/4}(\mathrm{e}^{i\pi/2})\frac{\mathrm{e}^{ikr}}{2i\sqrt{r}} \end{aligned} \tag{58}$$

showing that there is still a scattered wave so that interference with an incoming wave still happens, a fact surprising at first sight but well known in quantum mechanical scattering theory.

The wave amplitude at the site of the atom j', which came from the tunnelling tip and was scattered by atom j, is

$$a_{\mathrm{tip}}(r_j)a(r_{jj'}) \tag{59}$$

with $r_{jj'}$ denoting the distance between adatoms j and j'. The total amplitude for scattering once at the adatom at r_j and returning to the tip (single scattering) is

$$g_1(\vec{r}\,) = \sum_j a_{\mathrm{tip}}(r_j)a(r_j). \tag{60}$$

The amplitude scattered first from atom j and then from adatom j' and returning to the tip (double scattering) is

$$g_2(\vec{r}\,) = \sum_j \sum_{j'} a_{\mathrm{tip}}(r_j)a(r_{jj'})a(r_{j'}) = \vec{a}_{\mathrm{tip}}\bar{A}\vec{a}\ . \tag{61}$$

Now also scattering contributions up to infinite order can be taken into account leading to a geometric series

$$\begin{aligned} g_{\mathrm{tot}}(\vec{r}\,) &= g_1(\vec{r}\,) + g_2(\vec{r}\,) + g_3(\vec{r}\,) + \cdots \\ &= \vec{a}_{\mathrm{tip}}(1 + \bar{A} + \bar{A}^2 + \bar{A}^3 + \cdots)\vec{a} \\ &= \vec{a}_{\mathrm{tip}}(1 - \bar{A})^{-1}\vec{a} \end{aligned} \tag{62}$$

with $\vec{a}_{\mathrm{tip}}$ and $\vec{a}$ denoting vectors of dimension N, the number of scatterers, and $\bar{A}$ being the $N \times N$ matrix of adatom–adatom amplitudes, which is fixed for a given tunneling voltage according to the adatom–adatom configuration. $\vec{a}_{\mathrm{tip}}$ and $\vec{a}$ change with the position of the tunneling tip.

The intensity of the scattered wave is (with the amplitude $\sin(kr)/kr = 1$ at $r = 0$ of the wave emitted at the tip) given by

$$I(\vec{r}\,, k) = 2Re[g_{\mathrm{tot}}(\vec{r}\,)]. \tag{63}$$

It was shown by Heller et al. that this expression corresponds to the local density of states measured by the STM tip. The scattering formulas are programmed readily and as an example the standing wave pattern in the quantum stadium of Eigler et al. is shown in Fig. 77 (see Section 8.1.5). For comparison the single wave scattering result is also shown and demonstrates that the essential features of the standing wave pattern are qualitatively grasped already by single scattering, but that for detailed quantitative analyses summation of all multiple scattering terms is necessary.

8.1.2 Application of Heller's theory: Origin of the standing wave pattern around a Lander molecule A particularly surprising result concerning the origin of standing wave patterns around middle sized molecules is discussed here, because it was analyzed with Heller's theory, although it does not concern an artificial structure: an STM picture and a ball model of the Lander molecule $C_{90}H_{98}$ are shown in Fig. 74a and e, respectively. The same Lander molecule was used already in Section 5.2.3 for contacting its inner board with a metallic step edge. STS-images of the standing wave patterns occurring around such molecules on a terrace are shown for different energies in Fig. 74b–d. As the molecule rests with the four legs on the Cu(111) surface and the inner board is geometrically decoupled from the substrate, it was expected that the outer shape of the molecule would determine the shape of the standing wave pattern. The scattering calculations (Fig. 74f–h) showed, however, that only the poly-aromatic inner board scatters the surface electron waves and the di-*tert*-butyl-phenyl-legs do not contribute.

8.1.3 Resonators The first example is a pair of parallel steps, which can be regarded as the visualization of the quantum mechanics text book example of a particle in a 1D box like the resonator type corral of Fig. 75. The lateral

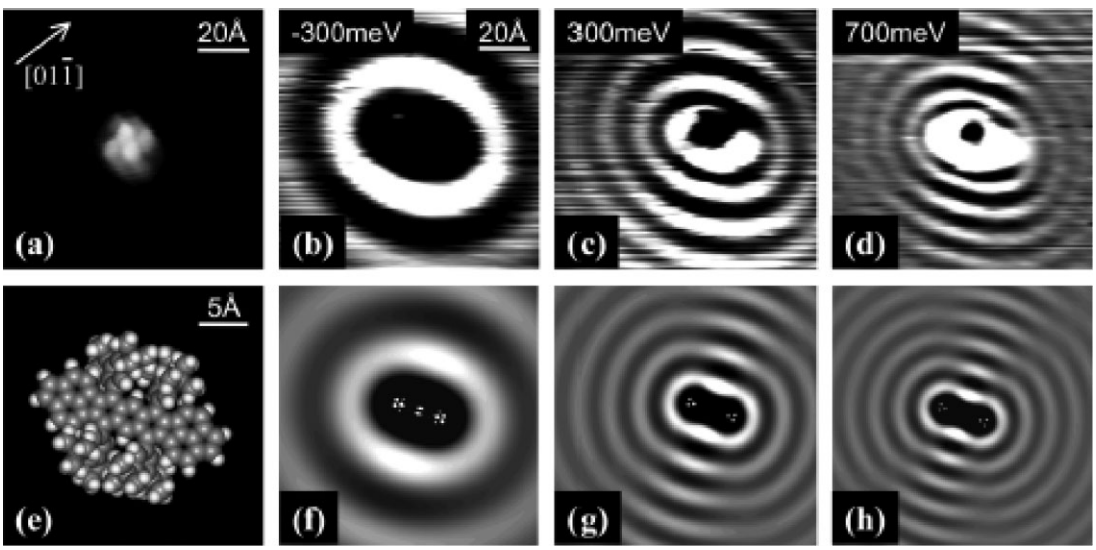

Figure 74 The standing wave patterns (b–d) around Lander molecules (STM image (a) taken at very small voltage) arise from the central board (see (e)) only. This is surprising as the board is geometrically decoupled from the substrate by the four *tert*-butyl-legs (e), which, although touching the substrate do not contribute to the surface wave scattering. The calculations with Heller's theory are shown for comparison with (b–d) in (f–h) (after Gross et al. [290]).

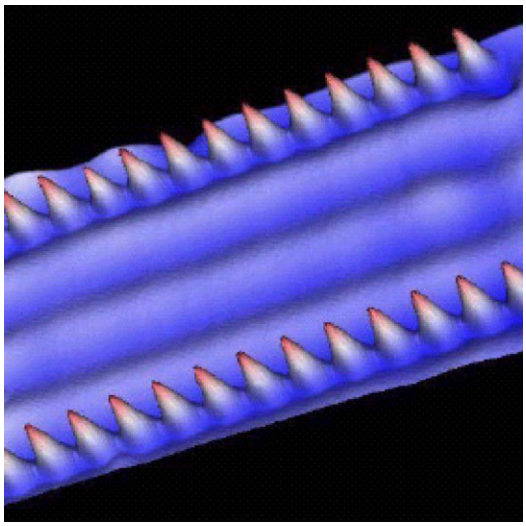

Figure 75 A textbook example for a particle in a box: an artificially constructed electron resonator consisting of two parallel rows of Ag adatoms, respectively, on a Ag(111) surface. Notice the standing wave pattern in the interior of the structure, which is visible in the STM image taken at low voltages and thus corresponding to a wavelength near the Fermi energy E_F. With d*I*/d*V* scans analogous pictures can be taken for a wide range of wavelengths (see Figs. 74 and 76; courtesy of Hla et al. [147]).

confinement can, however, also come from parallel steps extending over large distances at surfaces. Such steps are frequently found near places where the tip was dipped into the substrate. Line scans of such situations are shown in the upper part of Fig. 76 [291]: the left corresponds to a symmetric and the right to an asymmetric 1D box. The middle part shows the dependence of the standing wave patterns from energy as determined via STS-imaging. Notice the pronounced asymmetry in the pattern of the right structure, which has a step up at the right side and a step down on the left. This asymmetry is already indicative of a larger transparency of the down wall against scattering of the surface state electrons than in the step-up direction. In both cases the intensity appears highest close to the respective eigenstates. Although the authors used an analogous method to the optical Fabry-Perot interferometer for a quantitative analysis of these data [291], the theory of Heller can of course be applied as well. Both methods yield quantitative results for the different scattering powers of the up-walls and the down-walls.

By manipulating a single Co atom in the middle of similar Ag(111) terraces of different width the long discussed influence of surface state electrons on the formation on the surface Kondo effect was resolved [292]. The different positions of the Co atom

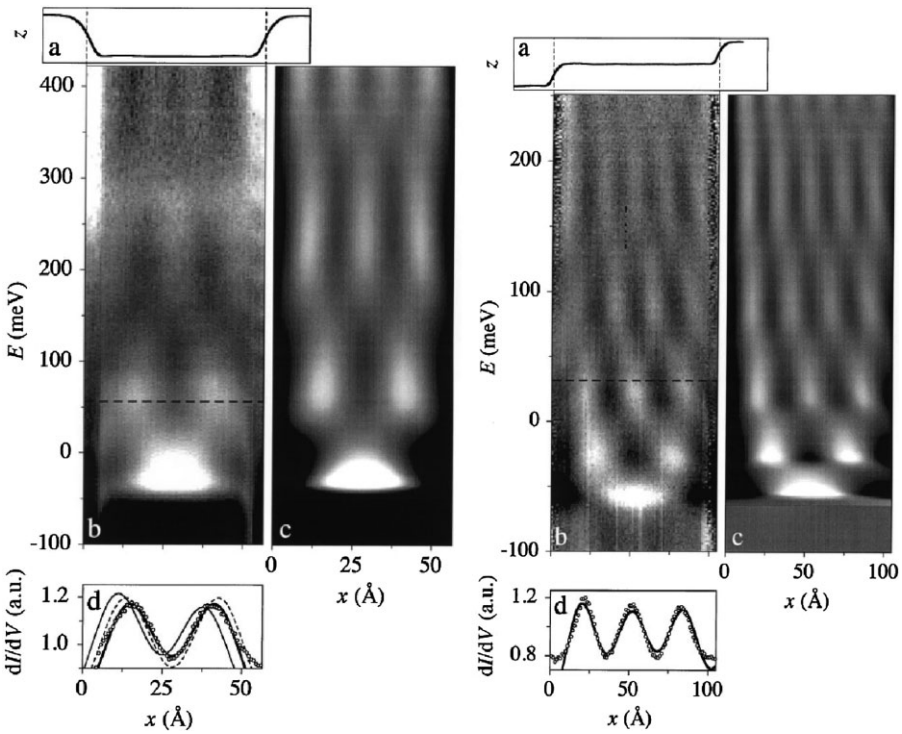

Figure 76 Energy dependence of standing waves determined via STS-imaging in symmetric and asymmetric 1D-boxes, left and right, respectively. Height profile is shown in (a). Notice that the intensity is highest close to the eigenstates of the systems. The asymmetry in the shape of the right structure can be taken into account in the scattering theory by Heller by assuming different scattering properties of the atoms at the step down and the step up. For comparison theoretical calculations (c) are displayed to the right of the experimental data (b). (d) shows a cut through the d*I*/d*V* where indicated in the d*I*/d*V* maps (b) (after Bürgi et al. [291]).

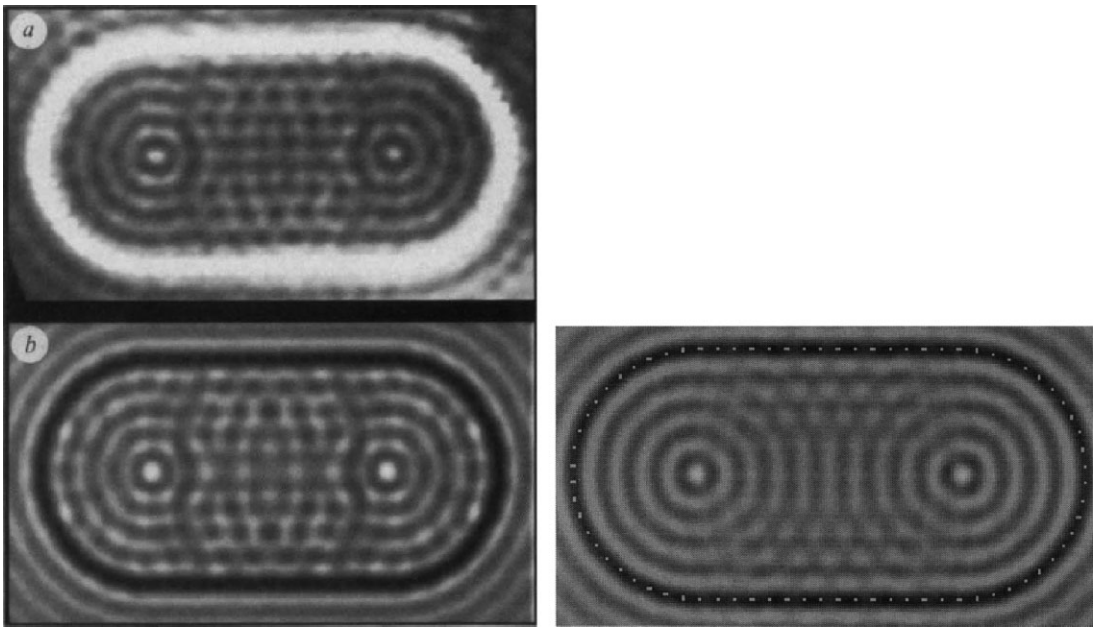

Figure 77 Quantum stadium: comparison of (a) experimental data with (b) multiple (left) and single (right) scattering calculations. Notice that the dominant pattern is already reproduced by simple single scattering theory, but that fine details observable in experiment need application of the full multiple scattering theory. For multiple scattering the agreement with experiment is perfect. (Parts (a) and (b, left) after Heller et al. [294], (b, right) courtesy of L. Gross).

correspond to a situation, where the surface state is "switched on and off" in experiments [26] very similar to analysis performed in theory. In general, tunnelling spectra obtained on and near Co atoms adsorbed on Ag(111) show a Kondo resonance that appears as a characteristic dip around the Fermi energy. The feature is present up to 1.5 nm around Co atoms adsorbed on terraces with the surface state onset in the occupied region of the density of states. On a narrow terrace, where the surface state onset lies in the unoccupied region of the density of states, it is only present up to 0.5 nm. This difference demonstrates directly the importance of the surface state electrons in the observation of the surface Kondo resonance. At some distance from the impurity the surface state maintains information on the coupling over greater distances than bulk states and reflection between surface steps hinders decay of the amplitude of the dip. Thus, when former measurements claimed that the surface state is important in formation of the Kondo resonance, because it can be measured at some distance away from the Kondo impurity, they were simply using the surface state as a probing channel. The unchanged Kondo temperature for terraces with and without surface state demonstrates that those claiming that mainly bulk states are responsible for the formation of the resonance were correct.

8.1.4 Circular corrals A circular corral consisting of 36 Ag adatoms on a Ag(111) surface showing circular standing waves in its interior is shown in Fig. 34. The very first circular corral was built by D. Eigler's group with 48 Fe atoms on a Cu(111) surface [22]. The analysis of the standing wave pattern was performed in [293] using cylindrical Bessel functions for a hard walled circumference, but can of course also be done with the scattering theory of Heller. The latter analysis [294] yielded for the scattering properties of the adatoms almost black scatterers and similar scattering properties were also found for Ag-adatoms on Ag (111) and other systems.

8.1.5 Quantum stadium In a search for quantum chaos, Eigler et al. also constructed a "quantum stadium", which is shown in Fig. 77. The stadium was built with 76 Fe atoms on a Cu(111) surface and had dimensions of 14.1 nm $\times$ 28.5 nm [295]. For this case, the full scattering theory of Heller had to be used, as the problem is not amenable to analytic solutions. Figure 77 compares the rather complicated experimental standing wave pattern of an imaging scan (thus the data correspond to the LDOS near E_F) with the results of the application of the full scattering theory. Remembering that the density of the Fe atom scatterers is not taken into account by the theory so that they appear black in the calculations, the agreement is practically perfect. The scattering properties of the Fe adatoms derived from optimum fitting are close to those of black scatterers. For didactic purposes, also the result of application of a single scattering calculation is shown in the lowest part: it shows that the main features of the rather complicated pattern in the interior of the stadium is already well described, but that reproduction of fine details requires application of the full theory. Thus for a coarse analysis of similar data the computationally very quick single scattering

method is advantageously applied. It should be noted that these elegant experiments and analysis did not yield evidence for quantum chaos within the stadium, probably due to the close to black dot behavior of the Fe atoms [295].

An elliptical corral structure with remarkable mirror properties also built by Eigler's group is discussed in Section 8.3 [293, 295]. For an extensive discussion of the standing wave patterns in rectangular corrals see [296].

8.2 Electronic properties of small chain and island structures

8.2.1 Chains with one sort of atoms The linear atomic chain serves in literally every text book on modern physics and solid state physics as didactic example, with which many basic physical concepts in electronic structure and dynamical properties of interacting systems can be introduced; the generalization to three dimensions often does not involve fundamentally new aspects. Topics discussed in connection with dynamic excitations concern phonons and magnons and with electronic properties involve the energy levels in small chains, the widening of the energy range with increasing chain length, the development of bands, the band dispersion, and the form of the wave functions. For both the dynamical and the electronic properties also the influences of single defects are often investigated.

Whereas physical chemists usually describe the electronic structure in the Hückel Picture [297], physicists use the tight binding (TB) approach [298], which, however, are intimately connected. In both cases the parameter α denotes the Coulomb integral at the site of the atom i

$$\alpha = -\int \mathrm{d}\tau \psi_i H \psi_i \tag{64}$$

and the parameter β the resonance or overlap or hopping integral

$$\beta = -\int \mathrm{d}\tau \psi_{i\pm1} H \psi_i, \tag{65}$$

whereby only nearest neighbor overlap is assumed to be important. (The ψ_i denote the relevant wave function at the site i and H is the interaction Hamiltonian).

The Hückel determinant for a chain of length $L = Na$ with N identical atoms at nearest neighbor distance a is of tridiagonal form with dimension N

$$\begin{vmatrix} -\alpha - E & -\beta & 0 & 0 & 0 \\ -\beta & -\alpha - E & -\beta & 0 & \\ 0 & -\beta & -\alpha - E & -\beta & \\ & & & & \\ 0 & 0 & 0 & & -\alpha - E \end{vmatrix} = 0 \tag{66}$$

and has as solution (for not too small N)

$$E_k = -\alpha - 2\beta \cos\left(\frac{\pi k}{N} + 1\right); \quad k = 1, 2, \ldots, N. \tag{67}$$

Using the Hückel determinant for a dimer ($N = 2$) the splitting of the initial atomic state (located at $E_a - \alpha$) in two states shifted by an amount of $\pm\beta$ is easily verified as is the splitting for a trimer by β, 0 and $-\beta$. It is important to realize that upon increase of N the levels become closer and closer, but that the asymptotic width for $N = \infty$ is 4β.

The tight binding picture used in solid state physics comes to an analogous result for the energy dispersion

$$E_k = -\alpha - 2\beta \cos(qa) \tag{68}$$

with q assuming the character of a wave vector ($|q| = 2\pi/\lambda$), whereby the counting of wave vectors differs according to the boundary conditions applied. For free boundary conditions the N q-values are restricted according to

$$qL = \pi k \text{ to the values } q = \frac{\pi k}{Na} \text{ with } k = 1, \ldots, N \tag{69}$$

whereas for periodic boundary conditions they are restricted according to

$$qL = 2\pi k \text{ to the values } q = \frac{2\pi k}{Na} \quad \text{with } k = -(N-2), \ldots, -2, 0, 2, \ldots, N. \tag{70}$$

The free electron wave functions of chains of length $L = Na$ (from $x = 0$ to $x = L$) are given by

$$\psi = \sin(qx) \text{ for } q = \frac{\pi k}{Na} \text{ with } k = 1, \ldots, N. \tag{71}$$

With the advent of atomic manipulation it has become possible to construct atomic chains of metal atoms of different lengths in an atom by atom manner on metallic surfaces and to visualize some of their basic electronic properties by STS. On first sight it appears surprising that metallic chains on metallic substrates would display behavior characteristic of isolated chains and it has been found that the necessary condition for sufficient electronic decoupling is the existence of a gap in the surface projected bulk density of states. Thus the first two systems investigated were NiAl(110) with Au adatoms [299] and Cu(111) with Cu adatoms [300]. The bulk projected density of states of Cu (111) is shown in Fig. 78. It exhibits at the Γ-point a gap between −1 eV (below the Fermi level) and 4.5 eV above E_F. A similar situation holds for NiAl(100).

Single Au atoms on NiAl(110) and single Cu atoms on Cu(111) exhibit in STS pronounced resonances at 1.9 and 3.2 eV, respectively. Manipulating a second atom to the nearest distance allowed by the substrate yields the expected splitting of this state due to the lateral interaction of the

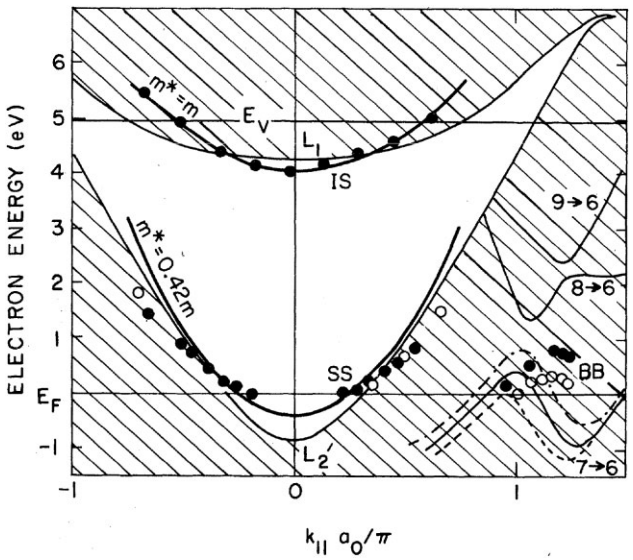

Figure 78 Surface projected bulk density of states of Cu(111) (shaded area). The parabolic dispersions of the surface localized electron state (SS) as well as the image state (IS) in the gap region are shown together with experimental data (after Hulbert et al. [302]).

atoms. Manipulation of a further atom towards the dimer leads to the expected three states. Extending the linear chain by adding further atoms leads to the observation of more energy levels and a further energetic splitting in accordance with the simple Hückel theory. The splitting for the dimer is nicely seen for the case of Au on NiAl(110) (Fig. 79a), whereas for Cu_2 only an average downward shift is observed, because an appreciable intracell diffusion of the dimers at the measurement temperature of 7 K smears out the spectroscopic results and also gives rise to is circular STM-appearance in Fig. 79b. For increasing chain lengths the splitting gets larger and more states are observed in the dI/dV signal. For example in the case of the Cu_7 chain four states were observed at 1.7, 2.0, 2.6, and 3.5 eV, respectively. dI/dV imaging at these energies yields pictures of the electron densities in the different states (Fig. 80), which are closely related to the wave functions (71) squared obtained in the simple theoretical pictures discussed above: notice that in the case of $N = 7$ the ground state $k = 1$ with a single lobe and the higher states $k = 2$, 3, 4 with two three and four density lobes are nicely seen. Cuts through the electron densities along the axis of the chain with $N = 15$ for $k = 3$–8 are presented at the right hand side of Fig. 80. The data for chains with lengths $N = 5$–15 and for $k = 3$–8 were collectively used to extract the 1D electronic band dispersion of the chains with the use of Eq. (69). The result is shown in Fig. 81 and corresponds to an electron band cantered at $E_a - \alpha = 3.1$ eV with an effective electron mass of $m^* = 0.68\ m_e$.

As outlined above, linear and cyclic chains differ with respect to mode counting (Eqs. 69 and 70). Therefore in a

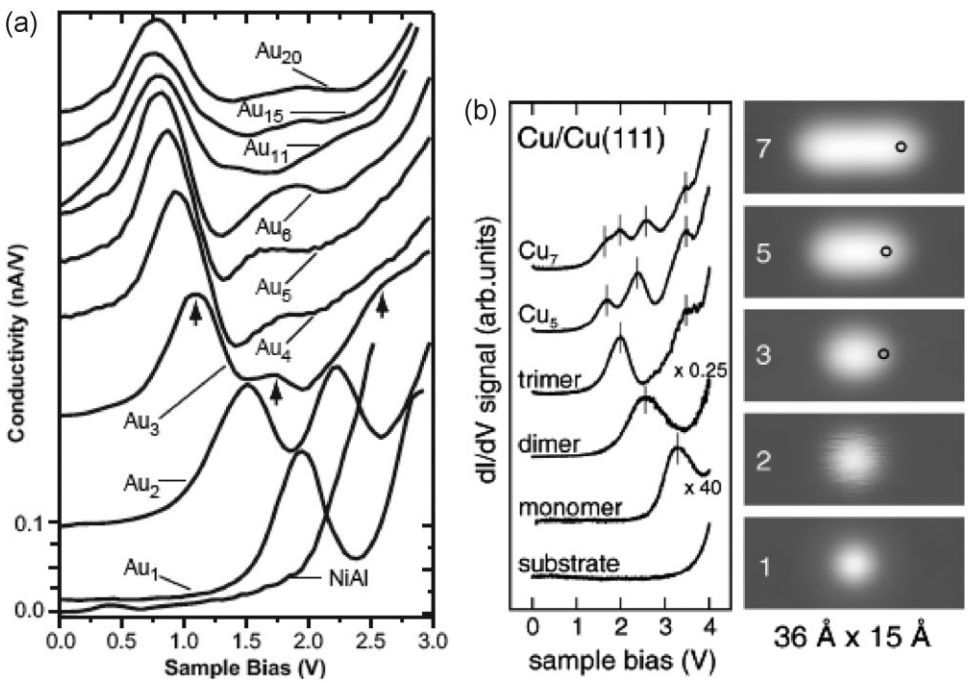

Figure 79 (a) Differential conductivity of bare NiAl(110) above Fermi energy and respective spectra for Au monomers, dimers, and linear Au chains up to $N = 20$. Notice the splitting of the monomer level for the dimer, the appearance of more states, and the gradual broadening of the energy range with increasing N. After Nilius et al. [299]. (b) The left side shows analogous dI/dV data for Cu-chains on Cu(111) and the right side presents STM images for the different chains. Notice the fuzzy and circular image of the Cu-dimer, which is due to intracellular diffusion even at the low substrate temperature of 7 K (after Fölsch et al. [300]).

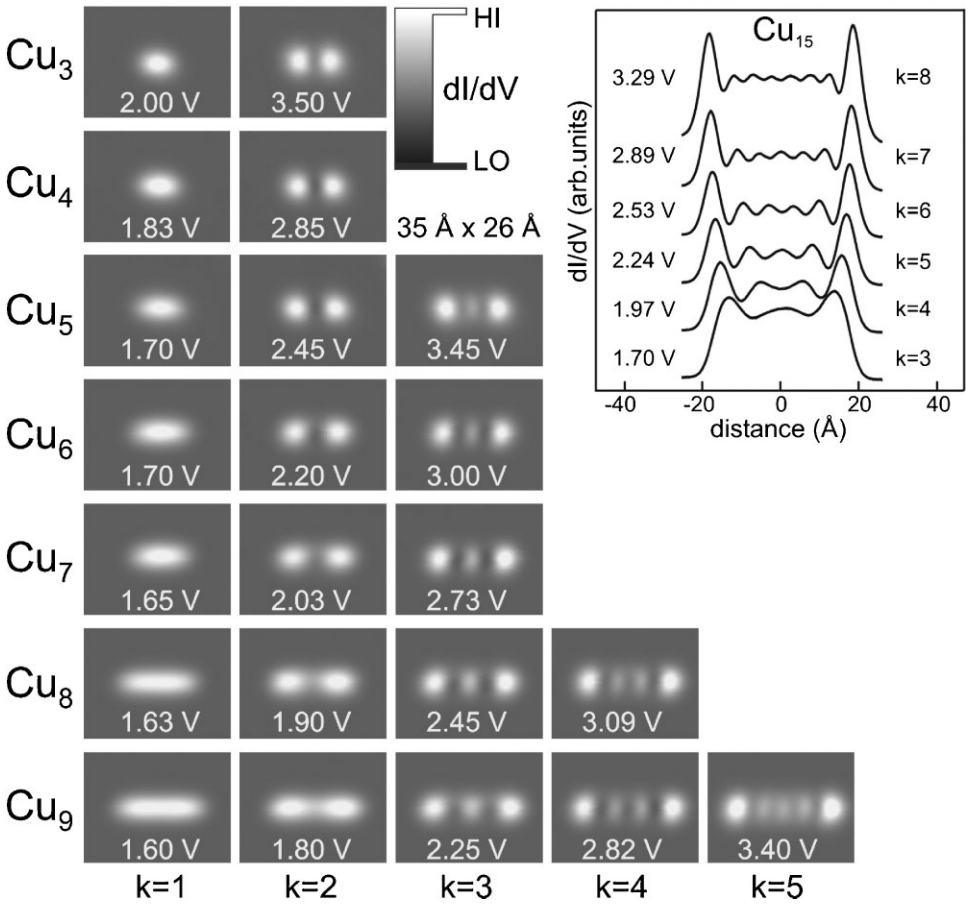

Figure 80 Left side: dI/dV maps of Cu chains with $N = 3$ to 9 for different states $k = 1$–5. Right side: cuts through electron densities along the chain axis for $N = 15$ and states $k = 3$–8 (after Fölsch et al. [300]).

cyclic ring, which is not closed, the situation should be analogous to the situations discussed above. For a closed ring, however, every second energy state should be missing. In closing and opening a ring by manipulating a single atom in and out of the rings perimeter, it should therefore be possible to switch off and on every second electronic state, which might have interesting consequences for applications. Furthermore, a very fundamental and often used concept in solid state physics would be eventually demonstrated in a direct way.

For a discussion of kinked and branched chains, which were also assembled atom by atom, see Ref. [301].

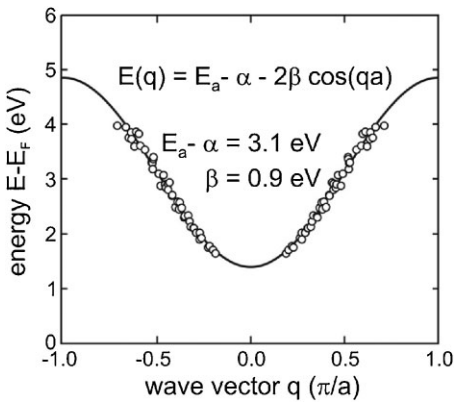

Figure 81 1D electronic dispersion of linear Cu-chains on Cu (111) as derived from the data shown in Figs. 79 and 81 (after Fölsch et al. [300]).

8.2.2 Electronic properties of linear atom chains with foreign atoms Due to their structural stability it is also possible to build up linear structures of Cu atoms on Cu (111) containing foreign atoms as shown by Fölsch et al. [303]. As an example in Fig. 82b an STM image of a Cu_3CoCu_4 chain is shown and compared to a Cu_8 chain, Fig. 82a. Corresponding tip height curves along the chain are shown in Fig. 82c. This single Co atom is visible, but constitutes only a small perturbation in the Cu chain, because the electronic Co–Cu coupling is very similar to the Cu–Cu coupling, as TB calculations have yielded. As the Co electronic energy is only slightly lower compared to the Cu value and the overlap is practically unchanged, quantum states delocalised over the entire chain are the consequence. These quantum states show only small changes in the

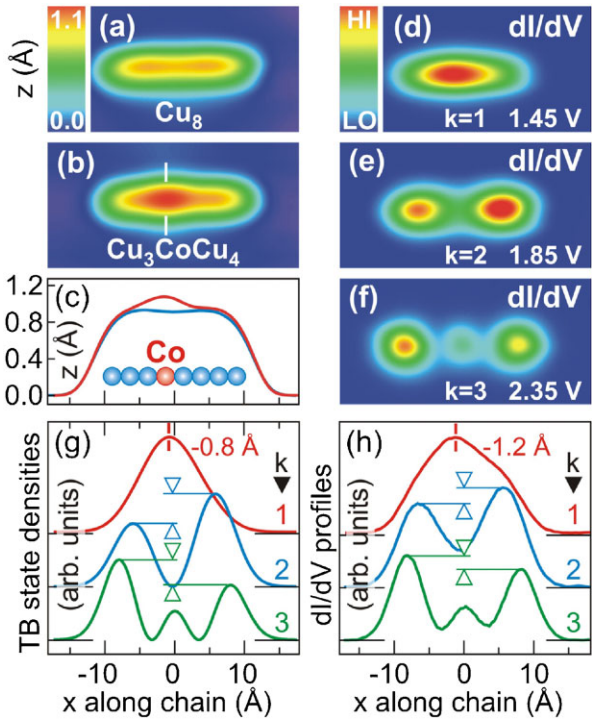

Figure 82 (a and b) Constant current images of Cu_8 and Cu_3CoCu_4 linear chains on Cu(111), respectively; (c) shows corresponding height profiles. (d–f) STS maps of the ground state as well as the first and second excited state of the Cu_3CoCu_4 chain. The main features of the measured LDOS profiles along the chain axis (h) are reproduced by TB calculations (g) (after Lagoute et al. [303]).

energies of the states against the Cu_8 chain and small but experimentally amenable modifications of their electron densities as seen in Fig. 82d–f and h, which could be qualitatively reproduced with TB calculations. It should be noted that similar investigations on Au chains containing Pd atoms yielded a quite different result, in that Pd forms a rather localized impurity state, which sort of cuts the Au chains apart [304]. The results in Refs. [303, 304] bear strong electronic analogies to the behavior of vibrational modes [305] with heavy impurity atoms in a lattice of light atoms on the one side and light atoms in a heavy surrounding, respectively.

8.2.3 Atom by atom assembled islands Size-specific cluster properties due to coordination and confinement effects are of fundamental and technological interest, as in transition metals, for example, new electronic, magnetic, and catalytic properties are expected. Clusters consisting of only a few atoms provide ideal model systems to explore how electronic properties evolve with size. To study islands of native adatoms on Cu(111) with increasing size assembled atom by atom with LT-STM were studied by Fölsch and coworkers [306]. Starting from a single Cu adatom, the formation of a series of quantum states is observed, which merge into the traditional Shockley surface state in the limit of large islands revealing the physical link between this property of extended surfaces, the quantum confinement in small adatom structures, and the sp hybrid state associated with the discrete adatom.

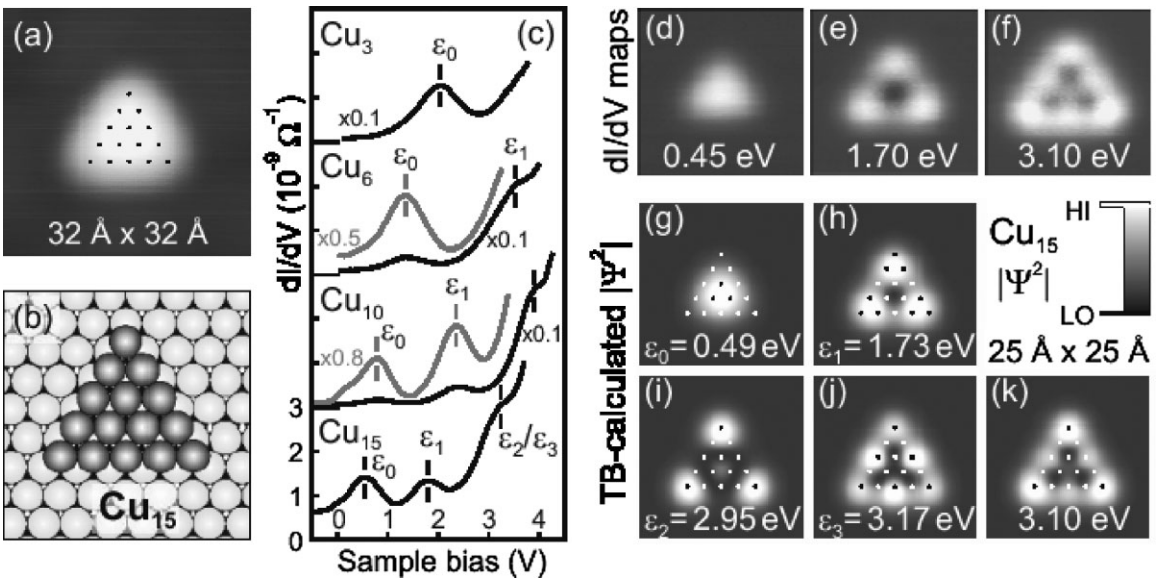

Figure 83 (a) Constant-current image of a Cu_{15}/Cu(111) island and (b) related sphere model. The dots in (a) visualize the atomic positions. (c) dI/dV spectra of triangular Cu islands comprised of 3, 6, 10, and 15 atoms (from top to bottom). For clarity, spectra are offset relative to the lowest curve. (d–f) Experimental dI/dV maps of the Cu_{15} island indicating the spatial LDOS variation of the quantum states. The data are well reproduced by the calculated squared wave function amplitude of the four lowest states (g–k). The map in (k) refers to an energy of 3.1 eV and results from the superposition of the resonance-broadened second (i) and third excited state (j) in good agreement with the experimental counterpart in (f) (after Lagoute et al. [306]).

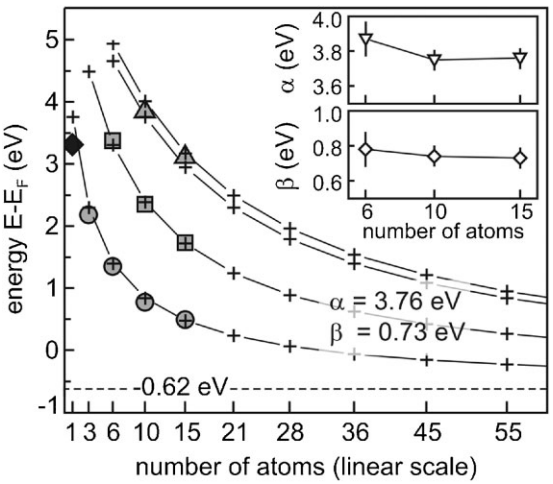

Figure 84 Measured energies of the ground state (circles), the first excited state (squares), and the high-energy shoulder (triangles) as a function of the number of atoms within the island; the energy of the adatom resonance is also indicated (black diamond). Energies of the four lowest states calculated with the TB parameters $\alpha = 3.76$ eV and $\beta = -0.73$ eV are marked by crosses. The dashed line at -0.62 eV marks the bottom of the TB energy band of a hexagonal 2D lattice with the intrinsic Cu–Cu spacing $a = 2.55$ Å and the α and β values as indicated.

The STM image in Fig. 83a shows a compact triangular island assembled from 15 Cu atoms; the corresponding sphere model in Fig. 83b visualizes the atomic arrangement of the structure. Figure 83c shows dI/dV spectra as a measure of the local density of states (LDOS) taken for the Cu_{15} island (bottom curve) as well as for smaller triangular islands comprised of ten, six, and three atoms. The data reveal that these atomic-scale structures exhibit unoccupied quantum states showing a downward shift in energy and a decreasing level spacing with increasing size of the structure. The measured state densities of the respective quantum states of the Cu_{15} island indicate a ground state with a single lobe in Fig. 83d, while for the first excited state in Fig. 83e the square of the wave function amplitude is cantered close to the corners of the triangle. The state density map of higher excited states in Fig. 83f indicates a more complex LDOS distribution, which peaks at the corners and is nonzero along the sides of the structure. These experimental observations are perfectly reproduced by a simple tight-binding (TB) parameterization, in which the secular determinant representing the two-dimensional (2D) structure is solved within the simple Hückel scheme. The state densities are reproduced by extracting the *linear-combination-of-atomic-orbitals* coefficients from the determinant (compare the experimental data in Fig. 83d–f and the calculation shown in Fig. 83d–k) and the quantum state energies are obtained from the eigenvalues. Figure 84 documents the agreement between the measured peak energies (open symbols) and the calculated energies of the four lowest states (crosses) for different island sizes defined by the number of atoms. This analysis provides direct insight into how a sp-derived Shockley surface state emerges from the coupling between sp hybrid adatom resonances [306]. Localized states associated with native adatoms as well as quantum confinement in atomic-scale structures will exist for various other metal systems known to exhibit surface states in the pseudo gaps of the projected bulk bands. Simple TB modeling is instructive to explore, how electronic properties evolve when building artificial surface structures atom by atom, which is essential for the ultimate goal of *tailoring* magnetic and electronic surface properties by controlling size, geometry, and composition at the atomic level.

8.3 Magnetic structures

8.3.1 Kondo effect The Kondo effect is an important many body effect in solid state physics [298, 307, 308]. It occurs in solid bulk when magnetic impurity atoms are embedded in a nonmagnetic metal and leads to the very well-known increase of the electric resistance of the dilute alloy at very low temperatures so that a resistance minimum is observed at a characteristic temperature, the Kondo temperature T_K. This effect is absent for nonmagnetic defects, where the alloys resistance levels off to a constant value (superconductors excepted). In Kondo systems also anomalies in specific heat and magnetic susceptibility are observed. The origin of the Kondo effect lies in spin-flip scattering processes of the delocalized conduction band electrons at the unpaired electron of the magnetic defect atoms. Below T_K the conduction electrons form an antiferromagnetic screening cloud around the magnetic defect. The impurity electron can quantum mechanically tunnel from the impurity and escape, if its energy lies above the Fermi level. However, taking an electron from the localized magnetic impurity state to an unoccupied state at the surface of the Fermi sea usually needs energies ε_0 of several electron volts and thus is classically forbidden. The Heisenberg uncertainty principle, however, allows such configurations for very short times of the order $\hbar/\varepsilon_0$. In this time another electron from the Fermi sea can tunnel towards the impurity, whereby the spin may point in the opposite direction so that the initial and final states at the impurity may have different spins. In the electronic structure a many-body non-magnetic ground state at the Fermi edge is formed, which in spectroscopic experiments gives rise to a narrow structure in the density of states at the Fermi energy level, called Kondo resonance [309]. The Kondo state is very effective in scattering electrons with energies close to the Fermi edge and as these electrons are responsible for the low temperature conductivity of a metal, Kondo state scattering influences the resistance appreciably, this being the reason that the Kondo effect was first observed in low temperature resistance measurements.

In STS, Kondo resonances can show up according to the interaction of the (spatially and energetically) localized electron density of the magnetic atom with the continuum of conduction electrons with different shapes, the so called

Fano profiles [310]:

$$\frac{\mathrm{d}I}{\mathrm{d}V} \propto \frac{(E+q)^2}{E^2+1} \tag{72}$$

with

$$E = \frac{eV + E_0}{kT_\mathrm{K}} \quad . \tag{73}$$

E_0 denotes the position of the resonance relative to E_F and the Fano coupling parameter q determines the line form of the resonance. T_K denotes the Kondo temperature of the system.

The first two examples of Kondo resonances observed with STM concerned Ce atoms on Ag(111) [311] and Co atoms on Au(111) [312]. dI/dV spectra taken over single Ce atoms on Ag(111) at low temperature yield a clear minimum at the Fermi energy, Fig. 85a [311]. According to the STS theory of Ref. [309], the probing of a localized state immersed in a continuum by STM can proceed either through the localized state or directly into the continuum leading to quantum interference. As in the case of Ce/Ag (111) the transition into the localized state approaches zero ($q \sim 0$) this results in a dip or anti-resonance as first elucidated by Fano [310]. Analogous STS-results obtained from Co atoms on Au(111) are shown in Fig. 85b. Here the higher transition rate into the localized state ($q \sim 0.7$) results in a typical asymmetric Fano line shape exhibiting a minimum and a maximum [312]. The q values were obtained by fitting the experimental data with Eq. (72) modified appropriately for the STS case [309].

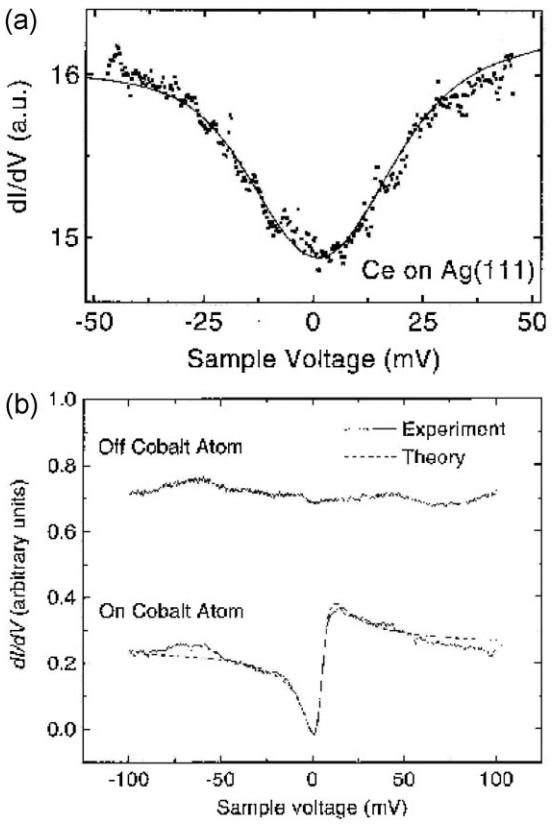

Figure 85 (a) dI/dV spectra of a Ce impurity on Ag(111) for an energy range around the Fermi energy showing a Kondo resonance. The solid line denotes a calculation using the Anderson single impurity model (reprinted from Ref. [311], with permission from APS). (b) The dI/dV spectra of a single Co atom adsorbed on a Au (111) surface is shown together with a calculation with a modified Fano theory ($q \sim 0.7$) (reprinted from Ref. [312]).

8.3.2 Dimer interaction of Kondo systems The lateral manipulation technique has enabled investigations of the coupling between several magnetic atoms exhibiting Kondo resonances. If a second magnetic impurity brought close to another one, magnetic interactions will become important, which modify the Kondo resonance: these interactions can arise from magnetic dipolar coupling, direct exchange due to overlap of d-orbitals, or the Rudermann–Kittel–Kasuya–Yosida (RKKY) interaction, which is an indirect spin–spin interaction mediated by conduction electrons of the host.

Artificially created Co dimers on Au(111) showed an abrupt disappearance of the Kondo signal at separations less than 0.6 nm (Fig. 86) resulting from a reduced exchange coupling between Au conduction electrons and ferromagnetic Co dimers [313]. Co on Cu(110) was investigated in an analogous way and it was found that compact dimers (atomic

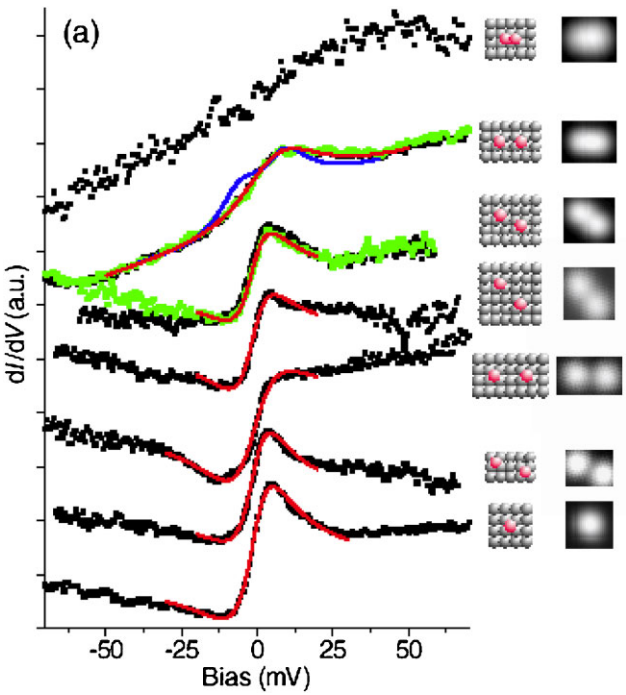

Figure 86 Behavior of Kondo effect for Co dimers artificially created with different distances on a Cu(100) surface. Whereas the compact dimer does not show a Kondo signature, at twice the distance a Kondo signature is observed, which, upon increasing the atomic distance, approaches that of an isolated Co atom. On the right side the different dimers are shown (after Wahl et al. [314]).

distance 0.256 nm) did not exhibit a Kondo signature but that at separations of 0.512 nm and larger a Kondo resonance occurred, which for large distances agreed with that of an isolated Co atom. Theoretical calculations reproduced this transition from ferromagnetic to anti-ferromagnetic coupling [313]. It should be noted that the different Co distances investigated here were obtained by a very peculiar manipulation method: the different dimers were fabricated by first forming Co-carbonyl complexes; the CO ligands inhibit nucleation and island formation and allow even the growth of chains. The CO ligands are removed after formation of the intended structure by tip induced dissociation [314].

Forming a linear Co trimer with the anti-ferromagnetically coupled Co-dimer (atomic distances 0.512 nm) yields a Kondo signature again and was interpreted as formation of a collective correlated state. Using lateral manipulation also different Cr trimer arrangements were fabricated on Au (111). The measurements showed that only some of the trimer configurations exhibit Kondo resonances [315].

8.3.3 Quantum mirages using the Kondo signature As one of the most striking examples of a man made structure with specific properties, elliptic quantum corrals have been constructed by Manoharan et al. [293, 295] and demonstrated that they can act as mirrors for electron waves: by dI/dV spectroscopy the Kondo resonance of a magnetic atom located in one focus was detected at the other focus. Figure 87 shows an elliptical quantum corral made of 36 cobalt atoms positioned on a copper (111) surface. When a magnetic cobalt atom is placed at a focus point of an elliptical corral (upper left), the Kondo resonance also appears at the other focus (lower left) while it does not when the atom is moved out of the focus. The projection of information from an atom to another place where there is no atom was named the "quantum mirage" effect, a possible application for data transfer in future nanoscale electronics is discussed [293, 295].

8.4 Chevrons, quantum cascades, and demonstrations of functional systems The hitherto largest functional structures with up to 545 ad-particles (!) able to perform logical operations were assembled by manipulation of CO molecules on a Cu(111) surface with a STM by Heinrich et al. [129]. Thereby a cascade effect was employed where the motion of one CO molecule caused the subsequent motion of another CO molecule, which itself caused a further CO molecule to move and so on. Linear arrangements of such a cascade can serve to transport one bit of information from one place to another. The crossed combination of several cascades made it possible to built logical gates and other devices. The base unit consists of three CO molecules initially arranged in a bent line, see Fig. 88. This configuration decays to an energetically favorable triangular arrangement. The underlying process was identified to be quantum tunnelling and temperature independent below 6 K. At higher temperatures the hopping rate is thermally activated with an anomalously low Arrhenius prefactor, resulting from tunnelling from an excited vibrational state. The hopping rate is furthermore sensitive to other surrounding adsorbates or defects and also dependent on the direction. These units, which are called "chevrons" can then be combined into a linear arrangement

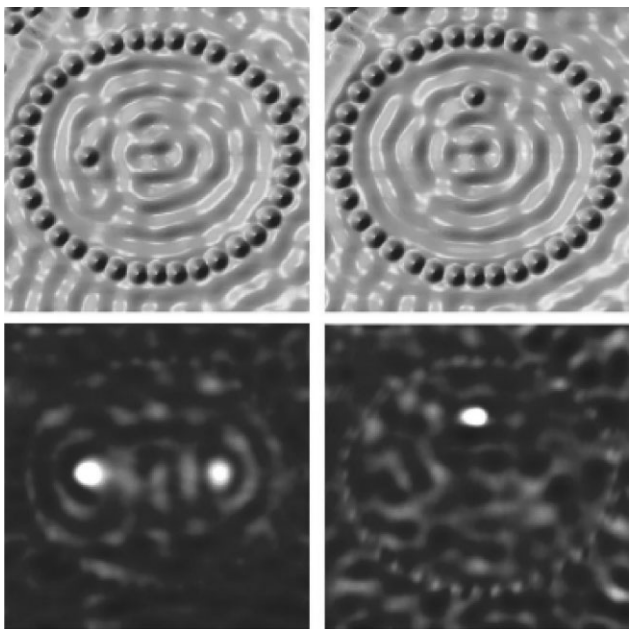

Figure 87 In the upper row STM images of an elliptical corral built with 36 Co atoms at its boundary are shown. If a single Co atom is placed in one of the foci of the ellipse (upper left), not only the single atom in the focus, but also its mirror image in the other focus shows up in STS maps ("quantum mirage", lower left). If the Co atom is not placed in a focus the mirage is missing (right side) (after Manoharan et al. [295]).

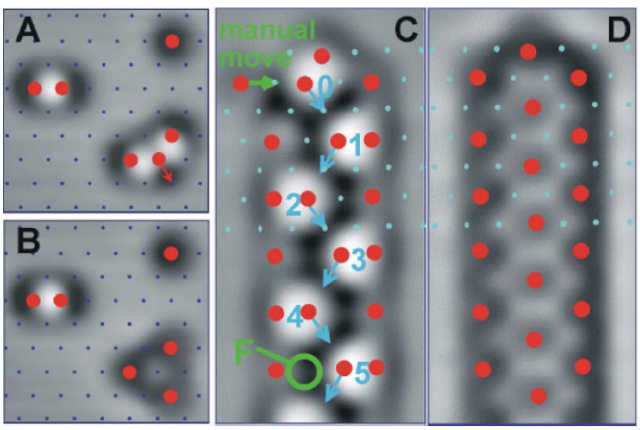

Figure 88 STM images showing CO molecules on a Cu(111) surface at 5 K. Solid red circles denote locations of CO molecules and blue dots surface-layer Cu atoms. (a) An isolated CO molecule, a dimer, and a trimer are shown. (b) After a few minutes the trimer has decayed into a new configuration. (c) A molecule cascade before and (d) after being manually initiated (reprinted from Ref. [129]).

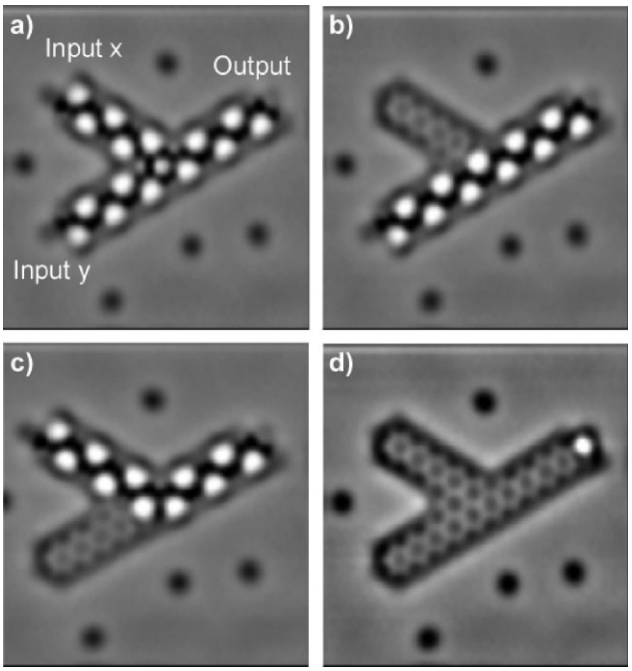

Figure 89 (a) Initial setup of a logic AND gate. Either input *y* (b) or input *x* (c) can be triggered first, and subsequently the other input, resulting in a logic 1 at the output (d) (reprinted from Ref. [129]).

yielding a cascade and with two cascades logical gates can be constructed, see Fig. 89. The combination of basic logical units then made it possible to construct a two-input sorter and a three-input sorter, the latter consisting of 545 CO molecules (Fig. 90). The decay time of a single chevron is typically 5 min at 5 K resulting in an operating time of about 1 h for the three input sorter. After the one-time operation the device needs to be reset by moving the CO molecules back into their initial position, which typically needs several hours.

9 Manipulation on thin insulating film

9.1 Growth and properties of thin insulating films Prospects for the application of atomic/molecular manipulation concern the formation of electronic and mechanical devices on the atomic or nanometer scale ranging from monomolecular devices [316] to structures build up atom by atom. Experiments on metallic surfaces face the problem that an atom or molecule adsorbed on a metal undergoes a strong electronic interaction with the reservoir of metal electrons. Therefore the electronic and mechanical properties of adsorbates are appreciably modified on metal substrates. With regard to applications it will be very important to decouple adsorbates electronically from the substrate, or to have the possibility to vary the strength of the electronic coupling. Decoupling from the substrate is obviously indispensable for devices like atomic relays, but is certainly also important for nanoscale systems.

Ultrathin films of insulating materials represent a convenient way to perform these kind of experiments.

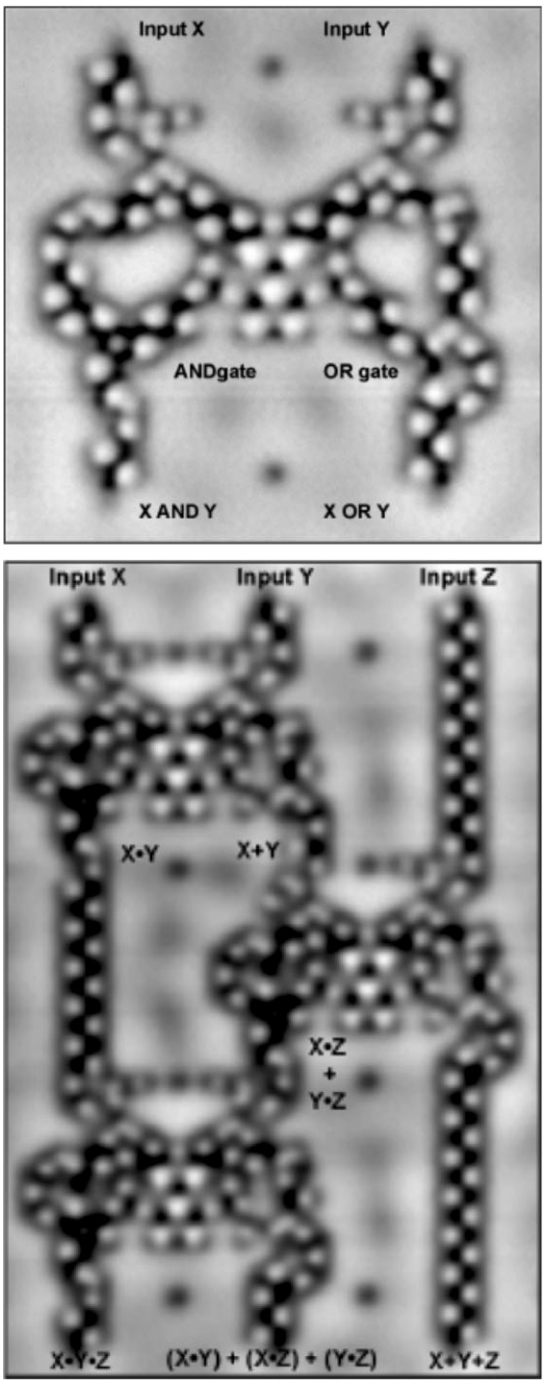

Figure 90 STM images showing a two-input sorter (top) and a three-input sorter (bottom) consisting of 545 CO molecules (reprinted from Ref. [129]).

Not only can the molecules be significantly decoupled with varying degree from the substrate by changing the thickness of the insulating layers, but it is also possible to continue to use STM to perform the experiments. For bulk insulators atomic force microscopy would be necessary, a technique, which has been improved strongly in the last few years, but its application in atomic manipulation is still very restricted [125].

Therefore application of the STM manipulation techniques is presently pursued for thin films of insulators like alkali halides and simple oxides [269, 317–320].

The ability of the STM to operate on insulating films relies on the fact that a finite density of electronic states extends from the metal substrate through the insulating film into the vacuum, allowing for a very small but still measurable tunnelling current. For example insulating layers of NaCl of up to a thickness of 4 ML can be routinely imaged with the STM [321] even with atomic resolution. These NaCl films can be grown in a surprisingly perfect and defect free manner on metal substrates like Cu(111) and Cu(100), with islands several micrometers in size extending smoothly even across substrate defect steps [320]. It has been shown by photoemission that NaCl layers of a thickness equal to or higher than two monolayers show a band gap with a width similar to bulk material. As an example an extended NaCl (100) island on Cu(111) is shown in Fig. 91 [317]. Upon deposition at room temperature and higher the growth starts with double-layer thickness. On this bilayer smaller islands grow to form a third layer on top. The bilayer islands show perfect nonpolar step edges.

The system NaCl on Cu(211) is of special interest as it is an example of a strong interaction of the ionic material, which is commonly believed to be rather inert, with the metal leading to a strong surface reconstruction. For substrate temperatures below 200 K chainlike NaCl islands with monatomic height can be grown. These NaCl chains can be cut by lateral manipulation, whereby the NaCl entities are pushed [317]. With growth temperatures exceeding ~300 K – where the kink site mobility for bare Cu(211) becomes appreciable – the (532) surface, which can be described as a kinked (211), reorganizes drastically upon NaCl submonolayer deposition [322]. This behavior is in sharp contrast to the common growth features of alkali halides on close-packed metal surfaces [320], which is characterized by weak interactions between the inert overlayer and the metal substrate. On Cu(211) a regular 1D hill-and-valley structure is formed, which is composed of (311) and (111) facets [323]. The facets are built up by incorporating additional Cu atom rows along the intrinsic step direction. Note that the resulting (311) facet is also a stepped plane, which exhibits a reduced step separation of 0.423 nm. Noticeably, NaCl grows selectively on the (311) facets only and thereby creates a regular surface pattern with alternating stripes of NaCl-covered areas and bare metal facets. The characteristic size of this surface pattern (i.e., the periodic facet separation) can be adjusted by the growth temperature and ranges from ~3 nm at 300 K to 23 nm at 600 K [323]. The restructuring process observed here is driven by an exceptionally high energetic stability of the NaCl(100)-covered (311) facets, which is due to Coulomb interaction between the ionic charges of the alkali halide layer and electrostatic dipoles associated with the steps of the metal template [322–324]. The dipoles at the steps arise from the well-known Smolouchowski smoothing effect of the electron charge [325] and have also shown to be responsible for bending of the NaCl layer across Ag(111) step edges [326]. This 1D patterning process should also be applicable to other ionic insulator/metal combinations since it is based on a stability criterion with rather general requirements: (a) a charge-modulated template – this is an inherent feature of stepped and kinked metal surfaces [325] and (b) lattice matching between the ions of the film and the charge modulation of the metal template. Due to the selectivity of the alkali halide-induced faceting process a modulation in surface chemical composition is established. Hence, one obtains a masking effect of the surface on the nanoscale, which can be controlled by the growth temperature. This provides a preformed substrate for the lateral structuring of subsequently deposited material by selective decoration [327]. Starting from a regularly kinked vicinal Cu(532)-surface the formation of regular pyramids was demonstrated recently. In this way 2D regular patterning can be achieved as only two sides of the pyramids are covered with NaCl leaving a 2D array of metallic areas, which can be used for further reactions [322]. Another noteworthy system consists of MoO_3 nanocrystals, which can be grown on a MoS_2 substrate. They can be machined with the tip of an AFM and a notch/latch system on nanoscale has been demonstrated [328]. Noticeably these experiments were performed at room temperature in a nitrogen filled glove box. These examples have important implications for further manipulation work: they show that the insulator films can be machined. Self-assembly can give rise to regular structures with alternating insulating and metallic parts. This could be used for example such that a conducting molecule is manipulated to lie on the insulator with one end touching the metal. The STM tip might then serve as second electrode; thus conductivity measurements may become feasible along the molecule.

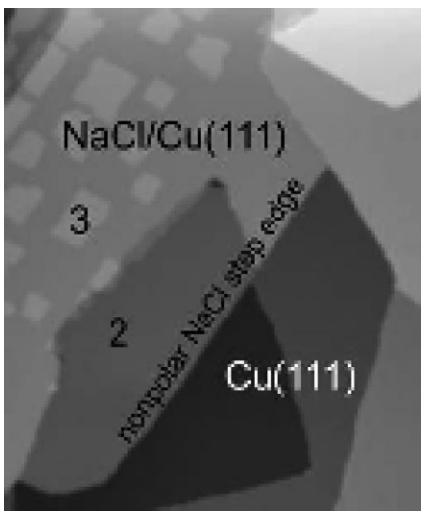

Figure 91 STM picture of an NaCl island on a Cu(111) substrate (210 nm × 250 nm). Numbers indicate the number of NaCl-layers. Substrate defect steps are overgrown in the carpet mode. Notice the straight nonpolar island step edges (after Repp [317]).

Early theoretical studies concerning manipulation experiments on insulators with Au atoms and the formation of Au dimers and trimers on NaCl(001) were performed by Bouju et al. [329]. Noticeably several difficulties have been foreseen, which result from the fact that the binding energy between metal atoms is in general much higher than the binding between the metal atoms and the insulator substrate.

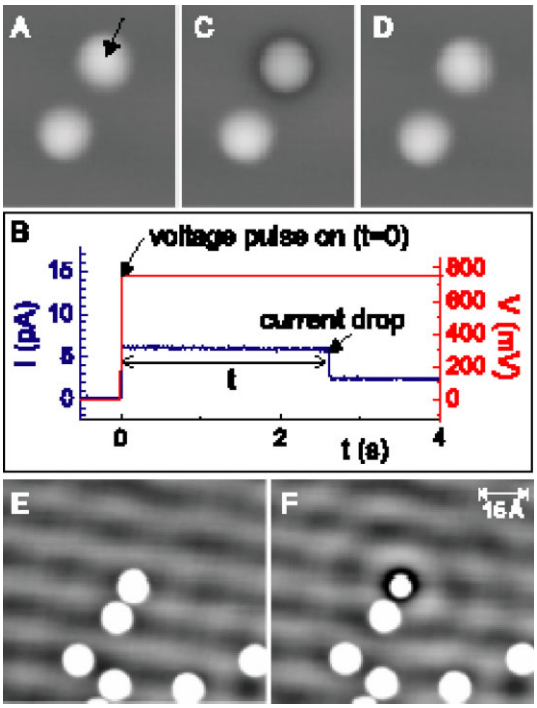

Figure 92 Manipulation of the Au adatom charge: (a) Image of two Au atoms. (b) A positive voltage applied to the sample with the tip positioned over the atom indicated by the arrow causes after some time a sharp drop in the tunnelling current. (c) The manipulated Au has a different appearance as it has adopted a negative charge. (d) Application of a negative pulse causes the Au atom to switch back to the neutral state. (e) Neutral Au atoms do not scatter the interface state electrons of NaCl/Cu(111), whereas (f) negatively charged Au atoms do (after Repp et al. [318]).

Thus the formation of metastable structures like atomic wires is more difficult than on metallic substrates. Analogously, the strong attractive interaction between the STM tip apex and the adsorbates might result in unwanted transfers of the metal atom to the tip even before the lateral force is large enough to move the adatom. These difficulties were indeed encountered in the experiments of Repp et al. [318] and Heinrich et al. [62]. Future successful manipulation experiments and the build-up of atomic scale structures will thus strongly rely on the rightly selected combination of the metal substrate and insulating film materials.

9.2 Manipulation of atomic charges LT-STM experiments with individual Au atoms adsorbed on a double layer of NaCl on Cu(111) showed that the metal atoms could be reversibly switched by IET between their neutral and negatively charged states. For this purpose, the tip is positioned above a Au atom and a positive voltage pulse $\geq$0.6 V is applied to the sample and the current is measured as a function of time. A sudden current drop indicates a change on the surface and an image taken afterwards shows that the Au atom has changed its appearance but is still found at the same place as can be seen from Fig. 92a–c. By applying another negative pulse of -1 V, the manipulated atom can be switched back to the initial state (Fig. 92d). A comparison of Fig. 92e and f shows that the new Au state scatters the interface state present at the Cu/NaCl boundary strongly, which indicates a more spread-out charge density as expected for a negatively charged atom. DFT calculations (Fig. 93) confirmed that both neutral and negative states are stable on NaCl and that in both cases the Au atom resides above a Cl^- ion (Fig. 93a and d). The charging process is connected with strong relaxations of the substrate: the Cl^- ion below the adatom is forced downwards by 0.6 A and the surrounding Na^+-ions move upwards by about the same amount (Fig. 93d). This relaxation creates an attractive potential for the extra charge on the Au, which is further stabilized by the screening charge in the metal and the electronic polarization of the NaCl film.

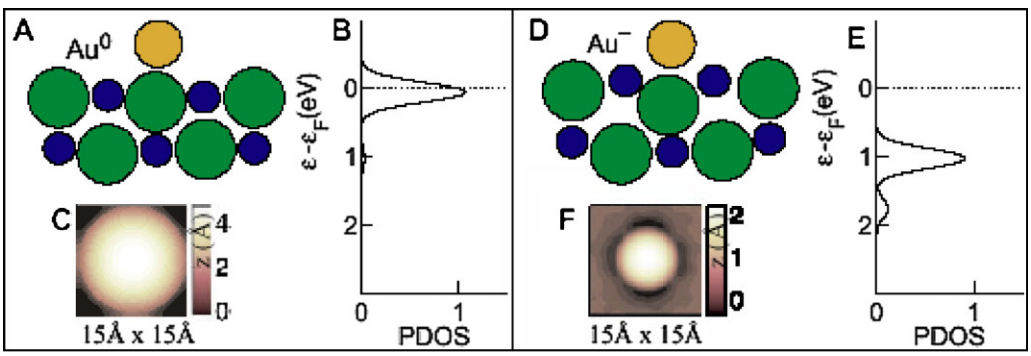

Figure 93 DFT calculations of the geometric and electronic properties of the Au atoms on NaCl/Cu(111) in the neutral (a–c) and the negatively charged states (d–f). In the sphere models the Au, Cl^-, and Na^+ species are coloured yellow, green, and blue respectively. (c) and (f) demonstrate reproduction of the experimental result concerning the STM images of Au in both states. (b and e) The 6s derived state is partially occupied in the neutral Au and fully occupied in its negative state (after Repp et al. [318]).

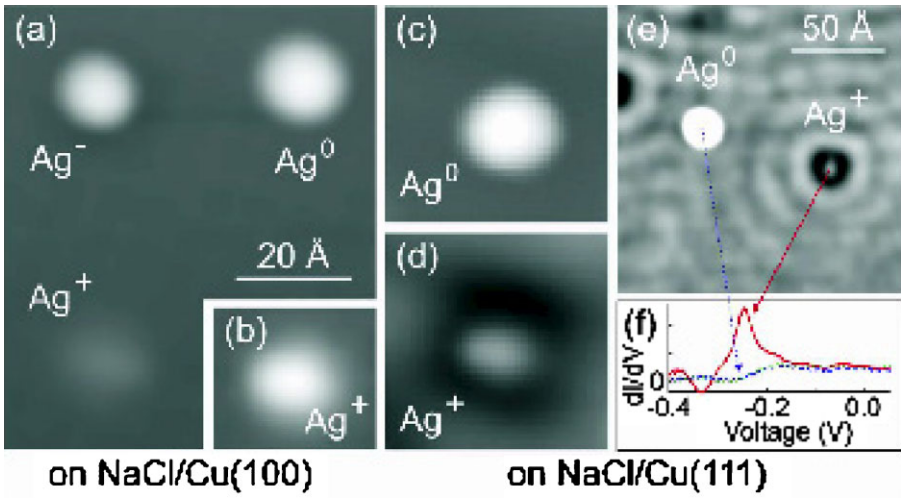

Figure 94 (a and b) STM images of a Ag atom on NaCl/Cu(100) in its neutral, negative, and positive state; (b) shows Ag^+ with enhanced contrast. (c–f) Analogous results were also obtained for Ag on NaCl/Cu(111) (after Olsson et al. [319]).

Recently, both on NaCl double layers on Cu(111) and Cu(100) not only neutral Ag^0 and negatively charged Ag^- atoms have been observed, but also positively charged Ag^+. Switching from Ag^0 to Ag^- could in analogy to the case of Au be achieved by electron tunnelling at voltages ≥ 1.3 V and switching back by hole tunnelling at voltages < -0.2 V. Switching from Ag^0 to Ag^+ was possible at voltages < -1.3 V and reverse switching at voltages ≥ 1.5 V. Images of all three Ag states are shown in Fig. 94. Whereas the negative Ag state is associated with a similar local reconstruction as for the case of Au^- the reconstruction around Ag^+ appears roughly inverted [319].

These results are of importance, as it is speculated that the control of charge states of single adatoms will allow for controlling the current in molecular scale devices.

9.3 Manipulating spins

9.3.1 Spin IETS Magnetic properties of structures at the nanometer scale are of high interest due to possible applications in new technologies like for example classical and quantum computing as well as data storage and handling. The magnetic properties are generally very sensitive to structural effects. On the atomic and nanoscale they are therefore expected to be strongly dependent on the local chemical and geometrical environment. With a LT-STM system placed in a high magnetic field B (up to 7 Tesla) it was shown by Heinrich et al. [62] that the spin excitation spectra of individual Mn atoms adsorbed on a surface can be measured. The substrate used was a partially oxidized NiAl(110) surface containing areas of bare metal and areas of Al_2O_3 islands (Fig. 95a and b). The technique applied is IETS and – in analogy to vibrational spectroscopy – the tunnelling electrons lose energy due to spin flip excitations. Ideally, the signature of Zeeman splitting in spin-flip IETS would be a step up in conductance at an energy, which is proportional to the applied magnetic field. Due to finite experimental resolution caused by

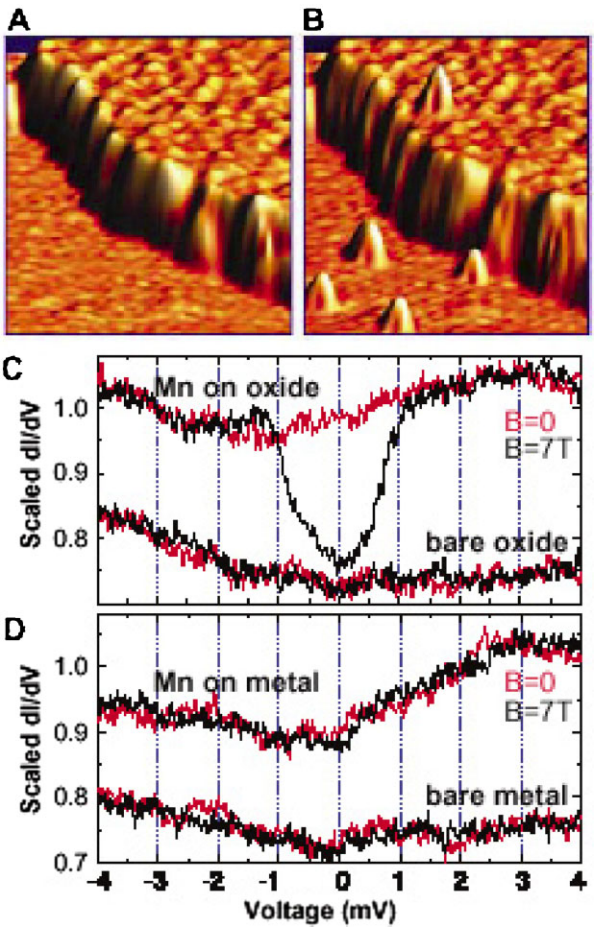

Figure 95 (a) STM constant-current image of a NiAl (110) surface with the edge of a Al_2O_3 island (20 nm $\times$ 20 nm). (b) Same area after deposition of Mn atoms. (c and d) Conductance spectra of Mn atoms on the oxide and the bare metal, respectively, proving that spin flip excitations occur, only if the Mn atoms are decoupled from the metal (after Heinrich et al. [62]).

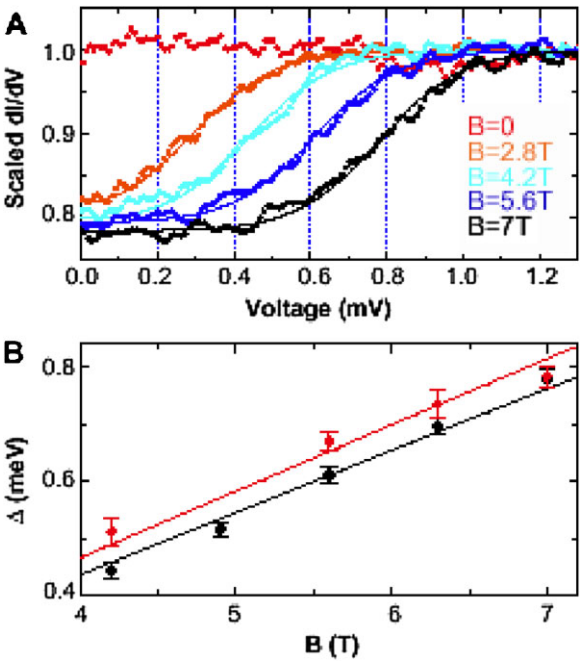

Figure 96 (a) Conductance spectra for isolated Mn atoms on aluminum oxide as function of magnetic field. Solid lines correspond to the step model described in the text with temperature broadening taken into account. (b) Magnetic field dependence of the Zeeman energy as derived from (a) (black points). The red points stem from Mn atoms near the step edge of the oxide. The difference is attributed to the sensitivity of the magnetic effects to the local surrounding of the Mn atoms (after Heinrich et al. [62]).

temperature effects as well as instrumental influences like the ac voltage modulation and noise, the expected conductance step up is broadened and smoothened as shown in Fig. 95c. The shift of the conductance step with increasing magnetic field is nicely visible in Fig. 96a (the curves are symmetric for negative biases as typical for IETS spectra, compare Fig. 95c, which shows the full curve for $B = 7$ T).

This behavior corresponds to Mn atoms on top of an Al_2O_3 island and is slightly dependent on the local surrounding of the Mn atom. It has to be stressed that the effect is completely absent for Mn atoms on the bare metal surface (Fig. 95d), which again demonstrates the importance of the electronic decoupling due to the oxide layer. The magnetic field dependence of the Zeeman energy $\Delta = g\mu_B B$ (with μ_B denoting the Bohr magneton and g the Lande factor) is shown in Fig. 96b for Mn atoms far and close to an oxide island edge, respectively. Linear fits constrained to $\Delta = 0$ at $B = 0$ yield slightly different g values, which – although both being close to the free electron value – is taken as indication for the influence of the local surrounding of the two different atoms.

9.3.2 Magnetic properties of artificially assembled linear spin chains Another way to modify the local spin is to bring several atoms close together as a similar discussion in connection with the Kondo systems above has shown. In experiments performed again by the group of A. Heinrich linear chains of different length were built up on thin insulating CuN islands grown on Cu(100) [330]. Figure 97a shows an STM image of a CuN island with

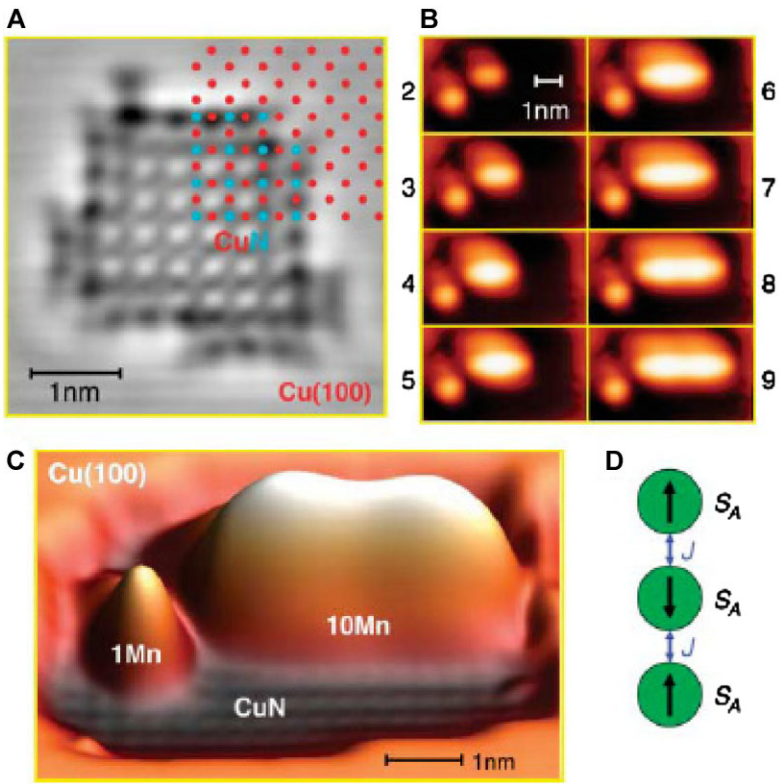

Figure 97 Mn chains on CuN. (a) STM image of a CuN island on Cu(100). Lattice positions of Cu (red dots) and N (blue dots) atoms are indicated. Notice that CuN islands appear as depressions. (b) STM images of the build-up of a chain of two to nine Mn atoms. Individual atoms in the chain cannot be resolved. (c) Perspective view of a chain of ten Mn atoms. The observed double-peak structure suggests the existence of one-dimensional delocalized electronic states as seen in metallic chains constructed on metal surfaces (see Section 8.3). (d) Scheme of AF coupling of three atomic spins described by the Heisenberg model (after Hirjibehedin et al. [330]).

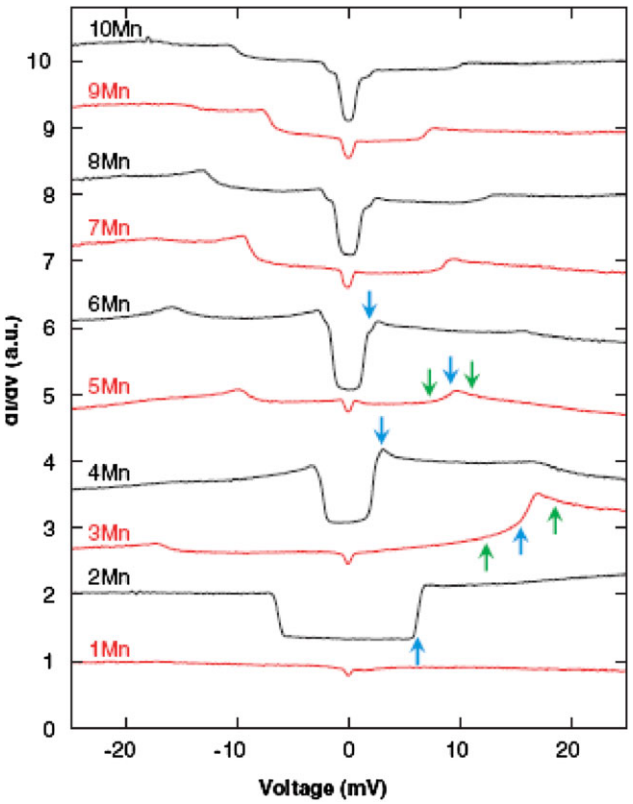

Figure 98 Conductance spectra of one to ten atom Mn chains on CuN taken with the tip positioned above the chain centers at $T = 0.6$ K and zero magnetic field. Spectra for odd numbered chains are in red and for even numbered chains in black. Notice that only the odd numbered chains show a similar behavior as the single atom due to their non-vanishing total spins (see text; after Hirjibehedin et al. [330]).

lattice positions of Cu (red dots) and N (blue dots) overlaid. In Fig. 97b the atom by atom build-up of linear chains of consisting of two to nine Mn atoms is shown and in Fig. 97c an STM image of a 10 atom chain is compared with that of a single atom. IETS investigations in magnetic fields of strength 0–7 Tesla proved the anti-ferromagnetic coupling of the Mn atoms (Fig. 97d) in the chains so that in even numbered chains the total spin is zero and in the odd numbered chains nonzero. Spin flip excitations in analogy to the single Mn atoms, which do not change the total spin but only the magnetic quantum number m, occur only for the odd numbered chains (Fig. 98). Steps in the conductance spectra in even numbered chains are interpreted to be due to changes of the total spin of the chain from the ground state with $S = 0$ and $m = 0$ to the excited state $S = 1$ and $m = -1, 0, +1$.

9.3.3 Further reading on magnetic IETS The pioneering work by Heinrich and co-workers that we have just reviewed has stirred a lot of activity in the field of controlled magnetic excitations. Recently, Hirjibehedin et al. [63] have extended the technique into a full-fledged magnetic IETS in which the magnetic anisotropy of atomic spins (Fe and Mn atoms) induced by the substrate has been measured and characterized. Furthermore, the same group showed exciting data on the interplay between Kondo physics and spin excitations in the case of a Co adsorbate [331], and later on they even studied the lifetime of excited spin states of an adatom [332, 333]. Other groups pursued spin IETS research by studying magnetic impurities in semiconductors [334], in molecules [335], on metal surfaces [336] producing a wealth of data and inciting more groups to produce excellent and exciting research that unfortunately is beyond the scope of this article. Theoretically, there has been some success explaining the main difference between spin and vibrational IETS [337] as well as producing quantitative accounts of the experimental data [338–340]. Reference [341] is a recent review that tries to summarize the state of the field from the experimental and theoretical perspective.

10 Outlook Manipulation of single atoms and molecules has certainly passed the stage, where company or university logos are produced on the nanoscale. Nowadays, it is used to investigate basic physics and chemistry on the single atom or molecular scale, including quantum phenomena or magnetic properties as outlined in Section 8 and specific reactions as outlined in Section 7. These possibilities are by far not exhausted nowadays. The critical size of quantum versus classical phenomena as well as for formation of macroscopic magnetism remains to be explored. The number of reactions to be investigated by manipulation is almost as unlimited as the number of existing molecules and their site dependence will only be resolvable by manipulation experiments. Solving the underlying physics and chemistry behind single atom and molecule interaction will furthermore allow in future to "create some lovely things" as envisioned by Primo Levi, a few of which have been outlined in Section 5, but most of them we so far not even have dreamed of.

Thus, future research will probably refer to topics like the following:

- Explore the basic laws of physics and basic interactions at the ultimate spatial limit.
- Create nano-materials with properties distinct from bulk material in all respects concerning their electric, thermal, and magnetic properties.
- Create meta-stable structures with specific functional properties that might be used in future nano-electronics.
- With respect to the former two points, manipulation into the substrate in atom by atom manner to create vertical artificial structures with thicknesses of a few layers is not at all exploited.

It is clear that these fascinating possibilities require also fresh and novel ideas!

We do not, however, believe that the art of analyzing and assembling compound matter with the STM (in the Milliped extension) will eventually reach the perfection of the fully automated board kitchen in the Star trek space ship, which is able to assemble in a very short time any dish as an exact copy of an earthly original on an atom by atom and molecule by molecule basis in macroscopic quantities. It is therefore very consolatory to observe that despite the preparation of atomically exact copies of his mother's "spaghetti al pesto" the Italian crew member always complains that they taste better in her kitchen than in outer space.

Acknowledgements The authors acknowledge all their collaborators at the physics department of the Free University Berlin for their scientific contributions and drive, especially Gerhard Meyer. Thanks to Leonhard Grill and Stefan Fölsch for valuable suggestions as well as Konrad Boom, Heiko Gawronski, Xin Ge, Jörg Henzl, Sarah Heidorn, Ming-Feng Hsieh, Fatih Kalkan, Ali Safiei, Carsten Sprodowski, Christopher Zaum at the Leibniz University of Hannover for critical reading of the manuscript. K.H.R. thanks the Max-Planck-Institut für Mikrostrukturforschung Halle, the Fritz-Haber-Institut Berlin of the MPG and the Sonderforschungsbereich 668, FB Physik/FU Berlin for their kind hospitality through several stays after his retirement.

References

[1] P. Levi, "The Monkey's Wrench" (Novel), Penguin Classics (Penguin Books, New York, 1995).
[2] G. Binnig and H. Rohrer, Rev. Mod. Phys. **59**, 615 (1987).
[3] D. M. Eigler and E. K. Schweizer, Nature **344**, 524 (1990).
[4] J. A. Stroscio and D. M. Eigler, Science **254**, 1319 (1991).
[5] G. Meyer, B. Neu, and K.-H. Rieder, Appl. Phys. A **60**, 343 (1995).
[6] L. Bartels, G. Meyer, and K.-H. Rieder, Phys. Rev. Lett. **79**, 697 (1997).
[7] Ph. Avouris, Acc. Chem. Res. **28**, 95 (1995).
[8] R. M. Nyffenegger and R. M. Penner, Chem. Rev. **97**, 1195 (1997).
[9] G. Binnig, H. Rohrer, Ch. Gerber, and E. Weibel, Phys. Rev. Lett. **49**, 57 (1982).
[10] G. Binnig, H. Rohrer, Ch. Gerber, and E. Weibel, Phys. Rev. Lett. **50**, 120 (1983).
[11] K. Morgenstern, Phys. Status Solidi B **242**, 773 (2005).
[12] S. Schintke, S. Messerli, K. Morgenstern, J. Nieminen, and W.-D. Schneider, J. Chem. Phys. **114**, 4206 (2001).
[13] H. Gawronski, J. Henzl, V. Simic-Milosevic, and K. Morgenstern, Appl. Surf. Sci. **253**, 9047 (2007).
[14] K. Morgenstern and J. Nieminen, J. Chem. Phys. **120**, 10786 (2004).
[15] W. Shockley, Phys. Rev. **56**, 317 (1939).
[16] F. Forstmann, Z. Phys. **235**, 69 (1970).
[17] S. D. Kevan and R. H. Gaylord, Phys. Rev. B **36**, 5809 (1987).
[18] P. O. Gartland and B. J. Slagsvold, Phys. Rev. B **12**, 4047 (1975).
[19] P. Heimann, H. Neddermeyer, and H. F. Roloff, J. Phys. C, Solid State Phys. **10**, L17 (1977).
[20] J. Tersoff and D. R. Hamann, Phys. Rev. B **31**, 805 (1985).
[21] M. F. Crommie, C. P. Lutz, and D. M. Eigler, Nature **363**, 524 (1993).
[22] M. F. Crommie, C. P. Lutz, and D. M. Eigler, Science **262**, 218 (1993).
[23] Ph. Avouris and I.-W. Lyo, Science **264**, 942 (1994).
[24] L. Bürgi, O. Jeandupeux, H. Brune, and K. Kern, Phys. Rev. Lett. **82**, 4516 (1999).
[25] P. T. Sprunger, L. Petersen, E. W. Plummer, E. Lægsgaard, and F. Besenbacher, Science **275**, 1764 (1997).
[26] K. Morgenstern, K.-F. Braun, and K.-H. Rieder, Phys. Rev. Lett. **89**, 226801 (2002).
[27] K. Morgenstern, K.-H. Rieder, and G. A. Fiete, Phys. Rev. B **71**, 155413 (2005).
[28] J. Li, W.-D. Schneider, R. Berndt, and S. Crampin, Phys. Rev. Lett. **80**, 3332 (1998).
[29] O. Jeandupeux, L. Bürgi, A. Hirstein, H. Brune, and K. Kern, Phys. Rev. B **59**, 15926 (1999).
[30] L. Bürgi, L. Petersen, H. Brune, and K. Kern, Surf. Sci. **447**, L157 (2000).
[31] W. A. Hofer, A. Garcia-Lekue, and H. Brune, Chem. Phys. Lett. **397**, 354 (2004).
[32] J. Bardeen, Phys. Rev. Lett. **6**, 57 (1961).
[33] I. Giaever, Phys. Rev. Lett. **5**, 147 (1960).
[34] J. Tersoff and D. R. Hamann, Phys. Rev. Lett. **50**, 1998 (1983).
[35] A. Baratoff, Physica **127B**, 143 (1984).
[36] P. Sautet and C. Joachim, Phys. Rev. B **38**, 12238 (1988).
[37] P. Sautet and C. Joachim, Chem. Phys. Lett. **185**, 23 (1991).
[38] J. Nieminen, S. Lahti, S. Paavilainen, and K. Morgenstern, Phys. Rev. B **66**, 165421 (2002).
[39] T. N. Todorov, G. A. D. Briggs, and A. P. Sutton, J. Phys.: Condens. Matter **5**, 2389 (1993).
[40] J. B. Pendry, A. B. Prêtre, and B. C. H. Krutzen, J. Phys.: Condens. Matter **3**, 4313 (1991).
[41] P. Sautet, Chem. Rev. **97**, 1097 (1997).
[42] P. Sautet and M.-L. Bocquet, Phys. Rev. B **53**, 4910 (1996).
[43] E. Niemi and J. Nieminen, Surf. Sci. **600**, 2548 (2006).
[44] B. N. J. Persson and J. E. Demuth, Solid State Commun. **57**, 769 (1986).
[45] B. N. J. Persson and A. Baratoff, Phys. Rev. Lett. **59**, 339 (1987).
[46] W. Ho, J. Chem. Phys. **117**, 11033 (2002).
[47] J. A. Stroscio, R. M. Feenstra, and A. P. Fein, Phys. Rev. Lett. **57**, 2579 (1986).
[48] N. D. Lang, Phys. Rev. B **34**, 5947 (1986).
[49] R. M. Feenstra, Phys. Rev. B **50**, 4561 (1994).
[50] B. Koslowski, C. Dietrich, A. Tschetschetkin, and P. Ziemann, Phys. Rev. B **75**, 035421 (2007).
[51] J. Nieminen, E. Niemi, V. Simic-Milosevic, and K. Morgenstern, Phys. Rev. B **72**, 195421 (2005).
[52] K. Morgenstern, J. Phys.: Condens. Matter **23**, 484007 (2011).
[53] M. C. Lennartz, V. Caciuc, N. Atodiresei, S. Karthäuser, and S. Blügel, Phys. Rev. Lett. **105**, 066801 (2010).
[54] M. Paulsson, T. Frederiksen, H. Ueba, N. Lorente, and M. Brandbyge, Phys. Rev. Lett. **100**, 226604 (2008).
[55] R. C. Jaklevic and J. Lambe, Phys. Rev. Lett. **17**, 1139 (1966).
[56] G. Binnig, N. Garcia, and H. Rohrer, Phys. Rev. B **32**, 1336 (1985).

[57] B. C. Stipe, M. A. Rezaei, and W. Ho, Science **280**, 1732 (1998).
[58] K. Morgenstern and K.-H. Rieder, J. Chem. Phys. **116**, 5746 (2002).
[59] L. J. Lauhon and W. Ho, Rev. Sci. Instrum. **72**, 216 (2001).
[60] J. Lambe and R. C. Jaklevic, Phys. Rev. **165**, 821 (1968).
[61] J. Klein, A. Léger, M. Belin, D. Défourneau, and M. J. L. Sangster, Phys. Rev. B **7**, 2336 (1973).
[62] A. J. Heinrich, J. A. Gupta, C. P. Lutz, and D. M. Eigler, Science **306**, 466 (2004).
[63] C. F. Hirjibehedin, C.-Y. Lin, A. F. Otte, M. Ternes, Ch. P. Lutz, B. A. Jones, and A. J. Heinrich, Science **317**, 1199 (2007).
[64] B. C. Stipe, M. A. Rezaei, and W. Ho, Phys. Rev. Lett. **82**, 1724 (1999).
[65] L. Vitali, S. D. Borisova, G. G. Rusina, E. V. Chulkov, and K. Kern, Phys. Rev. B **81**, 153409 (2010).
[66] A. Garcia-Lekue, D. Sanchez-Portal, A. Arnau, and T. Frederiksen, Phys. Rev. B **83**, 155417 (2011).
[67] L. Vitali, R. Ohmann, K. Kern, A. Garcia-Lekue, T. Frederiksen, D. Sanchez-Portal, and A. Arnau, Nano Lett. **10**, 657 (2010).
[68] H. Gawronski, K. Morgenstern, and K.-H. Rieder, Eur. Phys. J. D **35**, 349 (2005).
[69] N. Lorente, R. Rurali, and H. Tang, J. Phys.: Condens. Matter **17**, S1049 (2005).
[70] H. Gawronski, M. Mehlhorn, and K. Morgenstern, Science **319**, 930 (2008).
[71] M. Alducin, D. Sánchez-Portal, A. Arnau, and N. Lorente, Phys. Rev. Lett. **104**, 136101 (2010).
[72] N. Okabayashi, Y. Konda, and T. Komeda, Phys. Rev. Lett. **100**, 217801 (2008).
[73] N. Okabayashi, M. Paulsson, H. Ueba, Y. Konda, and T. Komeda, Phys. Rev. Lett. **104**, 077801 (2010).
[74] S. Monturet and N. Lorente, Phys. Rev. B **78**, 035445 (2008).
[75] C. Caroli, R. Combescot, P. Nozières, and D. Saint-James, J. Phys. C: Solid State Phys. **5**, 21 (1972).
[76] L. C. Davis, Phys. Rev. B **2**, 1714 (1970).
[77] Y. Meir and N. S. Wingreen, Phys. Rev. Lett. **68**, 2512 (1992).
[78] H. Haug and A.-P. Jauho, Quantum Kinetics in Transport and Optics of Semiconductors (Springer, Berlin, 2004).
[79] M. A. Gata and P. R. Antoniewicz, Phys. Rev. B **47**, 13797 (1993).
[80] C. Spataru and P. Budau, J. Phys.: Condens. Matter **9**, 8333 (1997).
[81] W. Domcke and L. S. Cederbaum, Phys. Rev. A **16**, 1465 (1977).
[82] J. P. Gauyacq, Dynamics of Negative Ions (World Scientific Publishing, Singapore, 1987).
[83] G. P. Salam, M. Persson, and R. E. Palmer, Phys. Rev. B **49**, 10655 (1994).
[84] S. Y. Tong, C. H. Li, and D. L. Mills, Phys. Rev. Lett. **44**, 407 (1980).
[85] J. Bonča and S. A. Trugman, Phys. Rev. Lett. **75**, 2566 (1995).
[86] N. Mingo and K. Makoshi, Surf. Sci. **438**, 261 (1999).
[87] N. Mingo and K. Makoshi, Phys. Rev. Lett. **84**, 3694 (2000).
[88] E. G. Emberly and G. Kirczenow, Phys. Rev. B **61**, 5740 (2000).
[89] N. Lorente and M. Persson, Phys. Rev. Lett. **85**, 2997 (2000).
[90] J. M. Soler, E. Artacho, J. D. Gale, A. García, J. Junquera, P. Ordejón, and D. Sánchez-Portal, J. Phys.: Condens. Matter **14**, 2745 (2002).
[91] M. Brandbyge, J.-L. Mozos, P. Ordejón, J. Taylor, and K. Stockbro, Phys. Rev. B **65**, 165401 (2002).
[92] N. Lorente, Appl. Phys. A **78**, 799 (2004).
[93] N. Lorente and M. Persson, Faraday Discuss. **117**, 277 (2000).
[94] N. Lorente, M. Persson, L. J. Lauhon, and W. Ho, Phys. Rev. Lett. **86**, 2593 (2001).
[95] L. D. Landau and L. M. Lifshitz, Quantum Mechanics, third edition (Pergamon Press, London, 1977).
[96] J. I. Pascual, J. Gómez-Herrero, D. Sánchez-Portal, and H.-P. Rust, J. Chem. Phys. **117**, 9531 (2002).
[97] M. S. Dresselhaus, G. Dresselhaus, and P. C. Eklund, Science of Fullerenes and Carbon Nanotubes (Academic Press, San Diego, 1996).
[98] J. R. Hahn, H. J. Lee, and W. Ho, Phys. Rev. Lett. **85**, 1914 (2000).
[99] A. A. Tseng and Z. Li, J. Nanosci. Nanotechnol. **7**, 2582 (2007).
[100] A. A. Baski, in: Advanced Semiconductor and Organic Nano-Techniques, edited by H. Morkoç (Academic Press, San Diego, 2002), chap. 3, p. 189.
[101] K.-F. Braun and K.-H. Rieder, Phys. Rev. Lett. **88**, 096801 (2002).
[102] L. Bartels, G. Meyer, and K.-H. Rieder, Appl. Phys. Lett. **71**, 213 (1997).
[103] L. J. Whitman, J. A. Stroscio, R. A. Dragoset, and R. J. Celotta, Science **251**, 1206 (1991).
[104] M. Alemani, M. V. Peters, S. Hecht, K.-H. Rieder, F. Moresco, and L. Grill, J. Am. Chem. Soc. **128**, 14446 (2006).
[105] L. Grill, K.-H. Rieder, F. Moresco, S. Stojkovic, A. Gourdon, and C. Joachim, Nano Lett. **6**, 2685 (2006).
[106] S. Hosoki, S. Hosaka, and T. Hasegawa, Appl. Surf. Sci. **60/61**, 643 (1992).
[107] S. Hosaka, S. Hosoki, T. Hasegawa, H. Koyanagi, T. Shintani, and M. Miyamoto, J. Vac. Sci. Technol. B **13**, 2813 (1995).
[108] J. B. Park, B. Jaeckel, and B. A. Parkinson, Langmuir **22**, 5334 (2006).
[109] Th. Schimmel, R. Kemnitzer, J. Küppers, H. Fuchs, and M. Lux-Steiner, Thin Solid Films **254**, 147 (1995).
[110] I.-W. Lyo and Ph. Avouris, Science **253**, 173 (1991).
[111] R. S. Becker, J. A. Golovchenko, and B. S. Swartzentruber, Nature **325**, 419 (1987).
[112] H. Uchida, D. Huang, F. Grey, and M. Aono, Phys. Rev. Lett. **70**, 2040 (1993).
[113] P. Molinàs-Mata, A. J. Mayne, and G. Dujardin, Phys. Rev. Lett. **80**, 3101 (1998).
[114] R. Bennewitz, J. N. Crain, A. Kirakosian, J.-L. Lin, J. L. McChesney, D. Y. Petrovykh, and F. J. Himpsel, Nanotechnology **13**, 499 (2002).
[115] S.-W. Hla, K.-F. Braun, and K.-H. Rieder, Phys. Rev. B **67**, 201402(R) (2003).
[116] A. W. Adamson and A. P. Gast, Physical Chemistry of Surfaces (Wiley, New York, 1997).

[117] M. Ternes, C. P. Lutz, C. F. Hirjibehedin, F. J. Giessibl, and A. J. Heinrich, Science **319**, 1066 (2008).
[118] G. Meyer, S. Zöphel, and K.-H. Rieder, Phys. Rev. Lett. **77**, 2113 (1996).
[119] G. Meyer, Rev. Sci. Instrum. **67**, 2960 (1996).
[120] B. Neu, G. Meyer, and K.-H. Rieder, Mod. Phys. Lett. B **9**, 963 (1995).
[121] G. Meyer, J. Repp, S. Zöphel, K.-F. Braun, S. W. Hla, S. Fölsch, L. Bartels, F. Moresco, and K. H. Rieder, Single Mol. **1**, 79 (2000).
[122] G. Meyer, L. Bartels, S. Zöphel, E. Henze, and K.-H. Rieder, Phys. Rev. Lett. **78**, 1512 (1997).
[123] J. J. Schulz, R. Koch, and K. H. Rieder, Phys. Rev. Lett. **84**, 4597 (2000).
[124] N. Pertaya, PhD Thesis, FU Berlin (2004).
[125] Y. Sugimoto, M. Abe, S. Hirayama, N. Oyabu, Ó. Custance, and S. Morita, Nature Mater. **4**, 156 (2005).
[126] L. Bartels, G. Meyer, and K.-H. Rieder, Chem. Phys. Lett. **273**, 371 (1997).
[127] D. L. Keeling, M. J. Humphry, R. H. J. Fawcett, P. H. Beton, C. Hobbs, and L. Kantorovich, Phys. Rev. Lett. **94**, 146104 (2005).
[128] M. Gajdoš, A. Eichler, J. Hafner, G. Meyer, and K.-H. Rieder, Phys. Rev. B **71**, 035402 (2005).
[129] A. J. Heinrich, C. P. Lutz, J. A. Gupta, and D. M. Eigler, Science **298**, 1381 (2002).
[130] A. Kühnle, G. Meyer, S. W. Hla, and K.-H. Rieder, Surf. Sci. **499**, 15 (2002).
[131] J. A. Stroscio and R. J. Celotta, Science **306**, 242 (2004).
[132] J. Li, R. Berndt, and W.-D. Schneider, Phys. Rev. Lett. **76**, 1888 (1996).
[133] J. Li, W.-D. Schneider, and R. Berndt, Appl. Phys. A **66**, S675 (1998).
[134] U. Kürpick and T. S. Rahman, Phys. Rev. Lett. **83**, 2765 (1999).
[135] K.-F. Braun, W.-H. Soe, C. F. J. Flipse, and K.-H. Rieder, Appl. Phys. Lett. **90**, 023118 (2007).
[136] C. Klein, A. Eichler, E. L. D. Hebenstreit, G. Pauer, R. Koller, A. Winkler, M. Schmid, and P. Varga, Phys. Rev. Lett. **90**, 176101 (2003).
[137] F. Moresco, G. Meyer, K.-H. Rieder, H. Tang, A. Gourdon, and C. Joachim, Appl. Phys. Lett. **78**, 306 (2001).
[138] F. Moresco, G. Meyer, K.-H. Rieder, H. Tang, A. Gourdon, and C. Joachim, Phys. Rev. Lett. **87**, 088302 (2001).
[139] T. A. Jung, R. R. Schlittler, and J. K. Gimzewski, Nature **386**, 696 (1997).
[140] F. Moresco, L. Gross, M. Alemani, K.-H. Rieder, H. Tang, A. Gourdon, and C. Joachim, Phys. Rev. Lett. **91**, 036601 (2003).
[141] L. Gross, F. Moresco, P. Ruffieux, A. Gourdon, C. Joachim, and K.-H. Rieder, Phys. Rev. B **71**, 165428 (2005).
[142] L. Gross, K.-H. Rieder, F. Moresco, S. M. Stojkovic, A. Gourdon, and C. Joachim, Nature Mater. **4**, 892 (2005).
[143] F. Chiaravalloti, L. Gross, K.-H. Rieder, S. M. Stojkovic, A. Gourdon, C. Joachim, and F. Moresco, Nature Mater. **6**, 30 (2007).
[144] L. Grill, K.-H. Rieder, F. Moresco, G. Rapenne, S. Stojkovic, X. Boujou, and C. Joachim, Nature Nanotechnol. **2**, 95 (2007).
[145] S.-W. Hla, Nature Nanotechnol. **2**, 82 (2007) (News and Views).
[146] F. Moresco, G. Meyer, K.-H. Rieder, H. Tang, A. Gourdon, and C. Joachim, Phys. Rev. Lett. **86**, 672 (2001).
[147] S.-W. Hla, K.-F. Braun, B. Wassermann, and K.-H. Rieder, Phys. Rev. Lett. **93**, 208302 (2004).
[148] M. Porto, M. Urbakh, and J. Klafter, Phys. Rev. Lett. **84**, 6058 (2000).
[149] L. Grill, F. Moresco, P. Jiang, C. Joachim, A. Gourdon, and K.-H. Rieder, Phys. Rev. B **69**, 035416 (2004).
[150] M. Böhringer, K. Morgenstern, W.-D. Schneider, and R. Berndt, Angew. Chem. **111**, 832 (1999); Angew. Chem. Int. Ed. **38**, 821 (1999).
[151] M. Böhringer, K. Morgenstern, W.-D. Schneider, R. Berndt, F. Mauri, A. De Vita, and R. Car, Phys. Rev. Lett. **83**, 324 (1999).
[152] K. H. Rieder, G. Meyer, K. F. Braun, S. W. Hla, F. Moresco, K. Morgenstern, J. Repp, S. Foelsch, and L. Bartels, Europhys. News **34**, 95 (2003).
[153] K.-H. Rieder, G. Meyer, F. Moresco, K. Morgenstern, S.-W. Hla, J. Repp, M. Alemani, L. Grill, L. Gross, M. Mehlhorn, H. Gawronski, V. Simic-Milosevic, J. Henzl, K. F. Braun, S. Foelsch, and L. Bartels, J. Phys. Conf. Ser. **19**, 175 (2005).
[154] K.-H. Rieder, G. Meyer, S.-W. Hla, F. Moresco, K. F. Braun, K. Morgenstern, J. Repp, S. Foelsch, and L. Bartels, Philos. Trans. R. Soc. Lond. A **362**, 1207 (2004).
[155] L. Grill, J. Phys.: Condens. Matter **22**, 084023 (2010).
[156] S. Selvanathan, M. V. Peters, J. Schwarz, S. Hecht, and L. Grill, Appl. Phys. A **93**, 247 (2008).
[157] J. Henzl, M. Mehlhorn, and K. Morgenstern, Nanotechnology **18**, 495502 (2007).
[158] Ch. Bombis, F. Ample, J. Mielke, M. Mannsberger, C. J. Villagómez, Ch. Roth, C. Joachim, and L. Grill, Phys. Rev. Lett. **104**, 185502 (2010).
[159] C. J. Villagómez, T. Sasaki, J. M. Tour, and L. Grill, J. Am. Chem. Soc. **132**, 16848 (2010).
[160] D. M. Eigler, C. P. Lutz, and W. E. Rudge, Nature **352**, 600 (1991).
[161] X. Bouju, C. Joachim, C. Girard, and P. Sautet, Phys. Rev. B **47**, 7454 (1993).
[162] X. Bouju, C. Joachim, and C. Girard, Phys. Rev. B **59**, R7845 (1999).
[163] X. Bouju, C. Joachim, C. Girard, and H. Tang, Phys. Rev. B **63**, 085415 (2001).
[164] N. Mingo and F. Flores, Thin Solid Films **318**, 69 (1998).
[165] N. Mingo and F. Flores, Surf. Sci. **395**, 342 (1998).
[166] R. Raval, S. F. Parker, M. E. Pemble, P. Hollins, J. Pritchard, and M. A. Chesters, Surf. Sci. **203**, 353 (1988).
[167] L. Bartels, G. Meyer, K.-H. Rieder, D. Velic, E. Knoesel, A. Hotzel, M. Wolf, and G. Ertl, Phys. Rev. Lett. **80**, 2004 (1998).
[168] S. Zöphel, J. Repp, G. Meyer, and K. H. Rieder, Chem. Phys. Lett. **310**, 145 (1999).
[169] J. A. Nieminen, E. Niemi, and K.-H. Rieder, Surf. Sci. **552**, L47 (2004).
[170] J. Repp, G. Meyer, S. M. Stojković, A. Gourdon, and C. Joachim, Phys. Rev. Lett. **94**, 026803 (2005).
[171] L. Lafferentz, F. Ample, H. Yu, S. Hecht, C. Joachim, and L. Grill, Science **323**, 1193 (2009).

[172] R. Temirov, A. Lassise, F. B. Anders, and F. S. Tautz, Nanotechnology **19**, 065401 (2008).
[173] N. Fournier, C. Wagner, C. Weiss, R. Temirov, and F. S. Tautz, Phys. Rev. B **84**, 035435 (2011).
[174] F. Kühner, M. Erdmann, and H. E. Gaub, Phys. Rev. Lett. **97**, 218301 (2006).
[175] S. K. Kufer, E. M. Puchner, H. Gumpp, T. Liedl, and H. E. Gaub, Science **319**, 594 (2008).
[176] C. Bombis, F. Ample, L. Lafferentz, H. Yu, S. Hecht, C. Joachim, and L. Grill, Angew. Chem. Int. Ed. **48**, 9966 (2009).
[177] M. Koch, F. Ample, C. Joachim, and L. Grill, Nature Nanotechnol. **7**, 713 (2012).
[178] K. Morgenstern, H. Gawronski, M. Mehlhorn, and K.-H. Rieder, J. Mod. Opt. **51**, 2813 (2004).
[179] H. Gawronski, J. Carrasco, A. Michaelides, and K. Morgenstern, Phys. Rev. Lett. **101**, 136102 (2008).
[180] K. Morgenstern and K.-H. Rieder, Chem. Phys. Lett. **358**, 250 (2002).
[181] V. Simic-Milosevic, M. Mehlhorn, K.-H. Rieder, J. Meyer, and K. Morgenstern, Phys. Rev. Lett. **98**, 116102 (2007).
[182] S. G. Tikhodeev and H. Ueba, Phys. Rev. B **70**, 125414 (2004).
[183] L. Soukiassian, A. J. Mayne, M. Carbone, and G. Dujardin, Phys. Rev. B **68**, 035303 (2003).
[184] R. E. Walkup, D. M. Newns, and Ph. Avouris, Phys. Rev. B **48**, 1858 (1993).
[185] S. Gao, M. Persson, and B. I. Lundqvist, Solid State Commun. **84**, 271 (1992).
[186] S. Gao, M. Persson, and B. I. Lundqvist, Phys. Rev. B **55**, 4825 (1997).
[187] J. W. Gadzuk, Phys. Rev. B **44**, 13466 (1991).
[188] H. Guo, P. Saalfrank, and T. Seideman, Prog. Surf. Sci. **62**, 239 (1999).
[189] S. Alavi, R. Rousseau, and T. Seideman, J. Chem. Phys. **113**, 4412 (2000).
[190] T. Seideman, J. Phys.: Condens. Matter **15**, R521 (2003).
[191] H. Ueba and B. N. J. Persson, Surf. Sci. **566–568**, 1 (2004).
[192] T. Mii, S. Tikhodeev, and H. Ueba, Surf. Sci. **502–503**, 26 (2002).
[193] H. Ueba, Surf. Rev. Lett. **10**, 771 (2003).
[194] S. Gao, Surf. Sci. **313**, 448 (1994).
[195] B. N. J. Persson and Ph. Avouris, Surf. Sci. **390**, 45 (1997).
[196] H. Ueba, T. Mii, N. Lorente, and B. N. J. Persson, J. Chem. Phys. **123**, 084707 (2005).
[197] J. I. Pascual, N. Lorente, Z. Song, H. Conrad, and H.-P. Rust, Nature **423**, 525 (2003).
[198] B. C. Stipe, M. A. Rezaei, and W. Ho, Phys. Rev. Lett. **81**, 1263 (1998).
[199] C. Matsumoto, Y. Kim, T. Okawa, Y. Sainoo, and M. Kawai, Surf. Sci. **587**, 19 (2005).
[200] B. C. Stipe, M. A. Rezaei, W. Ho, S. Gao, M. Persson, and B. I. Lundqvist, Phys. Rev. Lett. **78**, 4410 (1997).
[201] B. C. Stipe, M. A. Rezaei, and W. Ho, Science **279**, 1907 (1998).
[202] S.-W. Hla, L. Bartels, G. Meyer, and K.-H. Rieder, Phys. Rev. Lett. **85**, 2777 (2000).
[203] K. Morgenstern, Acc. Chem. Res. **42**, 213 (2009).
[204] K. Morgenstern, Surf. Interface Anal. **42**, 1634 (2010).
[205] K. Morgenstern, Prog. Surf. Sci. **86**, 115 (2011).
[206] J. Henzl, M. Mehlhorn, H. Gawronski, K.-H. Rieder, and K. Morgenstern, Angew. Chem. Int. Ed. **45**, 603 (2006); Angew. Chem. **118**, 617 (2006).
[207] T. Komeda, Prog. Surf. Sci. **78**, 41 (2005).
[208] L. Grill, J. Phys.: Condens. Matter **20**, 053001 (2008).
[209] H. Ueba, Surf. Rev. Lett. **10**, 771 (2003).
[210] B. C. Stipe, M. A. Rezaei, and W. Ho, Phys. Rev. Lett. **79**, 4397 (1997).
[211] J. Gaudioso, H. J. Lee, and W. Ho, J. Am. Chem. Soc. **121**, 8479 (1999).
[212] K. S. Nakayama, E. Graugnard, and J. H. Weaver, Phys. Rev. Lett. **89**, 266106 (2002).
[213] Y. Nakamura, Y. Mera, and K. Maeda, Surf. Sci. **531**, 68 (2003).
[214] Y. Nakamura, Y. Mera, and K. Maeda, Surf. Sci. **487**, 127 (2001).
[215] K. Maeda and Y. Nakamura, Surf. Sci. **528**, 110 (2003).
[216] T. Komeda, Y. Kim, M. Kawai, B. N. J. Persson, and H. Ueba, Science **295**, 2055 (2002).
[217] K. Liu and S. Gao, Phys. Rev. Lett. **95**, 226102 (2005).
[218] S. G. Tikhodeev and H. Ueba, Phys. Rev. Lett. **102**, 246101 (2009).
[219] T. Kumagai, S. Hatta, H. Okuyama, and T. Aruga, J. Chem. Phys. **126**, 234708 (2007).
[220] M. Ohara, Y. Kim, S. Yanagisawa, Y. Morikawa, and M. Kawai, Phys. Rev. Lett. **100**, 136104 (2008).
[221] K. Motobayashi, C. Matsumoto, Y. Kim, and M. Kawai, Surf. Sci. **602**, 3136 (2008).
[222] K. Motobayashi, Y. Kim, H. Ueba, and M. Kawai, Phys. Rev. Lett. **105**, 076101 (2010).
[223] T. Kumagai, M. Kaizu, H. Okuyama, S. Hatta, T. Aruga, I. Hamada, and Y. Morikawa, Phys. Rev. B **79**, 035423 (2009).
[224] H. L. Tierney, C. J. Murphy, A. D. Jewell, A. E. Baber, E. V. Iski, H. Y. Khodaverdian, A. F. McGuire, N. Klebanov, and E. C. H. Sykes, Nature Nanotechnol. **6**, 625 (2011).
[225] C. Manzano, W.-H. Soe, H. S. Wong, F. Ample, A. Gourdon, N. Chandrasekhar, and C. Joachim, Nature Mater. **8**, 576 (2009).
[226] D. Écija, W. Auwärter, S. Vijayaraghavan, K. Seufert, F. Bischoff, K. Tashiro, and J. V. Barth, Angew. Chem. Int. Ed. **50**, 3872 (2011).
[227] R. S. Becker, G. S. Higashi, Y. J. Chabal, and A. J. Becker, Phys. Rev. Lett. **65**, 1917 (1990).
[228] T.-C. Shen, C. Wang, G. C. Abeln, J. R. Tucker, J. W. Lyding, Ph. Avouris, and R. E. Walkup, Science **268**, 1590 (1995).
[229] K. Stokbro, C. Thirstrup, M. Sakurai, U. Quaade, B. Y.-K. Hu, F. Perez-Murano, and F. Grey, Phys. Rev. Lett. **80**, 2618 (1998).
[230] E. T. Foley, A. F. Kam, J. W. Lyding, and Ph. Avouris, Phys. Rev. Lett. **80**, 1336 (1998).
[231] C. Thirstrup, M. Sakurai, T. Nakayama, and M. Aono, Surf. Sci. **411**, 203 (1998).
[232] L. Bartels, M. Wolf, T. Klamroth, P. Saalfrank, A. Kühnle, G. Meyer, and K.-H. Rieder, Chem. Phys. Lett. **313**, 544 (1999).
[233] S. N. Patitsas, G. P. Lopinski, O. Hul'ko, D. J. Moffat, and R. A. Wolkow, Surf. Sci. **457**, L425 (2000).
[234] P. A. Sloan, M. F. G. Hedouin, R. E. Palmer, and M. Persson, Phys. Rev. Lett. **91**, 118301 (2003).

[235] M. Sicot, O. Kurnosikov, O. A. O. Adam, H. J. M. Swagten, and B. Koopmans, Phys. Rev. B **77**, 035417 (2008).
[236] G. Dujardin, R. E. Walkup, and Ph. Avouris, Science **255**, 1232 (1992).
[237] M. A. Rezaei, B. C. Stipe, and W. Ho, J. Chem. Phys. **109**, 6075 (1998).
[238] St. J. Dixon-Warren, E. T. Jensen, and J. C. Polanyi, J. Chem. Phys. **98**, 5938 (1993).
[239] P. H. Lu, J. C. Polanyi, and D. Rogers, J. Chem. Phys. **111**, 9905 (1999).
[240] P. A. Sloan and R. E. Palmer, Nature **434**, 367 (2005).
[241] P. A. Sloan and R. E. Palmer, Nano Lett. **5**, 835 (2005).
[242] Y. Nakamura, Y. Mera, and K. Maeda, Surf. Sci. **601**, 2189 (2007).
[243] R. Martel, Ph. Avouris, and I.-W. Lyo, Science **272**, 385 (1996).
[244] J. K. Gimzewski, T. A. Jung, M. T. Cuberes, and R. R. Schlittler, Surf. Sci. **386**, 101 (1997).
[245] L. J. Lauhon and W. Ho, Phys. Rev. Lett. **84**, 1527 (2000).
[246] L. J. Lauhon and W. Ho, J. Phys. Chem. A **104**, 2463 (2000).
[247] T. Komeda, Y. Kim, Y. Fujita, Y. Sainoo, and M. Kawai, J. Chem. Phys. **120**, 5347 (2004).
[248] Y. Kim, T. Komeda, and M. Kawai, Phys. Rev. Lett. **89**, 126104 (2002).
[249] M. Mehlhorn, H. Gawronski, and K. Morgenstern, Phys. Rev. Lett. **101**, 196101 (2008).
[250] S.-W. Hla, G. Meyer, and K.-H. Rieder, Chem. Phys. Lett. **370**, 431 (2003).
[251] J. R. Hahn and W. Ho, J. Chem. Phys. **122**, 244704 (2005).
[252] C. Sprodowski, M. Mehlhorn, and K. Morgenstern, J. Phys.: Condens. Matter **22**, 264005 (2010).
[253] H.-J. Shin, J. Jung, K. Motobayashi, S. Yanagisawa, Y. Morikawa, Y. Kim, and M. Kawai, Nature Mater. **9**, 442 (2010).
[254] Y. Mera, M. Yoshino, Y. Nakamura, K. Saishu, and K. Maeda, Surf. Sci. **601**, 5207 (2007).
[255] P. Maksymovych, D. C. Sorescu, K. D. Jordan, and J. T. Yates, Jr., Science **322**, 1664 (2008).
[256] M.-F. Hsieh, H.-D. Li, D.-S. Lin, and K. Morgenstern, J. Phys. Chem. C **114**, 14173 (2010).
[257] Y. Jiang, Q. Huan, L. Fabris, G. C. Bazan, and W. Ho, Nature Chem. **5**, 36 (2013).
[258] U. J. Quaade, K. Stokbro, C. Thirstrup, and F. Grey, Surf. Sci. **415**, L1037 (1998).
[259] U. J. Quaade, K. Stokbro, R. Lin, and F. Grey, Nanotechnology **12**, 265 (2001).
[260] X. H. Qiu, G. V. Nazin, and W. Ho, Phys. Rev. Lett. **93**, 196806 (2004).
[261] M. Lastapis, M. Martin, D. Riedel, L. Hellner, G. Comtet, and G. Dujardin, Science **308**, 1000 (2005).
[262] J. A. Stroscio, F. Tavazza, J. N. Crain, R. J. Celotta, and A. M. Chaka, Science **313**, 948 (2006).
[263] J. Repp, G. Meyer, S. Paavilainen, F. E. Olsson, and M. Persson, Science **312**, 1196 (2006).
[264] V. Simic-Milosevic, J. Meyer, and K. Morgenstern, Phys. Chem. Chem. Phys. **10**, 1916 (2008).
[265] J. Henzl and K. Morgenstern, Phys. Chem. Chem. Phys. **12**, 6035 (2010).
[266] J. Henzl and K. Morgenstern, J. Phys. Chem. C **115**, 10056 (2011).
[267] J. Henzl, T. Bredow, and K. Morgenstern, Chem. Phys. Lett. **435**, 278 (2007).
[268] M. Bazarnik, J. Henzl, R. Czajka, and K. Morgenstern, Chem. Commun. **47**, 7764 (2011).
[269] A. Safiei, J. Henzl, and K. Morgenstern, Phys. Rev. Lett. **104**, 216102 (2010).
[270] J. Henzl, P. Puschnig, C. Ambrosch-Draxl, A. Schaate, B. Ufer, P. Behrens, and K. Morgenstern, Phys. Rev. B **85**, 035410 (2012).
[271] C. Dri, M. V. Peters, J. Schwarz, S. Hecht, and L. Grill, Nature Nanotechnol. **3**, 649 (2008).
[272] V. Simic-Milosevic, J. Meyer, and K. Morgenstern, Angew. Chem. Int. Ed. **48**, 4061 (2009).
[273] M. Parschau, D. Passerone, K.-H. Rieder, H. J. Hug, and K.-H. Ernst, Angew. Chem. Int. Ed. **48**, 4065 (2009).
[274] S. Selvanathan, M. V. Peters, S. Hecht, and L. Grill, J. Phys.: Condens. Matter **24**, 354013 (2012).
[275] T. Kumagai, M. Kaizu, S. Hatta, H. Okuyama, T. Aruga, I. Hamada, and Y. Morikawa, Phys. Rev. Lett. **100**, 166101 (2008).
[276] T. Kumagai, A. Shiotari, H. Okuyama, S. Hatta, T. Aruga, I. Hamada, T. Frederiksen, and H. Ueba, Nature Mater. **11**, 167 (2012).
[277] Y. Ootsuka, T. Frederiksen, H. Ueba, and M. Paulsson, Phys. Rev. B **84**, 193403 (2011).
[278] K. Teichmann, M. Wenderoth, S. Loth, R. G. Ulbrich, J. K. Garleff, A. P. Wijnheijmer, and P. M. Koenraad, Phys. Rev. Lett. **101**, 076103 (2008).
[279] A. Saedi, A. van Houselt, R. van Gastel, B. Poelsema, and H. J. W. Zandvliet, Nano Lett. **9**, 1733 (2009).
[280] V. Simic-Milosevic and K. Morgenstern, J. Am. Chem. Soc. **131**, 416 (2009).
[281] A. Sperl, J. Kröger, and R. Berndt, Phys. Rev. B **81**, 035406 (2010).
[282] T. Kudernac, N. Ruangsupapichat, M. Parschau, B. Maciá, N. Katsonis, S. R. Harutyunyan, K.-H. Ernst, and B. L. Feringa, Nature **479**, 208 (2011).
[283] J. Schaffert, M. C. Cottin, A. Sonntag, H. Karacuban, C. A. Bobisch, N. Lorente, J.-P. Gauyacq, and R. Möller, Nature Mater. **12**, 223 (2013).
[284] M. A. Gata and P. R. Antoniewicz, Phys. Rev. B **60**, 8999 (1999).
[285] K. Stokbro, B. Y.-K. Hu, C. Thirstrup, and X. C. Xie, Phys. Rev. B **58**, 8038 (1998).
[286] D. Teillet-Billy, J. P. Gauyacq, and M. Persson, Phys. Rev. B **62**, R13306 (2000).
[287] S. Alavi, R. Rousseau, S. N. Patitsas, G. P. Lopinski, R. A. Wolkow, and T. Seideman, Phys. Rev. Lett. **85**, 5372 (2000).
[288] S. Tikhodeev, M. Natario, K. Makoshi, T. Mii, and H. Ueba, Surf. Sci. **493**, 63 (2001).
[289] N. Lorente and J. I. Pascual, Philos. Trans. R. Soc. Lond. A **362**, 1227 (2004).
[290] L. Gross, F. Moresco, L. Savio, A. Gourdon, C. Joachim, and K.-H. Rieder, Phys. Rev. Lett. **93**, 056103 (2004).
[291] L. Bürgi, O. Jeandupeux, A. Hirstein, H. Brune, and K. Kern, Phys. Rev. Lett. **81**, 5370 (1998).
[292] J. Henzl and K. Morgenstern, Phys. Rev. Lett. **98**, 266601 (2007).
[293] G. A. Fiete, J. S. Hersch, E. J. Heller, H. C. Manoharan, C. P. Lutz, and D. M. Eigler, Phys. Rev. Lett. **86**, 2392 (2001).

[294] E. J. Heller, M. F. Crommie, C. P. Lutz, and D. M. Eigler, Nature **369**, 464 (1994).
[295] H. C. Manoharan, C. P. Lutz, and D. M. Eigler, Nature **403**, 512 (2000).
[296] J. Kliewer, R. Berndt, and S. Crampin, New J. Phys. **3**, 22 (2001).
[297] P. Atkins, Physical Chemistry, fourth and later editions (Oxford University Press, Oxford, 2002).
[298] N. W. Ashcroft and N. D. Mermin, Solid State Physics (Cengage Learning EMEA, Andover, UK, 1976).
[299] N. Nilius, T. M. Wallis, and W. Ho, Science **297**, 1853 (2002).
[300] S. Fölsch, P. Hyldgaard, R. Koch, and K. H. Ploog, Phys. Rev. Lett. **92**, 056803 (2004).
[301] J. Lagoute, X. Liu, and S. Fölsch, Phys. Rev. B **74**, 125410 (2006).
[302] S. L. Hulbert, P. D. Johnson, N. G. Stoffel, W. A. Royer, and N. V. Smith, Phys. Rev. B **31**, 6815 (1985).
[303] J. Lagoute, C. Nacci, and S. Fölsch, Phys. Rev. Lett. **98**, 146804 (2007).
[304] T. M. Wallis, N. Nilius, G. Mikaelian, and W. Ho, J. Chem. Phys. **122**, 011101 (2005).
[305] A. S. Barker Jr., and A. J. Sievers, Rev. Mod. Phys. **47**, S1 (1975).
[306] J. Lagoute, X. Liu, and S. Fölsch, Phys. Rev. Lett. **95**, 136801 (2005).
[307] M. D. Daybell, in: Magnetism, Vol. 5, edited by G. T. Rado and H. Suhl (Academic Press, San Diego, 1973), p. 121.
[308] A. Narath, in: Magnetism, Vol. 5, edited by G. T. Rado and H. Suhl (Academic Press, San Diego, 1973), p. 149.
[309] M. Plihal and J. W. Gadzuk, Phys. Rev. B **63**, 085404 (2001).
[310] U. Fano, Phys. Rev. **124**, 1866 (1961).
[311] J. Li, W.-D. Schneider, R. Berndt, and B. Delley, Phys. Rev. Lett. **80**, 2893 (1998).
[312] V. Madhavan, W. Chen, T. Jamneala, M. F. Crommie, and N. S. Wingreen, Science **280**, 567 (1998).
[313] W. Chen, T. Jamneala, V. Madhavan, and M. F. Crommie, Phys. Rev. B **60**, R8529 (1999).
[314] P. Wahl, P. Simon, L. Diekhöner, V. S. Stepanyuk, P. Bruno, M. A. Schneider, and K. Kern, Phys. Rev. Lett. **98**, 056601 (2007).
[315] T. Jamneala, V. Madhavan, and M. F. Crommie, Phys. Rev. Lett. **87**, 256804 (2001).
[316] C. Joachim, J. K. Gimzewski, and A. Aviram, Nature **408**, 541 (2000).
[317] J. Repp, Ph.D. Thesis, Freie Universität Berlin (2002).
[318] J. Repp, G. Meyer, F. E. Olsson, and M. Persson, Science **305**, 493 (2004).
[319] F. E. Olsson, S. Paavilainen, M. Persson, J. Repp, and G. Meyer, Phys. Rev. Lett. **98**, 176803 (2007).
[320] J. Repp and G. Meyer, Appl. Phys. A **85**, 399 (2006).
[321] W. Hebenstreit, J. Redinger, Z. Horozova, M. Schmid, R. Podloucky, and P. Varga, Surf. Sci. **424**, L321 (1999).
[322] S. Fölsch, A. Riemann, J. Repp, G. Meyer, and K. H. Rieder, Phys. Rev. B **66**, 161409(R) (2002).
[323] S. Fölsch, A. Helms, A. Riemann, J. Repp, G. Meyer, and K. H. Rieder, Surf. Sci. **497**, 113 (2002).
[324] J. Repp, S. Fölsch, G. Meyer, and K. H. Rieder, Phys. Rev. Lett. **86**, 252 (2001).
[325] R. Smoluchowski, Phys. Rev. **60**, 661 (1941).
[326] F. Matthaei, S. Heidorn, K. Boom, C. Bertram, A. Safiei, J. Henzl, and K. Morgenstern, J. Phys.: Condens. Matter **24**, 354006 (2012).
[327] F. J. Himpsel, A. Kirakosian, J. N. Crain, J.-L. Lin, and D. Y. Petrovykh, Solid State Commun. **117**, 149 (2001).
[328] P. E. Sheehan and C. M. Lieber, Science **272**, 1158 (1996).
[329] X. Bouju, C. Joachim, and C. Girard, Phys. Rev. B **50**, 7893 (1994).
[330] C. F. Hirjibehedin, C. P. Lutz, and A. J. Heinrich, Science **312**, 1021 (2006).
[331] A. F. Otte, M. Ternes, K. von Bergmann, S. Loth, H. Brune, C. P. Lutz, C. F. Hirjibehedin, and A. J. Heinrich, Nature Phys. **4**, 847 (2008).
[332] S. Loth, K. von Bergmann, M. Ternes, A. F. Otte, C. P. Lutz, and A. J. Heinrich, Nature Phys. **6**, 340 (2010).
[333] S. Loth, M. Etzkorn, C. P. Lutz, D. M. Eigler, and A. J. Heinrich, Science **329**, 1628 (2010).
[334] A. A. Khajetoorians, B. Chilian, J. Wiebe, S. Schuwalow, F. Lechermann, and R. Wiesendanger, Nature **467**, 1084 (2010).
[335] N. Tsukahara, K.-i. Noto, M. Ohara, S. Shiraki, N. Takagi, Y. Takata, J. Miyawaki, M. Taguchi, A. Chainani, S. Shin, and M. Kawai, Phys. Rev. Lett. **102**, 167203 (2009).
[336] T. Balashov, A. F. Takács, W. Wulfhekel, and J. Kirschner, Phys. Rev. Lett. **97**, 187201 (2006).
[337] N. Lorente and J.-P. Gauyacq, Phys. Rev. Lett. **103**, 176601 (2009).
[338] M. Persson, Phys. Rev. Lett. **103**, 050801 (2009).
[339] J. Fransson, Nano Lett. **9**, 2414 (2009).
[340] J. Fernández-Rossier, Phys. Rev. Lett. **102**, 256802 (2009).
[341] J.-P. Gauyacq, N. Lorente, and F. D. Novaes, Prog. Surf. Sci. **87**, 63 (2012).